



UNIVERSITAT_{DE}
BARCELONA

Colloidal dynamics in artificial particle ice systems

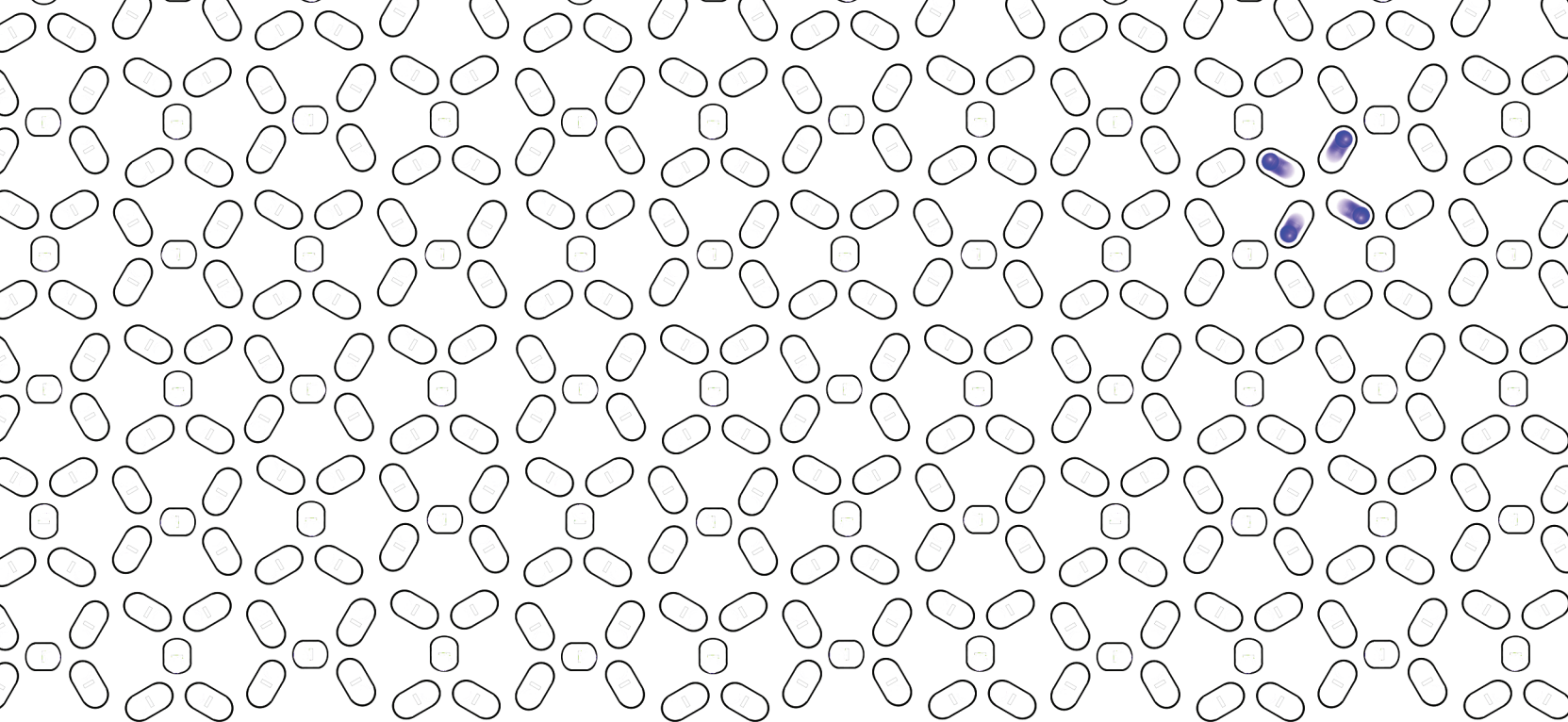
Carolina Rodríguez Gallo



Aquesta tesi doctoral està subjecta a la llicència **Reconeixement- NoComercial – Compartir Igual 4.0. Espanya de Creative Commons.**

Esta tesis doctoral está sujeta a la licencia **Reconocimiento - NoComercial – Compartir Igual 4.0. España de Creative Commons.**

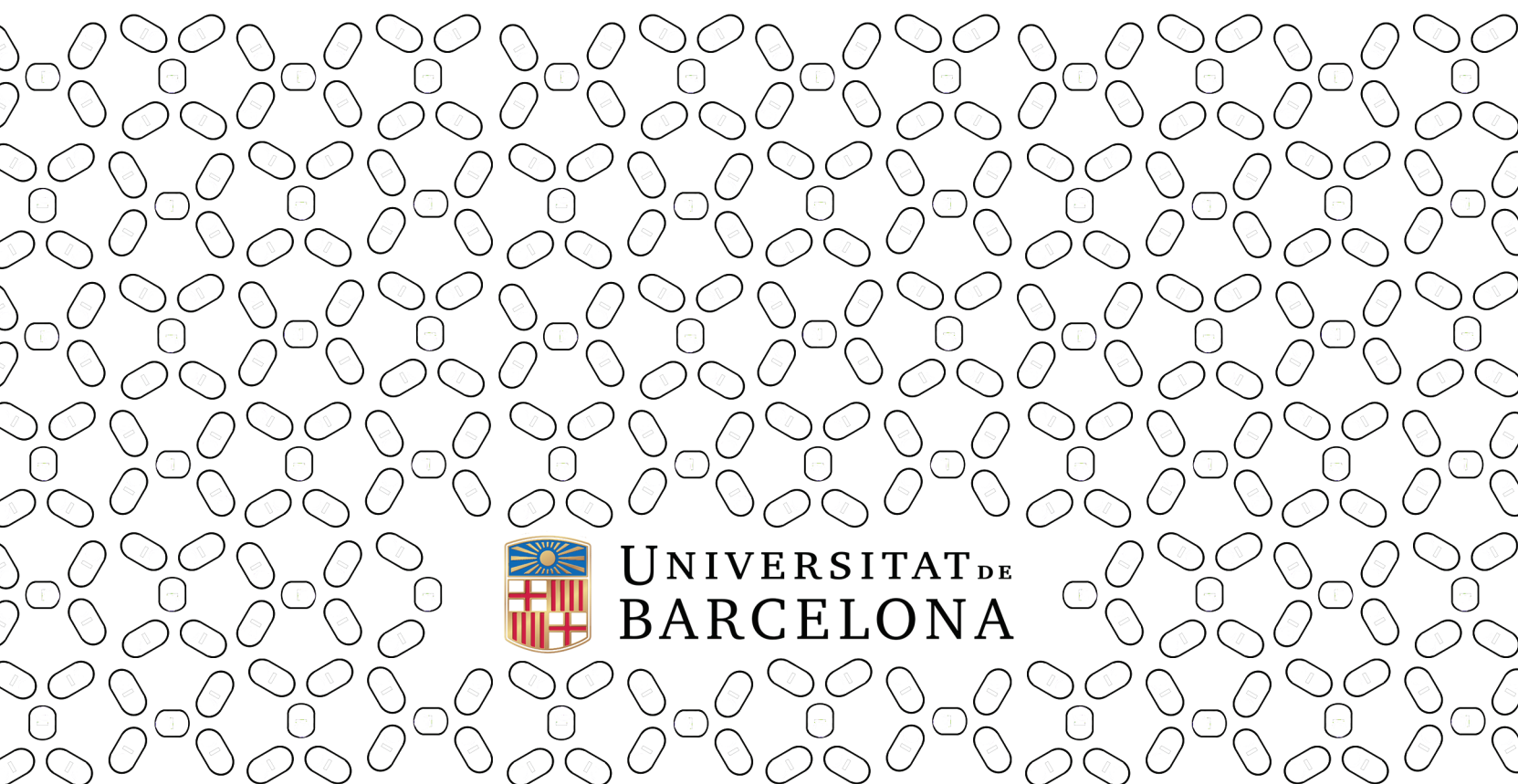
This doctoral thesis is licensed under the **Creative Commons Attribution-NonCommercial-ShareAlike 4.0. Spain License.**



Ph.D. Thesis

Colloidal dynamics **in artificial particle ice systems**

Carolina Rodríguez-Gallo



UNIVERSITAT DE
BARCELONA

Colloidal dynamics in artificial particle ice systems

Carolina Rodríguez-Gallo

Directors: Pietro Tierno i Antonio Ortiz-Ambriz

Programa de doctorat en Física

Tutor: Giancarlo Franzese

Departament de Física de la Matèria Condensada

Facultat de Física

Barcelona



UNIVERSITAT DE
BARCELONA

ABSTRACT

Geometric frustration is a general phenomenon influencing the behavior of diverse natural systems across different length scales. Geometric frustration arises when the symmetry of the interaction between the elements and the system geometry do not match. This incompatibility generates competing interactions, which could give rise to a rich phenomenology. In systems where geometrical frustration is present, we may have a degenerate ground state at zero temperature, a rich phase diagram, or intrinsic disorder. Nowadays, due to technological advances, scientists can construct artificial systems displaying geometric frustration at the nanometer scale. These systems have the potential to be used as a novel magnetic-based logic and memory device, but they can also help us further comprehend the nature of this exotic phenomenon. In this thesis, I used an Artificial Colloidal Ice (ACI) as a platform to investigate the geometric frustration in systems that can be characterized by spin degree of freedom. Colloidal particles are the interacting units of an ACI and present the advantage of having accessible time and length scales. In addition, colloidal particles have demonstrated the capability to behave as model systems for atoms or molecules; both systems display length scales that make them more difficult to be characterized. In this thesis, I have combined numerical simulations using the LAMMPS molecular dynamics simulator and experimental realizations. For the experimental work, I used video optical microscopy, state-of-art soft lithography techniques, and holographic optical tweezers. This thesis presents the result of four projects that study the ACI system under different conditions, which have resulted in four publications. In the first project, I investigated the effects of finite-size boundaries of different type in ACI. As a result, I observed that the boundaries can influence the bulk behavior; and in particular, antiferromagnetic boundaries can reach a full ground state of the system, faster than other types of boundaries. In the second project, I computed the colloidal and lattice parameters to achieve an extensive degeneracy in a square ACI. In particular, I observed a reentrant behavior: the system, starting from a disordered configuration, reaches a low-energy state to then achieve disorder again. The third project studied the effects of changing the geometry of an ACI without altering its topology. I observed that excitations of the ground state with opposite topological charges can be accumulated in a certain sublattice location in a mixed coordination lattice or be balanced. Finally, in the fourth project, I investigated the low-energy states of a Cairo ACI, a lattice made of irregular pentagons. The Cairo ACI presents a high degree of degeneracy, exhibiting a disordered ensemble at low-energy states that correspond to a frustrated antiferrotoroid.

CONTENTS

Resumen en castellano	v
Resum en català	vi
Publications	vii
List of Figures	ix
Symbols	xiii
Acronyms	xiv
I INTRODUCTION	1
1 GENERAL INTRODUCTION	3
1.1 Thesis aims and structure	3
II FROM NATURAL TO ARTIFICIAL SYSTEMS	5
2 FROM NATURAL TO ARTIFICIAL SYSTEMS	7
2.1 Geometrical frustration	7
2.2 Natural frustrated systems	7
2.2.1 Water Ice	9
2.2.2 Spin Ice	10
2.3 Ice-rule	11
2.4 Properties and challenges	12
2.5 Artificial systems	14
2.5.1 Artificial spin ice	14
2.5.2 Artificial colloidal ice	16
III ARTIFICIAL COLLOIDAL ICE	19
3 ARTIFICIAL COLLOIDAL ICE	21
3.1 Colloidal particles	21
3.1.1 Brownian motion and diffusion	21
3.1.2 Overdamped dynamics	24
3.1.3 Colloidal interactions	25
3.2 Paramagnetic colloids	30
3.3 Realization of artificial colloidal ice	32
3.4 Properties of artificial colloidal ice	37
3.4.1 Single coordination lattices	38
3.4.2 Decimated and mixed coordination lattices	42
3.4.3 Degeneracy recovery	43
3.4.4 Interactions between topological charges	47
IV METHODS	49
4 SIMULATIONS	51
4.1 Brownian dynamics simulations	51

4.1.1	Workflow	53
4.1.2	Input parameters	54
4.1.3	Analyzing output trajectories	55
5	EXPERIMENTS	57
5.1	Magneto optic experimental set up	57
5.1.1	Optical tweezers	57
5.1.2	Holographic optical tweezers	59
5.1.3	Experimental setup	61
5.1.4	Magnetic fields	63
5.2	Microfabrication	64
5.2.1	AZ1512 HS resist	65
5.2.2	SU-8 resist and PDMS replica	68
5.3	Sample preparation	69
5.4	Data analysis	70
V	RESULTS	71
6	PUBLICATIONS	73
6.1	Publication 1	73
6.2	Publication 2	75
6.3	Publication 3	77
6.4	Publication 4	79
VI	CONCLUSIONS	81
7	CONCLUSIONS	83
VII	APPENDIX	87
A	PROTOCOL BASED ON AZ1512 HS RESIST	89
B	PROTOCOL USED TO REALIZE THE MICROSTRUCTURES BASED ON SU-8 AND PDMS REPLICA	91
C	BISTABLE GRAVITATIONAL TRAP CHARACTERIZATION FOR A THERMAL ARTIFICIAL COLLOIDAL ICE	93
	BIBLIOGRAPHY	95

RESUMEN EN CASTELLANO

A lo largo de estos cuatro años de tesis doctoral he tenido la oportunidad de estudiar en detalle los efectos de la frustración geométrica. En particular he estudiado sus efectos en un sistema modelo, compuesto de coloides paramagnéticos confinados gravitacionalmente en micro retículos con distintas geometrías. La frustración geométrica emerge en sistemas físicos que no son capaces de minimizar todas sus interacciones al mismo tiempo debido a restricciones de tipo geométrico, es decir en sistemas donde la simetría de la interacción no es compatible con la geometría del sistema. De esta manera se convierten en sistemas con interacciones en competición que generan fenomenología emergente. Ejemplos de esta fenomenología son la presencia de una entropía residual a bajas temperaturas y por lo tanto la propiedad de tener más de un estado de energía fundamental, lo que generara sistemas con un desorden intrínseco. Otras propiedades exóticas son la capacidad de aumentar el orden del sistema bajo los efectos de fluctuaciones térmicas o la rotura espontánea de simetría. Muchos sistemas, naturales o artificiales, a diferentes escalas presentan estas propiedades. Ejemplos son el agua cuando se hace hielo, los pirocloros de tierras raras y el hielo de espín artificial. El sistema modelo que he utilizado para hacer una pequeña contribución al entendimiento de estos tipos de sistemas físicos se llama hielo coloidal artificial. La ventaja de este sistema es el uso de coloides. Estos, debidos a su tamaño, en la micro escala, presentan una dinámica accesible con sistemas de microscopia óptica convencional. Además, hoy en día, la posición de partículas micrométricas se puede controlar mediante el uso de pinzas ópticas, facilitando así el control de la configuración inicial del sistema. Todo esto, sumado al hecho de haber demostrado ser sistemas modelos atómicos hacen de los coloides un excelente candidato para estudiar fenomenología también presente a otras escalas de longitud. Los métodos utilizados en esta tesis para estudiar este sistema han sido la realización de simulaciones numéricas de dinámica Browniana y realizaciones experimentales. Para esta última hemos utilizado técnicas de microfabricación en sala blanca, pinzas ópticas holográficas y video-microscopia óptica. Esta tesis se estructura de la siguiente manera. En la primera parte de la tesis contextualizo nuestro sistema modelo en el actual marco de investigación. Después de esto introduzco brevemente algunas propiedades de las partículas coloidales junto a la descripción detallada de nuestro sistema y las propiedades que ya se conocen de él. Seguidamente presento la metodología empleada en esta tesis y adjunto las cuatro publicaciones realizadas a lo largo de estos años de tesis doctoral. Finalmente hago un pequeño resumen de los objetivos y conclusiones de cada publicación y

las principales conclusiones de esta tesis junto con algunas perspectivas de futuro de este trabajo.

Al llarg d'aquests quatre anys de tesi doctoral he tingut l'oportunitat d'estudiar detalladament els efectes de la frustració geomètrica. En particular he estudiat els seus efectes en un sistema model, compost de col·loides paramagnètics confinats gravitacionalment en micro reticles amb diferents geometries. La frustració geomètrica emergeix en sistemes físics que no són capaços de minimitzar totes les seves interaccions al mateix temps a causa de restriccions de tipus geomètric, és a dir en sistemes on la simetria de la interacció no és compatible amb la geometria del sistema. D'aquesta manera es converteixen en sistemes amb interaccions en competició que generen fenomenologia emergent. Exemples d'aquesta fenomenologia són la presència d'una entropia residual a baixes temperatures i per tant la propietat de tenir més d'un estat d'energia fonamental, la qual cosa genera sistemes amb un desordre intrínsec. Altres propietats exòtiques són la capacitat d'augmentar l'ordre del sistema sota els efectes de fluctuacions tèrmiques o el trencament espontani de simetria. Molts sistemes, naturals o artificials, a diferents escales presenten aquestes propietats. Exemples són l'aigua quan es fa gel, els piroclors de terres rares i el gel d'espín artificial. El sistema model que he utilitzat per a fer una petita contribució a l'enteniment d'aquests tipus de sistemes físics es diu gel col·loidal artificial. L'avantatge d'aquest sistema és l'ús de col·loides. Aquests, deguts a la seva grandària, en la micro escala, presenten una dinàmica accessible amb sistemes de microscòpia òptica convencional. A mes a mes, avui dia, la posició de partícules micromètriques es pot controlar mitjançant l'ús de pinces òptiques, facilitant així el control de la configuració inicial del sistema. Tot això sumat al fet d'haver demostrat ser sistemes models atòmics fan dels col·loides un excel·lent candidat per a estudiar fenomenologia també present a altres escales de longitud. Els mètodes utilitzats en aquesta tesi per a estudiar aquest sistema han estat la realització de simulacions numèriques de dinàmica Browniana i realitzacions experimentals. Per a aquesta última hem utilitzant tècniques de microfabricació en sala blanca, pinces òptiques hologràfiques i vídeo-microscòpia òptica. Aquesta tesi s'estructura de la següent manera. En la primera part de la tesi contextualitzo el nostre sistema model en l'actual marc de recerca. Després d'això introduixo breument algunes propietats de les partícules col·loidals al costat de la descripció detalla del nostre sistema i les propietats que ja es coneixen d'ell. Seguidament presento la metodologia emprada en aquesta tesi i adjunto les quatre publicacions realitzades al llarg d'aquests anys de tesi doctoral. Finalment faig un petit resum dels objectius i conclusions de cada publicació i les principals conclusions d'aquesta tesi juntament amb algunes perspectives de futur d'aquest treball.

PUBLICATIONS

- C. Rodríguez-Gallo, A. Ortiz-Ambriz, C. Nisoli and P. Tierno. Ice rule breakdown and frustrated antiferrotoroidicity in an artificial colloidal Cairo ice. *New Journal of Physics* **25**, (2023) 103007
- C. Rodríguez-Gallo, A. Ortiz-Ambriz, C. Nisoli and P. Tierno. Geometric control of topological charge transfer in Shakti-Cairo colloidal ice. *Communications physics* **6**, (2023) 113
- C. Rodríguez-Gallo, A. Ortiz-Ambriz and P. Tierno. Degeneracy and hysteresis in a bidisperse colloidal ice. *Physical Review Research* **3**, (2021) 043023
- C. Rodríguez-Gallo, A. Ortiz-Ambriz and P. Tierno. Topological Boundary Constraints in Artificial Colloidal Ice. *Physical Review Letters* **126**, (2021) 188001

LIST OF FIGURES

Figure 1	Geometrical frustration	8
Figure 2	Water Ice	9
Figure 3	Spin ice	11
Figure 4	Analogy among water ice and spin ice	12
Figure 5	Magnetic monopoles	13
Figure 6	Artificial spin ice	15
Figure 7	Artificial colloidal ice	17
Figure 8	Colloidal particles	22
Figure 9	Hamaker theory	26
Figure 10	Electrical double layer	28
Figure 11	Deryaguin-Landau-Verwey-Overbeek theory	29
Figure 12	Magnetic dipole-dipole interaction	31
Figure 13	Double well grooves	32
Figure 14	Collective frustration	33
Figure 15	Colloids in double wells	34
Figure 16	Vertex energy hierarchy in a square ACI	36
Figure 17	Loss of degeneracy in 2D systems	37
Figure 18	Defects in single coordination lattice in ACI	38
Figure 19	Defects in single coordination lattice in ASI	39
Figure 20	Clockwise and counterclockwise mapping	40
Figure 21	Honeycomb lattice	41
Figure 22	Decimated square lattice	42
Figure 23	Quasidegeneracy in ACI	44
Figure 24	Degeneracy in ASI	46
Figure 25	Charge-charge interaction	47
Figure 26	Scheme simulation	52
Figure 27	Simulation workflow	53
Figure 28	Colloidal ice graph	55
Figure 29	Energy vertex hierarchy in square lattice	56
Figure 30	Scattering on a sphere	58
Figure 31	Spatial light modulator	59
Figure 32	Holograms	60
Figure 33	Experimental set-up	61
Figure 34	Diagram holographic optical tweezers	62
Figure 35	Sample stage	63
Figure 36	Particle trapping	64
Figure 37	Positive and negative photoresists	65
Figure 38	AZ1512 HS microstructures	66
Figure 39	Vertical profiles	67

Figure 40	SEM images of AZ1512 HS microstructures	67
Figure 41	Peeling off PDMS film	68
Figure 42	PDMS microstructures	69
Figure 43	Colloidal ice	70
Figure 44	Thermal colloidal ice	94

SYMBOLS

W	Number of ground state configurations
S	Entropy
k_B	Boltzmann constant
T	Temperature
μ_0	Vacuum permeability
μ_B	Bohr magneton
g	Landé factor
J	Coupling constant
σ	Spin state
D	Diffusion coefficient
γ	Drag coefficient
η	Fluid viscosity
ρ	Mass density
μ_f	Magnetic permeability of the fluid
χ	Volumetric magnetic susceptibility
B	Magnetic field
q	Topological charge
z	Lattice coordination
V	Volume
Re	Reynolds number
P	Laser power

ACRONYMS

ACI Artificial Colloidal Ice

ASI Artificial Spin Ice

SEM Scanning electron microscope

PEEM Photoelectron emission microscopy

XMCD X-ray magnetic circular dichroism

AFM Atomic force microscopy

MFM Magnetic force microscopy

LAMMPS Large-scale Atomic/Molecular Massively Parallel Simulator

HOT Holographic optical tweezers

DOE Diffractive optical element

SLM Spatial light modulator

LC Liquid crystal

CMOS Complementary Metal-Oxide-Semiconductor

PDMS Polydimethylsiloxane

DWL Direct write laser

TMAH tetranethyl-ammonium hydroxide

RPM Revolutions per minute

SDS Sodium dodecyl sulfate

Part I

INTRODUCTION

GENERAL INTRODUCTION

1.1 THESIS AIMS AND STRUCTURE

The aim of this thesis is to study the dynamics of colloidal particles confined to lattices that display geometric frustration. Colloidal particles can be used as a model system for atoms or molecules since, at the collective level, they are governed by similar statistical and thermodynamic laws, equations of state [1], crystallization processes [2, 3], and exhibit glassiness [4, 5], similarly to a collection of atoms. Of course, atoms and colloids are rather different when considered at the level of individual elements. Atoms need a quantum description and cannot be exactly localized due to the Heisenberg principle. On the other hand, colloids can be described in terms of the laws of classical physics. Moreover, interactions in colloids can be fine-tuned [6], and microscopic particles have accessible time and length scales, which can be determined via conventional optical microscopy techniques. For these reasons, we use colloidal particles as model systems to investigate different phenomena in condensed matter that interest not only atoms and molecules but also mesoscale magnetic systems. In particular, this thesis is centered on the effects of geometric frustration that emerge when interacting particles are confined within a lattice of lithographic double wells. This experimental system is realized using state-of-art microfabrication techniques and optical tweezers. The interaction between the particles was tuned by an external magnetic field, and the particle relative positions and the underlined lattice were carefully designed to mimic emergent behavior presented by other systems on smaller length scales, such as water ice and spin ice. This thesis is structured in six parts. After this first introduction in [Part i](#), We will present the main concepts related to this thesis in [Part ii](#). In particular, we will describe the concept of geometric frustration and its consequences in physical systems. Then, we will describe the discovery of some frustrated natural systems and the subsequent introduction of artificial systems, such as artificial spin ice, that were used as model systems for exotic magnetic materials. In [Part iii](#), we will introduce the main topic of this thesis, the Artificial Colloidal Ice, accompanied by a brief summary of the most important properties of colloidal particles. At the end of this part, we will mention the main contributions of this thesis. In [Part iv](#), we will explain the methods used in this thesis: the numerical simulation model and all the experimental techniques. In [Part v](#), four publications are included, which represent the results of this thesis. Finally, in [Part vi](#), we will summarize the main findings of the publications, present all the conclusions of the thesis and discuss the future prospects that this work opens.

Part II

FROM NATURAL TO ARTIFICIAL SYSTEMS

2.1 GEOMETRICAL FRUSTRATION

Geometrical frustration in condensed matter physics is observed in a wide variety of systems [7–16]. All of them have in common that geometrical constraints will not allow the interaction energies between the system units to be minimized at the same time. As a consequence of these competing interactions, the system may give rise to novel emergent phenomena. Geometrically frustrated systems may display some peculiar properties such as a residual entropy at low temperatures [15], a degenerate ground state [8, 10, 12], fractionalization of topological charges [8, 15], glassiness [7, 13, 16], order by disorder [17, 18] or symmetry breaking [9, 14]. To explain what geometrical frustration is, the canonical example is the case of a lattice of N interacting Ising spins, where geometric frustration can arise if the symmetry of the lattice does not match the symmetry of the interaction. The most popular example is the case of three antiferromagnetically coupled Ising-like spins located at the corners of a triangle. Once two of the spins are placed anti-aligned, i.e., they minimize the magnetic energy due to the antiferromagnetic interaction, the third one can no longer point in a direction opposite to both spins, and thus it generates a frustrated bond, see [Figure 1](#).

When there are no arrangements that satisfy all the pair interactions, the lattice geometry forbids the formation of a unique low-temperature ground state configuration. Another example of a simple geometry that produces frustration is locating Ising spins at the vertex of a square. Three of the spins at the vertices have a ferromagnetic interaction, and the other one has an antiferromagnetic one. Also in this case, the system is frustrated, and the ground state is degenerate. The study of geometrically frustrated systems focuses on understanding how frustration affects the physical properties and whether is possible to control them by controlling the system geometry.

2.2 NATURAL FRUSTRATED SYSTEMS

In the following section, we will introduce two natural frustrated systems: water ice and ferromagnetic pyrochlore oxides. Both systems, despite their intrinsically different properties, exhibit some similarities. In particular, they both follow similar rules at low temperatures, the so-called ice rule.

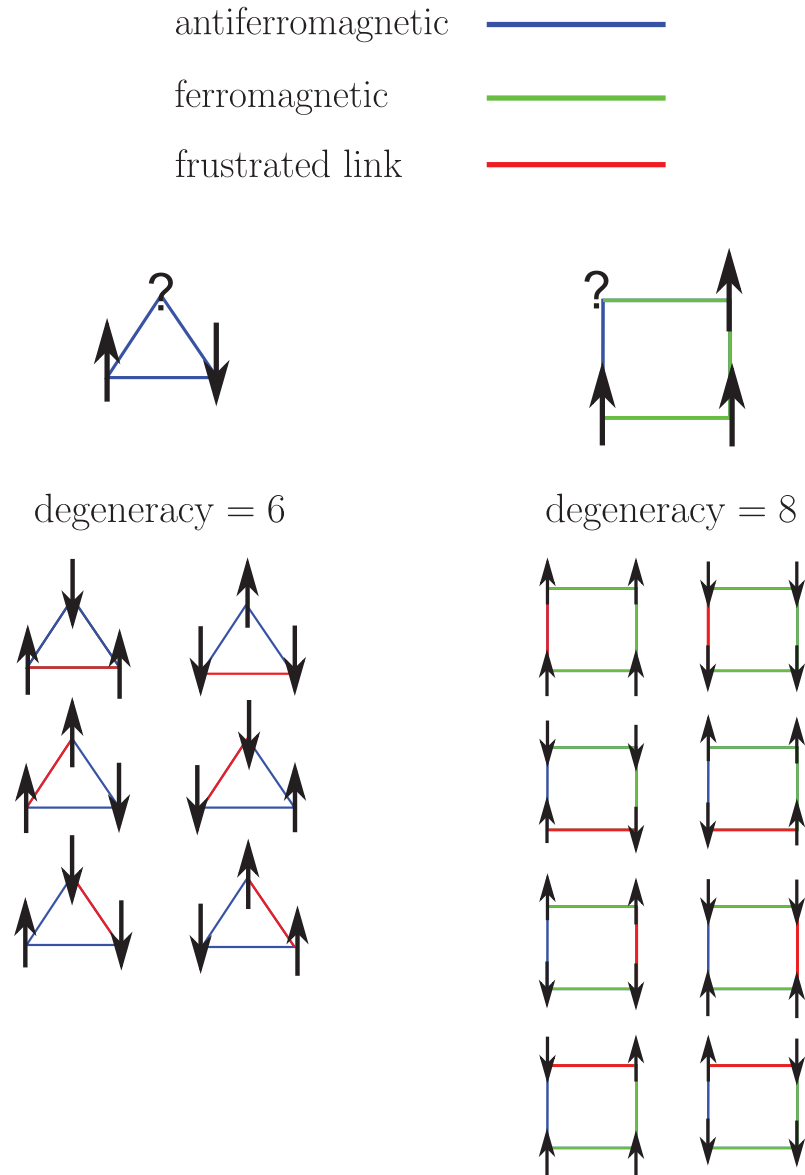


Figure 1: Examples of geometrically frustrated systems. In the triangular lattice all the interactions are antiferromagnetic (blue), while in the square lattice all the interactions are ferromagnetic (green) unless one link. Both systems have a degenerate ground state.

2.2.1 Water Ice

A distinctive feature of water ice is the presence of a residual entropy at very low temperatures. While the crystalline structure of Oxygen atoms in water ice was determined by X-ray studies in 1921 [19, 20], the location of Hydrogen atoms that give rise to such behavior is still discussed. As shown in Figure 2, the Oxygen atoms are known to be surrounded by four other Oxygen atoms, forming the structure of a tetrahedron.

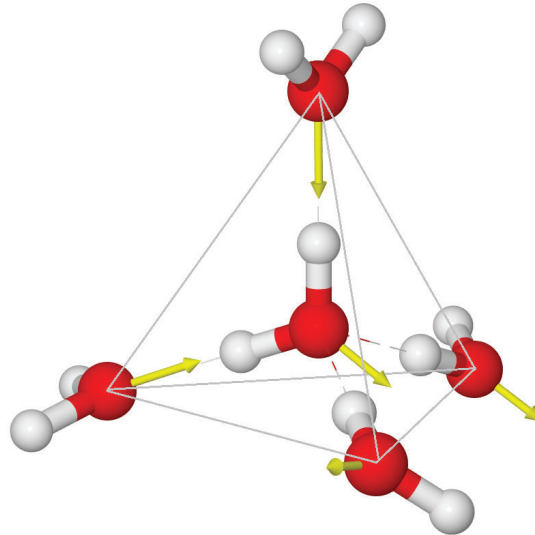


Figure 2: Schematic showing the arrangements of atoms in water ice. Big red spheres represent Oxygen atoms and white spheres Hydrogen atoms. Dashed lines represent hydrogen bonds and yellow arrows the electric dipole moment of the water molecules.

Between each O-O pair, we have one Hydrogen atom. By supposing that the Hydrogens in between two Oxygen atoms were either covalently bound or hydrogen bound to each Oxygen atom, Pauling, in 1935, was able to compute analytically the residual entropy at low temperatures [21].

He used the following argument: consider a lattice with N vertices (or Oxygen atoms) and $2N$ edges (Hydrogen/Covalent bonds). If we suppose that each edge has two possible configurations, we will have 2^{2N} possible configurations for a Hydrogen atom to be connected to the Oxygen. However, we have to consider the fact that the O at the center of a tetrahedron can only have two covalently bounded H and two hydrogen bounded H. This will add some constraints to reduce the number of available states. Thus, of the total $2^4 = 16$ possible configurations per tetrahedron, only 6 are possible (considering that we need to have 2 covalent bonds and two hydrogen bonds with the O at the center). As a consequence, the number of ground state configurations W is:

$$W = \left(\frac{6}{16}\right)^N 2^{2N} = \left(\frac{3}{8}2^2\right)^N = \left(\frac{3}{2}\right)^N \quad (1)$$

and thus the entropy, following the Boltzmann relationship, is:

$$\frac{S}{Nk_B} = \ln\left(\frac{3}{2}\right) \approx 0.405 \quad (2)$$

Using this assumption, Pauling was able to estimate the residual entropy of water at low temperatures, as previously measured by Giauque and Stout [22]. This hypothesis was developed a few years before by Muriel F. Ashley and W. F. Giauque (1932) [23].

Water ice has a complex phase diagram, and several phases at different pressure-temperature states have been observed. In fact, water ice is a polymorph, it has many crystalline forms [24] and it can also exhibit glassy behavior [25]. We can say, hence, that the atomic arrangement of water leads to extravagant properties, such as the increasing in volume by reaching the solid phase, the unexpected values of the heat capacity at constant pressure or the presence of liquid water in organic cells at temperatures as low as -20°C in insects, and -47°C in plants. Some works suggest that all these properties may be the clue to understanding why water played such an important role in the presence of life [26]. Understanding this system can also be crucial to understanding some water ice phases expected to be found in some planets, such as Neptune and Uranus, where its potentially excellent electrical conductivity might account for the huge magnetic fields [27].

2.2.2 Spin Ice

Similar to water ice, other natural magnetic compounds show a similar geometric frustration effect. Those materials are the ferromagnetic pyrochlore oxides $R_2Ti_2O_7$, with R = rare earth such as Ho or Dy [28, 29]. The magnetic cations of rare earth pyrochlores, Ho^{3+} or Dy^{3+} , hold a large magnetic moment (\approx ten Bohr magnetons, $\mu \approx 10\mu_B$), and are located on the sites of a lattice made by corner-sharing tetrahedral forming the so-called, pyrochlore lattice, [Figure 3](#).

These magnetic compounds are usually modeled by considering a set of Ising-like spins arranged on a pyrochlore lattice. These spins interact via a ferromagnetic dipole-dipole interaction and a weaker, antiferromagnetic exchange interaction [32, 33]. This model is called the nearest neighbor spin ice model, which is a truncation of the *dipolar spin ice* model [34, 35]. It is characterized by the Hamiltonian:

$$H = \frac{\mu_0 g^2 \mu_B^2}{4\pi} \sum_{i>j} \frac{\sigma_i \cdot \sigma_j - 3(\hat{\mathbf{r}}_{ij} \cdot \sigma_i)(\hat{\mathbf{r}}_{ij} \cdot \sigma_j)}{r_{ij}^3} - \sum_{\langle i,j \rangle} J_{ij} \sigma_i \cdot \sigma_j \quad (3)$$

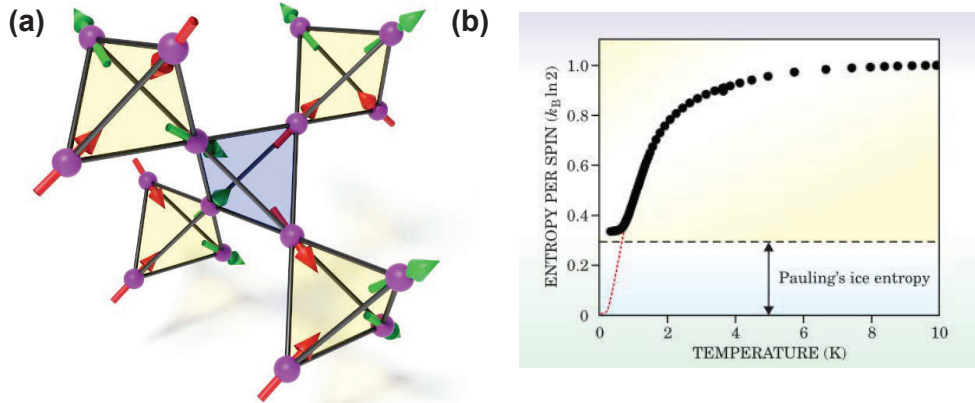


Figure 3: (a) Schematic showing the spin ice material with Ising-like spins arranged in the vertices of a pyrochlore lattice. Colored arrows indicate the magnetic moments of the rare earths. These moments can point either towards or away from the vertex center, which has tetrahedral geometry. Image reproduced from [30]. (b) The entropy per spin S of the spin-ice compound dysprosium titanate $DyC_2Ti_2O_7$ as a function of temperature T . Image reproduced from [31].

Where μ_0 is the vacuum permeability, μ_B the Bohr magneton, J_{ij} the ferromagnetic exchange constant, r_{ij} the distance between spins and σ_i the spins associated with particle i at location r_i .

Due to the interactions in Equation 3 and the constraints that the magnetic moments can align along the edge of the tetrahedron at each vertex, the system follows similar local rules as in water ice. The O atom at the center of the tetrahedron can form hydrogen bonds with only two of the four neighboring H atoms. Similarly, only two (of the four available) magnetic moments are allowed to point toward the center of the tetrahedron. The ground-state entropy of pyrochlore spin ice is thus expected to be similar to that of water ice. Indeed, it was demonstrated by Arthur P. Ramirez et al. [36], who performed specific heat measurements of $Dy_2Ti_2O_7$, that the resulting entropy agreed with the theoretical value estimated previously by Pauling for water ice, see Figure 3 (b).

2.3 ICE-RULE

Both the water ice and spin ice systems follow the ice-rules. These rules were introduced first by John Desmond Bernal and Ralph H. Fowler, thus also called the Bernal-Fowler rules [37], to describe the water ice's behavior. In both systems, there is the constraint of having a local balancing of atoms or spins in a

single tetrahedron. Satisfying the ice rule for water ice means having two H atoms inside the tetrahedron and covalently bound to the O atom at the center and two H atoms outside the tetrahedron and connected through hydrogen bonds with the O atom at the center. On the other hand, the ice-rule for natural spin ice systems is achieved when two spins point into the tetrahedron and two out of it, [Figure 4](#). To be in the ground state, one tetrahedron must satisfy this property. An excited state instead appears when there is an imbalance in the number of spins (or H atoms) pointing in (or out) to the tetrahedron.

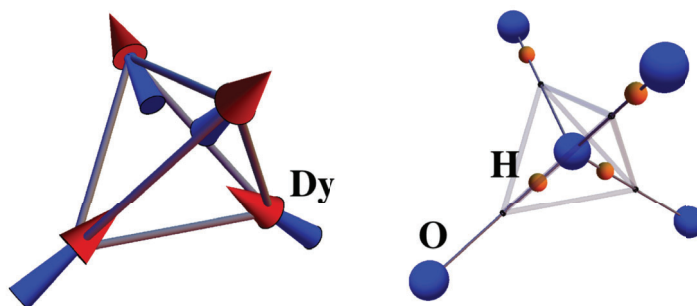


Figure 4: Analogy between water ice and spin ice. On the left, we have a tetrahedron with four Dy^{3+} magnetic moments at the vertices. On the right, a tetrahedron with a water molecule inside it. H atoms near the O at the center are covalently bound to it, and H atoms far away from the O at the center are connected through hydrogen bonds to the O at the center. Here we also have the nearest neighboring oxygen atoms that will be located in neighboring tetrahedra. Image reproduced from [38].

Another way to think of the ice rule is that no tetrahedron acts as a source or sink of hydrogen atoms or spins. But instead, the ground state could be conceived as a divergence free condition on an emergent vector field [39, 40].

2.4 PROPERTIES AND CHALLENGES

Some fascinating properties of the ferromagnetic pyrochlore oxides have been the subject of intense research in the field of frustrated magnetism. One particular example is the interest received by local spin excitations, which were theoretically conceived as emergent quasi-particles or magnetic monopoles. They are a manifestation of the correlations present in a strongly interacting many-body system. A simplified way to describe these excitations is by replacing the magnetic dipoles in the pyrochlore sites with dumbbells consisting of equal and opposite magnetic charges, see [Figure 5](#). By doing that, the energy of the system is equivalent to [Equation 3](#), up to corrections that are small everywhere and vanish algebraically as $1/r^5$. This way, if we locally violate

the ice rule (and thus invert one dumbbell), see Figure 5 (b)(d) we obtain in each tetrahedron a net magnetic charge with opposite sign (a pair monopole anti-monopole), with a magnetic interaction. In addition, those two emergent particles can be unconfined due to the extensive degeneracy of the ground state. By inducing more local flips, those two excitations can further move away from each other without implying any energy cost. Indeed, such unconfined monopoles feel a magnetic Coulomb interaction; more details can be found in [41, 42].

Given the complexity of three-dimensional magnetic compounds, and the impossibility of directly visualizing the spin texture within the bulk, researchers have developed two-dimensional model-systems of them. In fact, 2D analogs of magnetic spin systems were studied theoretically [43–46], numerically and experimentally [47, 48].

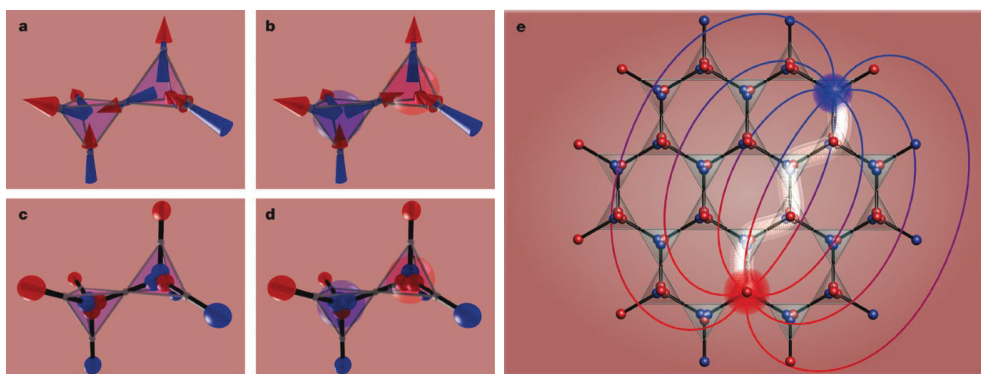


Figure 5: Dumbbell model and emergence of magnetic monopoles in spin ice. In (a) we have two neighboring tetrahedra in an ice rule configuration. (b) shows an excitation from the ground state. (c) and (d) show the same configurations as (a) and (b), respectively, but within the dumbbell model. (e) shows the magnetic interaction among the emergent monopole and anti-monopole. Image reproduced from [41].

2.5 ARTIFICIAL SYSTEMS

We will now discuss some examples of two-dimensional model systems for ferromagnetic pyrochlore oxides. Those are the Artificial Spin Ice (ASI) and later on, a microscopic version, named Artificial Colloidal Ice (ACI).

2.5.1 *Artificial spin ice*

Artificial spin ice (ASI) was introduced in 2006 by Wang et al. [8]. Exploiting state-of-the-art nanofabrication techniques, they built a quasi two-dimensional square array of elongated permalloy nanoislands with a size of 80×220 nm and a thickness of 25 nm, i.e., single-domain ferromagnetic islands, see [Figure 6](#) (a). Those nanoislands interact via magnetic dipolar interaction ($\propto 1/r_{ij}^3$, with r_{ij} distance among nanoislands). This system allows observing the orientation of the magnetic moment in the nanoislands using a Magnetic Force Microscopy (MFM); see [Figure 6](#) (b). The authors prepared several samples with different lattice constants (i.e., interaction strengths) ranging from 320 nm to 880 nm and ordered the system by using an annealing protocol that consisted of rotating the sample within a magnetic field that decreased stepwise from above to below the coercive field. From the direction of the nanoislands' magnetic moments (or spin), obtained via MFM, the authors analyzed the fraction of vertices and found that the system tends to satisfy the local balance of magnetic moments pointing in and out at a vertex level, the two-in two-out ice rule, see [Figure 6](#). This work showed that using lithography, it is possible to design a two-dimensional structure of interacting magnetic moments that can be directly visualized. Therefore, it may be used as a model system to investigate the effect of geometric frustration or to engineer different types of lattice to control frustration effects. Indeed, the first realization of ASI was followed by several works on this topic [49]. For example, different annealing protocols have been developed and used to observe low-energy states. Different imaging methods were explored to follow the dynamics of the magnetic moments. The MFM visualization method was substituted by Photo Emission Electron Microscopy (PEEM), which captures the X-ray Magnetic Circular Dichroism (XMCD) contrast. This technique allowed the visualization of magnetic moment flips with a time step among images ranging from 300 s [50] to 7 s [51], instead of the visualization of static low-energy final state configurations as using MFM. Fabrication protocols were changed to allow the magnetic moments of the nanoisland to flip more easily their orientation due to thermal fluctuations [52–54]. Other works explored systems with similar characteristics as their natural spin-ice counterparts, such as an extensive degeneracy [51, 55–58]. The low-energy states of different lattices such as honeycomb [59–62], triangular [63], tetris [64], shakti [50, 65, 66], cairo [67] and so on, were investigated. It was also demonstrated how to flip an individual magnetic moment of a nanoisland within a lattice by using the tip of a magnetic force microscopy

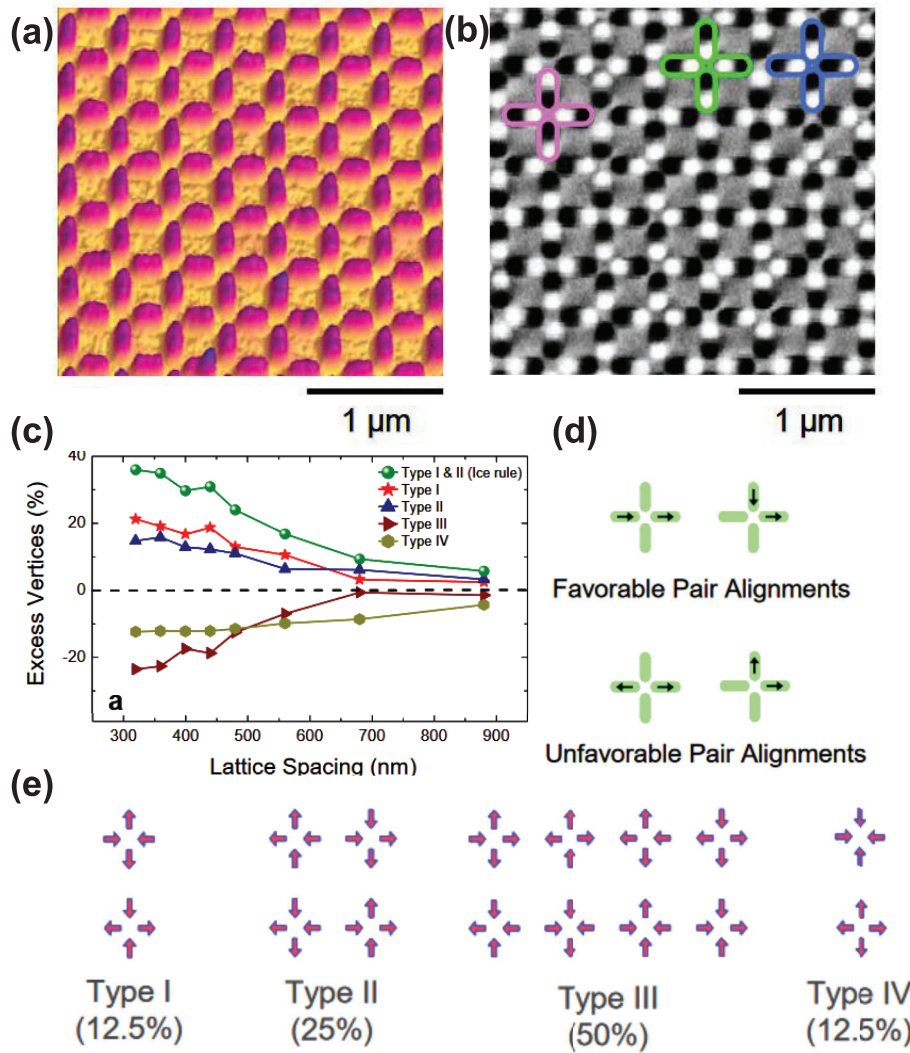


Figure 6: (a) Atomic force microscopy (AFM) topographic map of an Artificial Spin Ice (b) Magnetic force microscopy (MFM) image of an Artificial Spin Ice. Nanoislands are single-domain as indicated by the division of each island into black and white halves that correspond with the north and south magnetic poles. Purple, blue and green vertices correspond to type I, type II and type III respectively. (c) The excess percentages of different vertex types as a function of the lattice spacing, after applying the annealing protocol. (d) Emergence of frustration due to the incompatibility of energetically favorable and unfavorable dipole interactions between pairs. (e) The 16 possible magnetic moment configurations on a vertex with four nanoislands. Modified image from [8].

(MFM) [68]. Furthermore, the fabrication protocol was changed in such a way to pin the magnetic moment configuration of a nanoisland [69] and study its implications on the system.

2.5.2 *Artificial colloidal ice*

Only a few months after the publication of the first article on ASI another work, by A. Libál et al. [71], appeared to introduce a two-dimensional soft-matter system where geometric frustration was investigated by using soft colloidal particles. In this work, the authors used Brownian dynamics of electrostatically interacting colloids in an array of bistable optical traps. The system was inspired by previous experimental realizations of a colloidal particle confined in a bistable optical potential [72–74]. In this work, the authors demonstrate that also in this system, geometric frustration arises and the minimum energy configuration at a vertex level in a square lattice is obtained when two colloids are near the center and two far from it, recovering the ice-rule. Different methods for changing the colloid-colloid interaction strength were used in order to reach low-energy states. Such as increasing the colloidal electrostatic charge or decreasing the spacing between traps. While this pioneering work was only numerical, ten years later it was shown that the system could be realized in experiments, see Figure 7. The experimental realization of Artificial colloidal ice (ACI) was realized by using a lattice of microfeatured grooves instead of an array of optical traps. Within these traps, paramagnetic colloidal particles were deposited at a one-to-one filling ratio and made repulsive due to an external magnetic field [70]. The advantage of the particle-based system over the ASI is that the dynamics are accessible via simple optical microscopy techniques. Further, the pair interactions between the system elements, here the colloids, can be easily tuned from short to long range without the need to fabricate each time a different lithographic structure as in ASI. Another advantage of ACI over ASI is that it allows to control local and temporal spin configurations, i.e., the particle position within the double well, by using the optical tweezers. These tweezers are strongly focalized laser light that help move the particles manually across the substrate. With the tweezers, one can choose the initial colloidal positions (2016, [75]) or also reversibly pin some colloids to a certain direction (2021, [76]). Moreover, it is possible to design specific annealing procedures since the pair interactions between the particles are controlled by an external magnetic field. Due to these features, the colloidal system offers different capabilities than the ASI and could be used to explore similar phenomena related to geometric frustration from an entirely different point of view.

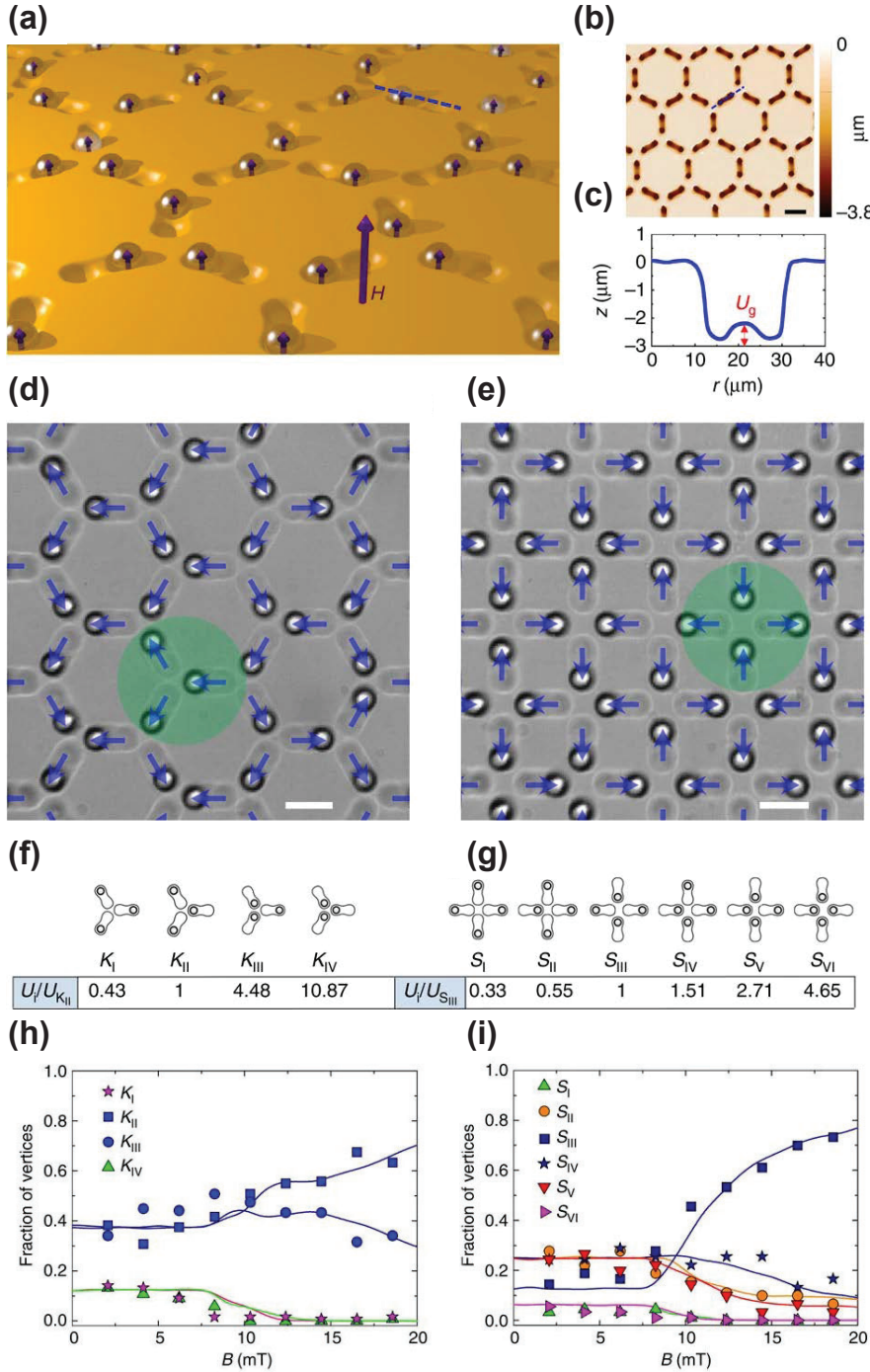


Figure 7: (a) Schematic showing paramagnetic colloidal particles confined in a honeycomb lattice of lithographic double well grooves. Little arrows inside the colloidal particles (spheres) stay for the induced magnetic moment generated in the presence of a magnetic field H . (b) Topographic map of the honeycomb double well lattice. (c) double well profile. (d) and (e) are optical microscope images of the honeycomb and square lattice with paramagnetic colloids (black and white disks). Blue arrows are the pseudospins associated to each double well-colloid pair. The pseudospin will point towards the direction of the colloid is located. Green circles highlight the low energy vertices in each lattice. (f) and (g) Vertex configurations of honeycomb and square lattice with the correspondent normalized magnetostatic energy. (h) and (i) average fraction of vertices at equilibrium vs magnetic field strength. Modified image from [70].

Part III

ARTIFICIAL COLLOIDAL ICE

Artificial colloidal ice (ACI) was introduced as a microscopic model system to investigate geometric frustration phenomena. The frustration in such a system can be deliberately designed by changing the type of lattice. In this chapter, we will first introduce the physics of colloidal particles, then we will explain in detail the experimental realization of a colloidal ice and finally talk about its main properties.

3.1 COLLOIDAL PARTICLES

Colloidal suspensions are stable dispersion of microscopic immiscible particles within another phase. The immiscible particles have a size range between a few nm to several μm [1, 77–79]. Colloids are ubiquitous in nature and in our daily lives since we can find them in paint, milk, and glue, among others [80]. Moreover, nowadays, colloidal particles can be synthesized in different sizes, shapes, or types of material, and their interaction can be tuned carefully by external fields [81]. Colloidal particles are characterized by accessible time and length scales, since their size is usually comparable to the visible wavelength and their dynamics are relatively slow, from ms to s . All these qualities make colloidal systems an excellent tool to be used as model systems for phase transitions [82–86], biological entities such as microswimmers [87–92] or transport through a biological pore [93, 94], or geometrical frustration, to cite some of them. In fact, colloids can crystallize [83, 95], be prepared in a glassy state [96] or even be self-propelled if properly designed [87–89, 97], see [Figure 8](#).

3.1.1 Brownian motion and diffusion

The dynamics of a spherical colloidal particle of radius a and mass m immersed in a fluid of viscosity η in one dimension follows the second Newton’s equation in one dimension:

$$m\ddot{x} = -\gamma\dot{x} + F(t) \quad (4)$$

According to the Stokes formula [99], $-\gamma\dot{x}$ is the friction force, \dot{x} the velocity of the particle, and $\gamma = 6\pi\eta a$ the friction coefficient of a spherical particle in bulk. $F(t)$ is a fluctuating force, that considers the particle fluctuations due to the continuous collisions with the solvent molecules.

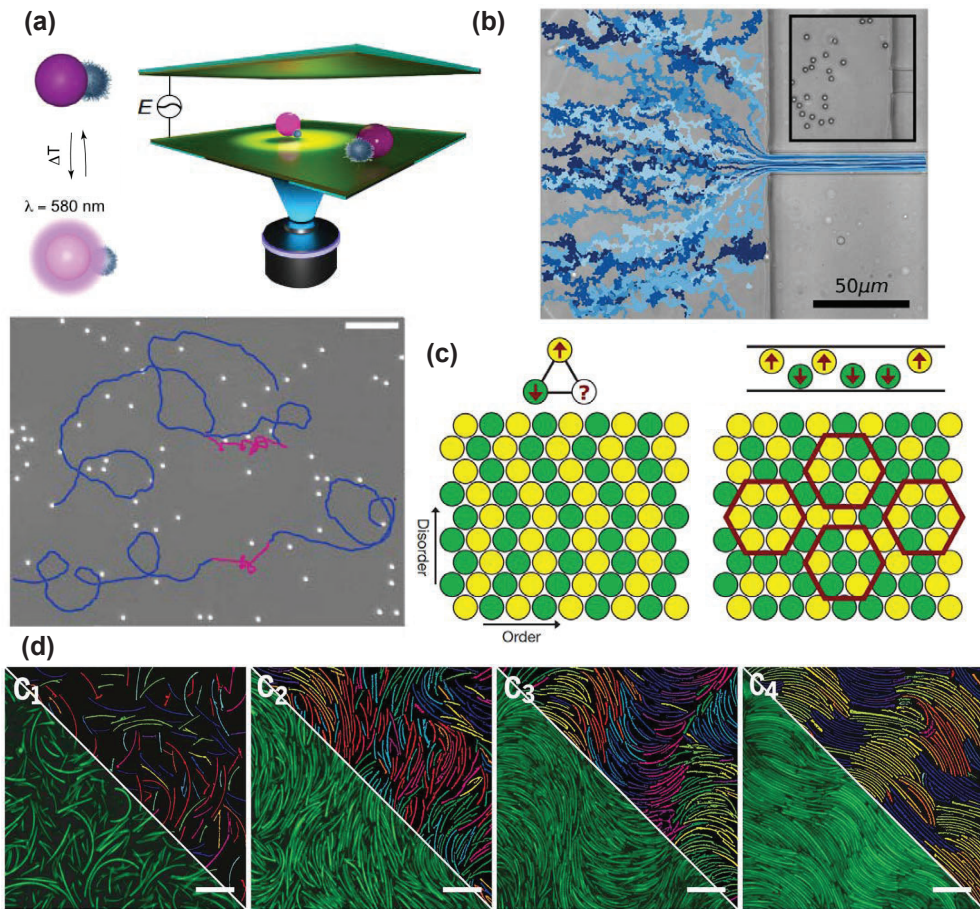


Figure 8: (a) Reconfigurable colloidal microsimmers. Below, an example of the particle trajectory is shown. The blue trajectory corresponds to a power density of $9 \text{ mW}/\text{mm}^2$ and the magenta trajectory to $54 \text{ mW}/\text{mm}^2$. The motility change is due to the laser heating the microgel above its volume phase transition temperature. Image modified from [90], (b) Trajectories of colloidal particles transported through microfluidic channels by pressure-driven flow. Image reproduced from [93]. (c) Geometrically frustrated system composed of closely packed diameter-tunable microgel colloidal spheres confined between two parallel walls. Image reproduced from [7]. (d) Phase behavior of banana-shaped colloidal particles at different packing fractions. In C_2 and C_3 the system shows a biaxial nematic ordering and in C_4 antipolar biaxial smectic structure. Image reproduced from [98].

This force is isotropic, and its mean value given by $\langle F(t) \rangle = 0$. If we multiply by x the previous equation [100, 101] we have:

$$mx\ddot{x} = -\gamma x\dot{x} + xF(t) \quad (5)$$

Averaging among many identical colloidal particles, we can apply $\langle xF(t) \rangle = \langle x \rangle \cdot \langle F(t) \rangle = 0$ since the fluctuating force is uncorrelated with the actual position of the Brownian particle. In addition, we use the identity $x\ddot{x} = \frac{d}{dt}(x\dot{x}) - \dot{x}^2$ and obtain:

$$m \left[\frac{d}{dt} \langle x\dot{x} \rangle - \langle \dot{x}^2 \rangle \right] = -\gamma \langle x\dot{x} \rangle \quad (6)$$

As the colloidal particles and the fluid are in thermodynamic equilibrium, we can use the equipartition theorem and assume that the average kinetic energy of a Brownian particle is $\frac{m\langle \dot{x}^2 \rangle}{2} = \frac{k_B T}{2}$. k_B is the Boltzmann constant and T the temperature of the bath.

$$\frac{d}{dt} \langle x\dot{x} \rangle + \frac{\gamma}{m} \langle x\dot{x} \rangle = \frac{k_B T}{m} \quad (7)$$

By applying the change $\langle x\dot{x} \rangle = y$, we can solve the first-order linear ordinary differential equation and obtain:

$$\langle x\dot{x} \rangle = C e^{-\frac{\gamma t}{m}} + \frac{k_B T}{\gamma} \quad (8)$$

By assuming as initial conditions $\langle x^2 \rangle = 0$ at $t = 0$ we can compute the C constant. $C = -\frac{k_B T}{\gamma}$ and apply the identity $\langle x\dot{x} \rangle = \frac{1}{2} \frac{d\langle x^2 \rangle}{dt}$.

$$\frac{1}{2} \frac{d\langle x^2 \rangle}{dt} = \frac{k_B T}{\gamma} [1 - e^{-\frac{\gamma t}{m}}] \quad (9)$$

And integrating the above equation:

$$\langle x^2 \rangle = \frac{2k_B T}{\gamma} \left[t - \frac{m}{\gamma} (1 - e^{-\frac{\gamma t}{m}}) \right] \quad (10)$$

We obtain the *mean square displacement* of a Brownian particle at a time t . If we study the case in which $t \ll m/\gamma$ and use the following Taylor series up to the second order $e^{-\frac{\gamma}{m}t} = 1 - \frac{\gamma}{m}t + \frac{1}{2} \frac{\gamma^2}{m^2} t^2 - \dots$

$$\langle x^2 \rangle = \frac{2k_B T}{\gamma} \left[t - \frac{m}{\gamma} \left(1 - 1 + \frac{\gamma}{m}t - \frac{1}{2} \frac{\gamma^2}{m^2} t^2 \right) \right] = \frac{k_B T}{m} t^2 \quad (11)$$

We obtain that in short time, we have ballistic diffusion. The particle moves at a constant speed. If we apply the diffusion limit $t \gg m/\gamma$ instead, the exponential part can be solved as: $e^{-\frac{\gamma t}{m}} \rightarrow 0$ and we have:

$$\langle x^2 \rangle = \frac{2k_B T}{\gamma} t \quad (12)$$

The particle in this case exhibits diffusive movements. This result is in one dimension. To have the mean square displacement of a Brownian particle at a time t in 3D, assuming isotropy along the other two directions, we have, $\langle r^2 \rangle = 3 \langle x^2 \rangle$ and hence $\langle r^2 \rangle = \frac{6k_B T}{\gamma} t$. The Stokes-Einstein relationship formula introduced by Einstein provides a relation between the diffusivity of a Brownian particle due to thermal motion and the drag coefficient for a viscous (dissipative) fluid:

$$D = \frac{k_B T}{\gamma} \quad (13)$$

The mean square displacement can be written in the long-time limit as:

$$\langle x^2 \rangle_{1D} = 2Dt \quad \text{or} \quad \langle r^2 \rangle_{3D} = 6Dt \quad (14)$$

Finally, the mean square displacement is a quantity that can be measured experimentally by following the particle's trajectory. We can obtain it by computing:

$$\langle r^2 \rangle = \frac{1}{N} \sum_{i=1}^N \langle [r_i(t) - r_i(0)]^2 \rangle \quad (15)$$

r_i is the position of particle i , N the total number of particles and $\langle \dots \rangle$ the average over different time origins. Computing experimentally the mean square displacement can help to characterize the dynamics of a colloidal particle under study. If the mean square displacement is linear with time t we have normal diffusion. If instead we have other dependencies we can have anomalous diffusions such as super diffusion or sub diffusion [102, 103].

3.1.2 Overdamped dynamics

The Navier-Stokes equations that describe the flow of an incompressible Newtonian fluid of viscosity η and mass density ρ are [104, 105]:

$$\rho \left(\frac{\partial \mathbf{v}(\mathbf{r}, t)}{\partial t} + \mathbf{v}(\mathbf{r}, t) \cdot \nabla \mathbf{v}(\mathbf{r}, t) \right) = -\nabla p(\mathbf{r}, t) + \eta \nabla^2 \mathbf{v}(\mathbf{r}, t) + \mathbf{f}(\mathbf{r}, t) \quad (16)$$

$$\nabla \cdot \mathbf{v}(\mathbf{r}, t) = 0 \quad (17)$$

Here, $\mathbf{v}(\mathbf{r}, t)$ is the velocity of the flow field at a point \mathbf{r} at the time t , $p(\mathbf{r}, t)$ is the pressure field and finally, $\mathbf{f}(\mathbf{r}, t)$ is the external body force field per unit volume acting in the fluid. The nature of this force can be diverse, from the presence of an applied electric or magnetic field to a gravitational force. The second equation comes from the continuity equation for a fluid with a constant density and is known as the compressibility condition.

The Navier-Stokes equations include both inertial effects, left-hand side terms in the equation proportional to ρ , and also fluid viscosity effects that are included in the term proportional to η . To compare the importance of those two effects, one can introduce the dimensionless Reynolds number, defined as:

$$Re = \frac{\text{inertial forces}}{\text{viscous forces}} = \frac{\rho LV}{\eta} \quad (18)$$

where the L and V are the characteristic length and velocity scales of the flow, respectively. This number, for microscopic entities, is typically of the order of 10^{-3} or even smaller. Thus, we can assume that inertial terms are not relevant and simplify the Navier-Stokes equations into the Stokes equation at a low Reynolds number.

$$-\nabla p(\mathbf{r}) + \eta \nabla^2 \mathbf{v}(\mathbf{r}) + \mathbf{f}(\mathbf{r}) = 0 \quad (19)$$

$$\nabla \cdot \mathbf{v}(\mathbf{r}) = 0 \quad (20)$$

These equations have no time dependence and are linear in velocity and pressure fields. In addition, if there is no force density, the instantaneous values of velocity and pressure depend on the momentary configuration and shape of particles and the system boundaries. Thus, there is no dependence on earlier flow history. Due to their small sizes and velocities, the flow fields generated by moving colloidal particles follow the Stokes equation, where inertial terms are negligible [106].

3.1.3 Colloidal interactions

The electrostatic interactions between colloidal particles can be attractive and repulsive. Here we will start to describe the attractive force among colloids which is very general, it occurs between particles in any suspension media.

The origin of these forces is the same as the Van der Waals forces [107]. The nature of Van der Waals forces comes from the temporary polarization of one molecule that induces a polarization in a neighboring molecule. These forces are known as the *London dispersion forces* [108]. The London attractive energy between two molecules is long-range and proportional to r^{-6} , where r is the distance among molecules. But, if instead of computing the interaction among two molecules, we want to know the interaction between two colloids, we need to make the assumption of the superposition principle, following the *Hamaker theory* [77]. By doing that, it can be demonstrated that the attractive force, in some cases, falls off much more slowly than the r^{-6} behavior for a molecular pair. The presence of long-range attractions may destabilize a colloidal suspension, inducing flocculation or coagulation phenomena. Here, we will compute the attraction between an atom and a semi-infinite plane, as shown in Figure 9 (a). Let's assume that the atom is located in the vacuum at a distance s from the plate.

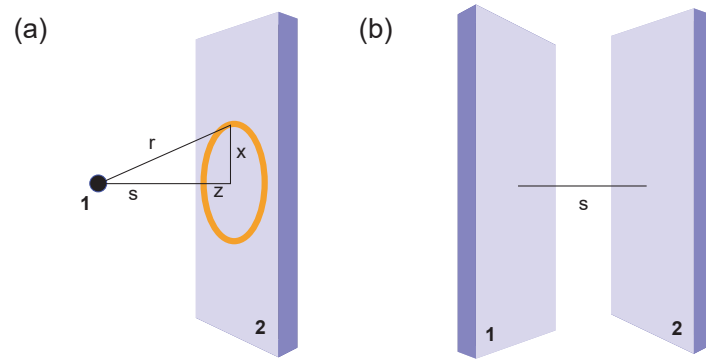


Figure 9: Schematic illustration of the Van der Waals interaction between an atom and a semi-infinite plane (a) and between two semi-infinite planes.

According to the London equation [109] the potential energy of attraction among two atoms at a distance r can be written as [110]:

$$V_L = -\frac{C_{12}}{r^6} \quad (21)$$

Here, C_{12} depends on the polarizability of the atoms. The polarizability of an atom measures the difficulty with which the electron distribution can be displaced, and is directly proportional to the volume of the atom. The total energy of attraction between atom 1 and plane 2 will be:

$$V_{\text{atom-plane2}} = \sum_{\text{plane2}} V_L = - \int_s^{\text{inf}} \int_0^{\text{inf}} C_{12} \rho_2 \frac{2\pi x dx dz}{(x^2 + z^2)^3} \quad (22)$$

Here the plane is divided into small rings of radius x and thickness dx in the x - y plane. The ring is at a distance z from the atom, parallel to the normal of

the semi-infinite plane and has a thickness in this direction of dz . The number of atoms of type 2 will be $dN = \rho_2 dV$. Being ρ_2 the density of atoms of the plane. Thus, the volume of each ring is $dV = 2\pi x dx dz$. We also applied the Pythagoras theorem $r^2 = x^2 + z^2$. After the change $2x dx = d(x^2)$:

$$= -2\pi C_{12} \rho_2 \int_{z=s}^{z=\text{inf}} dz \int_{x=0}^{x=\text{inf}} \frac{1}{2} \frac{d(x^2)}{(x^2 + z^2)^3} \quad (23)$$

And $y = (x^2 + z^2)$:

$$= -2\pi C_{12} \rho_2 \int_{z=s}^{z=\text{inf}} dz \int_{y=z^2}^{y=\text{inf}} \frac{1}{2} \frac{dy}{y^3} \quad (24)$$

$$= 2\pi C_{12} \rho_2 \int_{z=s}^{z=\text{inf}} \frac{1}{4} \frac{1}{z^4} dz \quad (25)$$

$$V_{\text{atom-plane2}} = -\frac{C_{12} \rho_2 \pi}{6s^3} \quad (26)$$

Being s the separation between the plane 2 and atom 1. Thus, by integrating the pairwise interactions, we end up increasing the range of the attractive Van der Waal interaction. This effect can be further enhanced if instead of a single atom, we have another plane, called plane 1, as shown in [Figure 9](#) (b). If the atom 1 now is located inside a material with a number density of atoms ρ_1 we can say that each atom of plate 1 at a distance s from the plane 2 will be attracted with an energy given by [Equation 26](#). If instead we want the interaction with a volume element, which contains $\rho_1 dz$ atoms, the energy of attraction between this volume element and the plane 2 will be given by:

$$V_{\text{column-plane2}} = -\int_s^{\text{inf}} C_{12} \rho_2 \rho_1 \frac{\pi dz}{6z^3} = C_{12} \rho_2 \rho_1 \frac{\pi}{12s^2} \quad (27)$$

As we integrated z between s and infinity, we computed the interaction between the whole plane 2 and a column of unit cross-section. Again, we observe that the interaction at the same distance is stronger. With a similar procedure, detailed in [\[78, 111\]](#), we can compute the interaction among two spheres in the case $s \ll a$, when the distance among colloids is smaller than the spherical colloidal particle radius. The result is given by:

$$V_{\text{shepre-sphere}} = -\frac{A_{12} a}{12s} \quad (28)$$

Where we have introduced the Hamaker constant A_{12} with value $A_{12} = \pi^2 C_{12} \rho_1 \rho_2$.

If only Van der Waals attractive forces are present, the colloidal suspension will be unstable. A colloidal suspension is unstable when the particles spontaneously attract and form compact aggregates. A stable suspension is obtained when the interaction between two colloidal particles can prevent the aggregation process. Stability can be achieved through two main processes: electrostatic stabilization or steric stabilization. The first one is obtained as follows: When a colloidal particle is immersed in a fluid, the surface of the particle will acquire a net charge due to the difference in affinities of cations and anions for the two phases. Imagine that the colloidal surface is negatively charged. This surface charge will attract counterions from the fluid that want to balance the surface charge. As a consequence, there is the creation of an ionic cloud around the particle, which is called the *electric double layer*.

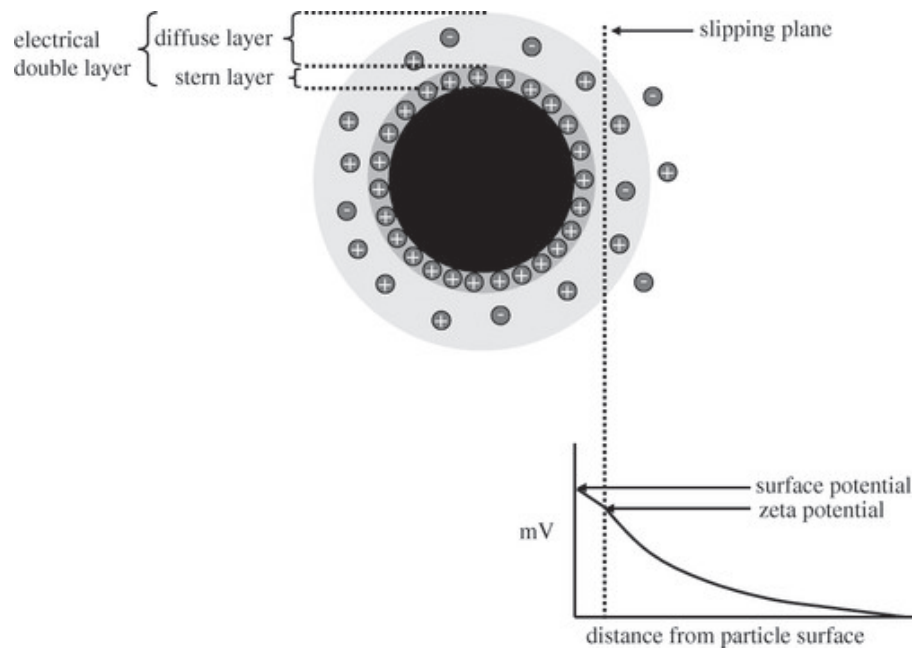


Figure 10: Schematic of the effect of introducing a colloid in an electrolyte solution. The surface of the colloid is negatively charged, generating a cloud of mobile ions which cover the colloidal particle. Image reproduced from [112].

The counterions feel the electrostatic attraction of the surface, but at the same time, they are mobile because of thermal motion. The outcome is a compromise wherein their concentration is elevated near the surface and gradually decreases until the bulk value is attained at a certain distance. The cations, on the other hand, are repelled from the surface. Their concentration will be very low near the surface and will increase gradually until the bulk value is again reached. Thus, a double layer can be divided generally into two parts: the Stern layer and the diffuse layer, see Figure 10. The first one is made of immobile ions fixed on the particle surface, while the second one is composed of mobile ions that can leave or enter the double layer due to thermal fluctuations. As a consequence of the diffusive layer, there is a concentration

gradient from the particle surface to the bulk. Thus, when two colloidal particles approach each other, the compression of the diffusive layer creates an osmotic pressure, which opposes further approach of the particles, giving rise to electrostatic repulsive interactions.

Instead, The steric stabilization is achieved when the surface of the particles can be covered by a layer of another substance (for example, a polymer) that will prevent aggregation after collision. In this case, the repulsion is independent on the electrolyte concentration and usually has a short range. In an aggregate state, attractive forces overcome repulsive ones and induce irreversible clustering; in contrast, a stable colloidal dispersion is characterized by the presence of repulsive interactions due to a large double layer (electrostatic) or long polymer chain on the surface (steric) which prevent the particle from coming into contact. Thus, in a colloidal suspension, the stability is determined by the interplay between the attractive *Van der Waals* forces and the repulsive ones of steric or electrostatic origin. The *Deryaguin-Landau-Verwey-Overbeek* or *DLVO theory* considers the interplay between the Van der Waals and the electrostatic forces, allowing one to calculate a potential barrier, as shown in [Figure 11](#).

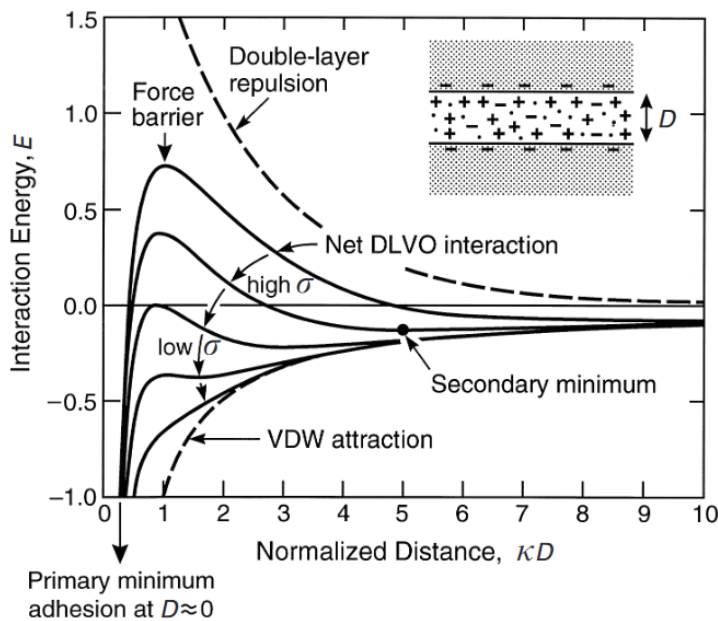


Figure 11: Interaction energy as a function of the normalized distance between two charged surfaces in an electrolyte solution at different charge densities, σ . $1/\kappa$ is the Debye length, the characteristic decay length of the interaction. Image reproduced from [113].

3.2 PARAMAGNETIC COLLOIDS

Another type of interaction between colloids can be induced by an external field, such as an electric or magnetic one [114–117]. For example, paramagnetic colloids under the presence of a magnetic field can exhibit either attractive or repulsive interactions, depending on the orientation of the applied field [118]. In this thesis, we used paramagnetic polymer particles that are doped with supermagnetic nanoparticles (iron oxide Fe_2O_3 / Fe_3O_4). A paramagnet is a material that, lacking a magnetic field, does not present a net magnetization; magnetic domains are randomly ordered. In the presence of a magnetic field, \mathbf{B} , a net magnetization is observed. Similarly, in paramagnetic colloids in the presence of a magnetic field \mathbf{B} an induced magnetic moment \mathbf{m} appears, it follows $\mathbf{m} = V\chi\mathbf{B}/\mu_0$, where V is the volume of the colloidal particle, χ it is the volume magnetic susceptibility, and $\mu_0 = 4\pi \times 10^{-7}$ H/m. Hence, under this condition, we have dipolar magnetic interaction among the magnetic moments of the paramagnetic colloidal particles. In the point dipole approximation, and assuming a negligible demagnetization effect of the particle surface, the expression for the interaction energy is the following:

$$U_{ij} = \frac{\mu_0}{4\pi} \left[\frac{\mathbf{m}_i \cdot \mathbf{m}_j}{r_{ij}^3} - \frac{3}{r_{ij}^5} (\mathbf{m}_i \cdot \mathbf{r}_{ij})(\mathbf{m}_j \cdot \mathbf{r}_{ij}) \right] \quad (29)$$

Where r_{ij} is the magnitude of the vector connecting the two particle centers and \mathbf{m}_i and \mathbf{m}_j are the dipole moments of the particles i and j . For the particular case where $\mathbf{m}_i = \mathbf{m}_j$ the interaction reduces to the expression:

$$U_{ij} = \frac{\mu_0 m^2}{4\pi r_{ij}^3} (1 - 3 \cos^2 \theta) \quad (30)$$

Here, θ is the angle between the line that connects the two particles and the direction of the magnetic field. We can observe from [Figure 12](#) that from $\theta = 0^\circ$ to $\theta = 54.73^\circ$ the interaction is attractive, favoring the formation of chains of particles, whereas from $\theta = 54.73^\circ$ to $\theta = 90^\circ$ the interaction is isotropic and repulsive, in the plane of the colloidal particles. $\theta = 54.73^\circ$ is called the magic angle, where there is no net interaction among paramagnetic colloids. In polar coordinates, the interaction defined by [Equation 30](#) will generate a force [119]:

$$F(r_{ij}, \theta) = \frac{3\mu_0 m^2}{4\pi r_{ij}^4} \left[(1 - 3 \cos^2 \theta) \hat{r} - \sin 2\theta \hat{\theta} \right] \quad (31)$$

Here \hat{r} is the direction joining the two centers and $\hat{\theta}$ is the azimuthal direction of the dipole moments.

In an Artificial Colloidal Ice, the magnetic dipolar interactions between the particles are isotropic and repulsive. This is achieved by applying a magnetic

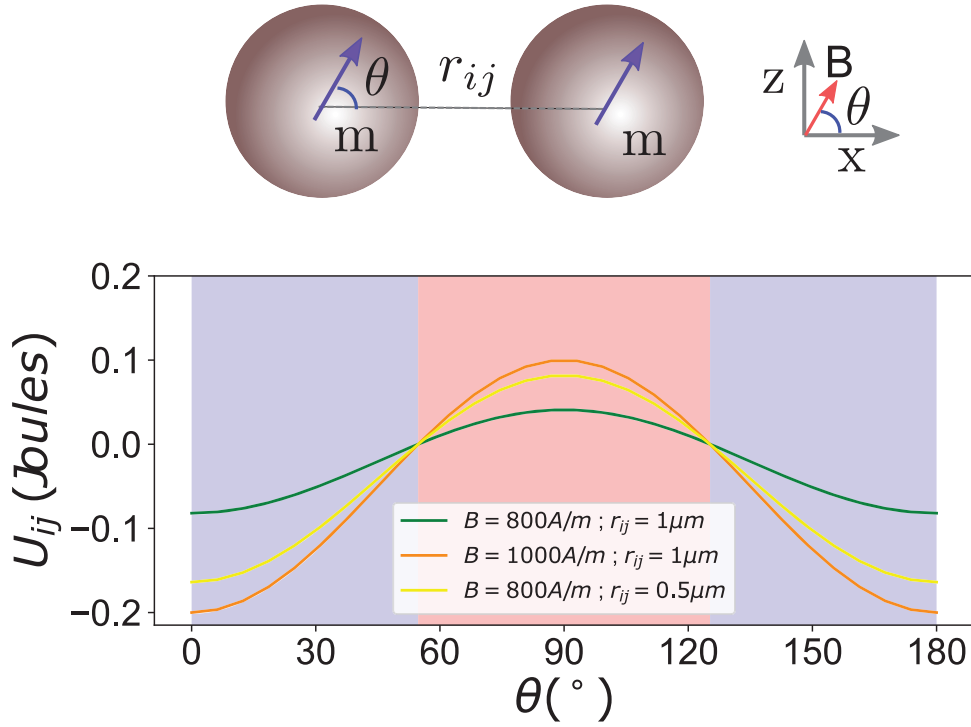


Figure 12: Interaction energy between two paramagnetic colloids in the presence of a magnetic field vs θ . The interaction energy is computed in Joules. We used the values $\mu_0 = 4\pi 10^{-7}$ H/m, $V = 1\mu\text{m}^3$, $\chi = 1$. The Blue (red) shaded area corresponds to θ values where the interactions between colloids is attractive (repulsive).

field perpendicular to the lattice plane. Thus, the induced dipolar magnetic moments in the colloids will be parallel one to another. The angle θ will be $\theta = 90^\circ$ obtaining then the following interaction and force:

$$U_d = \frac{\mu_m m^2}{4\pi r_{ij}^3} \quad ; \quad F(r_{ij}, \theta = 90^\circ) = \frac{3\mu_0 m^2}{4\pi r_{ij}^4} \hat{r} \quad (32)$$

Where r_{ij} is the distance between two colloids and m the dipole moment. Thus, when a magnetic field is applied, perpendicularly to the sample, the paramagnetic particles will want to be as far away as possible. In a 2D densely confined colloidal suspension with repulsive interactions, the low-energy state is achieved when the particles are located along a triangular lattice [120]. To generate geometrical frustration, in this thesis, a square lattice (or other types of lattices) of double wells was designed such that the pair interaction between the particles cannot be simultaneously satisfied since the symmetry is different than the triangular one.

3.3 REALIZATION OF ARTIFICIAL COLLOIDAL ICE

We used soft lithography to fabricate the topographic double wells that are used to confine by gravity the paramagnetic colloids. The fabrication procedure is described in [Section 5.2](#), [Appendix A](#) and [Appendix B](#). These double wells are lithographic elliptical indentations such that a confined particle cannot escape. To escape, a colloidal particle of diameter $10\mu\text{m}$ and volume V has to overcome the gravitational potential $U_g = \Delta\rho Vgh \sim 2000k_B T$. Where h is the height of the groove and is around $3\mu\text{m}$, $\Delta\rho$ the density mismatch among the colloidal particle and the surrounding fluid. Those lithographic elliptical traps are composed of two wells connected with a central hill. Each groove allows two possible stable positions of the colloidal particles; they have a biharmonic character, see [Figure 13](#). The central hill prevents the particle from being located in the middle and ensures bistability. Colloidal particles can jump from one gravitational minima to the other due to the repulsive interactions among paramagnetic colloids under a magnetic field. To finally generate the ACI, the bistable traps are arranged in one of several lattices, such as square, honeycomb, shakti or cairo.

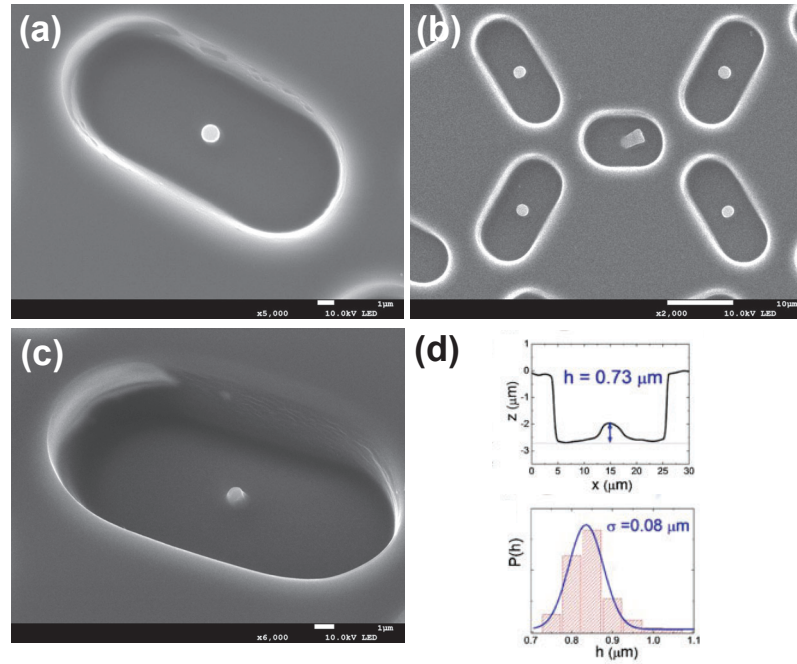


Figure 13: Bistable traps. (a) Scanning Electron Microscope (SEM) image of a bistable trap where the two gravitational minima are separated by a pillar. (b) SEM image of a lying pillar, responsible for generating the central hill in the bistable trap. (c) SEM image of double well groove with a central hill. (d) Height profile for a bistable trap, images reproduced from [75]. (e) Probability height distribution of the truncated pillars. Randomness comes from the formation process. Image reproduced from [75].

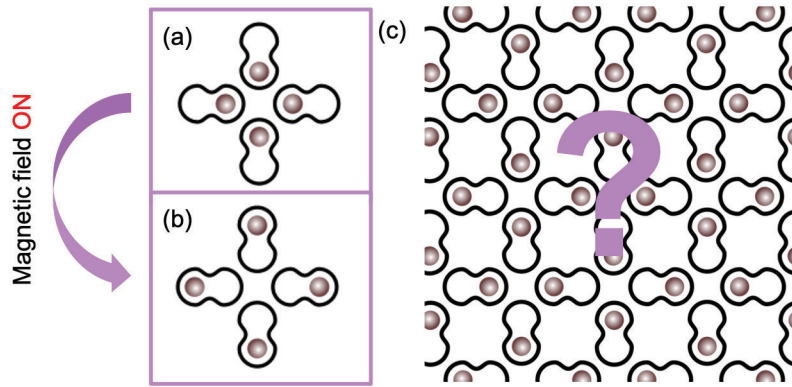


Figure 14: (a) Single square vertex with all the colloids/spins pointing toward the vertex center. (b) Final configuration of a single square vertex after applying a magnetic field perpendicular to the plane. To obtain this state, the dipolar repulsive interactions between colloids must be higher than the energy barrier generated by the central hill of the bistable trap. (c) The final state of a colloidal ice under a perpendicular magnetic field is geometrically frustrated. Configuration of (b) cannot be satisfied at a single vertex level.

Geometric frustration in this system emerges as follows: Imagine one single vertex of a square lattice, with all the colloids located close to the vertex center, [Figure 14](#) (a). Under a perpendicular magnetic field, the particles will experience isotropic dipolar repulsion that will try to separate them as far as possible one from another, [Figure 14](#) (b). The strength of the applied magnetic field is such that $U_g > U_d > U_{hill}$, where U_{hill} is the gravitational potential to surmount the hill. Thus, at the single vertex level, the system is not frustrated, since there will be only one way to minimize the interaction energy. If instead we have a square lattice of double wells, not all the particles can be expelled from each vertex at the same time. Thus, in a colloidal ice, frustration arises at a collective level, i.e., it arises in a lattice where collective interactions between the particles oppose the local energetics and enforce the ice rule. Instead of all the vertices expelling out the particles, the final state will be obtained by a local balance of particles pointing in and out of the vertex center.

Comparison with Artificial spin ice (ASI)

This contrasts with the ASI, where also an isolated square vertex will have nanoislands with the magnetic moment arranged in the ice rule, i.e., two in and two out. The difference in behavior is because the magnetic dipoles in ASI and ACI are aligned differently. In ASI, the permanent moments of the magnetic nanoislands are along the plane and thus can be attractive or repulsive depending on their relative location, as shown in [Figure 6 \(d\)](#). In contrast, in an ACI, the field-induced dipole moments are parallel to each other and perpendicular to the sample plane; thus, the interaction is isotropic and repulsive, see [Equation 29](#).

The analogy with spin ice systems can be done by associating an Ising-like spin to each double well, such that it points toward the direction of the colloid, see [Figure 15](#). Hence, the trap-colloid pair is discretized and is considered a unitary vector with a fixed direction and two possible senses, effectively having Ising spin degrees of freedom. By doing that, one can analyze an ACI using similar tools than that in spin ices and graph theory and thus relating these apparently different fields [[121](#)].

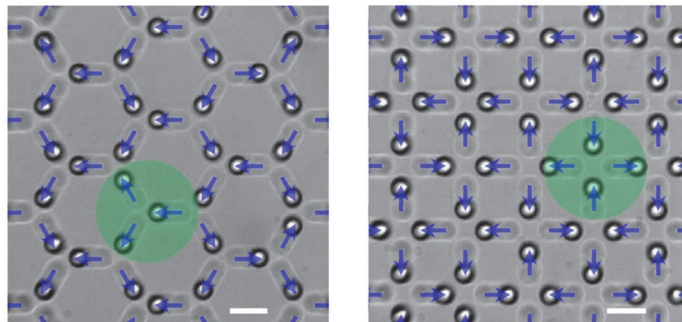


Figure 15: Experimental optical microscopy images of colloids in bistable gravitational grooves in a honeycomb lattice (a) and a square lattice (b). White circles with a black corona are the $10 \mu\text{m}$ diameter paramagnetic colloids. Elongated white ellipses are the bistable traps. Blue arrows correspond with the pseudospins that point through the location of the colloid. The green area indicates a single vertex. The scale bar is $20 \mu\text{m}$ in both figures. Image reproduced from [[70](#)].

The system's initial configuration is obtained by randomly placing the colloids in the double wells. After that, one applies an external magnetic field, and the colloids try to rearrange in the topographic constraints to lower the interaction energy. Since not all the types of vertices minimize the energy, see [Figure 16](#), only the low-energy vertices in a collective ensemble are favored. Then, with no magnetic field applied, the system will be disordered at constant thermodynamic temperature. By increasing linearly the magnetic field and therefore the interactions between colloids, the degree of disorder in the

system decreases and low-energy vertex configurations appear, in analogy with systems at low temperatures.

Comparison with Artificial spin ice (ASI)

Formally, for artificial spin ice (ASI) it has been justified that the increasing of the magnetic field is analogous to a decrease in the effective temperature of the system. As the interaction scales as $U_d \propto B^2$ and $\rho_{\text{defects}} \propto \exp(-\frac{U_d}{T})$ is linear, we can consider $T_{\text{eff}} \propto 1/B^2$ as an effective temperature [122]. Being ρ_{defects} the population of vertices that are not in the ground state.

In an Artificial Colloidal Ice (ACI) with double wells arranged along the square lattice (or for any other lattice), one can distinguish the different vertex types based on their magnetostatic energy and pseudospin arrangement. Vertex types and energies are shown in Figure 16, where all the $2^z = 2^4 = 16$ possible configurations that a vertex of coordination $z = 4$ can have are shown. Based on the energetic weight, one can classify the different vertex types. One can make an analogy between the colloidal ice and an ASI if one assigns an Ising-like spin to each double well, such that it points where the particle is located Figure 15. A topological charge in the context of artificial colloidal ice is defined as a vertex property and follows the equation:

$$q_n = 2n_{in} - z \quad (33)$$

Where the z is the coordination of the lattice, $z = 4$ for a square lattice and $z = 3$ for a honeycomb lattice, and n_{in} is the number of particles located near to the center of the vertex. Those charges are called “topological” because they depend on the connectivity of the lattice, and thus, its definition does not change for continuous deformations of the lattice. In addition, these charges are conserved: charges can only be created and annihilated in opposite pairs and the total topological charge of the system is conserved.

By using this definition, each group of vertices with the same energy also has the same topological charge. This is, in general, true, but not for the $q = 0$ vertices (2-in 2-out configurations) in 2D lattices; see Figure 16. This is a consequence of the loss of degeneracy at a single vertex level in comparison to 3D natural systems, generated by the simplification of having a 2D square lattice. In the process of projecting the 3D tetrahedral lattice into a 2D square lattice, some geometrical properties are lost. In particular, the distance between all the interacting units located at the vertex of the tetrahedron is no longer conserved. In fact, as it can be observed in Figure 17, the shift in energy between type 3 and type 4 vertices is due to the difference in distances among colloids, $D > d$, not present in a 3D tetrahedral lattice such as in water ice or rare earth pyrochlores. Indeed, the magnetostatic energy of a vertex will be obtained by summing all the pair-dipolar distance-dependent interactions.

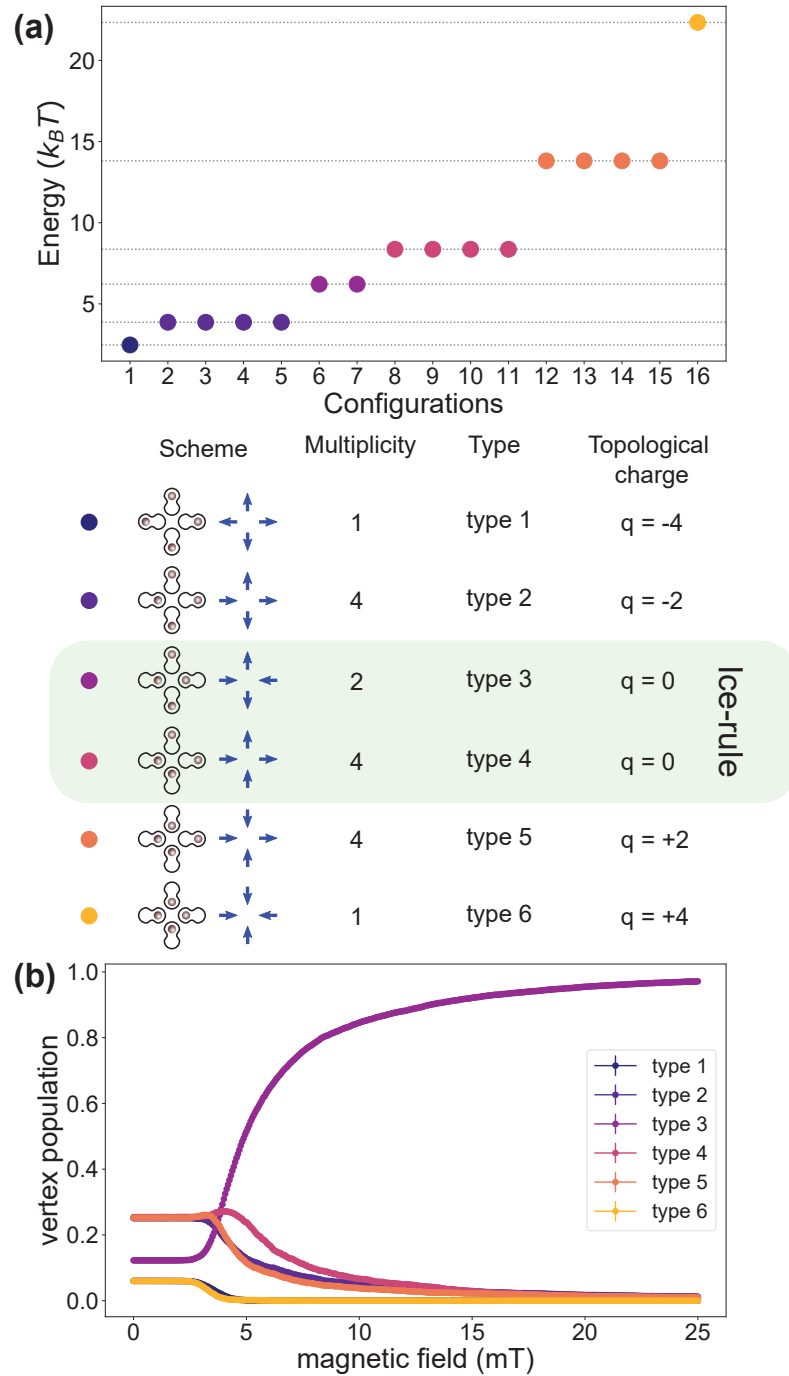


Figure 16: (a) Vertex energy vs. vertex configuration. The energy was computed for a magnetic field value of 10 mT perpendicular to the vertex. Below the image, we have the legend of the points with the corresponding vertex configuration, multiplicity, type name, and topological charge. (b) Vertex population vs. magnetic field. The initial configuration is random, and at high magnetic field values, the type 3 vertices prevail.

The ice rules, i.e., 2-in 2-out configurations, are still favored, but contrary to 3D systems with a 6-fold ground state degeneracy at a tetrahedron level,

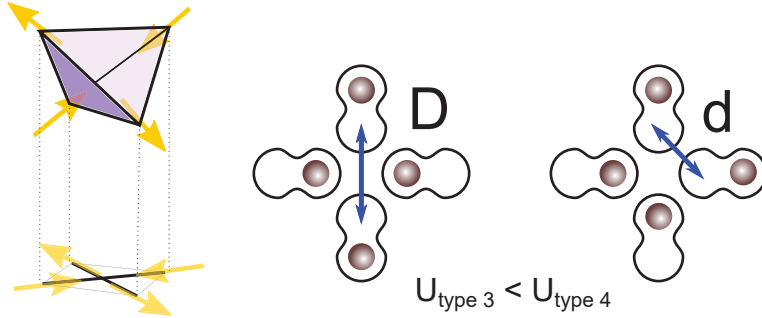


Figure 17: Degeneracy loss at single vertex level. In the tetrahedron, all the ice rule configurations (2-in 2-out configuration) are energetically equivalent. In the square $2D$ projection of the lattice, this degeneracy is lost. Not all the 2-in 2-out square vertices have the same magnetostatic energy. Since the energy is distance-dependent and $D > d$.

in the 2D square ACI systems we have a 2-fold ground state degeneracy. In fact, we observe that in a 2D square ACI, the favored vertices are not the ones with lower energy, $q = -4$, but instead the vertices satisfying the ice rule, 2-in 2-out. This fact can be understood by considering that if we have one $q = -4$ vertex, we will also need to have one $q = +4$ vertex, due to the conservation of topological charge in the system, i.e., the number of colloids is conserved. Then topological charges appear in pairs, and the energy cost of having a pair of $q = -4$ and $q = +4$ defects is higher than having two $q = 0$ vertices. This point can be demonstrated by performing the following experiment: After ordering the colloidal particles randomly in the double wells, we will increase the magnetic field value linearly (i.e., interaction strength) and count the vertex population at each magnetic field value. We observe that at 0 mT the distributions of vertices correspond to what is expected due to their multiplicity value. Type 1 and type 6 vertices ($q = \pm 4$) have a population of $1/16 = 0.0625$. Type 2, type 4 and type 5 ($q = \pm 2, 0$) with multiplicity 4 are the more abundant vertices with a fraction of $4/16 = 0.25$. Finally, type 3 vertices have a concentration of $2/16 = 0.125$. However, by increasing the magnetic field value, we observe that the favored vertices are the type 3 vertices. The ones that respect a local balance of spins pointing in and out (2-in 2-out or $q = 0$) with the lower energy value, as shown in Figure 16 (a).

3.4 PROPERTIES OF ARTIFICIAL COLLOIDAL ICE

Since an Artificial Colloidal Ice (ACI) displays geometric frustration, it could show similar phenomena as other condensed matter systems characterized by different length scales, including Artificial Spin Ice and rare earth pyrochlores [8, 41, 123, 124]. However, it also exhibits different and emergent effects that result from its mesoscopic character and that are, not present in previously

studied frustrated spin-like systems [125, 126]. In this section, we will review these novel properties that ACI exhibits compared to other existing geometrically frustrated systems.

3.4.1 Single coordination lattices

It was theoretically predicted that, for a lattice of single coordination number, the colloidal ice and the artificial spin ice behave similarly in terms of the fraction of vertices [126, 127]. Both systems for large interactions between the vertex elements try to minimize the absolute value of the topological charge $|q|$. A square lattice in its ground state is characterized by two-in two-out vertices. However, thermal fluctuations can induce the emergence of excitations in the form of defect lines that connect vertices with opposite and non zero topological charge. Those lines of defects will try to be as short as possible, since increasing their length requires a higher energy cost. However, their emergence depends on how fast or slow the applied field increases. If the field is applied too fast, there can be formation of grain boundaries, namely defect lines that separate regions of ground state that are both energetically low but compete with each other. This phenomenon was observed for ACI in the square [70] and triangular lattice [128], with respectively vertices of coordination 4 and 6 and a 2-fold degenerate ground state. In Figure 18, we show the distribution of topological charges in a square lattice, by starting from a random configuration and then linearly increasing the magnetic field (i.e., interaction strength). Only intermediate and high magnetic values are shown.

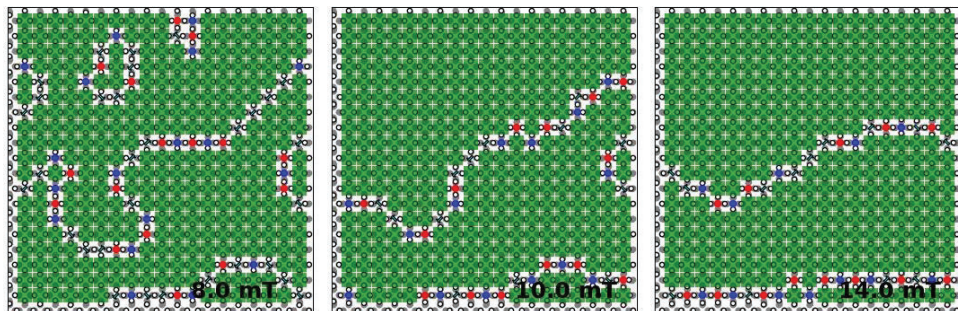


Figure 18: Defects in square artificial colloidal ice (ACI) at different magnetic interactions. Brownian's dynamics of an ACI under an annealing process. In the simulation, we linearly increase the magnetic field from 0 mT to 25 mT. Hence, we linearly increase the particle-particle dipolar interaction. From left to right we have the resulting frames at 8 mT, 10 mT and 14 mT. Green areas are ground state patches, whereas defects generate lines of non ground state vertices.

Comparison with Artificial spin ice (ASI)

In [Figure 19](#) the ground state domains of an ASI can be observed at several nanoisland separations, i.e., magnetic interaction energy. By decreasing the nanoisland separation, the magnetic interaction is increased, and from the images, it is observed that the ground state domains' growth, and lines of defects almost disappear. A similar trend is followed by the ACI at different magnetic interactions. By increasing the interaction strength, i.e., the magnitude of the perpendicular magnetic field value, the ground state domains grow and the lines of defects almost disappear.

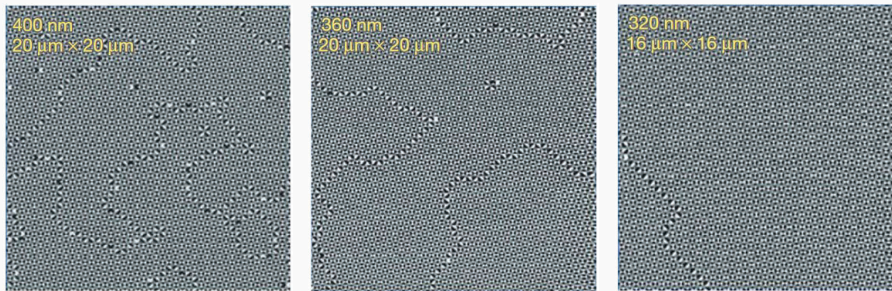


Figure 19: Defects in square artificial spin ice (ASI) at different magnetic interactions. MFM images of annealed artificial square spin ice. From left to right, the lattice constant of the ASI system is 400 nm, 360 nm and 320 nm. Hence, the magnetic interaction increases from left to right. At higher magnetic interaction, the ground state domains are bigger, and the density of lines of defects decreases. The image sizes are respectively, from left to right, $20 \times 20 \mu\text{m}$, $20 \times 20 \mu\text{m}$ and $16 \times 16 \mu\text{m}$. Images reproduced from [59].

In addition, both square and triangular lattices in their ground state can be entirely mapped by alternating clockwise and counterclockwise pseudospin plaquettes around the vertices, see [Figure 20](#), representing an alternative way to visualize the two available ground states. Both lattices have a 2-fold degenerate ground state: the one shown in this figure and the one obtained by replacing blue plaquettes by red plaquettes.

The square and triangular lattices are characterized by a single coordination with even coordination number ($z = 4$ square, $z = 6$ triangular). In contrast, lattices with odd coordination number, as the hexagonal ($z = 3$), in general, the low-energy states do not satisfy either the ice rule, or the local charge minimization $|q| = 0$. Furthermore, the ground state cannot be achieved by alternating clockwise and counterclockwise plaquettes. Due to symmetry restrictions, they have to satisfy $q = \pm 1$. Hence, low-energy vertices have to be $q = +1$ or $q = -1$, and this is called the pseudo ice-rule ([Figure 21](#)). This gener-

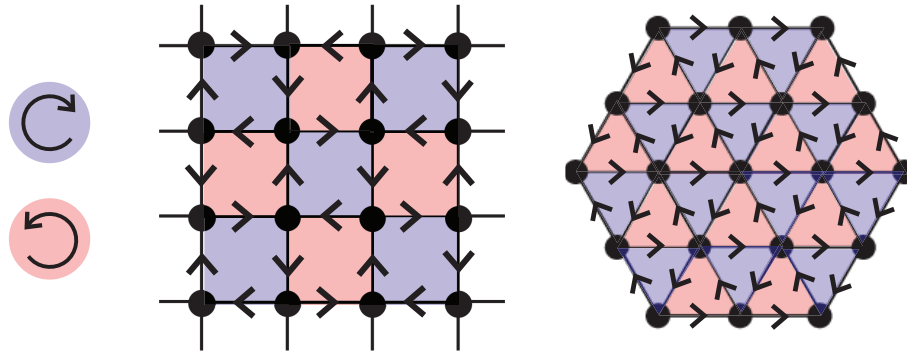


Figure 20: Alternated clockwise and counterclockwise plaquettes mapping the square and hexagonal lattice. Both lattices have a 2-fold degenerate ground state: the one shown in this figure and the one obtained by replacing blue plaquettes by red plaquettes.

ates an intrinsically extensive degeneracy, since the number of spatial charge configurations is higher. For a honeycomb lattice, it was found via Monte Carlo simulations that the system undergoes two consecutive second-order phase transitions [129, 130].

Comparison with Artificial spin ice (ASI)

For a honeycomb lattice in ASI, muon spin relaxation measurements were performed to demonstrate the presence of these transitions [61]. Only the Ice II phase, when positive and negative charges alternate, was observed experimentally for ACI. It was shown, theoretically [127], that the analogy between colloidal ice and the ASI system is valid for lattices of single coordination numbers. However, other theoretical works [131] predict different phases than the ones predicted by ASI for hexagonal colloidal ice due to their differences in energetics and frustration [132].

In the context of single coordination lattices, we have investigated the effect of tuning the boundaries and finite size effects on a single coordination square lattice. These results are shown in Publication 1 (in [Chapter 6, Section 6.1](#)).

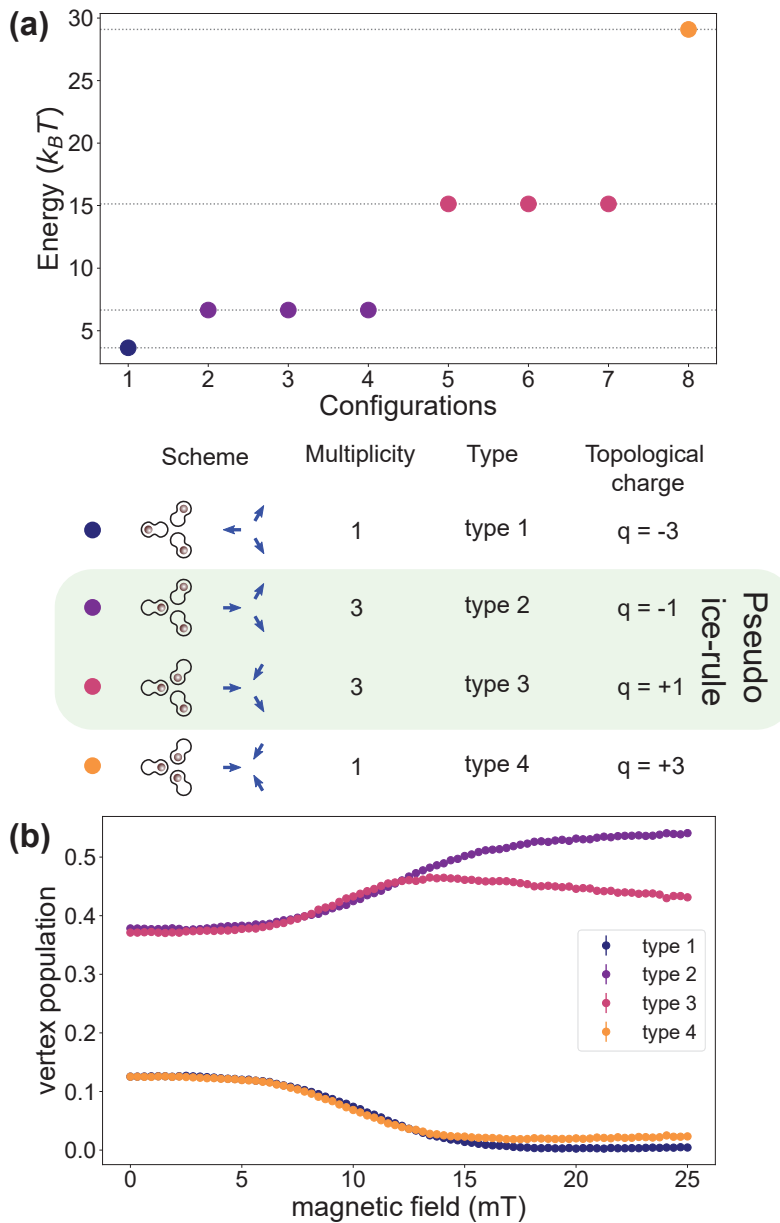


Figure 21: (a) Vertex energy vs. vertex configuration. The energy was computed for a magnetic field value of 10 mT perpendicular to the vertex. Below the image we have the legend of the points with the corresponding vertex configuration, multiplicity, type name and topological charge. (b) Vertex population vs. magnetic field. The initial configuration is random, and at high magnetic field values, type 2 and type 3 vertices prevail.

3.4.2 Decimated and mixed coordination lattices

When considering mixed coordination lattices, the ice rule or pseudo ice-rule can be broken locally.

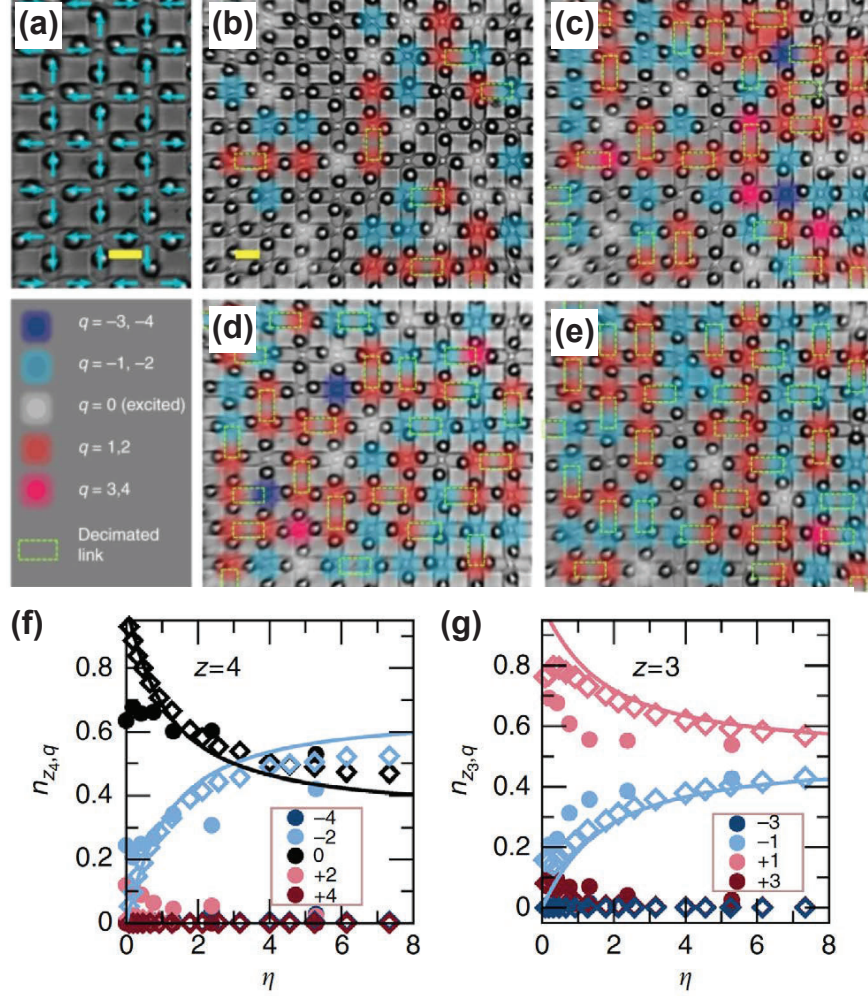


Figure 22: (a) Optical microscope image of a square artificial colloidal ice that shows the expected antiferromagnetic ordered configuration. The blue arrows are the spins associated to each double well trap-particle pair. (b-e) Optical microscope images of the colloidal system at increasing decimation. (b) $\eta = N_{z_3}/N_{z_4} = 0.19$, $\epsilon = N_d/N_v = 0.04$, (c) $\eta = 1.3158$, $\epsilon = 0.142$, (d) $\eta = 2.3846$, $\epsilon = 0.176$, (e) $\eta = 5.2857$, $\epsilon = 0.21$. N_{z_3} and N_{z_4} is the number of vertices of coordination $z = 3$ and $z = 4$ respectively. ϵ is the decimation density. Scale bars are $20\mu m$. (f) and (g) Show the comparison between experiments (bullets), numerics (diamonds) and theoretical predictions (solid lines). Vertex statistics $n_{z_4, q}$ ($n_{z_3, q}$) at equilibrium vs. η for the $z = 4$ ($z = 3$) vertices grouped by topological charge q . Modified image from [125].

Comparison with Artificial spin ice (ASI)

Indeed, the fragile “ice manifold” of the ACI that can be easily destabilized in mixed coordination lattices is particular of the colloidal system, since in ASI systems the ice rules are rather robust against decimation or mixed coordination lattices [64–67, 133]. This is related to the difference in alignment (and interaction) of the dipole moments. In fact, a single vertex of an ASI can follow the two-in two-out ice rule since it is characterized by in-plane dipoles. In contrast, a single vertex of an ACI will not follow the ice rule, as colloids will repel due to their out-of-plane dipoles.

It was previously reported [125] that for a colloidal ice in a decimated square lattice, a spontaneous charge transfer and charge screening appears, generating a net accumulation of topological charges to a certain sublattice location. In particular, it was observed that negative charges accumulate on the $z = 4$ vertices and positive charges on the $z = 3$ vertices, see Figure 22.

In this thesis, we focused on investigating the transition from two mixed coordination geometries: the Cairo and the Shakti. These two geometries are different but display the same topology, i.e., connectivity of the network. With these lattices, we demonstrated that accumulation of negative (positive) charges can occur in $z = 3$ ($z = 4$) or vice versa. We also showed that the transfer of topological charges between the two lattices invert, and in the point where these charges are balanced the analogy between the colloidal ice and artificial spin ice is restored. Results are shown in Publication 3 (Chapter 6, Section 6.3).

3.4.3 Degeneracy recovery

In magnetic materials such as 3D rare earth compounds, the magnetic moments lie on the vertex of a tetrahedron, and they have the same distance between them. This makes the system degenerate at low temperatures and excitations in the form of magnetic monopoles are free to move due to thermal fluctuations without any energy cost. In contrast, artificial spin ice (ASI) and colloidal ice (ACI) represent a projection on a plane of the 3D structure. This effect has important consequences, such as the fact that the low-energy vertices obeying the ice rule (two-in two-out) are not all energetically equivalent, and the 6-fold degeneracy at one tetrahedron (vertex) level is lost in the 2D square vertex analog.

Different strategies have been developed with a colloidal ice to restore the degeneracy of the square lattice. For example, in [134] the authors design a sheared version of the square colloidal ice that allowed them to reduce the energy gap between the type 3 vertex and a newly created type 4a vertex, as shown in Figure 23. However, even making those energies comparable, not a full degeneracy is obtained since, of all the vertex configurations that satisfy

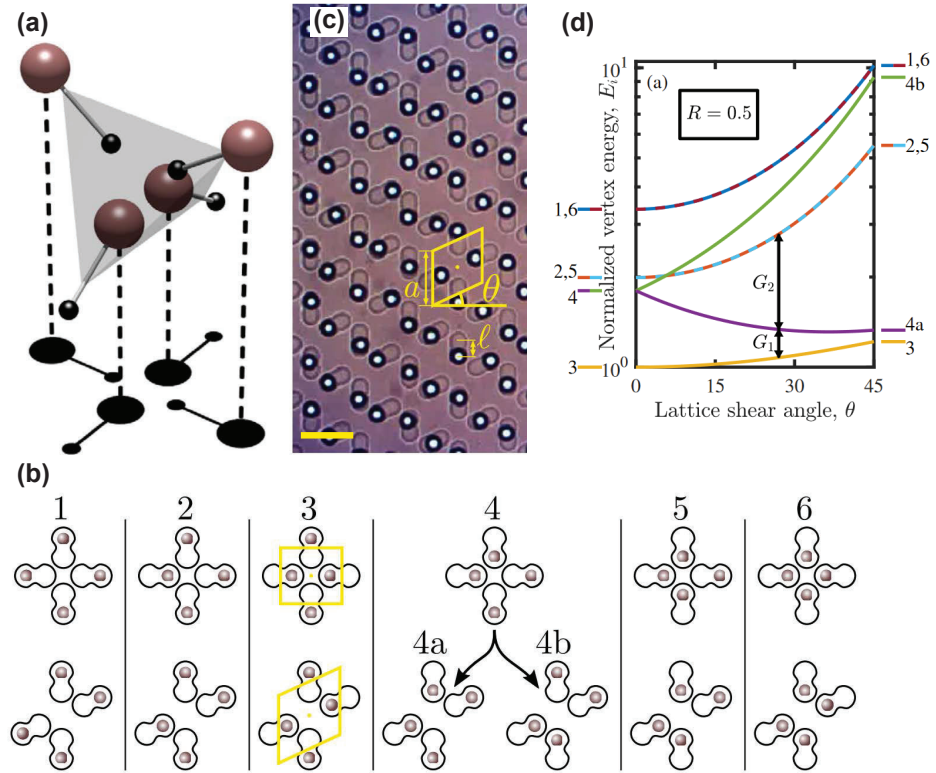


Figure 23: (a) Schematic of the result of projecting the 3D tetrahedral lattice into a 2D square lattice. (b) Types of vertices ordered in increasing energies from left to right. The upper row indicates the energy hierarchy for a square colloidal ice. The lower row shows the split in energy of the type 4 vertices when the lattice is sheared. (c) Microscope image of the experimental realization of the sheared colloidal ice with $\theta = 25^\circ$. The scale bar is $30 \mu\text{m}$. (d) Evolution of the magnetostatic energy of the different types of a single vertex with increasing shear angle, ranging from the unsheared square lattice ($\theta = 0^\circ$), to the maximally sheared lattice ($\theta = 45^\circ$). Modified image from [134].

the ice rules, only four of them have the same magnetostatic energy. In addition, it was observed that the presence of type 4a vertices was topologically connected with type 2 and 5 excitations, which prevented reaching a ground state at high interaction strength made only of type 3 and 4a vertices.

A second attempt to realize a degenerate square colloidal ice is reported in this thesis in Publication 2 (Chapter 6, Section 6.2). In this case, the energy gap among type 3 and 4 vertices was filled by changing two main parameters, the volumetric magnetic susceptibility of the particles and the distances between gravitational minima in the traps.

Besides a square lattice, extensive degeneracy can be obtained in other geometries. An example of a lattice with a degenerate ground state is the Cairo

lattice, which is made of irregular pentagons that allow to tessellate the entire space. In this thesis, we have investigated the low-energy state of a colloidal ice in this geometry, and we found that it corresponds to a frustrated antiferrotoroid, see Publication 4 ([Chapter 6](#), [Section 6.4](#)).

Comparison with Artificial spin ice (ASI)

Whereas some ASI studies access full degenerate ground states [55, 135–137] in a Colloidal Ice system, it remains elusive. The two main strategies to increase the 2-fold degeneracy to a 6-fold degeneracy at one vertex level in a square artificial spin ice (ASI) are the following. The first approach was to slightly vary the height of half of the permalloy nanoislands. By doing that, researchers were tuning the nearest-neighbour coupling strengths between orthogonal (J_1) and collinear (J_2) nanomagnets, see Figure 24 (a-c). Thus, restoring the same energetic weights to all the ice rule (two-in, two-out) configurations. The second approach to achieve this goal was to add an interaction modifier at the center of each square vertex. The researchers used slave-mesospins in the form of discs, within which the mesospin is free to rotate in the disc plane to tailor the strength and the ratio of the interaction energies, see Figure 24 (d-f).

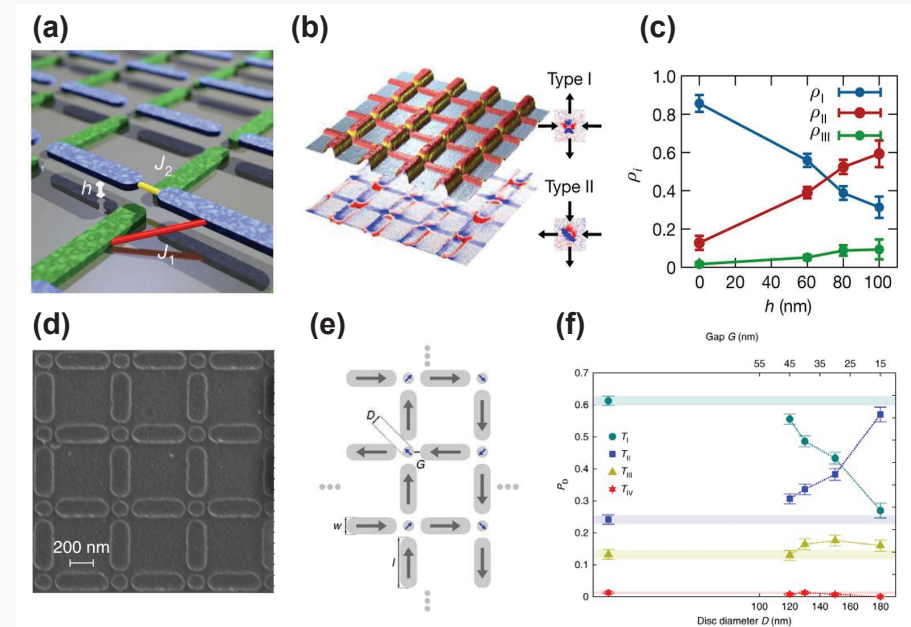


Figure 24: (a) Schematic of artificial spin ice (ASI) in which one of the two sublattices (blue) is lifted by a height offset h above the other (green). The nearest-neighbor coupling strengths between orthogonal (J_1) and collinear (J_2) nanomagnets are indicated in red and yellow, respectively. (b) In the upper image, an Atomic force microscopy (AFM) image of the lattice in (a). Nanomagnets are colored in red, and the bases are yellow. The substrate is gray. In the bottom image, there is the magnetic force microscopy (MFM). Here, blue and red stand for negative and positive magnetic charges, respectively. The inset shows the typical contrast obtained on type I and II vertices. (c) Vertex density of type i vertices (ρ_i) as a function of the height offset (h). (d) representative scanning electron image (SEM). (e) Illustration of square artificial spin ice with the interaction modifiers in the center of the vertices. (f) Normalized vertex population P_D as a function of the disc diameter D . Modified image from [135, 136].

3.4.4 Interactions between topological charges

One intriguing aspect of ACI is the interaction between topological charges. A colloidal ice has the advantage, compared to ASI or 3D natural spin ice, that it allows the control of the initial configuration, i.e., position of the particles, since colloids are ordered in the double wells with optical tweezers. As a result, the interaction between two high-charge defects artificially created was directly visualized and studied in ACI [75]. In this work, it was shown that the interactions among topological charges generated in the ACI system have a small Coulombic term, similar to 2D artificial spin ice systems [138–140]. However, the attraction among topological charges was mainly due to the existence of a strong line tension, which was measured to be one order of magnitude larger than in an ASI (Figure 25).

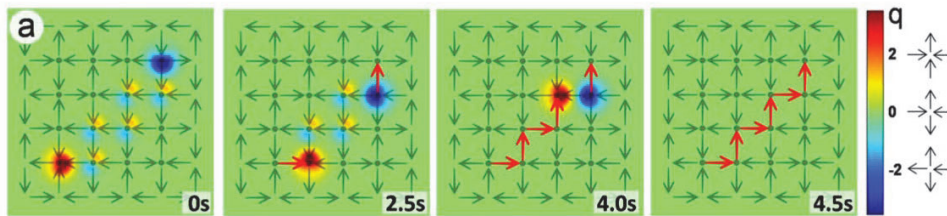


Figure 25: Experimental realization of two topological charges interacting in a ground state background and connected via a line of defects, i.e., high-charged vertices. The color map shows the topological charge associated with each vertex. At 0s the field was suddenly turned on perpendicular to the sample at $25.7mT$. Image reproduced from [75].

Comparison with Artificial spin ice (ASI)

In 3D magnetic materials and ASI, there are different works in this direction. In 3D systems, it was experimentally shown that topological monopoles interact via a Coulombic potential [141]. In studies of 2D ASI systems, it was observed that the interaction was also mediated by a Coulombic potential plus a string tension between the topological defects [142]. The explanation of the difference in interactions is due to the loss of full degeneracy. In a three-dimensional magnetic spin ice, the dipole moments arranged at a vertex of a tetrahedron have the same distance. Thus, the ground state is truly degenerate (all the two-in two-out configurations are energetically equivalent) and follows the two-in two-out ice rules. This allows to separate two magnetic monopoles without implying any energy cost. This is not true for a 2D system (ASI or ACI), where the difference in distance between the spins in a vertex makes the ground state non-degenerate (not all the two-in two-out configurations are energetically equivalent) and, as a consequence, two created topological defects tend to combine due to the presence of a strong line tension. Due to the difficulty of experimentally isolating only one pair of monopoles in 2D ASI or either choosing “à la carte” the initial conditions, only theoretical predictions of charge-charge interaction were obtained.

Part IV

METHODS

SIMULATIONS

Numerical simulations represent an excellent tool to investigate the particle dynamics by knowing a priori the pair interaction between them. The knowledge of the forces involved in the dynamics of a real system is not trivial and is often hidden. Hence, the combination of numerical simulations and experimental data could be crucial to determining the pair interactions and interpreting the system dynamics. In addition, simulations are more versatile than experiments, where we can choose parameters, initial conditions, and other quantities “à la carte”. For instance, in numerical simulations, we can adjust the magnetic volume susceptibility of the paramagnetic colloids to any desired value, χ , which is not trivial to achieve experimentally, since it depends on the particular batch of particles.

4.1 BROWNIAN DYNAMICS SIMULATIONS

In this work, we used Brownian dynamics to investigate the colloidal dynamics in a particle ice. Since colloids obey the classical laws, we integrate the equation of motion given by second Newton’s equation. This is described by the second-order differential equation:

$$m_i \ddot{\mathbf{r}}_i = \mathbf{F}_i^{\text{viscous}} + \mathbf{F}_i^{\text{dd}} + \mathbf{F}_i^{\text{trap}} + \boldsymbol{\eta} \quad (34)$$

Where $\boldsymbol{\eta}$ is a random force that describes thermal fluctuations characterized by a zero mean $\langle \boldsymbol{\eta} \rangle = 0$ and $\langle \boldsymbol{\eta}(t) \boldsymbol{\eta}(t') \rangle = 2k_B T \gamma(t - t')$. Here, \mathbf{r}_i is the position of particle i of mass m . The rest of the forces follow the expressions:

$$\mathbf{F}_i^{\text{viscous}} = -\gamma \dot{\mathbf{r}}_i \quad (35)$$

$\mathbf{F}_i^{\text{viscous}}$ is the viscous force generated by the surrounding fluid and is proportional to the velocity $\dot{\mathbf{r}}_i$ of the colloid and γ , the drag coefficient. γ measures how strongly the surrounding fluid resists the motion of the particle and depends on the shape, size, and viscosity of the fluid. It can be derived experimentally by computing the mean square displacement and using the Stokes-Einstein relationship [Section 3.1.1 \[143\]](#).

$$\mathbf{F}_i^{\text{dd}} = \frac{3\mu_o}{4\pi} \sum_{j \neq i} \frac{\mathbf{m}^2 \hat{\mathbf{r}}_{ij}}{|\mathbf{r}_{ij}|^4} \quad (36)$$

The dipolar force, F_i^{dd} , appears when a magnetic field induces a net magnetization and hence a dipolar moment in the paramagnetic particles. As the magnetic dipolar moments will point along the same direction as the applied magnetic field, those moments will be parallel, and the interaction will be isotropic, repulsive, and inversely proportional to the cube of the distance between particles, r_{ij} , see [Section 3.2](#). $\mathbf{m} = V\chi\mathbf{B}/\mu_0$ is the magnetic moment induced in the paramagnetic particles by the magnetic field \mathbf{B} , $\mu_0 = 4\pi \times 10^{-7} \text{H/m}$, χ is the magnetic susceptibility, V is the particle volume. $\hat{\mathbf{r}}_{ij} = (\mathbf{r}_i - \mathbf{r}_j)/|\mathbf{r}_i - \mathbf{r}_j|$ is the unit vector connecting two colloids and r_{ij} the distance between their centers, see [Figure 26 \(a\)](#).

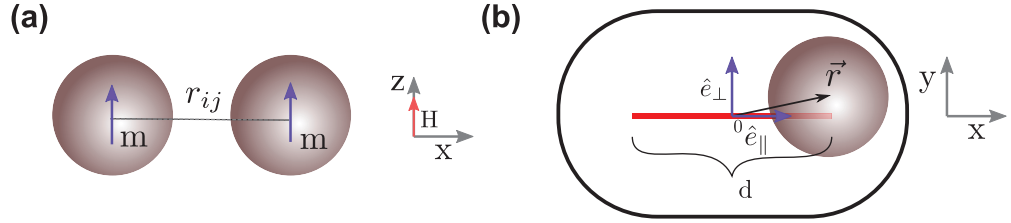


Figure 26: (a) Schematic of the magnetic dipole-dipole interaction induced by a magnetic field H applied in the z direction. m is the magnetic dipolar moment of the colloidal particle, and r_{ij} is the distance between particles. (b) Scheme of a colloidal particle inside a bistable gravitational trap. The vector \mathbf{r} connects the center of the double well trap with the center of the particle. d is the distance between gravitational minima.

$$\mathbf{F}_i^{\text{trap}} = -\hat{\mathbf{e}}_{\perp} k_{\text{trap}} r_{\perp} + \hat{\mathbf{e}}_{\parallel} \begin{cases} k_{\text{hill}} r_{\parallel} & |r_{\parallel}| \leq \frac{d}{2} \\ k_{\text{trap}} (|r_{\parallel}| - \frac{d}{2}) \text{sign}(r_{\parallel}) & |r_{\parallel}| > \frac{d}{2} \end{cases} \quad (37)$$

The $\mathbf{F}_i^{\text{trap}}$ is the force which mimics the micropatterned substrate. Such force is described in the following way: along the parallel axis, as a spring force with a positive and repulsive value for the hill region, and with a negative and attractive value within the gravitational minima. In the perpendicular direction, the force is negative and attractive.

The vector \mathbf{r} goes from the trap to the particle center, r_{\parallel} and r_{\perp} are the parallel and perpendicular components of the vector joining the two stable positions of the trap, separated by a distance d . $\hat{\mathbf{e}}_{\parallel}$ and $\hat{\mathbf{e}}_{\perp}$ are the unit vectors along the parallel and perpendicular directions and k_{trap} and k_{hill} are respectively the stiffness that keeps the particle confined in the trap and the one that prevents the particle to be in the middle.

Since the particle dynamics occur effectively at low Reynolds number, $Re \ll 1$, where $Re = \frac{\text{Inertial forces}}{\text{Viscous forces}}$, the term on the right in [Equation 34](#) can be neglected, and we obtain the overdamped Langevin equation:

$$\gamma \dot{\mathbf{r}}_i = \mathbf{F}_i^{\text{dd}} + \mathbf{F}_i^{\text{trap}} + \boldsymbol{\eta} \quad (38)$$

We integrated this equation and used an Euler scheme to compute the trajectories of N particles. We used a custom version of LAMMPS (Large-scale Atomic/Molecular Massively Parallel Simulator) and a custom-made python program to write the input parameters and to analyze the output data.

4.1.1 Workflow

LAMMPS is a classical molecular dynamics simulation software designed to run efficiently on parallel computers. It was a cooperative project between the Sandia USA national laboratories and three different companies. It is an open-source software, distributed freely under the terms of the GNU Public License Version 2 (GPLv2). Due to its open-source nature, LAMMPS is continuously modified and enlarged. In fact, the 95 % of its source code results from contributions [144]. However, modifying LAMMPS is not an easy task. Only introducing one new parameter through the input data file involves modifying at least six classes. After modifying LAMMPS one needs to compile the packages to build the new LAMMPS version. In this thesis, we used a modified and compiled version (.exe) of LAMMPS already used in previous works [70, 75]. What we modified during my thesis were the input data files for the compiled version of LAMMPS and the routes to analyze the desired quantities from the data. Figure 27 shows a typical workflow.

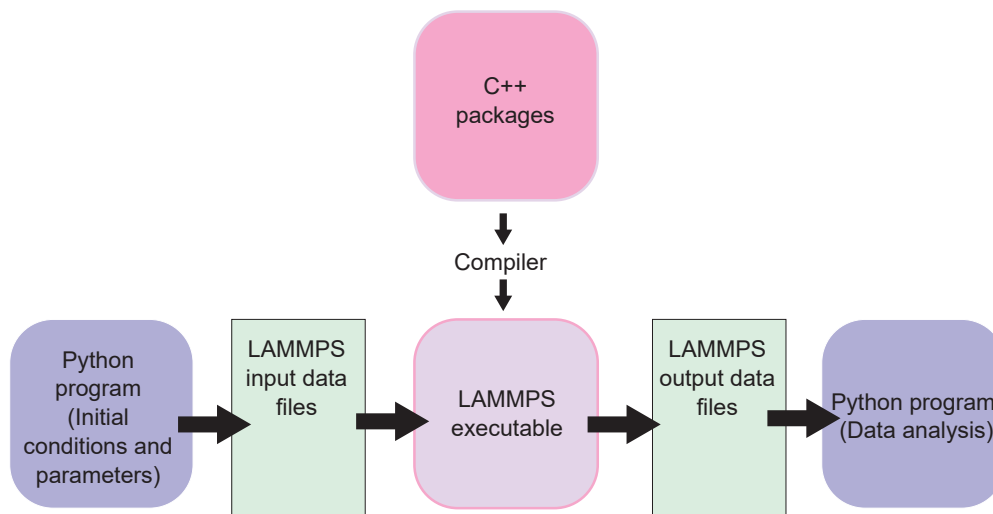


Figure 27: Typical workflow used in this thesis to perform Brownian dynamics and analyze the simulated data.

This .exe program will need a determined input data file to compute the desired simulation. After the integration procedure, the LAMMPS program will create the output files with the desired data. The input files are generated by using a custom-made Python program. During this procedure, we define the units, the system size, boundary conditions, lattice geometry and simulation

parameters such as, time step, initial positions, colloidal properties, etc. Finally, the output data files are read with a python script and special functions were created to analyze the trajectories and measure different order parameters such as spin directions, topological charges, and correlations between these quantities.

4.1.2 *Input parameters*

To generate a colloidal ice, one must first design its underlying lattice and choose the corresponding unit cell. The lattices that we used in this thesis are the square, the shakti, the cairo and a mixed coordination geometries between the last two [76, 145–147]. Once the type of lattice to be used is established, we must fill it with traps and with colloids. The colloidal particles are characterized by the following parameters:

- Radius of the particles, in μm . (10 μm in [76, 146, 147], 2 μm in [145])
- Volumetric magnetic susceptibility, dimensionless (χ).
- Diffusion coefficient, in $\mu m^2/s$.
- Density, in kg/m^3

One can also use particles characterized by different physical properties and combine them, as in ref [145]. Increasing the temperature will increase the diffusion coefficient, due to the stronger thermal fluctuations. On the other hand, at parity of the applied field, increasing the magnetic susceptibility of the particles increases the dipole-dipole interactions between them, reducing the effect of such fluctuations.

After prescribing the properties of the colloidal particles, we have to define the gravitational bistable traps where the colloids will be located. The traps are characterized by the following parameters:

- d , distance among gravitational minima, in μm .
- h_{hill} energy barrier, in $pN \cdot nm$.
- k_{trap} stiffness, in pN/nm .

h_{hill} defines the energy barrier that colloids need to overcome to switch from one stable position to the other. It is related to k_{hill} thought $k_{hill} = 8h_{hill}/d^2$. k_{trap} prevents the colloids from escaping from the double well, by generating a restoring force that pushes the particles toward one of the two potential wells.

If several species of colloids and traps are defined, it is necessary to specify their positions in the lattice. For instance, in [145] we combine two particles

characterized by different values of their magnetic susceptibility in a square lattice.

The properties used for the simulation are:

- Temperature of the bath, in K .
- Magnetic field applied along the experiment, in mT
- Cut off of the dipolar interaction, in μm
- Boundary type
- Time step, in s
- Total time, in s

The magnetic field applied can be static or time dependent.

4.1.3 Analyzing output trajectories

The usual procedure to simulate an ACI was to initialize a colloidal ice with a random initial configuration and apply a linearly increasing magnetic field along the perpendicular direction. Integrating the equation of motion, we can compute the position of the particles at each magnetic field value and observe the evolution of the system from a disordered state to a low-energy and more ordered state.

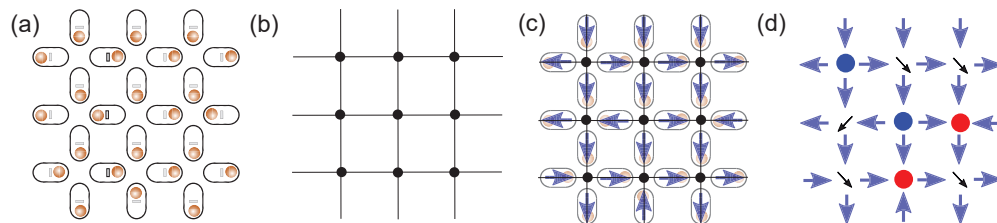


Figure 28: Inferring vertex topological charge. (a) Particles position in the double-well traps. (b) Square lattice and vertex positions (black dots) (c) Pseudospins (d) Topological charge of each vertex. Blue dots are $q = -2$ charge (type 2 vertices), red dots are $q = +2$ (type 5 vertices) and arrows indicate $q = 0$ (type 4 vertices).

Once we have the computed trajectories, we characterize the system by calculating the pseudo-spin associated with each colloid. By knowing the particle position and the underlying lattice geometry, we can reconstruct the graph shown in [Figure 28](#). The direction of the edges of the graph will be defined by the underlined lattice, and the sense of the edge will be obtained by the position of the colloid in the trap. In this graph, the nodes will be the vertices of

the colloidal ice (black dots, [Figure 28 \(b\)](#)). And each vertex will have a topological charge associated with it and an energy value. The topological charge is defined as the number of pseudospins pointing into the vertex minus the number of spins pointing out to the vertex, and for a square lattice, it can take values of $q = 0, \pm 2, \pm 4$. The energy of each vertex will be obtained by computing the sum of the dipolar interactions of all the colloids belonging to the vertex. In [Figure 29](#), all the possible vertices for a square lattice are presented with the corresponding topological charge, energy, and degeneracy.

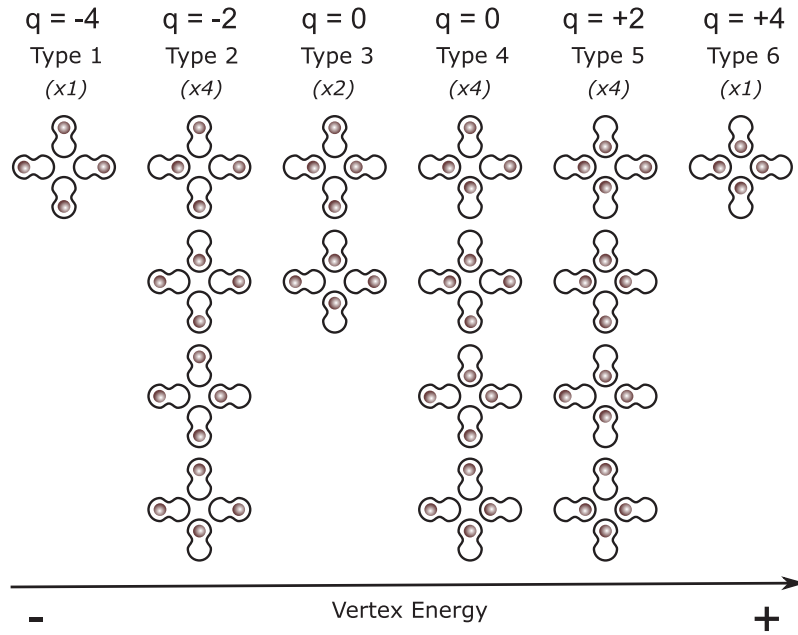


Figure 29: Energy vertex hierarchy in a square lattice. From left to right, the total magnetostatic energy of the vertex increases. All the $2^4 = 16$ possible vertex configurations are shown with the associated topological charge value, name and multiplicity, in parentheses.

The first type of analysis performed using the particle position was to identify the fraction of vertices corresponding to a given topological charge. Indeed, we have measured how this fraction varies as a function of the applied magnetic field, which controls the interaction strength between particles. Further analysis of the system was done by measuring different quantities as the spatial distribution of topological charges in [Publication 1 \(Section 6.1\)](#). In a following work, we have calculated correlation functions between chirality values as in [Publication 4 \(Section 6.4\)](#), spin overlap order parameter to measure return point memory effect in [Publication 2 \(Section 6.2\)](#).

EXPERIMENTS

In this chapter, we describe the experimental techniques used in this thesis. In particular, we used lithographic microfabrication techniques to generate lattices of topographic double wells. Holographic optical tweezers (HOT) to control the position of the magnetic particle within the double well. Microscopy techniques to visualize the particle dynamics and magnetic coils to apply fields that induce and control the pair-dipolar interactions between magnetic particles.

5.1 MAGNETOPTIC EXPERIMENTAL SET UP

5.1.1 *Optical tweezers*

The optical tweezers represent versatile scientific tools that can be used in a wide range of applications. They have been successfully used in the past in cell biology [148–150], colloidal science [151–153], lab-on-a-chip devices [154–156] and many others applications[157]. In this thesis, we used optical tweezers as a tool to distribute the particles in the double wells of the colloidal ice. The main operating principle of optical tweezers is the fact that a beam of light which carries momentum is scattered by an object. In this process, the beam momentum can change direction and by conservation of momentum, it exerts a resultant force acting on a dielectric object. If we imagine a beam of light that collides perpendicularly to a mirror, all the beam will be reflected, generating a resultant force [158–160]:

$$\mathbf{F}_{\text{reflection}} = \frac{2P}{c} \hat{\mathbf{u}} \quad (39)$$

This is the maximum force that can be generated by a laser beam of power P . Here, c is the speed of light in vacuum, and $\hat{\mathbf{u}}$ the unit vector indicating the original direction of motion of the photon. With these assumptions, if we have a laser beam power of 45 mW (typical operational power inside the sample during this work) we obtain a maximum force of 3×10^{-10} N or equivalently 300 piconewtons. Even though this force is small, comparable to the forces that we use in our daily life, it is relevant at the μm length scale. Cells, bacteria, or colloids deal with forces that are in this range. Of course, the above case is an idealization. In most of the cases, we have non-normal incidence and non-planar surfaces that will complicate the overall picture and reduce the applied force.

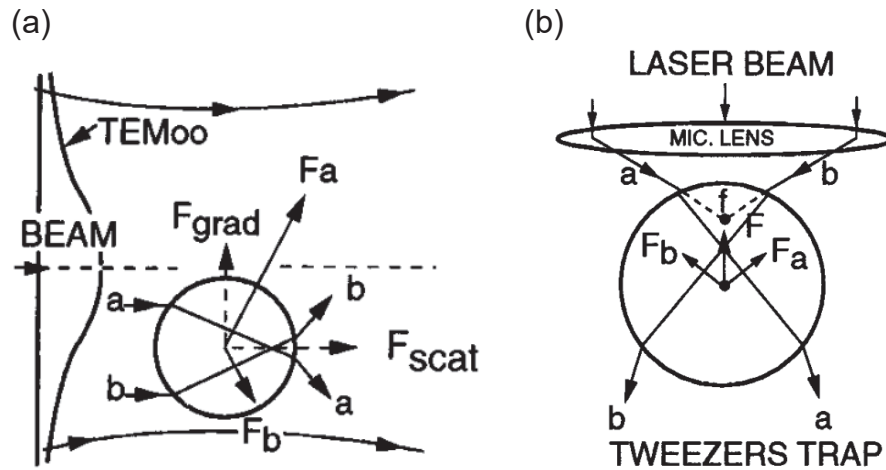


Figure 30: (a) Schematic of the origin of the forces F_{gradient} and $F_{\text{scattering}}$ for a high diffracting index sphere subjected to a Gaussian laser beam. (b) Diagram showing the ray optics of a spherical particle trapped in water by the highly convergent light of a single-beam gradient force trap. Images reproduced from [158, 160].

During the experimental demonstration of this radiation pressure, another force, not considered until that moment, was observed. Indeed, once an object is irradiated by light, it also tries to be in the highest intensity regions. As shown in Figure 30 (a), we can understand the origin of this force if we consider a high refractive index sphere with a diameter larger than the light wavelength, and placed off axis in a focused Gaussian beam. In the ray optics approximation, we can draw two rays, “a” and “b”, hitting the sphere symmetrically from its center. These two rays will refract through the particle, generating the forces F_a and F_b , that point along the direction of the momentum change. The force F_a is higher than F_b because the intensity in “a” is higher than in “b”. If we now consider all the rays that impinge on the particle, we will obtain a resultant force with two components, $F_{\text{scattering}}$ and F_{gradient} . The $F_{\text{scattering}}$, called the scattering force component, points in the direction of the incident light. F_{gradient} called the gradient component because it is caused by the gradient in light intensity points transversely towards the high intensity region of the beam. In Figure 30 (b) we have a particle in a stable position, generated by the balance between the $F_{\text{scattering}}$ and F_{gradient} . Stable trapping requires the axial gradient force to dominate, and is achieved when the beam diverges rapidly away from the focal point. Stable trapping of colloidal microspheres requires high numerical aperture microscope objective to focalize the light beam.

5.1.2 Holographic optical tweezers

We used Holographic Optical Tweezers (HOTs), which are characterized by a computer-controlled diffracting optical element (DOE) to tune the laser beam properties. This computer controlled DOE, is generated by using a Spatial Light Modulator (SLM). This device has the capability of dynamically shaping trapping patterns, which allows us to tailor the gradient forces and the scattering forces and hence change the incoming beam of light [161–164]. The SLM is a reflective phase modulator that allows changes in the amplitude or phase of the light that is reflected from it with high spatial resolution. The working principle consists of applying a voltage to reorient a liquid crystal (LC), a birefringent material with an anisotropic refractive index. By biasing individual pixels, the LC orientation can be locally modified, creating a refractive index landscape that translates into different local phase retardation experienced by the incoming light field [165], see Figure 31. In the SLM used in this work, we have 792×600 pixels of pitch $20 \mu\text{m}$.

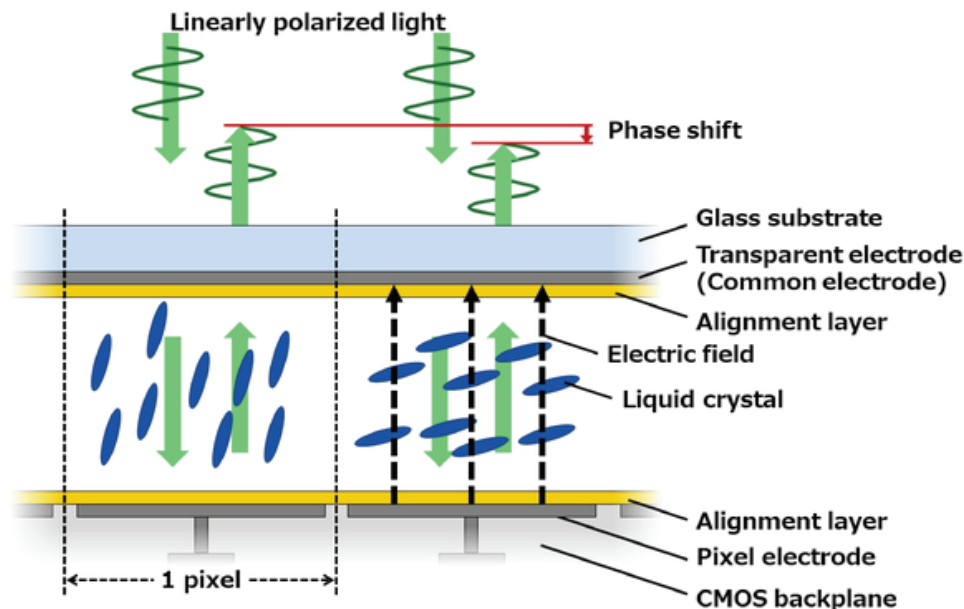


Figure 31: Schematic of the working principle of a Spatial Light Modulator (SLM). Image reproduced from [166].

In the optical setup the SLM is placed in the back focal plane of the microscope objective. In this way, a plane wave which is characterized by an electric field $E_{\text{beam}}(x, y) = A(x, y) \exp(i\psi)$ and a constant phase is projected onto the SLM. After being reflected by the SLM screen, the wave acquires a phase modulation $\phi(x, y)$ which encodes the desired pattern. The electric field $E_f(x, y)$ at the image plane, which in this case is the focal plane inside

the sample, is related to the electric field $E_{SLM}(x, y)$ in the plane of the SLM by the generalized Fourier transform :

$$E_f(x, y) = \frac{e^{2ik_0f}}{i\lambda_0f} 4\pi^2 E_{SLM}(f_x, f_y) \quad (40)$$

Hence, the field at a certain position in the focal plane is proportional to the amplitude of an input spatial frequency in the SLM plane. In this way, we can create individual traps by modulating the phase with specific spatial frequencies.

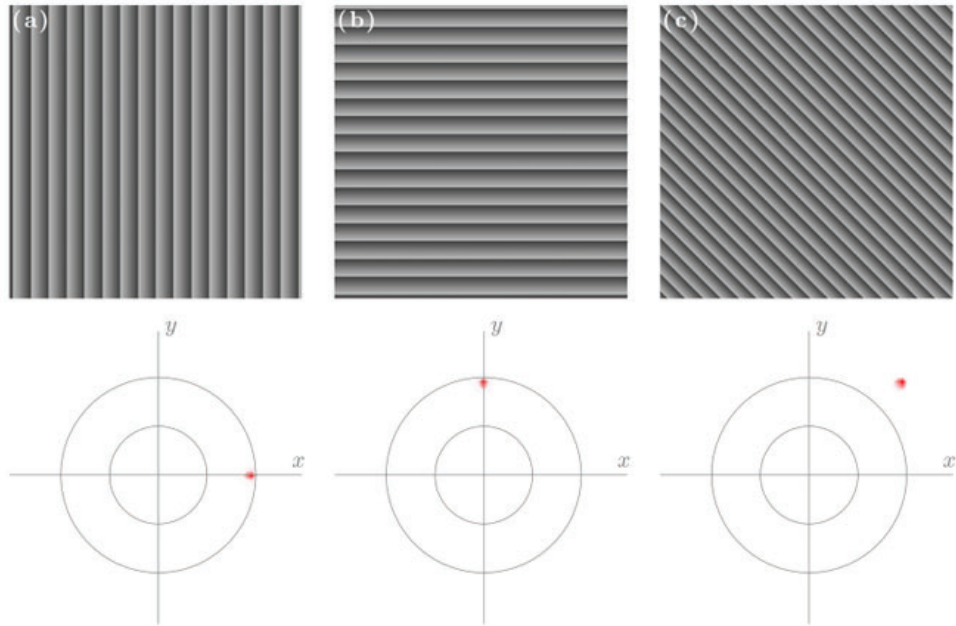


Figure 32: Holograms used to displace the laser beam from the center to the right (a), in the upper direction (b) and along a diagonal direction (c).

Thus, given a desired intensity distribution in the front focal plane, by taking its inverse Fourier transform we can determine the appropriate phase modulation, called hologram, to place on the SLM. However, in many situations the result is a hologram that modulates both the phase and the amplitude. Amplitude modulation would remove power from the beam, directing light away from the desired traps and into ghosts and other undesired artifacts, generating a reduction of trapping efficiency. As a result, it is more convenient to employ a hologram which control only the phase, called kinoform, or at least to reduce as much as possible the loss of intensity power using alternative methods. For example, if we desire to have only one optical trap that can move along the x , y and z directions we can employ the *grating and lenses method*, that is computationally very fast [167]. An example of the holograms obtained

with this method is shown in [Figure 32](#). If, instead, a more sophisticated intensity profile is needed in the focal plane, there are other approaches. Some of them are the *Gerchberg-Saxon algorithm* [168] and the adaptive-additive algorithm, that uses iterative computational methods to obtain the optimized hologram.

5.1.3 Experimental setup

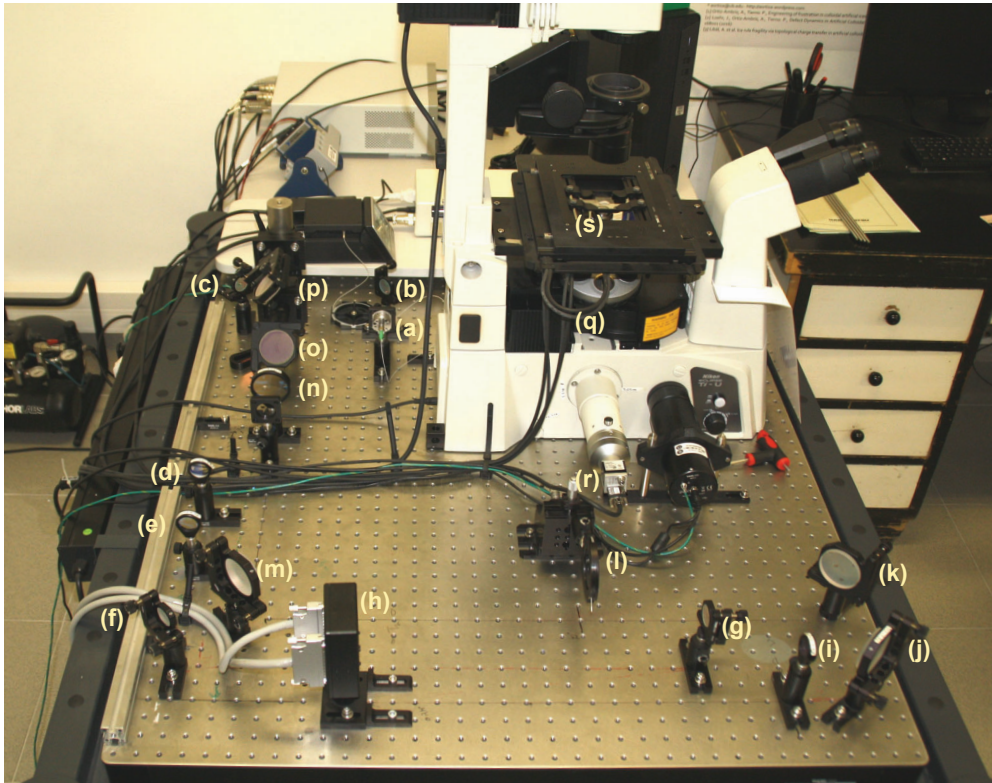


Figure 33: Setup showing the different optical elements. (a) optical fiber (b)(c) mirror, (d) lens of focal $f = -75\text{mm}$, (e) lens $f = 175\text{mm}$, (f)(g) mirror, (h) Spatial Light Modulator (SLM), (i) lens $f = 500\text{mm}$, (j)(k) mirror, (l) diaphragm, (m) mirror, (n) lens $f = 750\text{mm}$, (o)(p) mirror, (q) dichroic beamsplitter, (r) CCD camera and (s) copper coils and microscope objective.

[Figure 33](#), displays an image of the experimental set-up, and [Figure 34](#) a diagram of the path of the laser beam through all the optical elements. Each element is labelled with a Latin letter. In (a), we have an optical fiber from a butterfly laser diode ($\lambda = 976\text{ nm}$, Power = 300 mW, BL976-SAG300 Thorlabs). Elements (b) and (c) are mirrors (BB1 Eo3, Thorlabs) used to align the laser beam before the telescope, composed of lenses (d) and (e). In optical systems, two mirrors are usually placed before an optical element. This procedure facilitates the alignment task and allows us to control the laser beam direction.

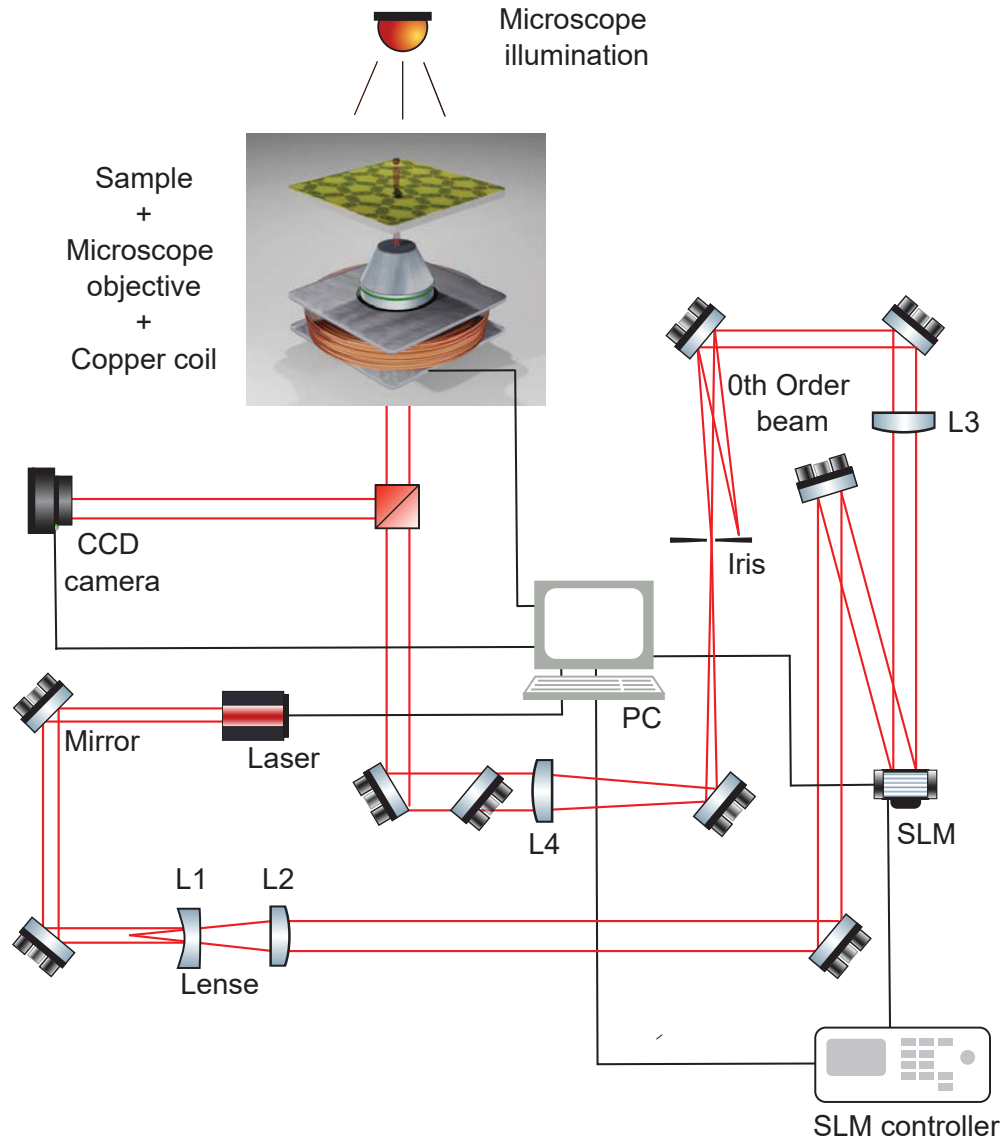


Figure 34: Schematic diagram showing the optical path of the HOT.

Then, before each lens or any other crucial optical element, we placed two mirrors of the same characteristics as the previous ones. By including the first telescope, we changed the laser beam size to fill the objective back aperture and to generate a robust optical trap. In (h), we have the SLM (Hamamatsu X10468-03). We control the SLM through computer-generated holograms, which are produced with a custom-made Python and LabView programs. After the SLM, we have another telescope, composed of lenses (i) and (n) to conjugate the SLM plane at the back focal plane of the microscope objective. This configuration takes the name of the $4f$ (2 lenses) optical tweezers configuration [169, 170]. In the middle of this second telescope, we find a pinhole (l) that allows us to work in an *off-axis* configuration, by adding a blazed grating to the phase mask, as the one in Figure 32 (a). With this configuration, only the first order

diffracted light is used for imaging, whereas the other diffraction orders of the SLM are physically blocked by (l). With mirrors (o) and (p), we change the z-plane of the modified laser beam to fit within the rear port of an inverted optical microscope (TiU, Nikon). Here, the laser is separated by a dichroic beam splitter such that it reaches the chamber while a fraction of light that is used to observe the sample reaches the Complementary Metal-Oxide-Semiconductor (CMOS) camera, (r). The used objective was a 40 \times oil immersion (Nikon, NA = 1.3), (s). The strategy used to move the optical trap through the field of view of the optical microscope is by moving the sample stage. This was achieved with a High-Speed Motorized XY Scanning Stages (Thorlabs) and a joystick (Thorlabs) connected to a controller (apt Brushless Servo Controller, Thorlabs), see [Figure 35](#).

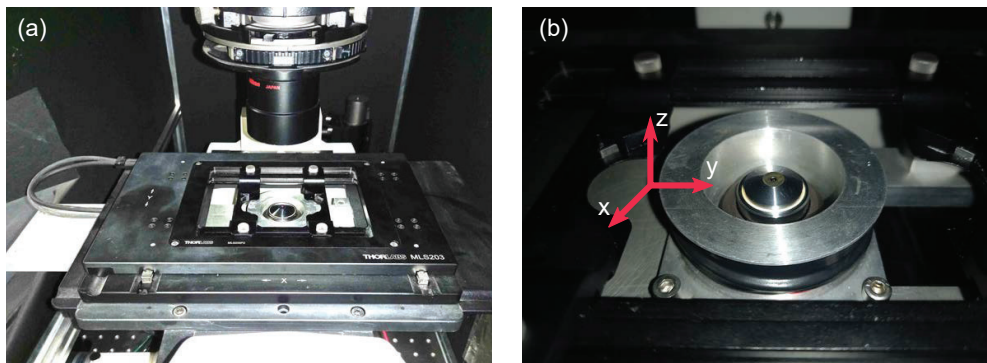


Figure 35: (a) Sample stage (b) Zoom of the microscope objective and coupled copper coil.

The complete diagram of the HOT experimental set up and the ray's diagram is shown in [Figure 34](#)

Finally, we shape the laser beam profile to mimic a ring with a diameter similar to that of the particle. This was done to obtain a stable optical trap and to reduce the heating of the surrounding fluid due to the absorption of light from the magnetic nanodomains of the particles [171]. In [Figure 36](#), we show a particle in an initial position [Figure 36](#) (a) and in the final position [Figure 36](#) (b), after 28 s, being moved by a ring of light shown also in [Figure 36](#) (b).

5.1.4 Magnetic fields

The external field is applied with a custom-made copper coil with the main axis aligned with the z-axis; see [Figure 35](#) (b). To control and increase the magnetic field strength, we control the applied voltage. To achieve that, we use a power amplifier (BOP-20 10M, KEPCO) connected to a National Instruments card managed through a custom-made LabView program. With this configuration, we can reach magnetic field values that range from 0 mT to 20 mT. The coil was placed as near as possible to the sample to optimize the field

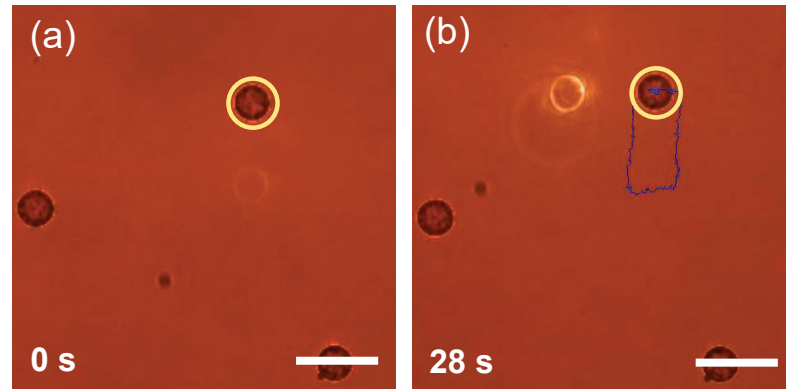


Figure 36: Optical microscope images of a (a) Free particle at 0 s. (b) New position of the particle, after 28 s. The particle has been transported along a distance of a few μm and then released to visualize the light ring next to the trapped particle (yellow circumference). The blue line corresponds with the particle trajectory. Scale bar is $20\mu\text{m}$

strength. We calibrated the magnetic field with a Teslameter (FM 205, Projekt Elektronik GmbH) before each experiment. To avoid heating problems because of the high currents applied, a piece of aluminum is placed in contact with the coil, to reduce temperature and dissipate heat.

5.2 MICROFABRICATION

The first step in the microfabrication protocol is the design of the photomask. The photomask will contain the design of the lattice of double wells of the colloidal ice. We used a Cr photomask (resolution limit $\approx 1\mu\text{m}$, [172]), and design the microfeatures with AutoCAD (Adobe). The realization of the photomask and subsequent lithographic procedures are performed in a cleanroom. Typically, cleanrooms are classified depending on the number of airborne particles per m^3 . The one that we used to build our colloidal ice present 10.000 particles/ m^3 . The monitored environmental conditions are pressure, humidity, and temperature. In the used cleanroom, the temperature is kept between $20\text{ }^\circ\text{C}$ and $22\text{ }^\circ\text{C}$, humidity between $45\%HR - 55\%HR$ and a pressure gradient is created to bring impurities and contaminants outside the cleanroom. The used microfabrication technique is photolithography, which is a multi-step technique where light generates micropatterns within a polymer layer [173]. The building material is a photoresist. There are mainly two types of resists: positive and negative. The classification depends on the effect of light on the molecular structure of the resist. Exposed positive resists become soluble to photoresist developer, and exposed negative resists become insoluble to photoresist developer, see Figure 37.

When I started my Ph.D., the microfabrication protocol used to build the microstructures, was based on a positive photoresist built directly on the top

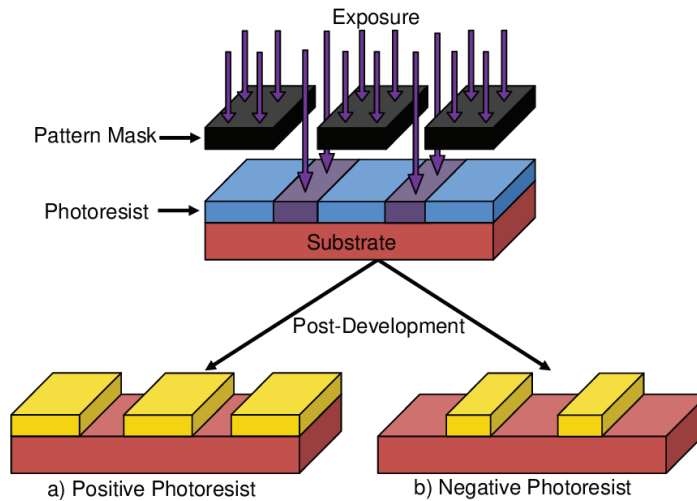


Figure 37: (a) Positive and (b) negative resist during exposure and development [174].

of a cover glass. However, it was difficult to work with the resulting sample. A frequent problem was that even before starting the experiments, colloids were irreversibly stuck in the microstructure. After trying to avoid this phenomenon unsuccessfully, by coating the magnetic colloids or the substrate, we decided to improve and change the protocol to have a more stable and re-usable structure. We make a summary of those fabrication methods from the AZ1512 HS (Microchem) positive resist built directly on a thin glass slide, used in Publication 1 (Section 6.1) to the SU-8 3005 (Microchem) fabrication on a Si wafer for then generating PDMS replica, used in Publications 3 and 4 (Section 6.3 and Section 6.4).

This work was developed in the MicroFabSpace cleanroom at the Institute for Bioengineering of Catalonia (IBEC). I used the following equipment: a Direct Write Laser (Heidelberg Instruments, DWL 66FS) to generate the Chromium masks, a hot plate (P selecta, Plactronic), a Mask aligner (SÜSS Microtec, MJB4) and (Kloé S.A., UV-KUB3) to expose the photoresists, Oven (P Selecta), Spin coater (Laurell Tech., WS-650MZ 23NPP/lite and WS-400A 6TFM/lite), Plasma cleaner (Harrick, PCD-022-CE).

5.2.1 AZ1512 HS resist

AZ1512 HS is a commercially available positive photoresist. It is part of the AZ Series that allows to realize films having a range of thickness from $0.5 \mu\text{m}$ to $6 \mu\text{m}$. The main difference with other protocols used in this thesis is the fact that we build the structure directly on the top of a coverglass of $24 \times 50 \text{ mm}$ size and $0.13 - 0.16 \text{ mm}$ thick (Menzel-gläser). This methodology reduces the number of steps to obtain one sample since it is directly built on the final substrate. On the other hand, the lifetime and reproducibility of

the microstructures are consequently reduced. As mentioned, repeating the protocol can generate slight changes due to fluctuations in temperature or humidity. The used protocol was explained in detail in [Appendix A](#).

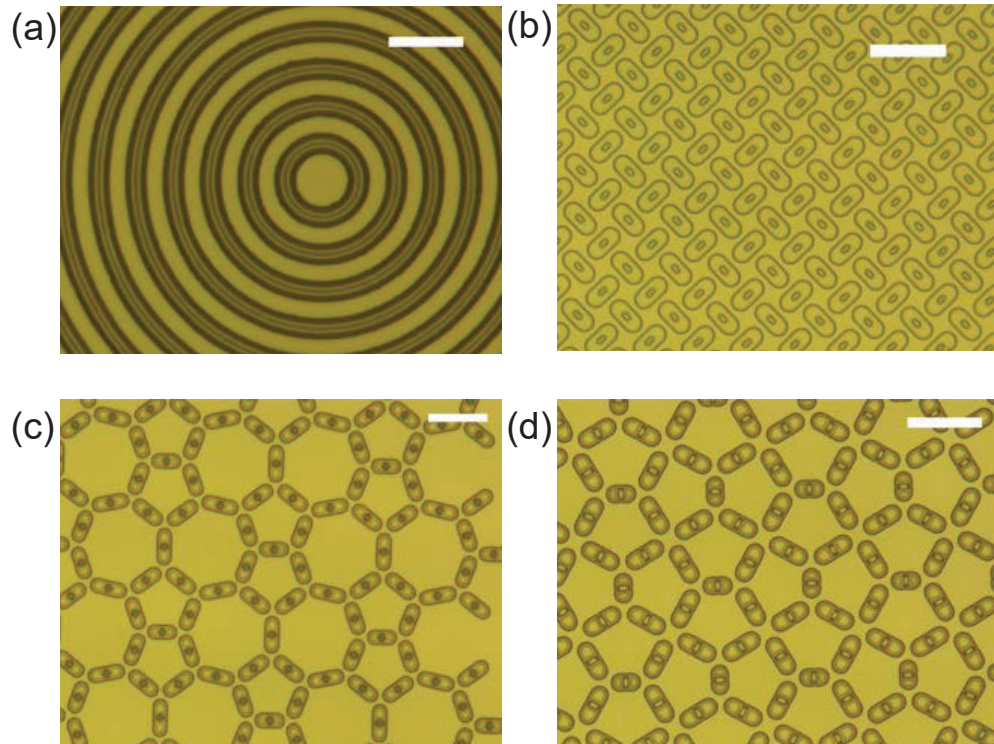


Figure 38: AZ1512 HS microstructure on top a coverglass. Scale bar is $20 \mu\text{m}$ in (a) and $40 \mu\text{m}$ in (b),(c) and (d).

In this protocol, we used a TI primer (Microchem), an adhesion promoter, that improves resist adhesion on the substrate and AZ 726 MIF (Microchem) a tetranethyl-ammonium hydroxide (TMAH) based photoresist developer.

We obtained satisfactory results, as shows [Figure 38](#), and we used this protocol to realize the experiments in [76], where we study the finite size effects and the dynamics of a colloidal ice by fixing the boundary conditions. The protocol was changed to reduce the size of the double wells to use smaller paramagnetic colloids. With this technique, we realized a colloidal ice where the role of thermal fluctuations are relevant, see [Appendix C](#).

To further miniaturize the sample, the AZ resist on top of a cover glass is not the best choice. This type of resist, even under optimal working conditions, does not generate straight vertical profiles; see [Figure 39](#). The best you can achieve under this condition is an overcut profile of 85° , critical on a small structure. In addition, by building a structure on the top of a rectangular coverglass, one could provoke further problems such as a severe edge bead, an accumulation of photoresist in the borders of the substrate, which will generate a non-desired mask-resist gap during exposure [172, 175]. In

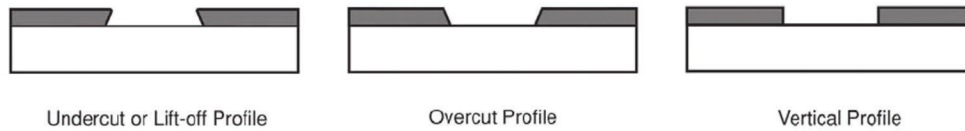


Figure 39: Schematic diagram showing the types of profiles that can be achieved during a microfabrication process.

in addition, we have also back scattering reflections due to light that can also cross the transparent coverglass and re-enter the substrate from the backside [176]. Both phenomena generate exposure of non-desired areas and then a lower feature resolution. Figure 40 shows samples where these results have produced patterns of blurred double wells.

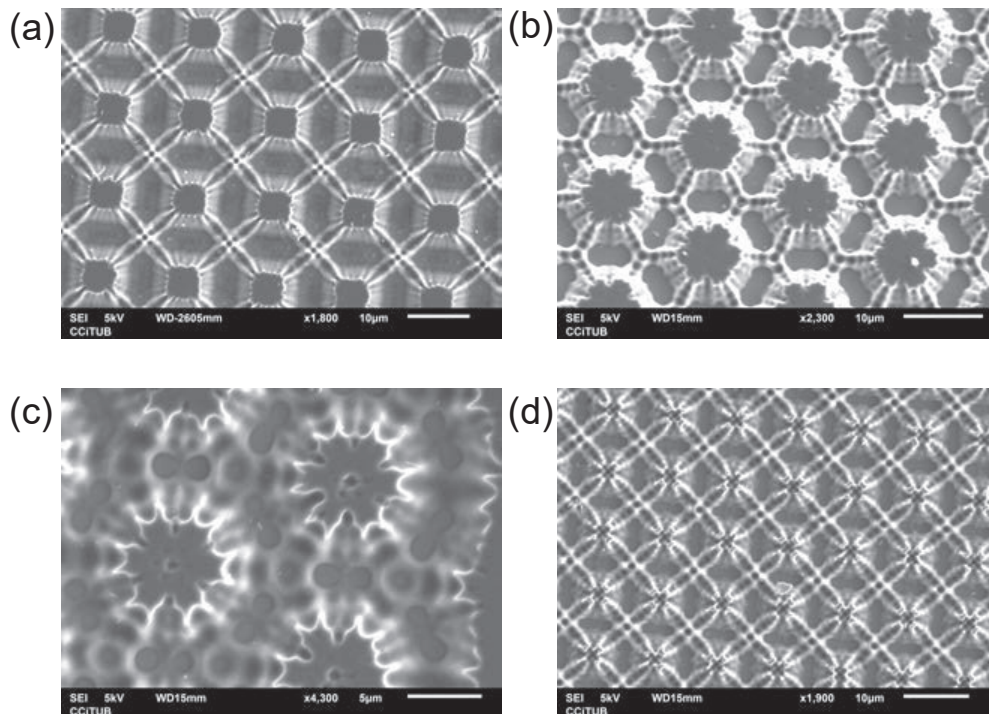


Figure 40: SEM images of AZ1512 HS photoresist on top a coverglass. The effects of backscattered light from UV exposure and edge bead can be observed. Here, lattices are not well-defined due to UV light exposition of non-desired areas. (a) and (d) are results of the transfer of patterns from a mask that was originally with a square lattice. (b) and (c) of honeycomb lattices.

These drawbacks were solved using different fabrication protocols.

5.2.2 SU-8 resist and PDMS replica

SU-8 is a negative photoresist extensively used in the literature [177–180]. It is an excellent choice to build high aspect ratio microstructures, up to 1:100 [172]. Protocols based on the use of SU-8 photoresist can be used to produce films of thickness ranging from a few micrometers up to 250 μm in height. To further increase the structure's thickness, one can add more layers. In contrast, to reduce the SU-8 thickness, one can dilute with solvents to reduce viscosity [173, 181]. Typically, SU-8 microstructures are built on top of a silicon wafer, which increases the adhesion and reduces the back scattered light during light exposure. Thus, one can avoid poor adhesion problems and enhance the lithography resolution. In this thesis, we used the SU-8 patterns as a PDMS mold. The SU-8 microstructure is not used as the final substrate, instead, it is an intermediate step in the fabrication process. To optically access the sample, we need to have a thin PDMS layer, due to the small working distance of the microscope objective ($\approx 170 \mu\text{m}$) and to avoid beam absorption. Hence, PDMS was not directly poured on the structure, as done in most SU-8 protocols where the PDMS thickness can be as high as few mm [182, 183], but instead, it was spin-coat at high RPM to obtain a thin layer, with a film thickness of $\approx 13 \mu\text{m}$. The protocol used in Publications 3 and 4 (Section 6.3 and Section 6.4) is also explained in more details in Appendix B.

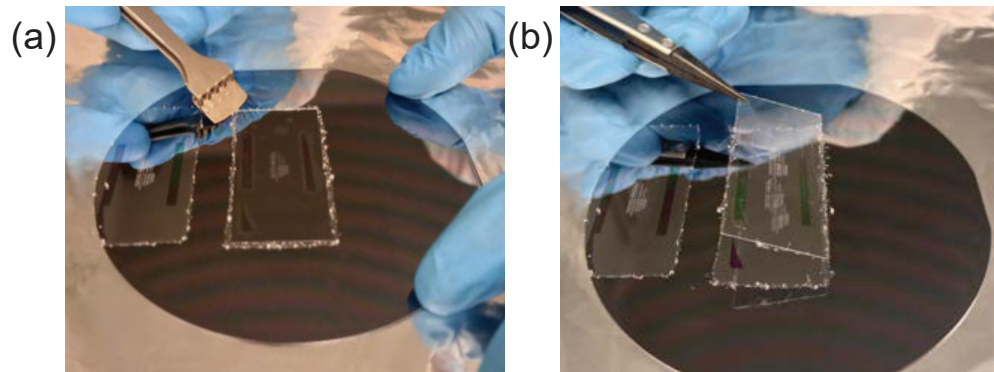


Figure 41: Peeling off procedure. In (a) is shown the glass on the top of the PDMS layer and the SU-8 structure, and in (b) the glass and the PDMS after peeling off.

The materials used in this protocol are silicon wafer, 100 mm of diameter (Siegert wafer), SU-8 3005 (Microchem), silicon elastomer (SYLGARDTM 184 Silicon Elastomer Base) and silicon elastomer curing agent (SYLGARDTM 184 Silicon Elastomer Curing Agent) and the propylene-glycol monomethyl ether acetate developer (Sigma Aldrich). With this protocol, we realized the lithographic structures shown in fig Figure 42. Hence, by changing the protocol used in previous works [70, 75, 76, 128, 134] we were able to obtain chemically stable, long-lasting and reusable microstructures. The problem of having irreversibly attached particles to the substrate was solved, the ability

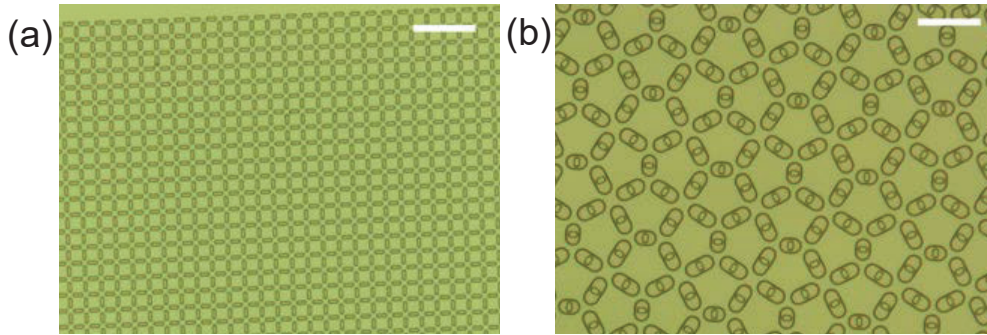


Figure 42: PDMS double well microstructures on the top of coverglass. A square lattice is shown in (a) while (b) shows a Cairo lattice. The Scale bar is $50 \mu\text{m}$ long.

to replicate the sample reduces sample preparation time once the SU-8 master is fabricated, and the possibility of washing the sample extends its useful lifetime.

5.3 SAMPLE PREPARATION

Once the micropatterned substrate was built, we prepared the colloidal suspension to place on top of it. We mainly used two sizes of paramagnetic colloidal particles. The $10.4 \mu\text{m}$ diameter microparticles (Sigma Aldrich, 49664), used in works Publications 1, 3 and 4 ([Section 6.1](#), [Section 6.3](#) and [Section 6.4](#)) and the $2.8 \mu\text{m}$ diameter microparticles (Dynabeads M-270, Dynal) used in the project illustrated in [Appendix C](#). Moreover, these two types of particles have different magnetic susceptibilities and surface properties. While, the $2.8 \mu\text{m}$ sized particles are chemically stable, since they are functionalized with surface carboxylic acid groups. The $10.4 \mu\text{m}$ diameter microparticles need to be pretreated, to avoid the particle-particle aggregation, and to better stabilize them close to the substrate.

The $10.4 \mu\text{m}$ particles were stabilized with a surfactant, which promotes the adhesion of hydrophobic-hydrophilic molecules to the surface of the particles and then enhances particle-particle repulsion and particle-substrate repulsion [184]. The used surfactant was the Sodium dodecyl sulfate (SDS), and the concentration used in deionized water is about 0.1 %. Then, we place the colloidal suspension in a rotor, with an angular speed $\omega = 5RPM$, inside a fridge for at least four hours.

Finally, the colloidal ice was realized by depositing a drop of the colloidal suspension above the topographic substrate and seal the sample using a coverglass and a glue (silicon paste, geneframe[®], parafilm[®]...) to avoid drainage or evaporation. Using this protocol, the sample could be stable up to one week.

5.4 DATA ANALYSIS

After all these preparation steps, we have a closed cell with the colloidal particles dispersed in water and floating above the microstructure. We used optical tweezers to fill the bistable gravitational traps one by one and obtain an initial random distribution of particles similar to the microscope image shown in [Figure 43](#). The initial positions of the colloids are chosen randomly according to a random number generator, and thereafter, we start recording a video while we apply a magnetic field ramp. The particles, thus, move within the traps due to repulsive dipolar interaction with their neighbours, and acquire positions which minimize the local magnetostatic energy configuration. To analyze the experimental data, we extract the position of the colloidal particles from the recorded videos using a version of the tracking code developed by John C. Crocker and David G. Grier [185]. Further, we use a custom-made python program to calculate the vertex configuration, following the procedure detailed in [Section 4.1.3](#) and similar custom programs are used to calculate different statistical quantities.

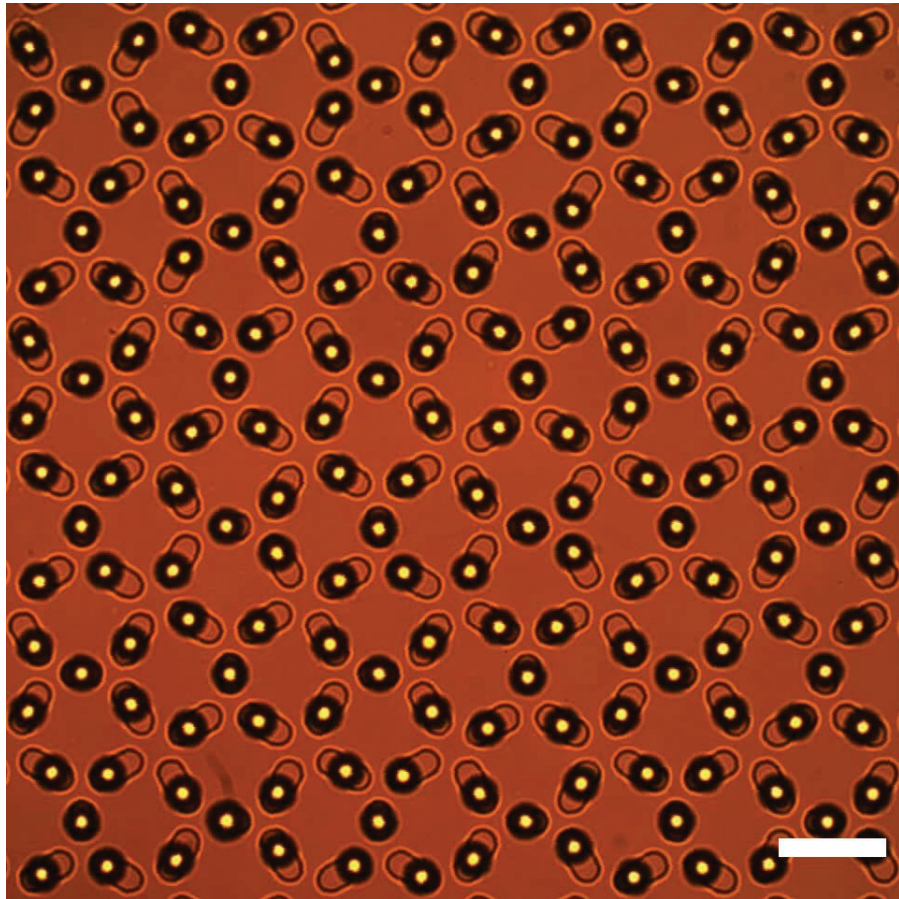


Figure 43: Optical microscope image showing the realization of a Cairo artificial colloidal ice sample. Scale bar is $40 \mu\text{m}$.

Part V

RESULTS

6.1 PUBLICATION 1

Topological boundary constraints in Artificial Colloidal Ice

Carolina Rodríguez-Gallo^{1,2}, Antonio Ortiz-Ambriz^{1,3} and Pietro Tierno^{1,2,3}

Physical Review Letters **126**, (2021) 188001

¹ Departament de Física de la Matèria Condensada, Universitat de Barcelona, 08028, Barcelona, Spain

² Universitat de Barcelona Institute of Complex Systems (UBICS), Universitat de Barcelona, 08028, Barcelona, Spain

³ Institut de Nanociència i Nanotecnologia (IN2UB), Universitat de Barcelona, 08028, Barcelona, Spain



Topological Boundary Constraints in Artificial Colloidal Ice

Carolina Rodríguez-Gallo^{1,2}, Antonio Ortiz-Ambríz^{1,3,*} and Pietro Tierno^{1,2,3}

¹*Departament de Física de la Matèria Condensada, Universitat de Barcelona, 08028, Barcelona, Spain*

²*Universitat de Barcelona Institute of Complex Systems (UBICS), Universitat de Barcelona, 08028, Barcelona, Spain*

³*Institut de Nanociència i Nanotecnologia (IN2UB), Universitat de Barcelona, 08028, Barcelona, Spain*

 (Received 14 December 2020; revised 17 March 2021; accepted 7 April 2021; published 6 May 2021)

The effect of boundaries and how these can be used to influence the bulk behavior in geometrically frustrated systems are both long-standing puzzles, often relegated to a secondary role. Here, we use numerical simulations and “proof of concept” experiments to demonstrate that boundaries can be engineered to control the bulk behavior in a colloidal artificial ice. We show that an antiferromagnetic frontier forces the system to rapidly reach the ground state (GS), as opposed to the commonly implemented open or periodic boundary conditions. We also show that strategically placing defects at the corners generates novel bistable states, or topological strings, which result from competing GS regions in the bulk. Our results could be generalized to other frustrated micro- and nanostructures where boundary conditions may be engineered with lithographic techniques.

DOI: [10.1103/PhysRevLett.126.188001](https://doi.org/10.1103/PhysRevLett.126.188001)

In the thermodynamic limit, the bulk properties of a statistical ensemble are no longer influenced by its boundaries. However, in frustrated spin systems, the boundaries can induce configurations that propagate far into the bulk [1,2]. Among several examples of frustrated systems in nature, the most representative one is spin ice [3–5], which can be considered the magnetic “analog” of the water ice [6]. Artificial spin ice systems (ASIs) based on lithographic engineering recently emerged as a versatile experimental platform to investigate geometric frustration effects [7]. An ASI is composed by a lattice of nanoscale ferromagnetic islands, arranged to induce frustration [8–10]. In contrast to natural magnets, an ASI allows one to directly visualize the spin arrangement, a feature that has been used to investigate the effect of disorder [11–13], thermalization [14,15], and degeneracy in many geometries [16–20]. Alternative realizations include arrays of nanowires [21], patterned superconductors [22,23], macroscopic magnets [24], Skyrmions in liquid crystals [25,26], superconducting qubits [27], and colloidal particles in bistable potentials [28].

In such systems, the presence of disorder or a finite temperature often prevents them from reaching the ground state (GS), and, instead, they fall to a metastable state containing defects in the form of charged vertices. These defects can be characterized by a topological charge Q and have a topological nature, since they can be destroyed only when annihilating with other defects of opposite charge. In the GS, the vertices satisfy the ice rule that prescribes a minimization of the local charge, $Q = 0$. While much attention has been placed on how temperature or external fields drive a system toward its GS, the role of boundaries in finite systems has been often overlooked. This is of especial importance when dealing with interacting

magnetic systems where the interaction energies are governed by long-range dipolar forces.

Here, we show how boundaries can be engineered to control the bulk behavior and the formation of topological states such as point defects and topological domain walls spanning the bulk. We demonstrate this concept with an artificial colloidal ice, a system that recently emerged as a microscale soft-matter analog to ASI [29]. Colloidal ice consists of an ensemble of paramagnetic colloids two-dimensionally (2D) confined by gravity in topographic double wells, where the particles may sit in two stable positions and an external magnetic field \mathbf{B} induces repulsive dipolar interactions [Fig. 1(a)]. One can assign a vector (analogous to a spin) to each well such that it points toward the vertex’s center (spin in) or away from it (spin out); see Fig. 1. When arranged in a square lattice, one can classify six possible vertex types, each of them with an associated topological charge $Q = 2n - c_N$, where n is the number of particles in and c_N the lattice coordination number. For the square, it is $c_N = 4$. Thus, vertices of type III and type IV have $Q = 0$ and fulfill the ice rule, and type III gives rise to the GS. Topological defects are charged vertices with $Q \neq 0$ or closed loops of type-IV vertices [Fig. 1(e)].

To simulate colloidal ice, we perform Brownian dynamics, carefully parametrized to mimic the experiments [28]. We consider a 2D array of double wells, each filled by one paramagnetic colloid of diameter $d = 10.3 \mu\text{m}$ and magnetic volume susceptibility $\chi = 0.048$. The overdamped equation of motion for one colloid at position \mathbf{r}_i is

$$\gamma \frac{d\mathbf{r}_i}{dt} = \mathbf{F}_i^T + \mathbf{F}_i^{\text{dd}} + \boldsymbol{\eta}, \quad (1)$$

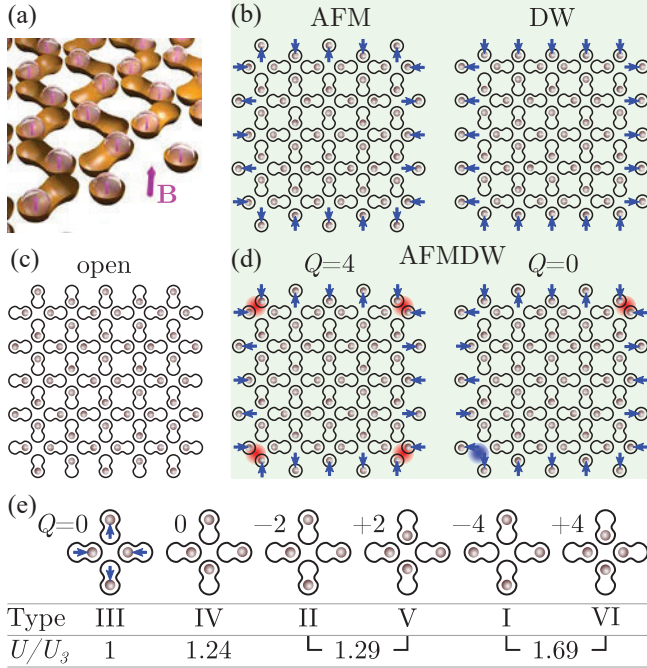


FIG. 1. (a)–(e) Different schematics showing (a) the double-well geometry with paramagnetic colloids and the method of fixing the boundaries by using a single well; (b),(c) the three basic types of boundary conditions, antiferromagnetic (AFM), domain wall (DW), and (c) open boundaries; and (d) AFMDW boundaries designed with defects which can carry a net charge ($Q = 4$, left) or can be neutral ($Q = 0$, right). The shaded region indicates boundaries which topologically protect the enclosed charge. (e) Different vertex types with their effective normalized energetic weight (bottom) and topological charge (side). Vertices are ordered by increasing energetic ratio respect to type III. The associated spins are shown on the type-III vertex.

where $\gamma = 0.032 \text{ pN s } \mu\text{m}^{-1}$ and \mathbf{F}_i^T is the force from the double well which is modeled as a bistable harmonic potential; more details are in the Supplemental Material [30]. The dipolar force acting on particle i due to the neighboring colloids is $\mathbf{F}_i^{\text{dd}} = (3\mu_0/4\pi) \sum_{j \neq i} (\mathbf{m}^2 \hat{r}_{ij} / |r_{ij}|^4)$, where $\mathbf{m} = \chi V \mathbf{B} / (\mu_0)$ is the dipole moment induced by the external field \mathbf{B} , $\mu_0 = 4\pi \times 10^{-7} \text{ H/m}$, and $\hat{r}_{ij} = (\mathbf{r}_i - \mathbf{r}_j) / |\mathbf{r}_i - \mathbf{r}_j|$. To consider long-range dipolar interactions between the particles, we apply a large cutoff of $200 \mu\text{m}$. Finally, $\boldsymbol{\eta}$ represents a random force due to thermal fluctuation, with zero mean, $\langle \boldsymbol{\eta} \rangle = 0$ and delta correlated, $\langle \boldsymbol{\eta}(t) \boldsymbol{\eta}(t') \rangle = 2k_B T \gamma \delta(t - t')$, with a temperature $T = 300 \text{ K}$. Simulations are performed for different system sizes, ranging from $L = 3$ to $L = 40$, where L is the number of vertices along the side. We increase B linearly up to $B = 25 \text{ mT}$, at a rate 0.03125 mT/s . For $B = 25 \text{ mT}$, the pair potential between two particles in the closest (farthest) place of two double wells is $U = 1176k_B T$ ($U = 115k_B T$). Our strategy to fix the boundary consists in placing a particle in a single harmonic well at a location such that it corresponds to a spin pointing in or out.

We consider four different situations: two fixed boundary conditions, namely, antiferromagnetic (AFM) and domain wall (DW), illustrated in Fig. 1(b). In AFM boundaries, colloids are placed alternately pointing in and out. However, flipping a subset of the colloids in an AFM boundary can create defects that are topologically constrained to the inner region, as illustrated in Fig. 1(d). This is the basis of the Gauss' law analog introduced in Ref. [27] for a qubit system. As constructed, the AFM state has a neutral charge at the boundaries. This charge neutrality is broken when a spin is changed from out to in and two defects are created on the AFM state. With this strategy, we introduce in Fig. 1(d) the antiferromagnetic domain wall (AFMDW), where we mix AFM boundaries with DW corners. This configuration produces different behavior with system size L . With L even, two corners point in, two point out, and the charge is $Q = 0$. Instead, with L odd, the four corners point either in or out, and a total charge $Q = \pm 4$ is locked inside the bulk. Furthermore, we also ran simulations with periodic boundaries, that are similar to previous simulations on particle-based ice [31,32], and with open boundaries, which represent the experiments with no fixed particles [Fig. 1(c)].

To show how borders can be manipulated in experiments, we realize a square colloidal ice with antiferromagnetic domain walls. The system setup has been described in Ref. [33]. Here, we modify the boundaries of an isotropic lattice by adding nonmagnetic silica particles to the corresponding double wells. The silica particles induce local jamming, fixing the paramagnetic particle to a stable location, as shown below.

We start by showing in Fig. 2(a) how the four different boundary conditions influence the bulk behavior in terms of the fractions of type-III vertices (top) and of the average vertex charge (bottom). Both the open and DW frontiers show very similar trends, failing to reach the GS for all sizes. For these type of boundaries, the system accumulates charged defects at the boundaries, which are all negative for open boundaries and positive (negative) for inward-pointing (outward-pointing) spins in the DW. Only open boundaries allow the appearance of a net nonzero topological charge, which converges to a size-dependent negative value at high field, as shown in the bottom in Fig. 2(a). This effect can be appreciated also from the time evolution of the system in Fig. 2(b) and in Video S1 [30]. Above $B = 16.6 \text{ mT}$, all the borders exhibit particles displaced toward the outer region (spins out), a radial polarization effect predicted in Ref. [34]. Such an effect arises since the analogy between spin and colloidal ice is broken near the boundaries due to the repulsive interactions between the particles, while in ASIs nanoislands interact due to in-plane dipolar forces. In contrast, periodic, AFM, and DW satisfy the conservation of topological charge Q for all field values and system sizes. As shown in Fig. 2(b) and Videos S2 and S3 [30], we find that a system with periodic or DW

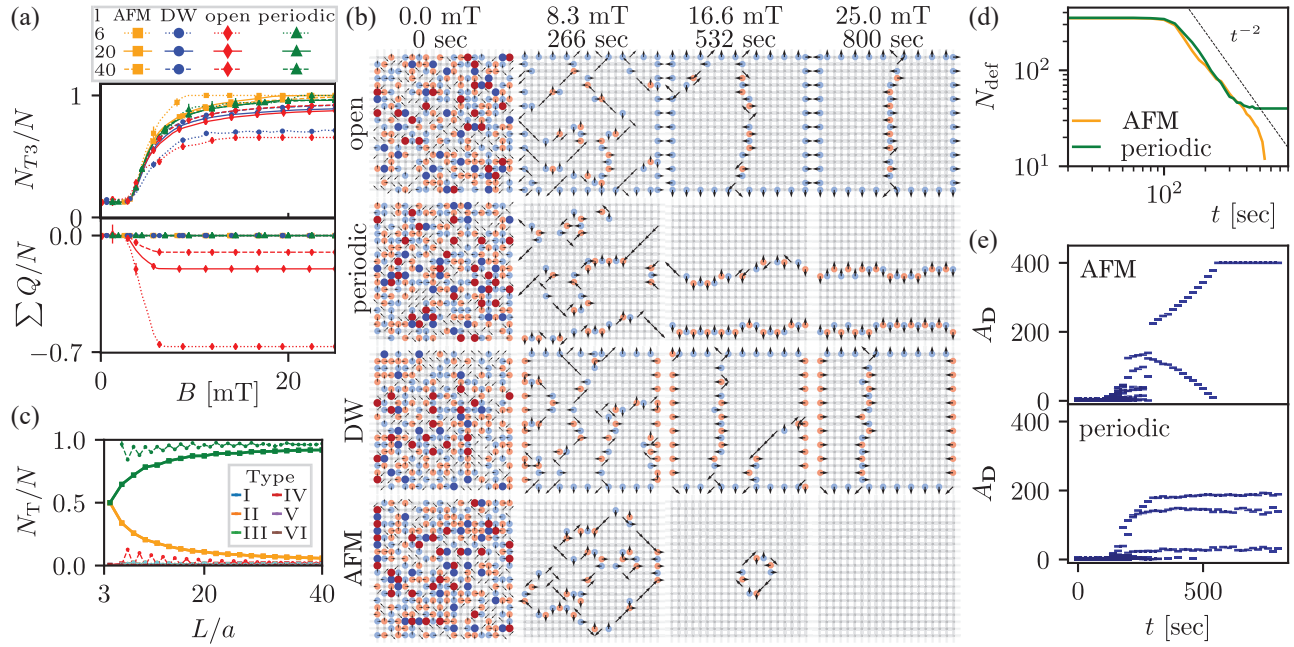


FIG. 2. (a) Fraction of type-III vertices (top) and average vertex charge (bottom) for different system sizes (numbers) and type of boundaries (symbols). (b) Maps of defects for different types of boundaries. The colored circles indicate charges, while colorless arrows indicate type-IV defects. The system width is $L = 20$ vertices. (c) Fraction of vertices at the maximum field ($B = 25$ mT) versus system size, for open (solid lines) and periodic (dotted lines) boundaries. (d) Number of defects N_{def} vs time for the AFM and periodic case; the line denotes t^{-2} scaling. (e) Type-III domain area A_D vs time for AFM (top) and periodic (bottom).

boundaries induces the formation of system-spanning domain walls, not allowed by the AFM (Video S4 [30]). These defect lines are very difficult to erase by increasing B further, as they require the simultaneous flipping of large GS regions in the bulk. In a system with periodic boundaries, the parity of the domain walls is also topologically protected: When the boundaries are of even size ($L \in 2\mathbb{Z}^+$), defect lines can appear only in pairs. In contrast, for odd values of L , at least one defect line is always present. This effect appears also in Fig. 2(c), where the periodic boundaries exhibit a zigzag trend: Odd lengths have an excess of type-IV vertices, which become less relevant as the boundary to bulk ratio becomes smaller. In contrast, we found that AFM boundaries can equilibrate to the GS faster and at lower fields, since they restrict the phase space as predicted in Ref. [1]. The kinetics of the defects is analyzed in Fig. 2(d) for AFM boundaries and compared to the periodic case. Both display coarsening dynamics with a power law scaling. This behavior can be also appreciated from the time evolution of the type-III domains in Fig. 2(e). Initially, both systems create similar domain structures, but, while a system with periodic boundaries falls to a metastable state with several smaller domains, the AFM creates a single loop of defects that continuously shrink, giving rise to the GS.

We now explore the behavior when boundaries are fixed in the AFMDW state. Figure 3 shows a system with $Q = -4$, where, if the energy of the type-IV vertices were

similar to that of type III, the charge would be contained in a single type-I vertex, with four lines of type IV connecting it to the corners. However, due to line tension, as the applied field increases, it becomes more stable to break up the excess of charges and distribute them along two lines connecting the four corners. This leads to a symmetry breaking, where the system must choose whether to arrange the two connecting lines horizontally [state 0 in the left of Fig. 3(a) and Video S5 [30]] or vertically (state 1 in the right of Fig. 3(a) and Video S6 [30]). We quantify this bistability using the order parameter $\Phi = \langle |\mathbf{s} \cdot \hat{\mathbf{e}}_x| - |\mathbf{s} \cdot \hat{\mathbf{e}}_y| \rangle$, where \mathbf{s} is a sum over the vectors associated to charged vertices and $\langle \dots \rangle$ is an average calculated over all vertices. By definition, Φ acquires a positive (negative) value for defects arranged in the state 0 (state 1) [Fig. 3(b)]. As shown in Fig. 3(c), we observe a bifurcation starting from $B \sim 5.6$ mT. The process of choosing one of these two states develops via a coarsening of small type-III domains and consequent reduction of the highly charged defects until three main domains are formed at $B \sim 9.4$ mT. From here, the rest of the process consists of pulling, through line tension, the defect line toward the edges.

Another type of AFMDW boundary condition can be imposed by introducing only two defects in opposite corners. This constraint creates two equal and incompatible type-III regions that meet along the diagonal and are separated by a string of type-IV vertices. The corresponding evolution from a disordered state is shown in Figs. 4(a) and 4(b) and in

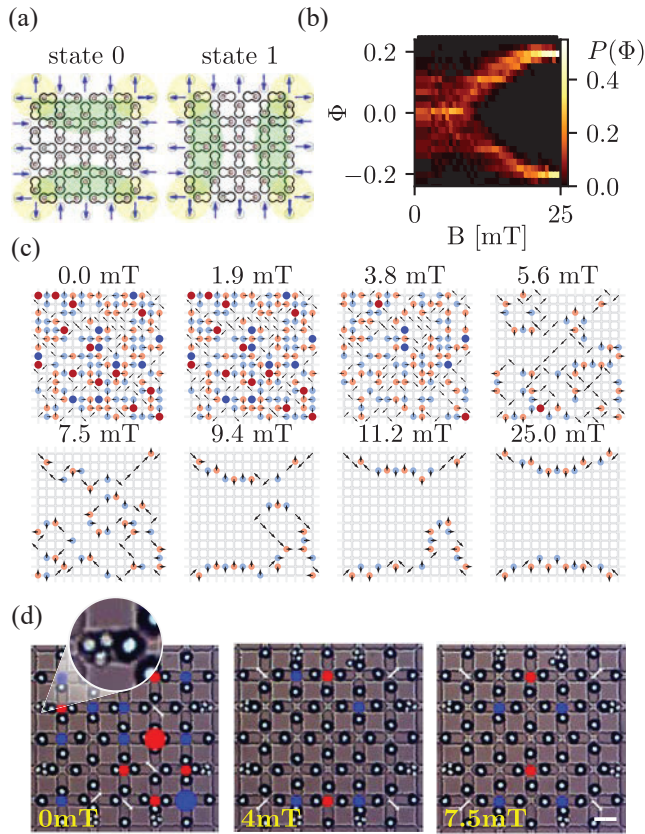


FIG. 3. (a) Schematics showing two states that appear after application of the field when using the AFMDW configuration. Here, topological charges can be connected either horizontally (right) or vertically (left). (b) Bifurcation of the order parameter observed for $N = 100$ simulations. (c) Color map showing the field-induced symmetry breaking where the system chooses the state 0. (d) Experimental observation of the first type of defect pattern; the second one is in Supplemental Material [30]. The enlargement shows the trap jammed by silica particles. The scale bar is $20 \mu\text{m}$, and red (blue) dots indicate positive (negative) Q .

Video S7 [30]. In the simulations, after $B \sim 5$ mT, the system nucleates two type-III regions which coarsen to the two final domains at $B = 25$ mT. The final straightening process of the topological string results from line tension, as also confirmed by experiments [Fig. 4(b)]. However, we find that this defect line is not always completely stretched, and defects might appear in the form of small distortions connected by a string of type-IV vertices, parallel and pointing along the opposite direction from the main defect line (Fig. S1 [30]). We capture this effect by measuring in Fig. 4(c) the distribution of the number of defects. As the field increases, the system gets rid of all non-type-III vertices, until it reaches a steady state close to the topologically protected minimum number of defects, which is equal to L [dotted white line in Fig. 4(c)]. Nevertheless, the inset shows that such a minimum value is not reached by many of the realizations, since many systems fall to a state with a small number of defects distributed along the domain wall and deviating from the diagonal.

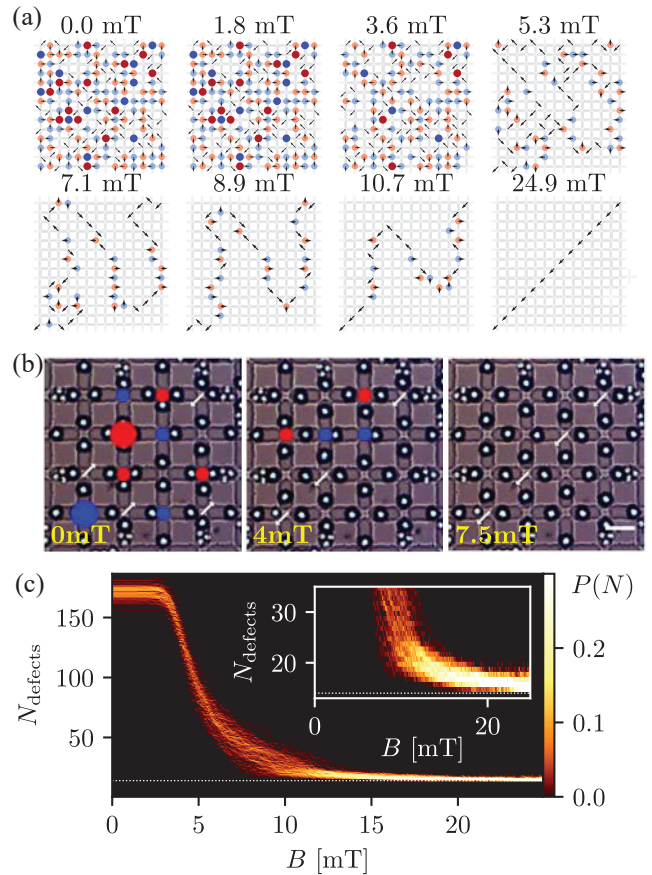


FIG. 4. (a) Color map illustrating the time evolution of the topological line connecting two edge defects in the AFMDW configuration. (b) Experimental realization of the line of defects using the AFMDW configuration. The scale bar is $20 \mu\text{m}$. (c) The probability of finding a specific number of defects in a system, as a function of the field. The dotted line indicates the system's width ($L = 14$). The inset shows an enlargement of the central portion of the curve.

In conclusion, we show how to engineer different boundary conditions to control the bulk behavior in a geometrically frustrated soft-matter system. We demonstrate this concept with an artificial colloidal ice combining numerical simulation and experimental realizations. Topological defects placed at the boundaries propagate inside the bulk, forming bistable states with symmetry breaking or topologically protected strings. The fact that the observed phenomena display a topologically protected nature suggests that they could be observed on other systems such as nanomagnetic artificial ice. This could be tested experimentally, for example, by using lithography to design smaller and compact islands such as ferromagnetic cubes [35], cylinders [36], or disks [37] at the system edges to impose a desired bulk configuration. From the technological perspective, writing or erasing defect lines in the GS region can be used to freeze information into the system by applying a bias during the equilibration process [38].

We thank Demian Levis and Leticia Cugliandolo for pointing us towards their work on Arctic regions in vertex models. Experiments were realised with the help of the MicroFabSpace and Microscopy Characterization Facility at IBEC. This project has received funding from the European Research Council (ERC) under the European Union’s Horizon 2020 research and innovation program (Grant Agreement No. 811234). P.T. acknowledges support the Generalitat de Catalunya under Program “ICREA Acadèmia.”

*aortiza@fmc.ub.edu

- [1] Y. Han, Phase-space networks of geometrically frustrated systems, *Phys. Rev. E* **80**, 051102 (2009).
- [2] Y. Han, Phase-space networks of the six-vertex model under different boundary conditions, *Phys. Rev. E* **81**, 041118 (2010).
- [3] M. J. Harris, S. T. Bramwell, D. F. McMorrow, T. Zeiske, and K. W. Godfrey, Geometrical Frustration in the Ferromagnetic Pyrochlore $\text{Ho}_2\text{Ti}_2\text{O}_7$, *Phys. Rev. Lett.* **79**, 2554 (1997).
- [4] A. P. Ramirez, A. Hayashi, R. J. Cava, R. Siddharthan, and B. S. Shastry, Zero-point entropy in spin ice, *Nature (London)* **399**, 333 (1999).
- [5] S. T. Bramwell and M. J. P. Gingras, Spin ice state in frustrated magnetic pyrochlore materials, *Science* **294**, 1495 (2001).
- [6] W. Giaque and J. Stout, The entropy of water and the third law of thermodynamics. The heat capacity of ice from 15 to 273 k, *J. Am. Chem. Soc.* **58**, 1144 (1936).
- [7] R. F. Wang, C. Nisoli, R. S. Freitas, J. Li, W. McConville, B. J. Cooley, M. S. Lund, N. Samarth, C. Leighton, V. H. Crespi, and P. Schiffer, Artificial ‘spin ice’ in a geometrically frustrated lattice of nanoscale ferromagnetic islands, *Nature (London)* **439**, 303 (2006).
- [8] C. Nisoli, R. Moessner, and P. Schiffer, Colloquium: Artificial spin ice: Designing and imaging magnetic frustration, *Rev. Mod. Phys.* **85**, 1473 (2013).
- [9] L. F. Cugliandolo, Artificial spin ice and vertex models, *J. Stat. Phys.* **167**, 499 (2017).
- [10] S. H. Skjærsvø, C. H. Marrows, R. L. Stamps, and L. J. Heyderman, Advances in artificial spin ice, *Nat. Rev. Phys.* **2**, 13 (2020).
- [11] W. R. Branford, S. Ladak, D. E. Read, K. Zeissler, and L. F. Cohen, Emerging chirality in artificial spin ice, *Science* **335**, 1597 (2012).
- [12] G.-W. Chern, C. Reichhardt, and C. J. O. Reichhardt, Avalanches and disorder-induced criticality in artificial spin ices, *New J. Phys.* **16**, 063051 (2014).
- [13] J. Drisko, T. Marsh, and J. Cumings, Topological frustration of artificial spin ice, *Nat. Commun.* **8**, 14009 (2017).
- [14] J. P. Morgan, A. Stein, S. Langridge, and C. H. Marrows, Thermal ground-state ordering and elementary excitations in artificial magnetic square ice, *Nat. Phys.* **7**, 75 (2011).
- [15] A. Farhan, P. M. Derlet, A. Kleibert, A. Balan, R. V. Chopdekar, M. Wyss, J. Perron, A. Scholl, F. Nolting, and L. J. Heyderman, Direct Observation of Thermal Relaxation in Artificial Spin Ice, *Phys. Rev. Lett.* **111**, 057204 (2013).
- [16] Y.-L. Wang, Z.-L. Xiao, A. Snezhko, J. Xu, L. E. Ocola, R. Divan, J. E. Pearson, G. W. Crabtree, and W.-K. Kwok, Rewritable artificial magnetic charge ice, *Science* **352**, 962 (2016).
- [17] I. Gilbert, Y. Lao, I. Carrasquillo, L. O’Brien, J. D. Watts, M. Manno, C. Leighton, A. Scholl, C. Nisoli, and P. Schiffer, Emergent reduced dimensionality by vertex frustration in artificial spin ice, *Nat. Phys.* **12**, 162 (2016).
- [18] B. Canals, I.-A. Chioar, V.-D. Nguyen, M. Hehn, D. Lacour, F. Montaigne, A. Locatelli, T. O. Mente, B. S. Burgos, and N. Rougemaille, Fragmentation of magnetism in artificial kagome dipolar spin ice, *Nat. Commun.* **7**, 11446 (2016).
- [19] Y. Perrin, B. Canals, and N. Rougemaille, Extensive degeneracy, Coulomb phase and magnetic monopoles in artificial square ice, *Nature (London)* **540**, 410 (2016).
- [20] D. Shi, Z. Budrikis, A. Stein, S. A. Morley, P. D. Olmsted, G. Burnell, and C. H. Marrows, Frustration and thermalization in an artificial magnetic quasicrystal, *Nat. Phys.* **14**, 309 (2016).
- [21] E. Mengotti, L. J. Heyderman, A. F. Rodríguez, F. Nolting, R. V. Hügli, and H.-B. Braun, Real-space observation of emergent magnetic monopoles and associated Dirac strings in artificial kagome spin ice, *Nat. Phys.* **7**, 68 (2011).
- [22] A. Libál, C. J. Olson Reichhardt, and C. Reichhardt, Creating Artificial Ice States Using Vortices in Nanostructured Superconductors, *Phys. Rev. Lett.* **102**, 237004 (2009).
- [23] M. L. Latimer, G. R. Berdiyrov, Z. L. Xiao, F. M. Peeters, and W. K. Kwok, Realization of Artificial Ice Systems for Magnetic Vortices in a Superconducting MoGe Thin Film with Patterned Nanostructures, *Phys. Rev. Lett.* **111**, 067001 (2013).
- [24] P. Mellado, A. Concha, and L. Mahadevan, Macroscopic Magnetic Frustration, *Phys. Rev. Lett.* **109**, 257203 (2012).
- [25] F. Ma, C. Reichhardt, W. Gan, C. J. Olson Reichhardt, and W. S. Lew, Emergent Geometric Frustration of Artificial Magnetic Skyrmion Crystals, *Phys. Rev. B* **94**, 144405 (2016).
- [26] A. Duzgun and C. Nisoli, Skyrmion Spin Ice in Liquid Crystals, *Phys. Rev. Lett.* **126**, 047801 (2021).
- [27] A. D. King, C. Nisoli, E. D. Dahl, G. Poulin-Lamarre, and A. Lopez-Bezanilla, Quantum artificial spin ice, [arXiv: 2007.10555](https://arxiv.org/abs/2007.10555).
- [28] A. Ortiz-Ambriz and P. Tierno, Engineering of frustration in colloidal artificial ices realized on microfeatured grooved lattices, *Nat. Commun.* **7**, 10575 (2016).
- [29] A. Ortiz-Ambriz, C. Nisoli, C. Reichhardt, C. J. O. Reichhardt, and P. Tierno, Colloquium: Ice rule and emergent frustration in particle ice and beyond, *Rev. Mod. Phys.* **91**, 041003 (2019).
- [30] See Supplemental Material at <http://link.aps.org/supplemental/10.1103/PhysRevLett.126.188001> for two supplemental videos and figures to support the main results.
- [31] A. Libál, C. Reichhardt, and C. J. Olson Reichhardt, Realizing Colloidal Artificial Ice on Arrays of Optical Traps, *Phys. Rev. Lett.* **97**, 228302 (2006).
- [32] A. Libál, C. Nisoli, C. J. O. Reichhardt, and C. Reichhardt, Inner Phases of Colloidal Hexagonal Spin Ice, *Phys. Rev. Lett.* **120**, 027204 (2018).

- [33] E. C. Oğuz, A. Ortiz-Ambriz, H. Shem-Tov, E. Babià-Soler, P. Tierno, and Y. Shokef, Topology Restricts Quasidegeneracy in Sheared Square Colloidal Ice, *Phys. Rev. Lett.* **124**, 238003 (2020).
- [34] C. Nisoli, Unexpected Phenomenology in Particle-Based Ice Absent in Magnetic Spin Ice, *Phys. Rev. Lett.* **120**, 167205 (2018).
- [35] D. Louis, D. Lacour, M. Hehn, V. Lomakin, T. Hauet, and F. Montaigne, A tunable magnetic metamaterial based on the dipolar four-state potts model, *Nat. Mater.* **17**, 1076 (2018).
- [36] J. Sklenar, Y. Lao, A. Albrecht, J. D. Watts, C. Nisoli, G.-W. Chern, and P. Schiffer, Field-induced phase coexistence in an artificial spin ice, *Nat. Phys.* **15**, 191 (2019).
- [37] R. Streubel, N. Kent, S. Dhuey, A. Scholl, S. Kevan, and P. Fischer, Spatial and temporal correlations of xy macro spins, *Nano Lett.* **18**, 7428 (2018).
- [38] Y.-L. Wang, X. Ma, J. Xu, Z.-L. Xiao, A. Snezhko, R. Divan, L. E. Ocola, J. E. Pearson, B. Janko, and W.-K. Kwok, Switchable geometric frustration in an artificial-spin-icesuperconductor heterosystem, *Nat. Nanotechnol.* **13**, 560 (2018).

Supplementary Material for: Topological Boundary Constraints in Artificial Colloidal Ice

Carolina Rodríguez-Gallo,^{1,2} Antonio Ortiz-Ambriz,^{1,3,*} and Pietro Tierno^{1,2,3}

¹*Departament de Física de la Matèria Condensada, Universitat de Barcelona, 08028 Spain*

²*Universitat de Barcelona Institute of Complex Systems (UBICS), Universitat de Barcelona, 08028 Spain*

³*Institut de Nanociència i Nanotecnologia, Universitat de Barcelona, 08028 Spain*

(Dated: March 17, 2021)

SIMULATIONS

In our numerical simulations, we consider a double well topographic trap as a piecewise harmonic bistable potential. The force \mathbf{F}_i^T due to this well acting on a colloid i is given by:

$$\mathbf{F}_i = -\hat{\mathbf{e}}_{\perp} k_{\text{trap}} r_{\perp} + \hat{\mathbf{e}}_{\parallel} \begin{cases} k_{\text{hill}} r_{\parallel} & |r_{\parallel}| \leq \frac{d}{2} \\ k_{\text{trap}} \left(\frac{d}{2} - |r_{\parallel}|\right) \text{sign}(r_{\parallel}) & |r_{\parallel}| > \frac{d}{2} \end{cases} \quad (1)$$

where r_{\parallel} and r_{\perp} are components of the vector \mathbf{r} respectively parallel and perpendicular to the vector joining the two stable positions of the trap, which are separated by a distance d . The vector \mathbf{r} goes from the trap to the particle centre. The stiffness $k_{\text{trap}} = 6 \cdot 10^{-4}$ pN/nm keeps the particle confined to the elongated region around the center of the trap, and $k_{\text{hill}} = 5 \cdot 10^{-6}$ pN/nm creates a potential hill that pushes the particles away towards one of the bistable regions. We note that the ratio $k_{\text{hill}}/k_{\text{trap}}$ was chosen to match the experimental system. However, we believe that increasing k_{trap} will not significantly affect our main results.

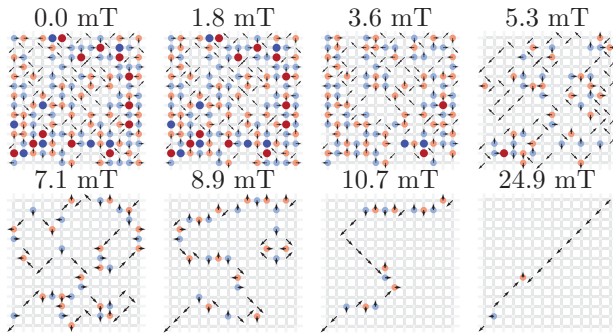


FIG. 1. Evolution of the spatial distribution of defects in a simulation with AFDW boundary conditions, and $Q=0$. In this case, the line separating both domains has a pair of charged defects connected by a parallel line of Type IV vertices.

* aortiza@fmc.ub.edu

To complete the results reported in the main test, we shown in Fig 1 of this Supporting information a system with AFDW boundaries where the line fails to reach the fully stretched configuration.

EXPERIMENTS

We provide further details on the experimental system to realize the square colloidal ice with fixed boundary conditions.

Microstructured lithography

We use a lithographic process to realize the bistable gravitational traps. The structures are built on a coverglass (Menzel-gläser, 24×50 mm size) that is previously cleaned using water, alcohol, acetone and finally isopropanol. After the cleaning process, the cover glasses are blown with N_2 until dry and free of dust. Then, the cover glasses are dehydrated in a hot plate at 120 °C for 10 min and spin coated with an adhesion promoter TI Prime (MicroChem) which is baked for 2min at 120 °C. Subsequently, we spin coat the substrate with a photoresist AZ1512 HS (MicroChem) during 5s at 500rpm and after that, 30s at 1000 rpm. Before exposure to UV light, we perform a soft bake process by placing the resist in a hot plate for 3min at 95 °C to evaporate the solvent and reduce the shear-stress introduced during the spin coat process. The desired structure is transferred from a Cr mask, fabricated by Direct Write Lithography (DWL66, Heidelberg Instruments Mikrotechnik GmbH), with a $\lambda = 405\text{nm}$ diode laser working at a $5.7\text{mm}^2/\text{min}$ writing speed. The Cr mask is aligned with the covered substrate, and then exposed to UV light at $21\text{mW}/\text{cm}^2$ (UV-NIL, SUSS Microtech) for 3.5 seconds. After that, the microfeatures are developed by submerging the sample for 7s in a developer solution (AZ726MIF).

Sample preparation

To avoid sticking between the particles and the substrate we performed the following procedure. First, we prepare a solution of 0.9g of sodium dodecyl sulfate (SDS,

Sigma-Aldrich) in 0.11 ultrapure water (Direct-Q, Merk Millipore). We then add to 1000 μ L of this solution, 10 μ l of 10 μ m paramagnetic polystyrene particles doped with iron oxide (49664 Sigma-Aldrich) and 10 μ l of 6 μ m silica particles (Microparticles GmbH, SiO₂ Research particles). The latter non magnetic particles are used to fix the position of the magnetic particles at the boundaries. Before use, the suspension was kept in a rotor (Mini LabRoller) until the ionic surfactant (SDS) is adsorbed on the particle surface: at least 4h. We also functionalize the surface of the microstructured lithography using layered polyelectrolites, according to the protocol described in the supporting information of Ref. [1]. The protocol consists of a layer-by-layer adsorption technique in order to give a net charge to the substrate. We prepare two stock solutions containing, respectively, 0.375g of polyallilamide hydrochloride (PAH Sigma Aldrich), in 75ml of high deionized water (MilliQ system, Millipore) and the second with 0.375g of polysodium styrene sulfonate (PSS Sigma Aldrich) in 75ml of high deionized water. Then, we add 2.19g of NaCl to both solutions to facilitate the adhesion of the polymer to the photoresist. The structures are submerged in the PAH solution for 30 min, then washed with high deionized water before submerging it in the PSS solution for 30 min. This procedure is repeated three times, so each sample has a layer-by-layer deposition process of 3h. Finally, a drop of the colloidal suspension is sandwiched between the functionalized lithography and another cleaned coverslip and sealed with a silicon paste (Thorlabs) to slow down the drying process, and the absorption of CO₂. A sample built by this method is stable for about a week.

Experimental procedures

The sample is located on an inverted microscope (TiU,Nikon) equipped with an oil immersion 40 \times objective (Numerical aperture 1.4, Nikon). We use a long-pass color filter (FEL0500, Thorlabs) to prevent the sample from exposure to the UV light. Before the experimental realization we wait a few minutes until particles sediment on the microstructured lithography due to density mismatch.

We use optical tweezers to place the colloidal particles (magnetic and non-magnetic) one by one in a bistable gravitational trap. The initial particle configuration within a double well is chosen at random using a random number generator. The optical tweezers are realized by expanding the beam of a butterfly laser diode ($\lambda = 976$ nm, 300mW, operated at 70mW, BL976-SAG300 Thorlabs), introducing it through the epi-illumination module of the microscope, through a dichroic mirror (FF825-SD01-25x36x2.0, Semrock) and into the observation objective. Due to the magnetite doping, the paramagnetic colloidal particles can absorb the focused

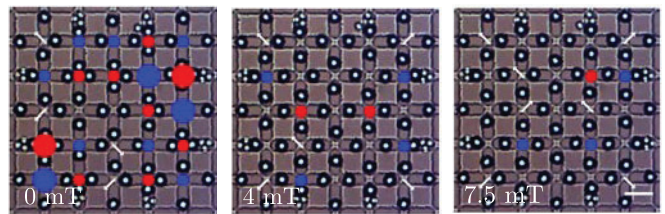


FIG. 2. Experimental observation of the state 1. Scale bar is 20 μ m.

light of the laser, and create convective flows that destabilize the trap. This is normally addressed by keeping the laser power very low, and to a lesser extent by modifying the beam profile using an SLM (Hamamatsu X10468-03). To fix the magnetic particle position at the boundaries we block one bistable position in the gravitational trap by filling one of the gravitational minima with three non magnetic silica particles having 6 μ m diameter.

The magnetic dipolar interactions are induced by an external magnetic field, generated with a single coil located below the sample. The coil is connected to a power amplifier (BOP-20 10M, KEPCO), which is controlled through a digital analogue card (NI 9269) and a custom made LabVIEW program. The sample is located perpendicularly to the coil axis, therefore the field has a component only along this direction (z -axis). We increase the magnetic interaction by raising the field at a slow ramp of 0.03125mT/s and record the particle trajectories using a digital camera (MQ013CG-E2,Ximea) working at 30fps.

In Fig. 2 we show an experimental realization of the bistable state reported in Fig.3 of the main text, but where the system chose the state 1 in the symmetry breaking process.

VIDEOS

- VideoS1:** Simulation of a system with open boundary conditions.
- VideoS2:** Simulation of a system with periodic boundary conditions.
- VideoS3:** Simulation of a system with Domain Wall (DW) boundary conditions.
- VideoS4:** Simulation of a system with Antiferromagnetic (AF) boundary conditions.
- VideoS5:** Experimental system with AFDW boundaries with four defects ($\sum Q = -4$), falling to a state 0.
- VideoS6:** Experimental system with AFDW boundaries with four defects ($\sum Q = -4$), falling to a state 1.

VideoS7: Experimental system with AFDW boundaries
with two defects ($\sum Q = 0$).



- [1] A. Ortiz-Ambriz and P. Tierno, Nat. Commun. **7**, 10575 (2016).

Degeneracy and hysteresis in a bidisperse colloidal ice

Carolina Rodríguez-Gallo^{1,2}, Antonio Ortiz-Ambriz^{1,3} and Pietro Tierno^{1,2,3}

Physical Review Research **3**, (2021) 043023

¹ Departament de Física de la Matèria Condensada, Universitat de Barcelona, 08028, Barcelona, Spain

² Universitat de Barcelona Institute of Complex Systems (UBICS), Universitat de Barcelona, 08028, Barcelona, Spain

³ Institut de Nanociència i Nanotecnologia (IN2UB), Universitat de Barcelona, 08028, Barcelona, Spain



Degeneracy and hysteresis in a bidisperse colloidal ice

Carolina Rodríguez-Gallo ^{1,2} Antonio Ortiz-Ambriz,^{1,2,3,*} and Pietro Tierno ^{1,2,3,†}

¹Departament de Física de la Matèria Condensada, Universitat de Barcelona, 08028, Spain

²Universitat de Barcelona Institute of Complex Systems (UBICS), Universitat de Barcelona, 08028, Spain

³Institut de Nanociència i Nanotecnologia, Universitat de Barcelona, 08028, Spain



(Received 28 July 2021; accepted 10 September 2021; published 8 October 2021)

We use numerical simulations to investigate the low-energy states of a bidisperse colloidal ice, realized by confining two types of magnetic particles into double wells of different lengths. For this system, theoretical calculations predict a highly degenerate ground state where all the vertices with zero topological charge have equal energy. When raising the applied field, we find a re-entrant transition where the system passes from the initial disordered state to a low-energy one and then back to disorder for large interaction strengths. The transition is due to the particle localization on top of the central hill of the double wells, as revealed from the position distributions. When we decrease the applied field, the system displays hysteresis in the fraction of low-energy vertices, and a small return point memory by cycling the applied field.

DOI: [10.1103/PhysRevResearch.3.043023](https://doi.org/10.1103/PhysRevResearch.3.043023)

I. INTRODUCTION

Geometrically frustrated systems, such as water ice I_h [1,2] and magnetic spin ice materials [3–8], feature a degenerate ground state (GS) at low temperature. Such degeneracy produces novel physical phenomena, including a residual entropy and dipolar spin-spin correlations, and has attracted much attention by the scientific community both in natural and artificial systems [9–16].

In spin ice materials, the dipole moments carried out by rare-earth ions sit on a lattice of corner-sharing tetrahedra. At each vertex, these spins have equal distances, and at low temperature they tend to follow the “ice rules” [17], where two spins point towards the center of the tetrahedron and two away from it. The multiple configurations of these low-energy states give rise to the GS degeneracy. However, when the spin lattice is projected onto a two dimensional (2D) plane, as in lithographically designed artificial spin ice systems (ASIs) [18–22], some features may be lost due to the reduced dimensionality [23]. In a square ASI, the distance between the ferromagnetic islands at each vertex is not the same, since opposing spins are separated by greater distances than adjacent ones, and the corresponding interaction energies are not equivalent. As a result, the degeneracy is lost, and the GS becomes an antiferromagnetic order filled only by one type of vertices (type 3, see Fig. 1). A way to recover the GS degeneracy in such systems was suggested by Möller and Moessner

[24], based on the idea of introducing a height displacement between the ferromagnetic islands. Changing the elevation of only two of the four nanoislands at each vertex effectively relieves degeneracy, but it requires a complex nanofabrication procedure, as demonstrated recently [25]. Another possibility relies on the use of bicomponent systems [26,27], characterized by ferromagnetic nanoislands with different size and distances, and thus interaction strengths.

The artificial colloidal ice is an alternative soft matter system to investigate the complex physics emerging from geometric frustration, by using confined colloids as analog of interacting spins [28–36]. For lattices characterized by a single coordination number c_N , it was shown both by theory [37] and experiments [38] that the collective interactions between the particles lead to similar vertex energetics than ASIs. Thus the square colloidal ice, similar to the square ASI, also has its GS degeneracy lifted. However, the flexibility of the colloidal system in changing the structure and tuning the pair interactions enables us to search for alternative solutions to this problem.

Here we use numerical simulations to explore the low-energy states and the degeneracy of a bidisperse colloidal ice, composed of two populations of particles and double wells. We choose to explore this particular geometric arrangement since single vertex calculations of the magnetic interactions between the particles predict a degenerate GS, where all vertices that satisfy the ice rule have equal energy. We find that, by raising the interaction strength, the fraction of GS vertices first increases but later decreases reaching again a disordered state. We thus uncover a novel re-entrant effect which distinguishes the colloidal system with mobile particles from the ASI [39], and where the applied field can be used to disorder the system by raising its amplitude. This effect can be used to induces hysteresis in the fraction of GS vertices. We note that memory effects in colloidal [40] and artificial [41,42] spin ice systems have been reported in a few works,

*antonio.ortiz@fmc.ub.edu

†ptierno@ub.edu

Published by the American Physical Society under the terms of the Creative Commons Attribution 4.0 International license. Further distribution of this work must maintain attribution to the author(s) and the published article's title, journal citation, and DOI.

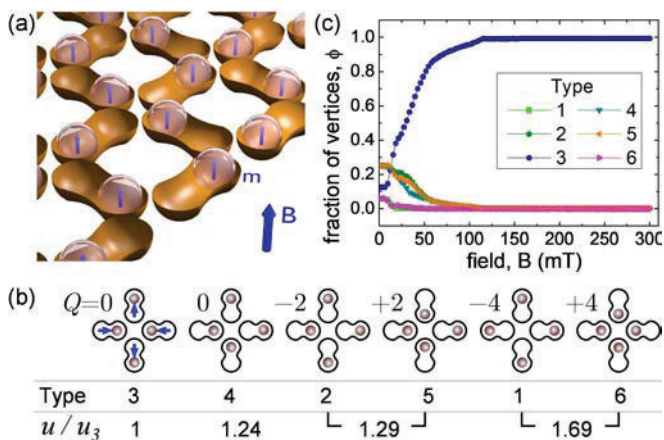


FIG. 1. (a) Schematic (not on a scale) showing a colloidal ice made of a square lattice of double wells, each filled with one paramagnetic colloidal particle. The vectors within the particles denote the magnetic moments \mathbf{m} induced by the external field \mathbf{B} . (b) Different types of vertices in the square colloidal ice with their associated topological charge Q . The ratio between the magnetostatic energy of one vertex u and that of the type 3 (u_3) is illustrated at the bottom. (c) Average fraction of vertices ϕ for the square colloidal ice vs the applied magnetic field B .

however those systems where driven by an in plane field rather than having tunable repulsive interactions induced by a perpendicular field.

II. NUMERICAL SIMULATIONS

We perform Brownian dynamics simulations of a 2D lattice of double wells, with lattice constant $a = 33 \mu\text{m}$ and each well featuring a central hill [43,44]. For the monodisperse case (Fig. 1) the traps have length $l_1 = 23 \mu\text{m}$ and they contain one paramagnetic colloid of diameter $d = 2 \mu\text{m}$ and magnetic volume susceptibility $\chi_1 = 0.5$. On the other hand, for the binary mixture we keep the values χ_1 and l_1 for half of the particles and traps while, for the rest we use $\chi_2 = 0.0675$ and $l_2 = 30.356 \mu\text{m}$ and keep constant the particle diameter d . In both cases, for each particle i at position \mathbf{r}_i we integrate the overdamped equation of motion:

$$\gamma \frac{d\mathbf{r}_i}{dt} = \mathbf{F}_i^{\text{dd}} + \mathbf{F}_i^{\text{T}} + \boldsymbol{\eta}, \quad (1)$$

where $\gamma = 0.032 \text{ pN s } \mu\text{m}^{-1}$ is the viscous drag. The first term on the right-hand side of Eq. (1) is given by, $\mathbf{F}_i^{\text{dd}} = \frac{3\mu_0}{4\pi} \sum_{j \neq i} \frac{\mathbf{m}_i \cdot \mathbf{m}_j}{|\mathbf{r}_{ij}|^4} \hat{\mathbf{r}}_{ij}$, where $\mathbf{m}_i = \chi_1 V \mathbf{B} / \mu_0$ is the induced moment from the applied field \mathbf{B} , $V = \pi d^3 / 6$ the particle volume, $\mu_0 = 4\pi \times 10^{-7} \text{ H/m}$ the magnetic permeability of the medium and $\hat{\mathbf{r}}_{ij} = (\mathbf{r}_i - \mathbf{r}_j) / |\mathbf{r}_i - \mathbf{r}_j|$ is the relative position unit vector between two particles (i, j). The second term in Eq. (1) is the force \mathbf{F}_i^{T} that acts on a colloid i due to the potential well, and it is given by

$$\mathbf{F}_i = -\hat{\mathbf{e}}_{\perp} k_{\text{trap}} r_{\perp} + \hat{\mathbf{e}}_{\parallel} \begin{cases} k_{\text{hill}} r_{\parallel} & |r_{\parallel}| \leq \frac{d}{2} \\ k_{\text{trap}} (\frac{\lambda}{2} - |r_{\parallel}|) \text{sign}(r_{\parallel}) & |r_{\parallel}| > \frac{d}{2} \end{cases}, \quad (2)$$

where r_{\parallel} and r_{\perp} are components of a vector \mathbf{r} parallel and perpendicular resp. to the line of length λ that joins the two minima in the double well. The stiffness $k_{\text{trap}} = 6 \times 10^{-4} \text{ pN/nm}$ keeps the particle confined to the elongated region around the center of the trap, and $k_{\text{hill}} = 5 \times 10^{-6} \text{ pN/nm}$ creates a potential hill that pushes the particles away towards one of the two potential wells. Finally, $\boldsymbol{\eta}$ represents a random force due to thermal fluctuation, with zero mean, $\langle \boldsymbol{\eta} \rangle = 0$ and delta correlated, $\langle \boldsymbol{\eta}(t) \boldsymbol{\eta}(t') \rangle = 2k_{\text{B}} T \gamma \delta(t - t')$. Here, $T = 300 \text{ K}$ is the ambient temperature.

The simulations are performed using a constant time step of 10 ms. We use always a square sample with a number of vertices on each side equal to $N = 20$, except for the calculations in Fig. 2(b) where we vary $N \in [1, 40]$. We increase B linearly up to $B = 300 \text{ mT}$, at a rate of $\alpha_B = 0.035 \text{ mT/s}$ for the initial simulations, and later change the rate when investigating hysteresis effects. Finally, we neglect hydrodynamic and electrostatic interactions between the particles since in the experiments such interactions are screened by the topographic double wells.

III. THE MONODISPERSE COLLOIDAL ICE

The essential features of the colloidal ice are shown in the schematic in Fig. 1(a). It is composed of a square lattice of double wells, each filled by one paramagnetic colloidal particle that is confined due to gravity. An external magnetic field \mathbf{B} perpendicular to the particle plane induces in each particle a dipole moment $\mathbf{m}_i \sim \chi_i \mathbf{B}$, and pair of particles (i, j) located at a distance $r = |\mathbf{r}_i - \mathbf{r}_j|$ experience a repulsive dipolar interaction:

$$u = \frac{\mu_0}{4\pi} \frac{\mathbf{m}_i \cdot \mathbf{m}_j}{r^3}, \quad (3)$$

which depends on both, the field amplitude and particle susceptibility. Thus particles located in close traps on the same vertex will repel each other, but the interaction strength is such that while they can cross the central hill, they cannot leave the double well. Geometric frustration in the system arises from the arrangement of the double wells, that do not allow the simultaneous minimization of all pairwise interactions.

The mapping between the colloidal and spin ice systems can be done by assigning a pseudospin to each double well, such that it points where the particle is located [28]. As shown in Fig. 1(b), this mapping allows to construct a set of vertex rules, and for the square lattice, six energetic configuration of the particles are possible. Also, to each vertex one can assign a topological charge $Q = 2n - c_N$ [45], where n is the number of pseudo spins that point toward the vertex center, and c_N the coordination number of the lattice, which for the square is $c_N = 4$. In this formalism, the vertices that satisfy the ice rules are those which cancel the topological charge, $Q = 0$, i.e., the type 3 and type 4, while low (type 1 with $Q = -4$, type 2 with $Q = -2$) and high (type 6 with $Q = +4$, type 5 with $Q = +2$) energetic vertices break the ice rule and represent topological defects. The topological nature of such defects arises from the fact that they can disappear only when annihilating with other defects of opposite charge, for example type 2 with -2 and so on.

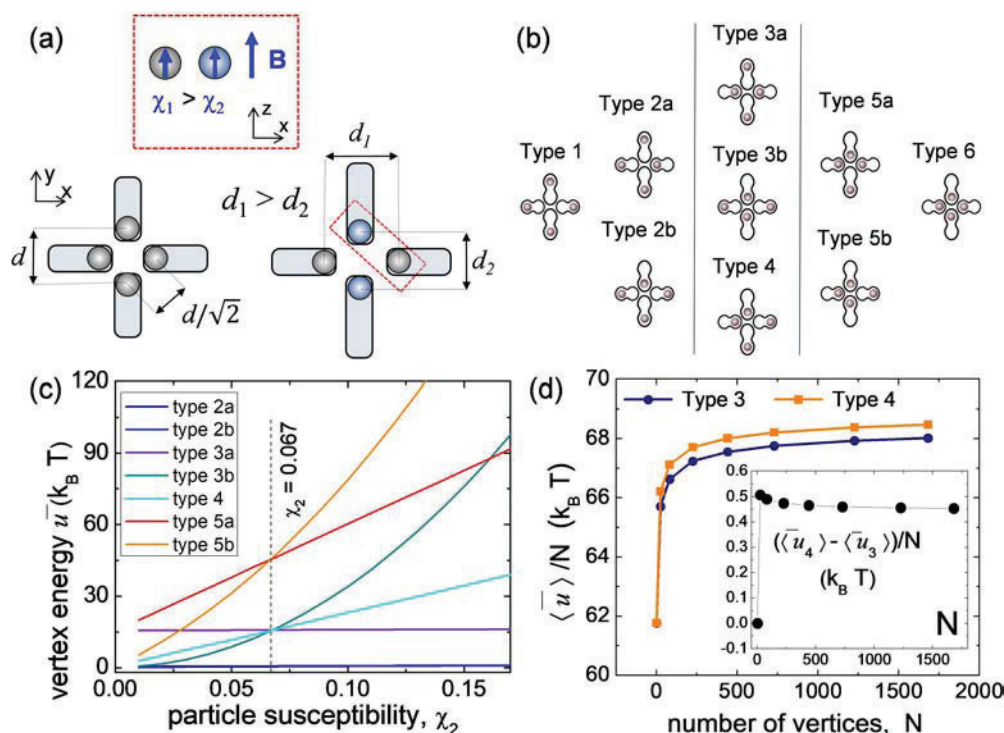


FIG. 2. (a) Comparison between one vertex in the monodisperse (left) and in the bidisperse (right) colloidal ice. In the latter case, the particles have different magnetic susceptibilities ($\chi_1 > \chi_2$) and distances ($d_1 > d_2$) at the vertex. (b) Energetic splitting of different types of vertices in the bidisperse ice. (c) Vertex energy \bar{u} vs magnetic susceptibility χ_2 for the bidisperse system with particles subjected to an applied field of amplitude $B = 13$ mT. For $\chi_2 = 0.067$, the energies $\bar{u}_{5a} \approx \bar{u}_{5b}$, $u_{5a}/u_{5b} = 0.99$ and $\bar{u}_{3a} = \bar{u}_{3b} = \bar{u}_4$. (d) Mean vertex energy $\langle \bar{u} \rangle / N$ vs total number of vertices N for a system composed of type 3 (squares) and type 4 (circles). Inset shows the energy difference $(\langle \bar{u}_4 \rangle - \langle \bar{u}_3 \rangle) / N$ vs N .

In Fig. 1(c), we show the simulation results for a square lattice composed of $N = 20$ vertices per side, and plot the fraction ϕ of different vertex types versus the amplitude of the applied field. We find that for the monodisperse ice, the system displays a clear tendency to follow the ice rules ($Q = 0$) at high interaction strength, and it reaches a GS filled only by type 3 vertices for $B > 115$ mT. This is also in agreement with the energy hierarchy showed in Fig. 1(b), and a similar situation is observed for artificial spin ice systems, where the GS is characterized by type 3 vertices that form local loop configurations with alternating chirality [46–49]. As a result, the degeneracy is lost, and the GS has a twofold antiferromagnetic order.

IV. THE BIDISPERSE COLLOIDAL ICE

To recover degeneracy, we designed a colloidal ice characterized by two types of traps and double wells such that the energetic weight of vertices of type 3 and 4 are the same. The idea is illustrated in Fig. 2(a), where we use two types of particles characterised by two different magnetic susceptibilities (χ_1, χ_2) and, thus, two different induced moments ($\mathbf{m}_1, \mathbf{m}_2$) under the same applied field. On each vertex, the particles with lower magnetic susceptibility (χ_2) are placed inside longer double wells (length l_2) that are located closer, i.e., at a distance $d_2 < d_1$. Instead the double wells occupied by the particles with larger magnetic susceptibility

($\chi_1 > \chi_2$) are located far away when pointing toward the vertex (distance d_1).

For arbitrary values of susceptibilities and trap lengths, this conformation breaks the symmetry, and splits the vertex energy as shown in Fig. 2(b): type 2 gives rise to 2a and 2b, type 3 to 3a and 3b, and type 5 to 5a and 5b. To engineer a degenerate vertex hierarchy, we fix the values (l_1, χ_1) and a , and we solve the system of equations,

$$\bar{u}_4(\chi_2, l_2) = \bar{u}_{3a}(\chi_2, l_2) = \bar{u}_{3b}(\chi_2, l_2), \quad (4)$$

being $\bar{u} = \sum u$ the sum of the dipolar interactions between the vertex elements [Eq. (3)], where (l_2, χ_2) are used as free parameters. The solution ensures that the pair interactions between opposing and adjacent particles at a vertex are the same and thus also the energetic weight of the type 3a, 3b and type 4, Fig. 2(c).

The previous calculations are performed on individual vertices, but do not reflect the collective nature of the colloidal ice and the fact that the paramagnetic colloids interact beyond the nearest neighbor level. To take into account these effects, we consider a lattice made of N vertices with fixed particles arranged to create a state with only type 3 or type 4. In these two configurations, we calculate the mean energy per vertex, $\langle \bar{u} \rangle / N$, to distinguish whether these two configurations are energetically equivalent. As shown in Fig. 2(d), the vertex energy grows with system size reaching a constant value of $\sim 69k_B T$ for $N > 1500$ vertices. However, the energetic difference between the types 4 and 3 is non zero, but it raises to

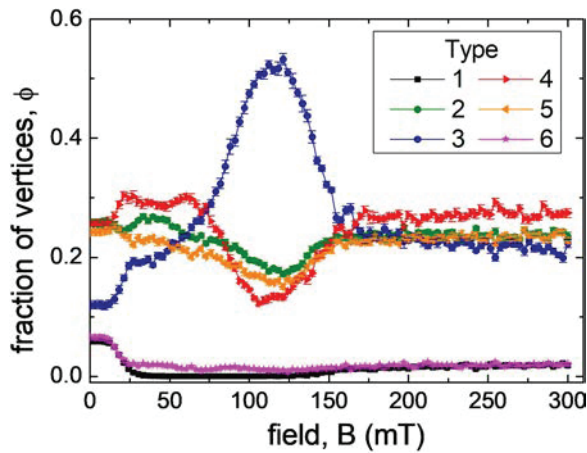


FIG. 3. Average fraction of vertices for different field values for the bidisperse square ice. The results from the simulations are averaged over 10 realizations.

$\sim 0.4k_B T$, as seen in the Fig. 2(d). This effect results from the collective interactions between the particles, that lower the energy of the type 3 vertices with respect to the type 4. Thus, at high interaction strength, the bidisperse colloidal ice is expected to reach a GS filled only by type 3.

To confirm this hypothesis, we run numerical simulations of the bidisperse system, see Fig. 3. Instead, we find that even though the fraction of type 3 vertices first raises rapidly from $\phi = 0.1$ to $\phi = 0.5$ at $B \sim 100$ mT, above $B \sim 110$ mT, it starts decreasing until it reaches a relative low value of $\phi = 0.2$ even for the highest applied field of $B \sim 300$ mT. Further, also the type 4 vertices first decrease from $\phi = 0.25$ to $\phi = 0.13$, but later increase again to recover almost their

initial disordered value of $\phi \sim 0.25$. Interestingly, intermediate energy vertices with charge $Q = \pm 2$, which are topologically bound, appear with nearly the same probability as the ice rule vertices. This is in contrast with high and low charge ($Q = \pm 4$) vertices, which completely disappear already above $B = 30$ mT, as in previous observations with the monodisperse systems (Fig. 1 and Ref [43]). In addition, this transition occurs at a similar magnetic field value when the monodisperse system reaches the GS, Fig. 1(c).

To understand this re-entrant behavior, we have analysed the distribution of particles positions within the double wells, shown in Fig. 4(b), where representative snapshots of the simulation system are shown for different values of B in Fig. 4(a). For low field, both types of particles remain confined within one of the two wells, and this behavior lasts until $B \sim 80$ mT. However, above this value we observe that the particles with high magnetic susceptibility and located in the short traps tend to localize close to the central hill rather than away from it, Fig. 4(b) second column. This effect is remarkable, and it raises much more the energy of the type 4, decreasing their statistical fraction within the ensemble. Above $B > 110$ mT the induced dipolar interactions are so strong that they force also the localization of the particles with smaller magnetic susceptibility close to the central hill, Fig. 4(b) third column. This localization becomes more pronounced at higher field strength as shown by the narrow particle distribution around the central hill for $B = 200$ mT. The system thus tends to disorder back to its initial configuration, with the only difference being the absence of type 1 and 6 vertices that causes an increase in the final fraction of type 3, while type 2 and 5 reaches practically the same initial value of ϕ .

The discovered re-entrant behavior is rather robust, as it was observed for a wide range of field rate α_B . By lowering

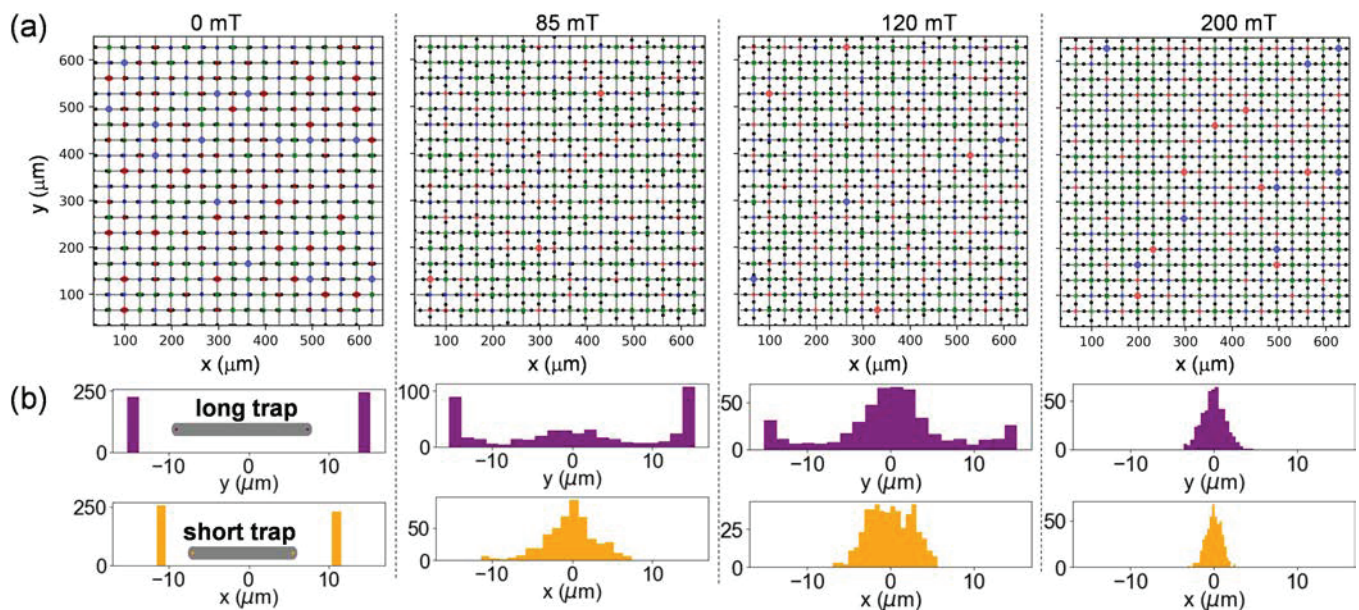


FIG. 4. (a) Snapshots of the numerical simulations of the bidisperse ice taken at $B = 0$ (first image), 85 (second) 120 (third), and 200 mT (fourth). The particles are indicated by the black disks on the square lattice, while the vertex defects are large blue (type 1, $Q = -4$), small blue (type 2, $Q = -2$), small red (type 5, $Q = +2$), and large red (type 6, $Q = +4$) disks. The green disks denote vertices which fulfill the GS ($Q = 0$). (b) Corresponding histograms of the particle positions in long horizontal traps (first row) and short vertical traps (second row) for the three field values.

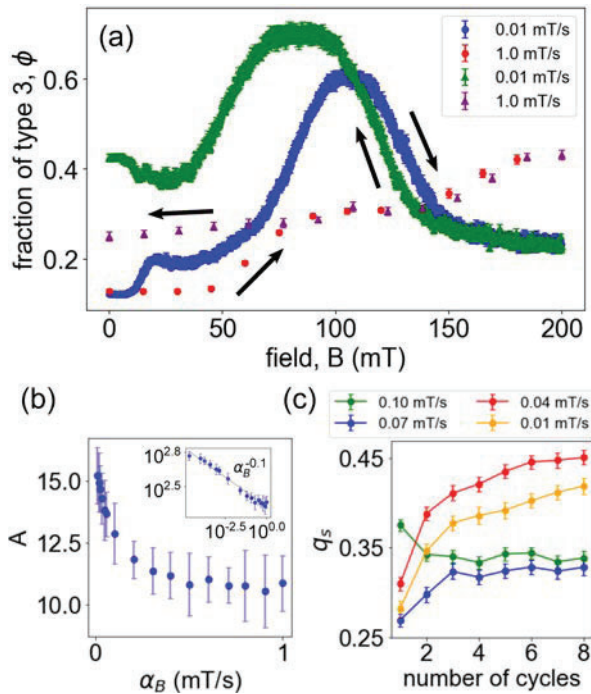


FIG. 5. (a) Average fraction ϕ of type 3 vertices vs applied field B obtained up to $B = 200$ mT (red and blue circles), and lowering back to $B = 0$ mT (green and purple triangles) at two different rates. (b) Hysteresis area A vs rate α_B of the applied field. Inset shows the same plot in the log-log scale. (c) Spin overlap order parameter q_s vs number of cycles calculated from a minor loop centered at the peak of the type 3 vertex fraction.

α_B , the fraction of type 3 vertices display a maximum at lower field amplitude and later reaches higher fraction ϕ , whereas increasing the rate causes this re-entrant phenomenon to occur later in time. In the latter case, the system does not have time to reorganize into low-energy state, and the fraction of type 3 vertices decreases rapidly. However, the final vertex count remains the same regardless of the field change rate. Thus this phenomenon represents an alternative way to disorder the system by raising now the applied field, rather than resetting the colloidal ice by repeating the experiment and relocalizing the particles randomly within the double wells.

We now explore the presence of hysteresis and memory in our system when cycling B . We measure this effect by considering the fraction GS vertices (type 3) and how it changes by first increasing and then decreasing the applied field. Some representative results are shown in Fig. 5(a) for different rates α_B . In general, we find that when the field is cycled sufficiently fast ($\alpha_B > 0.5$ mTs $^{-1}$) the fraction ϕ tends to retrace itself and there is a small detectable hysteresis. In contrast, for smaller rates ($\alpha_B < 0.1$ mTs $^{-1}$), the difference between both curves is significant as shown in Fig. 5(a). To better understand the rate dependent behavior, we plot in Fig. 5(b), such difference A between the area of the two curves versus the magnetic field rate α_B . Effectively, we find that the behavior is power law with an exponent ~ -0.1 [inset Fig. 5(b)], while $A \rightarrow 0$ starting from $\alpha_B \sim 0.25$ mTs $^{-1}$. This rate dependent behavior is the opposite than the one observed for other bistable systems, like

ferromagnets, where the area of the hysteresis loop increases with the rate of the field switching [50–52].

Another phenomenon that could arise in our system is the presence of return point memory, namely the possibility that our bidisperse colloidal ice could reproduce a microstate, i.e., a given particle configuration, when the field is cycled after the first minor loop. To quantify this effect, we follow previous works on colloidal [40] and artificial spin ice [42], and calculate the spin overlap order parameter defined as [53] $q_s = \frac{1}{N} \sum_i s_i^{(n)} s_i^{(n-1)}$. From the colloidal position, we associate an effective spin s to each of the bistable traps composing the lattice. Thus $s_i^{(n)}$ represents the magnetic moment associated to a bistable trap after a minor loop (n), while $s_i^{(n-1)}$ is calculated one minor loop earlier. This order parameter quantifies the presence of reproducible particle microstates ($q_s = 1$) after a certain number of minor loops starting from a virgin curve. In contrast, $q_s = 0$ indicates the total absence of correlation between the configuration of two subsequent loops n and $n - 1$. As shown in Fig. 5(c), the spin overlap parameter has two dramatically different behaviours as the magnetic ramp rate α_B is changed. For $\alpha_B < 0.7$ mTs $^{-1}$ the overlap increases, without reaching the fully reversible state ($q_s = 1$) after 7 minor loops. As the field rate increases, the overlap becomes smaller, which is expected since the system lives in more excited states, and has access to a larger phase space. However, surprisingly for $\alpha_B = 0.1$ mTs $^{-1}$, we find that the overlap suddenly increases in the first cycle, but then decreases until it almost reaches the same steady value as the case of $\alpha_B = 0.069$ mTs $^{-1}$. These results indicate that our colloidal ice does not present a strong memory of its previous state, and such effect could be attributed to the presence of noise as thermal fluctuations of the particles within the double well or disorder resulting from the different magnetic couplings between the two types of particles.

V. CONCLUSIONS

In this paper, we have investigated the low-energy states of an artificial colloidal ice composed of a binary mixture of particles and traps. Before this work, the colloidal ice had mainly been explored with monodisperse particles, and the emerging physics had been studied extensively for different types of lattices and interactions strength. However, novel effects may arise when changing the types of particles or double well traps. In particular, we uncover a re-entrant behavior which is induced at high interaction strength, and that can be used as an effective way to disorder the system. Such effect is absent in the monodisperse system, where the particles localize in one of the two double wells at all interaction strengths. Furthermore, it produces hysteresis and small memory effects when changing the magnetic field rate.

This work opens different future directions. For example, the idea of using a binary mixture of magnetic colloids to fill bistable traps suggests the exciting possibility of employing a polydisperse suspension which will modify the magnetic coupling between the particles at parity of the applied magnetic field. This is equivalent to varying the amount of disorder in the system, without altering its geometrical arrangement and thus, it could be used to uncover the emergence of glassiness on a periodic lattice [54–56].

ACKNOWLEDGMENTS

This project has received funding from the European Research Council (ERC) under the European Union's Horizon 2020 research and innovation programme (grant agree-

ment No. 811234). P.T. acknowledges support from the Ministerio de Ciencia, Innovación y Universidades (PID2019-108842GB-C21), AGAUR (2017-SGR-1061), and from Generalitat de Catalunya under Program "ICREA Acadèmia."

- [1] L. Pauling, The structure and entropy of ice and of other crystals with some randomness of atomic arrangement, *J. Chem. Phys.* **57**, 2680 (1935).
- [2] W. Giauque and J. Stout, The entropy of water and the third law of thermodynamics. the heat capacity of ice from 15 to 273, *J. Am. Chem. Soc.* **58**, 1144 (1936).
- [3] M. J. Harris, S. T. Bramwell, D. F. McMorrow, T. Zeiske, and K. W. Godfrey, Geometrical Frustration in the Ferromagnetic Pyrochlore $\text{Ho}_2\text{Ti}_2\text{O}_7$, *Phys. Rev. Lett.* **79**, 2554 (1997).
- [4] A. P. Ramirez, A. Hayashi, R. J. R. J. Cava, R. B. Siddharthan, and S. Shastry, Zero-point entropy in "spin ice", *Nature (London)* **399**, 333 (1999).
- [5] S. T. Bramwell and M. J. P. Gingras, Spin ice state in frustrated magnetic pyrochlore materials, *Science* **294**, 1495 (2001).
- [6] S. T. Bramwell, S. R. Giblin, S. Calder, R. Aldus, D. Prabhakaran, and T. Fennell, Measurement of the charge and current of magnetic monopoles in spin ice, *Nature (London)* **461**, 956 (2009).
- [7] S. J. Blundell, Monopoles, Magnetricity, and the Stray Field from Spin Ice, *Phys. Rev. Lett.* **108**, 147601 (2012).
- [8] Y.-L. Wang, Z.-L. Xiao, A. Snezhko, J. Xu, L. E. Ocola, R. Divan, J. E. Pearson, G. W. Crabtree, and W.-K. Kwok, Rewritable artificial magnetic charge ice, *Science* **352**, 962 (2016).
- [9] J.-F. Sadoc and R. Mosseri, *Geometrical Frustration*, Collection Alea-Saclay: Monographs and Texts in Statistical Physics (Cambridge University Press, Cambridge, 1999).
- [10] B. C. den Hertog and M. J. P. Gingras, Dipolar Interactions and Origin of Spin Ice in Ising Pyrochlore Magnets, *Phys. Rev. Lett.* **84**, 3430 (2000).
- [11] R. Moessner and A. P. Ramirez, Geometrical frustration, *Phys. Today* **59**(2), 24 (2006).
- [12] C. Castelnovo, R. Moessner, and S. L. Sondhi, Magnetic monopoles in spin ice., *Nature (London)* **451**, 42 (2008).
- [13] T. Fennell, P. P. Deen, A. R. Wildes, K. Schmalzl, D. Prabhakaran, A. T. Boothroyd, R. J. Aldus, D. F. McMorrow, and S. T. Bramwell, Magnetic coulomb phase in the spin ice $\text{HO}_2\text{Ti}_2\text{O}_7$, *Science* **326**, 415 (2009).
- [14] C. L. Henley, The coulomb phase in frustrated systems, *Annu. Rev. Condens. Matter. Phys.* **1**, 179 (2010).
- [15] L. J. Heyderman and R. L. Stamps, Artificial ferroic systems: novel functionality from structure, interactions and dynamics., *J. Phys.: Condens. Matter* **25**, 363201 (2013).
- [16] S. Petit, E. Lhotel, B. Canals, M. C. Hatnean, J. Ollivier, H. Mutka, E. Ressouche, A. R. Wildes, M. R. Lees, and G. Balakrishnan, Observation of magnetic fragmentation in spin ice, *Nat. Phys.* **12**, 746 (2016).
- [17] J. D. Bernal and R. H. Fowler, A theory of water and ionic solution, with particular reference to hydrogen and hydroxyl ions., *J. Chem. Phys.* **1**, 515 (1933).
- [18] R. F. Wang, C. Nisoli, R. S. Freitas, J. Li, W. McConville, B. J. Cooley, M. S. Lund, N. Samarth, C. Leighton, V. H. Crespi, and P. Schiffer, Artificial 'spin ice' in a geometrically frustrated lattice of nanoscale ferromagnetic islands, *Nature (London)* **439**, 303 (2006).
- [19] E. Mengotti, L. J. Heyderman, A. F. Rodríguez, F. Nolting, R. V. Hügli, and H.-B. Braun, Real-space observation of emergent magnetic monopoles and associated dirac strings in artificial kagome spin ice, *Nat. Phys.* **7**, 68 (2011).
- [20] Z. Budrikis, J. P. Morgan, J. Akerman, A. Stein, P. Politi, S. Langridge, C. H. Marrows, and R. L. Stamps, Disorder Strength and Field-Driven Ground State Domain Formation in Artificial Spin Ice: Experiment, Simulation, and Theory, *Phys. Rev. Lett.* **109**, 037203 (2012).
- [21] C. Nisoli, R. Moessner, and P. Schiffer, *Colloquium: Artificial spin ice: Designing and imaging magnetic frustration*, *Rev. Mod. Phys.* **85**, 1473 (2013).
- [22] S. H. Skjaervo, C. H. Marrows, R. L. Stamps, and L. J. Heyderman, Advances in artificial spin ice, *Nat. Rev. Phys.* **2**, 13 (2020).
- [23] G.-W. Chern, C. Reichhardt, and C. Nisoli, Realizing three-dimensional artificial spin ice by stacking planar nano-arrays, *Appl. Phys. Lett.* **104**, 013101 (2014).
- [24] G. Möller and R. Moessner, Artificial Square Ice and Related Dipolar Nanoarrays, *Phys. Rev. Lett.* **96**, 237202 (2006).
- [25] Y. Perrin, B. Canals, and N. Rougemaille, Extensive degeneracy, coulomb phase and magnetic monopoles in artificial square ice, *Nature (London)* **540**, 410 (2016).
- [26] F. S. Nascimento, L. A. S. Mól, W. A. Moura-Melo, and A. R. Pereira, From confinement to deconfinement of magnetic monopoles in artificial rectangular spin ices, *New J. Phys.* **14**, 115019 (2012).
- [27] S. Lendinez, M. T. Kaffash, and M. B. Jungfleisch, Emergent spin dynamics enabled by lattice interactions in a bicomponent artificial spin ice, *Nano Lett.* **21**, 1921 (2021).
- [28] A. Libál, C. Reichhardt, and C. J. O. Reichhardt, Realizing Colloidal Artificial Ice on Arrays of Optical Traps, *Phys. Rev. Lett.* **97**, 228302 (2006).
- [29] C. J. O. Reichhardt, A. Libál, and C. Reichhardt, Multi-step ordering in kagome and square artificial spin ice, *New J. Phys.* **14**, 025006 (2012).
- [30] A. Libál, C. J. O. Reichhardt, and C. Reichhardt, Doped colloidal artificial spin ice, *New J. Phys.* **17**, 103010 (2015).
- [31] A. Libál, C. Nisoli, C. Reichhardt, and C. J. O. Reichhardt, Dynamic control of topological defects in artificial colloidal ice, *Sci. Rep.* **7**, 651 (2017).
- [32] D. Y. Lee and P. Tierno, Energetics and the ground state quest in an artificial triangular colloidal ice, *Phys. Rev. Mater.* **2**, 112601(R) (2018).
- [33] A. Ortiz-Ambriz, C. Nisoli, C. Reichhardt, C. J. O. Reichhardt, and P. Tierno, Colloquium: Ice rule and emergent frustration in particle ice and beyond, *Rev. Mod. Phys.* **91**, 041003 (2019).
- [34] A. Libál, A. del Campo, C. Nisoli, C. Reichhardt, and C. J. O. Reichhardt, Quenched dynamics of artificial colloidal spin ice, *Phys. Rev. Research* **2**, 033433 (2020).

- [35] E. C. Oğuz, A. Ortiz-Ambriz, H. Shem-Tov, E. Babià-Soler, P. Tierno, and Y. Shokef, Topology Restricts Quasidegeneracy in Sheared Square Colloidal Ice, *Phys. Rev. Lett.* **124**, 238003 (2020).
- [36] C. Rodríguez-Gallo, A. Ortiz-Ambriz, and P. Tierno, Topological Boundary Constraints in Artificial Colloidal Ice, *Phys. Rev. Lett.* **126**, 188001 (2021).
- [37] C. Nisoli, Dumping topological charges on neighbors: Ice manifolds for colloids and vortices, *New J. Phys.* **16**, 113049 (2014).
- [38] A. Libál, D. Y. Lee, A. Ortiz-Ambriz, C. Reichhardt, C. J. O. Reichhardt, P. Tierno, and C. Nisoli, Ice rule fragility via topological charge transfer in artificial colloidal ice, *Nat. Commun.* **9**, 4146 (2018).
- [39] A. Le Cunuder, I. Frérot, A. Ortiz-Ambriz, and P. Tierno, Competing orders in colloidal kagome ice: Importance of the in-trap motion of the particles, *Phys. Rev. B* **99**, 140405(R) (2019).
- [40] A. Libál, C. Reichhardt, and C. J. Olson Reichhardt, Hysteresis and return-point memory in colloidal artificial spin ice systems, *Phys. Rev. E* **86**, 021406 (2012).
- [41] G. M. Wysin, W. A. Moura-Melo, L. A. S. Mól, and A. R. Pereira, Dynamics and hysteresis in square lattice artificial spin ice, *New J. Phys.* **15**, 045029 (2013).
- [42] I. Gilbert, G.-W. Chern, B. Fore, Y. Lao, S. Zhang, C. Nisoli, and P. Schiffer, Direct visualization of memory effects in artificial spin ice, *Phys. Rev. B* **92**, 104417 (2015).
- [43] A. Ortiz-Ambriz and P. Tierno, Engineering of frustration in colloidal artificial ices realized on microfeatured grooved lattices, *Nat. Commun.* **7**, 021406 (2016).
- [44] J. Loehr, A. Ortiz-Ambriz, and P. Tierno, Defect Dynamics in Artificial Colloidal Ice: Real-Time Observation, Manipulation, and Logic Gate, *Phys. Rev. Lett.* **117**, 168001 (2016).
- [45] A. Libál, C. Nisoli, C. J. O. Reichhardt, and C. Reichhardt, Inner Phases of Colloidal Hexagonal Spin Ice, *Phys. Rev. Lett.* **120**, 027204 (2018).
- [46] J. P. Morgan, A. Stein, S. Langridge, and C. H. Marrows, Thermal ground-state ordering and elementary excitations in artificial magnetic square ice., *Nat. Phys.* **7**, 75 (2011).
- [47] R. C. Silva, F. S. Nascimento, L. A. Mól, W. A. Moura-Melo, and A. R. Pereira, Thermodynamics of elementary excitations in artificial magnetic square ice, *New J. Phys.* **14**, 015008 (2012).
- [48] S. Zhang, I. Gilbert, C. Nisoli, G.-W. Chern, M. J. Erickson, L. O. Brien, C. Leighton, P. E. Lammert, V. H. Crespi, and P. Schiffer, Crystallites of magnetic charges in artificial spin ice, *Nature (London)* **500**, 553 (2013).
- [49] V. Kapaklis, U. B. Arnalds, A. Farhan, R. V. Chopdekar, A. Balan, A. Scholl, L. J. Heyderman, and B. Hjörvarsson, Thermal fluctuations in artificial spin ice., *Nat. Nano* **9**, 514 (2014).
- [50] P. Jung, G. Gray, R. Roy, and P. Mandel, Scaling Law for Dynamical Hysteresis, *Phys. Rev. Lett.* **65**, 1873 (1990).
- [51] S. Sengupta, Y. Marathe, and S. Puri, Cell-dynamical simulation of magnetic hysteresis in the two-dimensional ising system, *Phys. Rev. B* **45**, 7828 (1992).
- [52] N. E. Fettuouhi, J. Zemmouri, B. Segard, and B. Macke, Dynamical hysteresis of bistable systems: from the deterministic to the fluctuation-dominated case., *Phys. Lett. A* **204**, 251 (1995).
- [53] M. S. Pierce, C. R. Buechler, L. B. Sorensen, S. D. Kevan, E. A. Jagla, J. M. Deutsch, T. Mai, O. Narayan, J. E. Davies, K. Liu, G. T. Zimanyi, H. G. Katzgraber, O. Hellwig, E. E. Fullerton, P. Fischer, and J. B. Kortright, Disorder-induced magnetic memory: Experiments and theories, *Phys. Rev. B* **75**, 144406 (2007).
- [54] A. Sen and R. Moessner, Topological Spin Glass in Diluted Spin Ice, *Phys. Rev. Lett.* **114**, 247207 (2015).
- [55] D. Zhou, F. Wang, B. Li, X. Lou, and Y. Han, Glassy Spin Dynamics in Geometrically Frustrated Buckled Colloidal Crystals, *Phys. Rev. X* **7**, 021030 (2017).
- [56] Y. Shi, C. Nisoli, and G.-W. Chern, Ice, glass, and solid phases in artificial spin systems with quenched disorder, *Appl. Phys. Lett.* **118**, 122407 (2021).

Geometric control of topological charge transfer in Shakti-Cairo colloidal ice

Carolina Rodríguez-Gallo^{1,2}, Antonio Ortiz-Ambriz^{1,3,4},
Cristiano Nisoli⁵ and Pietro Tierno^{1,2,3}

Communications physics **6**, (2023) 113

¹ Departament de Física de la Matèria Condensada, Universitat de Barcelona,
08028, Barcelona, Spain

² Universitat de Barcelona Institute of Complex Systems (UBICS),
Universitat de Barcelona, 08028, Barcelona, Spain




³ Institut de Nanociència i Nanotecnologia (IN2UB), Universitat de
Barcelona, 08028, Barcelona, Spain

⁴ Tecnológico de Monterrey, Escuela de Ingeniería y Ciencias, Campus
Monterrey, 64849 Monterrey, Mexico

⁵ Theoretical Division and Center for Nonlinear Studies, Los Alamos
National Laboratory, Los Alamos, NM 87545, USA.



Geometrical control of topological charge transfer in Shakti-Cairo colloidal ice

Carolina Rodríguez-Gallo ^{1,2}, Antonio Ortiz-Ambríz ^{1,3,4}, Cristiano Nisoli⁵ & Pietro Tierno ^{1,2,3}✉

Lattice transformations that preserve the system topology, but not its geometry, are common in condensed matter systems. However, how geometric constraints influence the topological properties of the lattices is still unclear. Here we show that a geometric transformation between two mixed coordination lattices, from Shakti to Cairo in an artificial colloidal ice, leads to a breakdown of the ice rule in all but one specific geometry. We observe a transfer of topological charge among sublattices which can be controlled in sign and intensity, vanishing at the ice-rule point. These unusual topological effects are absent in magnetic spin ices and they are due to collective, non-local geometric frustration in the particle ice. By merging numerical simulations, theory and experiments, we demonstrate how the charge transfer occurs in the Cairo geometry. The broader implication of our results is that we demonstrate how geometric constraints can control the topological properties of a mesoscopic colloidal system.

¹Departament de Física de la Matèria Condensada, Universitat de Barcelona, 08028 Barcelona, Spain. ²Universitat de Barcelona Institute of Complex Systems (UBICS), Universitat de Barcelona, 08028 Barcelona, Spain. ³Institut de Nanociència i Nanotecnologia, Universitat de Barcelona, 08028 Barcelona, Spain. ⁴Tecnologico de Monterrey, Escuela de Ingeniería y Ciencias, Campus Monterrey, 64849 Monterrey, Mexico. ⁵Theoretical Division and Center for Nonlinear Studies, Los Alamos National Laboratory, Los Alamos, NM 87545, USA. ✉email: ptierno@ub.edu

In frustrated spin systems¹, geometric constraints impede the possibility of minimizing all interaction energies at a vertex, which leads to intriguing effects such as residual entropy², ground state degeneracy³, charge fractionalization⁴ and the emergence of magnetic monopoles^{5–7}. Modern advances in nanofabrication processes have allowed the realization of artificial spin ice (ASI), namely lithographically designed lattices of nanoscale islands^{8–10}. In ASI geometric frustration can be deliberately designed, and the spin orientation controlled by external fields¹¹. These capabilities allow to realize exotic phases of matter^{12–15}, to engineer topological states¹⁶ with direct connections to idealized statistical mechanics models^{17–20} but also have potential applications as artificial pinning^{21,22} or dissipation-free nanoscale logic systems^{23–25}.

Particle-based ices recently emerged as an alternative model for geometric frustration, where repulsive colloids are confined within a lattice of double wells²⁶. The mesoscopic length scale of colloidal particles simplifies their visualization and low intense external fields can be used to manipulate the particles or tune their interactions. Thus, strongly confined colloidal particles have been used as suitable model systems to investigate geometric frustration phenomena^{27–32}. In a particle ice, each double well is filled by one colloid, and an external field is used to induce tunable repulsive interactions³³ or to bias the particles along a crystallographic axis^{34–36}. For an unconstrained system, the particles will form a triangular lattice, the ground state for colloids that repel isotropically in two dimensions. However, arranging the double wells in a lattice with an incompatible symmetry, generates competing interactions and geometric frustration sets in. Thus, the colloidal ice features a similar frustration-by-design as ASI. Such analogy can be extended further. If we associate an Ising-like spin to each double well, with the arrow pointing toward the well filled by the particle, it is possible to construct a set of vertex rules similar to the frustrated spin ice and the pyrochlore system, Fig. 1a.

Spin ice is now a general concept for different systems spanning various geometries. Perhaps its best definition is in terms of

the topological charge q associated to a vertex^{37, 38}, which depends on the connectivity, and it is invariant upon continuous deformations of the lattice. A vertex of coordination number z with n spins pointing towards it (*in*), has charge $q = 2n - z$ corresponding to the number of spins pointing *in* minus those pointing *out*. Equivalently for a particle ice, it corresponds to the number of particles inside the vertex, minus the empty slots of the vertex. Thus, when $z = 4$ (square lattice), there are five possibilities ($q = 0; \pm 2; \pm 4$), and vertices that cancel the topological charge $q = 0$ obeying the ice rule. In contrast, when $z = 3$ as for the honeycomb lattice, there are no $q = 0$ vertices, but only positive or negative ones with $q = \pm 1; \pm 3$.

In general, the topological charge is a good quantifier of the ice rule because an ice rule manifold is a collection of spin configurations such that the absolute value of the topological charge is minimal: zero on even-coordinated vertices, or ± 1 on odd-coordinated ones. It has been noticed in previous works^{39–41} that the topological charge controls whether a colloidal ice behaves like a magnetic spin ice. It is not obvious that it should, because while an isolated vertex of a magnetic spin ice will always have an ice rule state of minimal absolute charge as its ground state, the ground state of a vertex made of traps and colloids corresponds to all colloids away from the vertex, and therefore to the maximum negative charge. It is only because of the collective integration of vertices that the ice rule can be regained, and not in all cases.

While the analogy between a magnetic spin ice and a colloidal ice was proved to be formally valid for a single coordinate lattice²⁶, it breaks down for a mixed coordination system^{39–41}. For example, in a decimated square lattice the ice-rule is spontaneously violated at the sublattice level, as negative topological charges $q = -2$ accumulate on the $z = 4$ vertices. Such topological charge transfer leads to the spontaneous screening of the $q = -2$ monopoles appearing on the $z = 4$ vertices, and was a clear manifestation of the fragile nature of the ice manifold of the particle ice system, in contrast to ASI, which were proven to be robust^{14,42–45}. Here fragile and robust refer to the possibility to destabilize this manifold by decimation. Thus, the ice-nature of a

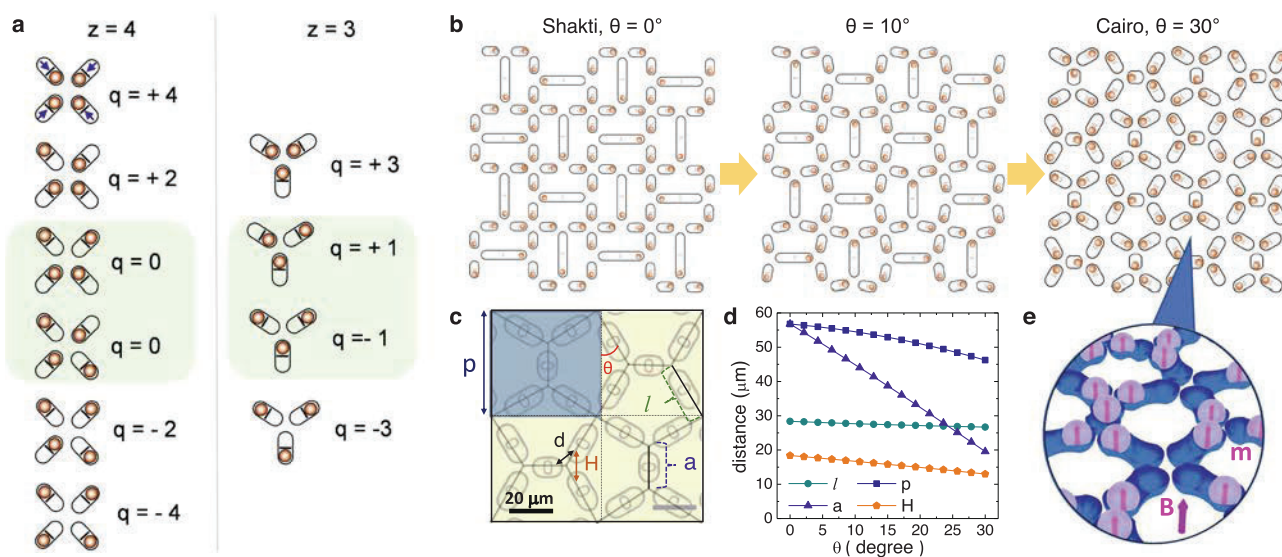


Fig. 1 Lattice transformation from Shakti to Cairo. **a** Configurations of colloidal particles within $z = 4, 3$ vertices and associated topological charges q . In the first $z = 4$ vertex are shown the Ising-like spins corresponding to each double well. The ice-rule obeying vertices are highlighted in a green box with $q = 0$ ($q = \pm 1$) for the $z = 4$ ($z = 3$ resp.) vertices. **b** Geometric transformation from Shakti to Cairo by increasing the bond angle θ . **c** Definition of the parameters used in the transformation overlaid on a lithographic structure of double wells, scale bar is $20 \mu\text{m}$. One plaquette of side p is highlighted in blue. **d** Variation of the parameters l (green disks), p (navy squares), a (blue triangles) and H (orange pentagons) used in the simulation versus bond angle θ . **e** Topographic double-wells in a Cairo lattice filled with paramagnetic colloids. An external field \mathbf{B} induces in the particles equal magnetic moments \mathbf{m} and tunable repulsive interactions.

colloidal system can be generally described in terms of topological charge and its transfer among sublattices.

Here we show that in an artificial colloidal ice, topologically invariant deformations of the geometry can control the transfer of topological charges between different sublattices, because geometrical changes affect the relative energy of the vertices. This result highlights the general phenomenon of the topological charge transfer and, more importantly, demonstrates that geometric transformations can be used to control topological effects in the lattice.

Results and discussion

Geometric transformation. Figure 1b shows the transformation used, where we start from a Shakti lattice^{44,46,47}, which can be considered as a decimated version of the square ice having a longer double well between two $z = 3$ vertices. We convert this lattice in a Cairo using a continuous deformation which shortens the longer double wells and induces an alternating buckling of the two islands in each $z = 3$ vertex. In particular, we vary the distance a among the $z = 3$ vertices, the distance l between the $z = 3$ and $z = 4$ vertices, the plaquette side p and the coupling distance H between two potential minima in $z = 3$ and $z = 4$ vertices, Fig. 1c. These quantities are related to the bond angle θ via the transformation:

$$a = 2\sqrt{2}l \sin\left(\frac{\pi}{4} - \theta\right). \quad (1)$$

In this way we tessellate the 2D space by alternating horizontal and vertical plaquettes. In order to reduce as much as possible the number of coupling among vertices, we fix all the distances d in the $z = 4$ vertices and $z = 3$ vertices, Fig. 1b. In the $z = 3$ vertices, d is kept constant due to the changes in the length of the trap in a and the only coupling that we vary is $H = 2d \cos(\theta/2 + \pi/4)$, as shown in Fig. 1d. Note that such transformation induces a change in distance between the double wells and thus a variation of the energy associated to each vertex. However, the transformation does not change the way topological charges are defined and identified in both the Shakti and the Cairo geometries.

Numerical simulations. The low energy states of the different lattices are investigated first by performing Brownian dynamics simulation, carefully parametrized to match the experimental system. We start from the simulation in order to span a wide range of geometries by varying θ without having to fabricate the structures each time. As shown in Fig. 1e, we consider a two-dimensional system of paramagnetic colloidal particles with diameter δ and effective magnetic volume susceptibility κ , placed in a lattice of topographic double wells at a one to one filling. Under an external field \mathbf{B} perpendicular to the plane of the particles, the colloids acquire a dipole moment $\mathbf{m} = \pi\delta^3\kappa\mathbf{B}/(6\mu_0)$, being μ_0 the permeability of the medium. Repulsive dipolar interactions between pair of particles (i, j) placed at distance $r = |\mathbf{r}_i - \mathbf{r}_j|$ arise in form of an isotropic potential, $U_m = \mu_0 m^2 / (4\pi r^3)$. For each colloidal particle i at position \mathbf{r}_i we integrate the overdamped equation of motion:

$$\gamma \frac{d\mathbf{r}_i}{dt} = \mathbf{F}_i^T + \mathbf{F}_i^{\text{dd}} + \boldsymbol{\eta}, \quad (2)$$

where γ is the friction coefficient, \mathbf{F}_i^T is the force from the topographic double well which is considered as a bistable harmonic potential, \mathbf{F}_i^{dd} the magnetic dipolar interaction that acts on the particle i due to its neighbors and $\boldsymbol{\eta}$ the random force due to thermal fluctuation, see Method section for more details. To take into account the effect of long-range dipolar interactions between the particles, we have applied a large cut-off of 200 μm . The external magnetic field \mathbf{B} is used to raise the repulsive forces and

it is applied via a ramp of 0.0125 mT s⁻¹ until a maximum value of $B = 25$ mT.

The geometric transformation is obtained by using Eq. (1). Following this prescription, we vary $\theta \in [0, 30]^\circ$ and determine for each bond angle the charge population q for all type of vertices by raising the field amplitude. Further, we extract the average topological charge per vertex type defined as $\bar{q} = \sum q_{z_i} / N_z$ for a number of vertices N_z .

Topological charge transfer. In Fig. 2 we show our main findings in terms of \bar{q} as a function of the applied field, for the three cases of the Shakti ($\theta = 0^\circ$, Fig. 2a), the angle $\theta = 27.3^\circ$ (Fig. 2b) and the Cairo ($\theta = 30^\circ$). Further, Fig. 2d, illustrates how \bar{q} varies as a function of θ for the maximum field value. The first thing to notice is that at all angles but with the exception of one point, $\theta = 27.3^\circ$, the system is not in a spin ice manifold. Indeed, charges are present, and they are partitioned by coordination, so that we can talk about a net charge transfer among vertices of different coordination. The Shakti ($\theta = 0^\circ$) shows an accumulation of negative monopoles $q = -2$ in the $z = 4$ vertices and their screening due to the positive monopoles $q = +1$ in the close $z = 3$ vertices, which induce a total charge difference of $\Delta\bar{q} = |\bar{q}_{z=3} - \bar{q}_{z=4}| = 3.56$ at $B = 25$ mT. This situation is similar to the behavior of a decimated square system⁴¹, and confirms the “fragile” nature of the colloidal ice manifold: the breakdown of the ice rule is observed for both cases.

Note that the colloidal manifold is “fragile” since it can be easily destabilized by topology when the system is decimated. Indeed, for a colloidal ice in a single coordination lattice the geometric frustration has a collective nature, and it obeys the ice rule as in ASIs. However, in a mixed coordination system the local energetics resulting from repulsive colloids at a vertex oppose the ice rule-breaking them locally. This contrasts with ASIs which are structurally “robust” ice, as local vertex energetics resulting from the in plane permanent moments enforce the ice rule, making them stable against decimation.

For the angle $\theta = 27.3^\circ$ we observe a re-entrant behavior: first the charge transfer starts similar to the Shakti lattice, where positive (negative) monopoles starts accumulating the $z = 3$ ($z = 4$) vertices. However, above $B \sim 15$ mT the trends invert and these defects redistribute in such a way that the charge transfer becomes zero at $B \sim 25$ mT. A closed inspection at the defect location in Fig. 2e shows that effectively most of the $z = 4$ vertices have no net charge while the $z = 3$ are filled by alternating dumbbells of $q = \pm 1$. Moreover, we find that in the Cairo lattice ($\theta = 30^\circ$) the charge transfer inverts, and a fraction of positive monopoles now accumulate in the $z = 4$ vertices being screened by negative ones in the $z = 3$, with a smaller charge difference than the Shakti, $\Delta\bar{q} = 0.26$. Such relatively small difference and the fluctuations in the determination of \bar{q} raise with the bond angle as shown in Fig. 2b, c. This increase results from the shortening of the central traps between the two $z = 3$ vertices, which further constrain the particle motion close to the central hill. In this situation, thermal fluctuations may help switching the particle position inducing a larger mobility of the charges in the Cairo system as also shown in the Supplementary Video 1. In contrast, in the Shakti system once the charge appear, they become pinned at a lattice location (Supplementary Video 2). The transition is continuous with the deformation, and it crosses the point at $\theta = 27.3^\circ$ where all charges are equally balanced and the decimated system recover a spin ice behavior, with no charge transfer, Fig. 2d.

Charge transfer can be understood in terms of the fundamental differences between particle ice and spin ice⁴⁸. By virtue of the dipole interaction, spin ice vertices are frustrated and thus their

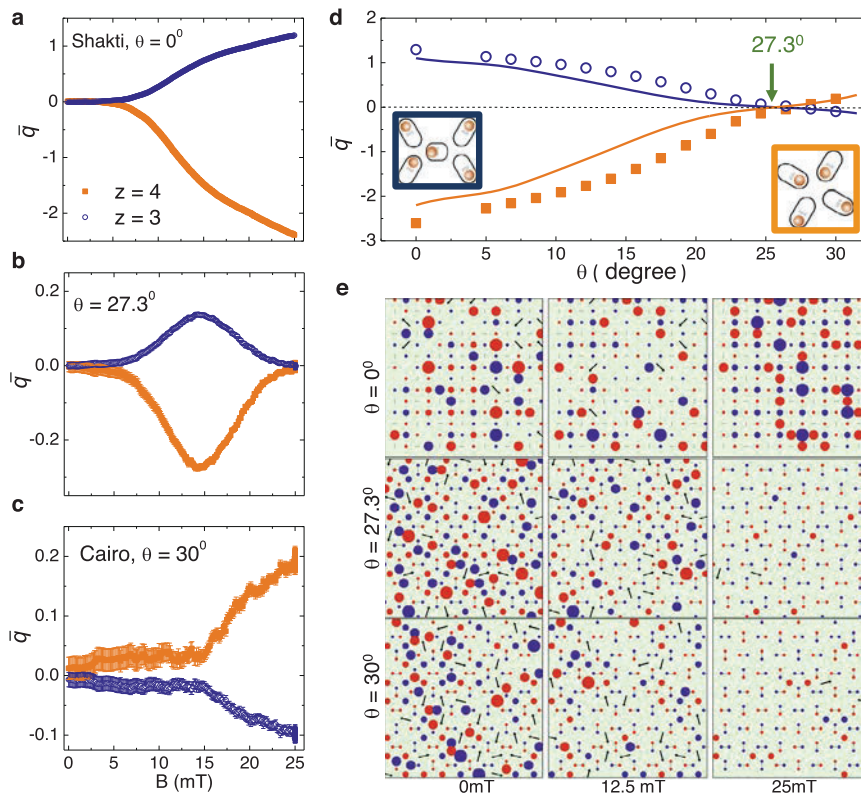


Fig. 2 Inverse topological charge transfer. **a–c** Mean fraction of topological charges \bar{q} versus applied field B in the $z = 3$ (navy circles) and $z = 4$ (orange squares) vertices for the Shakti (**a**), for $\theta = 27.3^\circ$ (**b**) and for the Cairo (**c**) lattices. The charge transfer in the Shakti ($\bar{q} > 0$ in z_3 , $\bar{q} < 0$ in z_4) inverts in the Cairo ($\bar{q} < 0$ in z_3 , $\bar{q} > 0$ in z_4) lattice. In all images error bars are obtained from the standard error. **d** Inversion of topological charge transfer by raising bond angle θ . Scattered data are simulation results at the maximum field $B = 25$ mT while continuous lines are non-linear regression from the theoretical predictions (Method section). Green arrow in the plot denotes the “spin ice” cross-over at $\theta = 27.3^\circ$ with no charge transfer between $z = 3, 4$ sublattices. **e** Evolution of the vertex charge q in the Shakti (top row), for $\theta = 27.3^\circ$ (middle row) and for the Cairo (bottom row) ice for three field amplitudes. Red (blue) disks denote vertices with $q > 0$ ($q < 0$), while the radius of the disks increase with the charge. Vertices with $q = 0$ are either green or have a small arrow if they are in a bias configuration. The panels show a central region with $N = 270$ particles (total region has $N = 2000$ particles).

lowest energy configurations naturally obey the ice rule. Indeed, unlike the present system, magnetic spin ices in the Shakti^{44, 46, 47} and Cairo⁴⁹ geometries both show no charges at low energy. Instead, colloids in particle ices repel each other, and the lowest energy configuration in each vertex corresponds to particles away from it, that give rise to a negative charge, as in Fig. 1a, while ice rule vertices have higher energy. Particle-based ice is also frustrated, but its frustration is collective: clearly it is not possible to set all vertices in the lowest energy state, of negative topological charge. Therefore, in a geometry of single coordination, all the vertices are equivalent, and thus must be equally charge-balanced in terms of charges. There, the ice rule emerges as a collective compromise among vertices. But when there are multiple coordinations, it has been proposed³⁹ and then shown experimentally⁴¹, that higher coordination vertices break the ice rule, becoming negatively charged and transferring positive charge to lower coordination ones. This we also see in Fig. 2e, for most angles, but, interestingly, not all. The same figure also shows that charge transfer can be inverted. This inversion is important, as it allows for a point of no-charge-transfer, $\theta = 27.3^\circ$, i.e. a spin ice point that corresponds to the intriguing topologically protected⁴⁷ Shakti ice.

Theory. The charge inversion is due to the change in the coupling of the vertices of coordination $z = 3$ due to the deformation. In general, they would receive a positive charge, but as the deformation increases, the energy cost of transferring the charge raises.

Thus, we describe this phenomenon by considering the energy of a given vertex of coordination z with n colloids as, $E = J_z n(n - 1)/2$, being J_z an effective coupling constant for a vertex. Using this framework, one can arrive at the total charge as:

$$q_{\text{tot}} = \frac{1}{Z_4} \sum_{n=0}^4 (2n - 4) \rho_{4,n} + \frac{2}{Z_3} \sum_{n=0}^3 (2n - 3) \rho_{3,n}, \quad (3)$$

Here $\rho(q, n)$ is the probability that a vertex of coordination z has a charge q , Z_z the partition function and the factor 2 before the second term is due to twice the abundance of $z = 3$ with respect of $z = 4$ vertices, see Method for more details. By minimizing Eq. (3), we determine the statistical frequencies for charges, and use it to compute the partial charges of the two set of vertices $z = 3, 4$. We find a good agreement with the data, as shown by the solid lines in Fig. 2e, by choosing $T = J_4/7$ and a linear dependence of $x = J_3/J_4$ in the angle θ such that $x = 0$ when $\theta = 0$ and $x = 1.75$ when $\theta = \pi/6$.

Experimental realization. We further strengthen our results by providing in Fig. 3 an experimental realization of the inverse charge transfer effect in the Cairo geometry, see also Supplementary Video 3. Note that the realization in the Shakti geometry was previously reported⁴¹. In contrast to previous works on different types of lattices³³, we use an alternative lithographic protocol to produce a chemically stable, biocompatible and reusable micropatterned substrate, see Method section for more details. This structure, shown in Fig. 3a is composed of elliptical wells

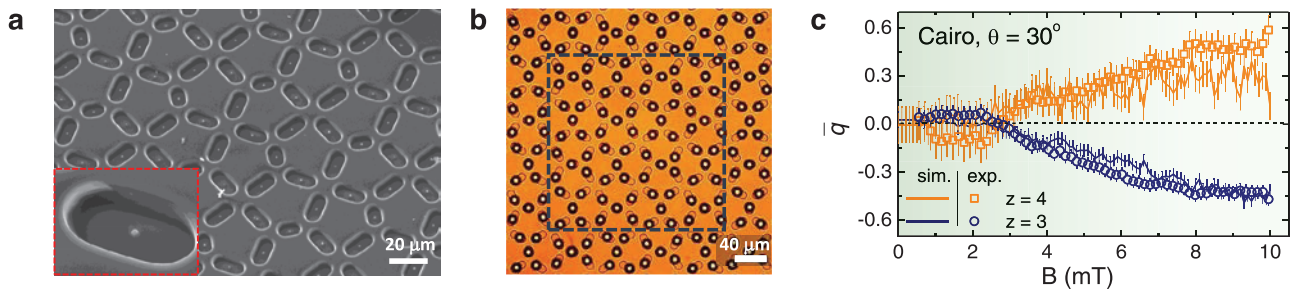


Fig. 3 Experimental realization of the Cairo colloidal ice. **a** Scanning electron microscope image of the topographic double in the Cairo lattice, scale bar is 20 μm . Inset shows enlargement of one double well. **b** A Cairo lattice of topographic double wells filled with paramagnetic colloids (black disks). Lattice parameters are $a = 19.54 \mu\text{m}$, $l = 26.7 \mu\text{m}$ and $p = 46.24 \mu\text{m}$ (Supplementary Video 3). The region outside the dashed square contains vertices excluded to avoid boundary effects. **c** Mean topological charge \bar{q} for $z = 3$ (navy circles) and $z = 4$ (orange squares) vertices versus applied field B . Symbols are experimental data, lines numerical simulations with adjusted parameters ($\kappa = 0.025$, $k_{\text{hill}} = 3 \text{ pN} \cdot \text{nm}$). All data are averaged over different independent measurements, and the error bars are obtained from the standard error.

with a central, cylindrical post that give rises to an effective double-well confinement. These wells are filled with paramagnetic colloids of size $\delta = 10 \mu\text{m}$ and effective magnetic volume susceptibility $\kappa = 0.0025$ using optical tweezers. The tweezers are used to place the particles within the double wells at a one-to-one filling, eliminating the excess of particle from the observation area. Once the particles are randomly located within the topographic traps, we induce repulsive interactions by applying a magnetic field ramp from $B = 0$ to $B = 10 \text{ mT}$ at a rate 0.05 mT s^{-1} . At the highest field the particles experience the strongest repulsion, so that for a distance $r = 13 \mu\text{m}$ (two particles in $z = 3$ vertex) the potential is $U_m = 524 k_B T$. Using digital video microscopy, we extract the position of $N = 180$ particles, performing an ensemble average over 30 separate experiments. A typical field of view is shown in Fig. 3b where, in order to avoid boundary effects and loss of topological charges, we excluded in the statistics the outer region of vertices.

The experimental results confirms the topological charge inversion for the Cairo ice, which starts already at $B \sim 3 \text{ mT}$, Fig. 3c. The difference with the previous simulation results arises from the finite size of the system limited by the optical field of view (Fig. 3b), and dispersion in the elevation of the central hill. Moreover, we find that for $B > 10 \text{ mT}$ the particles within the shorter double wells did not remain confined, but tend to pile up with their neighbors due to the strong dipolar forces. Such effect is difficult to prevent, as the particles are not strongly held by gravity within the double well, but float there due to electrostatic repulsion with the underlying lithographic structure. To adjust the simulation results to the experimental ones, we run further simulations with similar finite sizes and varying only two main parameters, particle susceptibility κ and the spring constant of the hill k_{hill} . By adjusting both values, we obtain a good match with the experiments observing the same charge separation of $\Delta\bar{q} = 0.88$, as testified from the continuous lines in Fig. 3c. Deviations between the experiments and simulation in the $z = 4$ vertices for high field strength could be due to presence of disorder in the experimental system, as unequal hills in the double wells or trap sizes.

Conclusions

In this article, we have explored numerically the effect of topologically equivalent geometrical deformations on the spin ice nature of our system, quantitatively described in terms of transfer of topological charge. We have then chosen one configuration, the Cairo lattice, and probed it experimentally. We have probed also that the inversion of topological charge occurs by changing the way the geometric transformation is performed, for example, by keeping the double well length constant. In the latter case we

observe again a spin ice crossover point but at a slightly large angular value. From the application side, we have designed a strategy to control and localize the topological charges in a two-dimensional lithographic network. These ideas could be implemented in other artificially engineered nanoscale systems to trap, control and direct the motion of magnetic charges or other entities, such as pinned vortices developed in superconducting systems⁵⁰. The main technological drive of such research points toward the design of magnetic device such as memory or ports where logic information can be transported by dipolar switching, and thus being effectively dissipation free. Indeed one further avenue of this work could be to design a composite lattice made of different patches from the Shakti and the Cairo, where topological charges may sequentially be stored or released upon a simple external field command.

Methods

Details of numerical simulations. We perform Brownian dynamics simulations to explore the transition from Shakti to Cairo colloidal ice by varying the bond angle θ and to obtain a large statistical data set. The numerical scheme consists of solving the overdamped Langevin equations given in the main text (Eqs. (1)) by Euler's method, where as friction coefficient we use the value of $\gamma = 0.033 \text{ pN s m}^{-1}$ equal to previous work performed on similar colloidal particles. The latter was estimated by measuring experimentally the diffusion coefficient of the paramagnetic colloids in water⁵¹. We model the force from the double well on a particle i , F_i^T , as a piecewise harmonic bistable potential given by:

$$F_i^T = -\hat{e}_\perp k_{\text{trap}} r_\perp + \hat{e}_\parallel \begin{cases} k_{\text{hill}} r_\parallel & |r_\parallel| \leq \frac{\delta}{2} \\ k_{\text{trap}} (\frac{\delta}{2} - |r_\parallel|) \text{sign}(r_\parallel) & |r_\parallel| > \frac{\delta}{2} \end{cases} \quad (4)$$

where r_\parallel and r_\perp are components of the vector r parallel and perpendicular to the line which join the two stable positions of the trap. These positions are separated by a distance δ . As stiffness we use $k_{\text{trap}} = 1 \cdot 10^{-4} \text{ pN/nm}$ which keeps the particle confined to the elongated region around the centre of the trap, and $k_{\text{hill}} = 2 \cdot 10^{-6} \text{ pN/nm}$ that creates a potential hill able to pushes the particles away towards one of the bistable regions. The ratio $k_{\text{hill}}/k_{\text{trap}}$ was chosen to match the experimental data.

The dipolar force on a particle i is given by,

$$F_i^{\text{dd}} = \frac{3\mu_0}{4\pi} \sum_{j \neq i} \frac{m^2 \hat{r}_{ij}}{|r_{ij}|^4}, \quad (5)$$

being m the magnetic moment induced by the external field B , and $\hat{r}_{ij} = (r_i - r_j)/|r_i - r_j|$. Dipolar interactions are calculate in an iterative form such that the global field H includes that generated by all other dipoles, and we apply a large cut-off of $200 \mu\text{m}$ to consider the effect of long range dipolar interactions.

The last term in Eq. (1) of the main text is a random force due to thermal fluctuation, which is given by η and characterized by a zero mean, $\langle \eta \rangle = 0$ and delta correlated, $\langle \eta(t) \eta(t') \rangle = 2k_B T \gamma \delta(t - t')$, being k_B the Boltzmann constant and $T = 300 \text{ K}$ the ambient temperature.

Our main simulations involve $N = 2000$ particles, namely 800 arranged along $z = 3$ vertices and 400 in $z = 4$ which is equivalent to a colloidal ice of 10×10 unit cells and open boundary conditions in order to mimic the experimental system. The statistics were taken neglecting the first shell of vertices, in order to minimize the effect of boundaries that may adsorb topological charges. To confirm that, for

our system size the effect of boundaries did not influence the bulk behaviour, we have run simulations also with periodic boundary conditions and observe no significant differences in the measured parameters. Here we use as parameters $\kappa = 0.005$ and the hill spring constant k_{hill} similar to a previous work on different lattices⁵². However, to match the experimental results, we also run simulations on a much smaller system, made of $N = 180$ particles arranged along 3×3 unit cells, and open boundary conditions. Further, to match the experimental data on the Cairo system (different lithographic substrate), we have also adjusted the effective magnetic susceptibility and hill elevation. We find that the best matching was obtained for $\kappa = 0.025$ and $k_{\text{hill}} = 3$ pN/nm. We numerically integrate the equation of motion using a time step of $\Delta t = 0.01$ s.

Details of the theoretical model. We explain here how we obtain the theoretical curves of Fig. 2e. It had been pointed out previously^{39,40} that the similarities in behaviour between particle-based ices and magnetic spin ices depend on topology³⁹ and geometry⁴⁰. In particular, ref. ³⁹ showed a way to compute topological charge transfers, which was later tested experimentally⁴¹. Presently, we use a modified version of the same method. The modification is needed to take into account that vertices of different coordination have different coupling constants due to the deformation, something not originally considered in ref. ³⁹.

In ref. ³⁹, there are strong approximations. Firstly, the energy for a given vertex of coordination z with n colloids in is given by only one coupling constant J , as

$$E_n = Jn(n-1)/2. \quad (6)$$

Considering that the topological charge of a vertex of coordination z is $q_{z,n} = 2n - z$ and thus depends only on n , in our approach differences in energy in vertices of the same charge are neglected. We know this is not true in general. However, if it is not too close to the ground state of the system, this method has been proven to work.

Secondly, correlation among vertices is also neglected. That, and imposing the conservation of the number of colloids, return a Boltzmann distribution for the probability of finding a vertex of coordination z with n colloids

$$\rho_{z,n} = \binom{z}{n} \frac{\exp(-E_{z,n}^\phi/T)}{Z(T, \phi)}. \quad (7)$$

(where $Z_z(T, \phi) = \sum_n \binom{z}{n} \exp(-E_{z,n}^\phi/T)$ is the partition function), but in new

effective energies $E_{z,n}^\phi$ which contain an electrostatic-like contribution from the emergent field ϕ coupled to the charge $q_{z,n}$:

$$E_{z,n}^\phi = E_n + q_n \phi, \quad (8)$$

and ϕ is a parameter to be determined by imposing that the total charge must be zero (that is, particle conservation). One sees that the temperature independent choice

$$\bar{\phi}_z/J = -(z-1)/4, \quad (9)$$

is the solution for a lattice of single coordination z . It returns the effective energies

$$E_{z,n}^\phi = J q_{z,n}^2/8 \quad (10)$$

(up to an irrelevant constant) which are quadratic in the topological charge, and are therefore spin-ice-like: the ensemble of lowest energy is the one where all vertices have minimal charge (± 1 if z is odd, 0 if z is even). This would explain the similarities in behaviours between magnetic spin ices and particle ices, despite the fact that their vertex energetics differ: particle ices are controlled by an effective energetics that is spin-ice-like.

Things become more interesting when there are multiple coordination. Then the same formalism applies to each subset of vertices, but ϕ (which is in fact an entropic field) is the same. One sees that in such case ϕ depends on temperature. Ref. ³⁹ shows how to deal with such situation at low temperature, and the result is the ice rule fragility: in the case of vertices of coordination $z = 4, 3$, vertices of coordination $z = 4$ become negatively charged, thus violating the ice rule, leaking charge to the subset of vertices of coordination $z = 3$. The latter do not, however, violate the ice rule. The reason is that $z = 3$ vertices already have a charge ± 1 in the ice manifold, and they can adsorb the positive charge by reducing the number of vertices of charge $+1$ and replacing them with vertices of charge -1 , so that overall charge neutrality is assured. This was demonstrated experimentally⁴¹ by progressively decimating a square lattice to create $z = 3$ randomly dispersed vertices, and observing negative charges progressively appear on $z = 4$ vertices. The same behaviour is shown by the present system below the critical angle.

Our Shakti-Cairo system, however, also shows a change in the entity of the charge transfer and also an inversion of its sign. That comes not from topology (our argument until here has only invoked coordination) but from geometry. As the system deforms, the coupling constants in the two set of vertices differ.

To describe very approximately this phenomenon in the context of this framework, we make the same approximations as above, because it has been proved sufficient by experiments. In particular, we use only a coupling constant per coordination: J_3 for vertices of coordination $z = 3$ and J_4 for coordination $z = 4$. Then in general Eq. (7) holds for each coordination number, and from that one obtains $\rho_{z,q}$, the probability that a vertex of coordination z has a charge q . Then ϕ is

found numerically by setting to zero the total charge given by Eq. (3) which of course depends on temperature and ϕ . Then, replacing ϕ in Eq. (7) one finds the statistical frequencies for charges, and uses it to compute the partial charges of the two set of vertices of coordination $z = 3, 4$, respectively. This formalism is at equilibrium and involves a temperature. The experimental system is essentially a-thermal. However, it had been previously shown theoretically^{39,53} and demonstrated experimentally^{33,35,41,48} that ramping up the perpendicular magnetic field leads to an equilibrium ensemble corresponding to low temperature, with respect of the coupling constants.

Experimental details. In contrast with previous works on colloidal ice^{33,52} we change our fabrication process to realize the lattice of topographic double wells in Polydimethylsiloxane (PDMS) rather than in a UV curable resin. The PDMS is an optically clear and inert organosilicon compound that allow us to realize a reusable substrate. The hydrophobicity of PDMS helps prevent particles from being irreversible attached to the substrate, and it is easy to clean, reuse and replicate.

To start, we use a commercial software (AutoCad, Adobe) to design the Cairo lattice. The mask containing the desired structure is fabricated on a 5-inch soda-lime glass covered with a 500 nm Chromium (Cr) layer. The designed motif are written via Direct Write Laser Lithography (DWL 66, Heidelberg Instruments Mikrotechnik GmbH) with a 405 nm laser diode working at a speed of $5.7 \text{ mm}^2 \text{ min}^{-1}$.

After drawn on the Cr mask, the double well lattice is then replicated in PDMS by first realizing an epoxy-based negative photoresist (SU-8) on the top of a silicon wafer. Then we cover the structure with liquid PDMS by spinning the sample at 4000 rpm for approximately during 1min with an angular speed of 2000 rpm/s (Spinner Ws-650Sz, Laurell). With this process we obtain a layer of $13 \pm 0.2 \mu\text{m}$ thickness, measured with a profilometer (DEKTA XT, Bruker). The PDMS is solidified by baking for 4 h at 65°C in a levelled oven. After solidification of the PDMS, we peel off the structure with the help of a cover glass (MENZEL-GLASER, Deckglaser) of $130\text{--}170 \mu\text{m}$ height. The resulting sample is only around $200 \mu\text{m}$ thick, enabling optical access.

Data availability

The data that support the findings of this study are available from the corresponding author upon reasonable request.

Received: 2 February 2023; Accepted: 10 May 2023;

Published online: 23 May 2023

References

- Diep, H. T. *Frustrated Spin Systems* (WORLD SCIENTIFIC, 2005). <https://doi.org/10.1142/5697>.
- Ramirez, A. P., Hayashi, A., Cava, R. J., Siddharthan, R. & Shastry, B. S. Zero-point entropy in 'spin ice'. *Nature* **399**, 333–335 (1999).
- Bramwell, S. T. & Gingras, M. J. Spin ice state in frustrated magnetic pyrochlore materials. *Science* **294**, 1495–501 (2001).
- Castelnovo, C., Moessner, R. & Sondhi, S. Spin ice, fractionalization, and topological order. *Annu. Rev. Condens. Matter Phys.* **3**, 35–55 (2012).
- Castelnovo, C., Moessner, R. & Sondhi, S. Magnetic monopoles in spin ice. *Nature* **399**, 42–45 (2008).
- Morris, D. J. P. et al. Dirac strings and magnetic monopoles in the spin ice $\text{Dy}_2\text{Ti}_2\text{O}_7$. *Science* **326**, 411–414 (2009).
- Giblin, S. R., Bramwell, S. T., Holdsworth, P. C. W., Prabhakaran, D. & Terry, I. Creation and measurement of long-lived magnetic monopole currents in spin ice. *Nat. Phys.* **7**, 252–258 (2011).
- Wang, R. F. et al. Artificial 'spin ice' in a geometrically frustrated lattice of nanoscale ferromagnetic islands. *Nature* **439**, 303–306 (2006).
- Nisoli, C., Moessner, R. & Schiffer, P. Colloquium: Artificial spin ice: Designing and imaging magnetic frustration. *Rev. Mod. Phys.* **85**, 1473–1490 (2013).
- Skjærvø, S. H., Marrows, C. H., Stamps, R. L. & Heyderman, L. J. Advances in artificial spin ice. *Nat. Rev. Phys.* **2**, 13–28 (2020).
- Mengotti, E. et al. Real-space observation of emergent magnetic monopoles and associated dirac strings in artificial kagome spin ice. *Nat. Phys.* **7**, 68 (2011).
- Branford, W., Ladak, S., Read, D., Zeissler, K. & Cohen, L. Emerging chirality in artificial spin ice. *Science* **335**, 1597 (2012).
- Zhang, S. et al. Crystallites of magnetic charges in artificial spin ice. *Nature* **500**, 553–557 (2013).
- Drisko, J., Marsh, T. & Cumings, J. Topological frustration of artificial spin ice. *Nature Comm.* **8**, 14009 (2017).

15. Saccone, M. et al. Direct observation of a dynamical glass transition in a nanomagnetic artificial hopfield network. *Nat. Phys.* **540**, 517–521 (2022).
16. Perrin, Y., Canals, B. & Rougemaille, N. Extensive degeneracy, coulomb phase and magnetic monopoles in artificial square ice. *Nature* **540**, 410–413 (2016).
17. Wu, F. Y. The potts model. *Rev. Mod. Phys.* **54**, 235–268 (1982).
18. Levis, D., Cugliandolo, L. F., Foini, L. & Tarzia, M. Thermal phase transitions in artificial spin ice. *Phys. Rev. Lett.* **110**, 207206 (2013).
19. Cugliandolo, L. F. Artificial spin-ice and vertex models. *J. Stat. Phys.* **167**, 499–514 (2017).
20. Louis, D. et al. A tunable magnetic metamaterial based on the dipolar four-state potts model. *Nat. Mat.* **17**, 1076–1080 (2018).
21. Latimer, M. L., Berdiyrov, G. R., Xiao, Z. L., Peeters, F. M. & Kwok, W. K. Realization of artificial ice systems for magnetic vortices in a superconducting moqe thin film with patterned nanostructures. *Phys. Rev. Lett.* **111**, 067001 (2013).
22. Wang, Y.-L. et al. Rewritable artificial magnetic charge ice. *Science* **500**, 553–557 (2016).
23. Gypens, P., Leliaert, J. & Van Waeyenberge, B. Balanced magnetic logic gates in a kagome spin ice. *Phys. Rev. Applied* **9**, 034004 (2018).
24. Arava, H. et al. Engineering relaxation pathways in building blocks of artificial spin ice for computation. *Phys. Rev. Applied* **11**, 054086 (2019).
25. Kaffash, M. T., Lendinez, S. & Jungfleisch, M. B. Nanomagnonics with artificial spin ice. *Physics Letters A* **402**, 499–514 (2021).
26. Libál, A., Reichhardt, C. & Olson Reichhardt, C. J. Hysteresis and return-point memory in colloidal artificial spin ice systems. *Phys. Rev. E* **86**, 021406 (2012).
27. Han, Y. et al. Geometric frustration in buckled colloidal monolayers. *Nature* **456**, 898–903 (2008).
28. Malins, A., Williams, S. R., Eggers, J., Tanaka, H. & Royall, C. P. Geometric frustration in small colloidal clusters. *J. Phys.: Cond. Matt.* **21**, 425103 (2009).
29. Francois, N., Saadatfar, M., Cruikshank, R. & Sheppard, A. Geometrical frustration in amorphous and partially crystallized packings of spheres. *Phys. Rev. Lett.* **111**, 148001 (2013).
30. Manoharan, V. N. Colloidal matter: Packing, geometry, and entropy. *Science* **349**, 942 (2015).
31. Tierno, P. Geometric frustration of colloidal dimers on a honeycomb magnetic lattice. *Phys. Rev. Lett.* **116**, 038303 (2016).
32. Zhou, D., Wang, F., Li, B., Lou, X. & Han, Y. Glassy spin dynamics in geometrically frustrated buckled colloidal crystals. *Phys. Rev. X* **7**, 021030 (2017).
33. Ortiz-Ambriz, A. & Tierno, P. Engineering of frustration in colloidal artificial ices realized on microfeatured grooved lattices. *Nat Commun* **7**, 10575 (2016).
34. Reichhardt, C. J. O., Libál, A. & Reichhardt, C. Multi-step ordering in kagome and square artificial spin ice. *New J. Phys.* **14**, 025006 (2012).
35. Loehr, J., Ortiz-Ambriz, A. & Tierno, P. Defect dynamics in artificial colloidal ice: Real-time observation, manipulation, and logic gate. *Phys. Rev. Lett.* **117**, 168001 (2016).
36. Libál, A., Nisoli, C., Reichhardt, C. & Reichhardt, C. J. O. Dynamic control of topological defects in artificial colloidal ice. *Sci. Rep.* **7**, 651 (2017).
37. Nisoli, C. The concept of spin ice graphs and a field theory for their charges. *AIP Advances* **10**, 115102 (2020).
38. Caravelli, F., Saccone, M. & Nisoli, C. On the degeneracy of spin ice graphs, and its estimate via the bethe permanent. *Proceedings of the Royal Society A* **477**, 20210108 (2021).
39. Nisoli, C. Dumping topological charges on neighbors: ice manifolds for colloids and vortices. *New J. Phys.* **16**, 113049 (2014).
40. Nisoli, C. Unexpected Phenomenology in Particle-Based Ice Absent in Magnetic Spin Ice. *Phys. Rev. Lett.* **120**, 167205 (2018).
41. Libál, A. et al. Ice rule fragility via topological charge transfer in artificial colloidal ice. *Nat. Comm.* **9**, 4146 (2018).
42. Li, J. et al. Comparing frustrated and unfrustrated clusters of single-domain ferromagnetic islands. *Phys. Rev. B* **82**, 134407 (2010).
43. Morrison, M. J., Nelson, T. R. & Nisoli, C. Unhappy vertices in artificial spin ice: new degeneracies from vertex frustration. *New Journal of Physics* **15**, 045009 (2013).
44. Gilbert, I. et al. Emergent ice rule and magnetic charge screening from vertex frustration in artificial spin ice. *Nature Physics* **10**, 670–675 (2014).
45. Gilbert, I. et al. Emergent reduced dimensionality by vertex frustration in artificial spin ice. *Nature Physics* **12**, 162–165 (2016).
46. Chern, G.-W., Morrison, M. J. & Nisoli, C. Degeneracy and criticality from emergent frustration in artificial spin ice. *Phys. Rev. Lett.* **111**, 177201 (2013).
47. Lao, Y. et al. Classical topological order in the kinetics of artificial spin ice. *Nature Physics* **14**, 723–727 (2018).
48. Ortiz-Ambriz, A., Nisoli, C., Reichhardt, C., Reichhardt, C. J. O. & Tierno, P. *Colloquium*: Ice rule and emergent frustration in particle ice and beyond. *Rev. Mod. Phys.* **91**, 041003 (2019).
49. Saccone, M. et al. Dipolar cairo lattice: Geometrical frustration and short-range correlations. *Phys. Rev. Materials* **3**, 104402 (2019).
50. Wang, Y.-L. et al. Switchable geometric frustration in an artificial-spin-ice-superconductor heterosystem. *Nature Nanotech.* **13**, 560–565 (2018).
51. Tierno, P., Muruganathan, R. & Fischer, T. M. Viscoelasticity of dynamically self-assembled paramagnetic colloidal clusters. *Phys. Rev. Lett.* **98**, 028301 (2007).
52. Rodríguez-Gallo, C., Ortiz-Ambriz, A. & Tierno, P. Topological boundary constraints in artificial colloidal ice. *Phys. Rev. Lett.* **126**, 188001 (2021).
53. Libál, A., Reichhardt, C. & Reichhardt, C. J. O. Realizing colloidal artificial ice on arrays of optical traps. *Phys. Rev. Lett.* **97**, 228302 (2006).

Acknowledgements

This project has received funding from the European Research Council (ERC) under the European Union's Horizon 2020 research and innovation programme (grant agreement no. 811234). P.T. acknowledge support the Generalitat de Catalunya under Program "ICREA Acadèmia".

Author contributions

C.R.-G. performed the experiments and the numerical simulations. C.N. developed the theoretical model. A.O. and P.T. supervised the work. P.T. wrote the paper. All authors discussed the results and commented on the manuscript at all stages.

Competing interests

The authors declare no competing interests.

Additional information

Supplementary information The online version contains supplementary material available at <https://doi.org/10.1038/s42005-023-01236-7>.

Correspondence and requests for materials should be addressed to Pietro Tierno.

Peer review information *Communications Physics* thanks the anonymous reviewers for their contribution to the peer review of this work. A peer review file is available.

Reprints and permission information is available at <http://www.nature.com/reprints>

Publisher's note Springer Nature remains neutral with regard to jurisdictional claims in published maps and institutional affiliations.



Open Access This article is licensed under a Creative Commons Attribution 4.0 International License, which permits use, sharing, adaptation, distribution and reproduction in any medium or format, as long as you give appropriate credit to the original author(s) and the source, provide a link to the Creative Commons license, and indicate if changes were made. The images or other third party material in this article are included in the article's Creative Commons license, unless indicated otherwise in a credit line to the material. If material is not included in the article's Creative Commons license and your intended use is not permitted by statutory regulation or exceeds the permitted use, you will need to obtain permission directly from the copyright holder. To view a copy of this license, visit <http://creativecommons.org/licenses/by/4.0/>.

© The Author(s) 2023

Ice rule breakdown and frustrated antiferrotoroidicity in an artificial colloidal ice

Carolina Rodríguez-Gallo^{1,2}, Antonio Ortiz-Ambriz^{1,3,4},
Cristiano Nisoli⁵ and Pietro Tierno^{1,2,3}

New Journal of Physics **25**, (2023) 103007

¹ Departament de Física de la Matèria Condensada, Universitat de Barcelona,
08028, Barcelona, Spain

² Universitat de Barcelona Institute of Complex Systems (UBICS),
Universitat de Barcelona, 08028, Barcelona, Spain

³ Institut de Nanociència i Nanotecnologia (IN2UB), Universitat de
Barcelona, 08028, Barcelona, Spain

⁴ Tecnológico de Monterrey, Escuela de Ingeniería y Ciencias, Campus
Monterrey, 64849 Monterrey, Mexico

⁵ Theoretical Division and Center for Nonlinear Studies, Los Alamos
National Laboratory, Los Alamos, NM 87545, USA.



PAPER • OPEN ACCESS

Ice rule breakdown and frustrated antiferrotoroidicity in an artificial colloidal Cairo ice

To cite this article: Carolina Rodríguez-Gallo *et al* 2023 *New J. Phys.* **25** 103007

View the [article online](#) for updates and enhancements.

You may also like

- [Ice rule correlations in stuffed spin ice](#)
R J Aldus, T Fennell, P P Deen *et al.*
- [Exact diagonalization for a 16-site spin-1/2 pyrochlore cluster](#)
C Wei and S H Curnoe
- [Dumping topological charges on neighbors: ice manifolds for colloids and vortices](#)
Cristiano Nisoli



PAPER

Ice rule breakdown and frustrated antiferrotoroidicity in an artificial colloidal Cairo ice

OPEN ACCESS

RECEIVED
7 May 2023REVISED
6 September 2023ACCEPTED FOR PUBLICATION
22 September 2023PUBLISHED
6 October 2023Original Content from
this work may be used
under the terms of the
[Creative Commons
Attribution 4.0 licence](#).Any further distribution
of this work must
maintain attribution to
the author(s) and the title
of the work, journal
citation and DOI.Carolina Rodríguez-Gallo^{1,2} , Antonio Ortiz-Ambriz^{1,3} , Cristiano Nisoli⁴  and Pietro Tierno^{1,2,5,*} ¹ Departament de Física de la Matèria Condensada, Universitat de Barcelona, 08028 Barcelona, Spain² Universitat de Barcelona Institute of Complex Systems (UBICS), Universitat de Barcelona, Barcelona 08028, Spain³ Tecnológico de Monterrey, Escuela de Ingeniería y Ciencias, Campus Monterrey, Monterrey 64849, Mexico⁴ Los Alamos National Laboratory, Los Alamos, NM 87545, United States of America⁵ Institut de Nanociència i Nanotecnologia, Universitat de Barcelona, Barcelona 08028, Spain

* Author to whom any correspondence should be addressed.

E-mail: ptierno@ub.edu**Keywords:** geometric frustration, colloids, magnetism, chirality

Abstract

We combine experiments and numerical simulations to investigate the low energy states and the emergence of topological defects in an artificial colloidal ice in the Cairo geometry. This type of geometry is characterized by a mixed coordination (z), with coexistence of both $z = 3$ and $z = 4$ vertices. We realize this particle ice by confining field tunable paramagnetic colloidal particles within a lattice of topographic double wells at a one to one filling using optical tweezers. By raising the interaction strength via an applied magnetic field, we find that the ice rule breaks down, and positive monopoles with charge $q = +2$ accumulate in the $z = 4$ vertices and are screened by negative ones ($q = -1$) in the $z = 3$. The resulting, strongly coupled state remains disordered. Further, via analysis of the mean chirality associated to each pentagonal plaquette, we find that the disordered ensemble for this geometry is massively degenerate and it corresponds to a frustrated antiferrotoroid.

1. Introduction

The Cairo geometry is a type of Euclidean plane tiling made of a sequence of connected pentagons which share vertices with two types of coordination numbers, namely $z = 3$ and $z = 4$ [1, 2]. Besides its aesthetic beauty, as testified by the presence of the Cairo geometry in numerous artistic paintings and pavements, especially in Egypt [3], such lattice is also important in frustrated spin systems. For example, it has been experimentally found in different magnetic compounds such as the $\text{Bi}_2\text{Fe}_4\text{O}_9$ [4] and the $\text{Bi}_4\text{Fe}_5\text{O}_{13}\text{F}$ [5], apart from being the subject of theoretical studies on Ising-type models [6–9]. Recently, such geometry has been considered as an interesting way to organize interacting dipolar nanoislands on a plane, also known as artificial spin ice systems (ASIs) [10–12]. ASIs are lattice of ferromagnetic elements that interact via in-plane dipoles and are arranged to produce geometric frustration effects [13–20]. In the Cairo geometry, recent experimental works have found a rich behavior due to frustration [21, 22], while Monte Carlo simulations reported the presence of long-range order [23]. Even mechanical analogues of Cairo artificial spin ice were realized via 3D-printing [24].

Particle ice systems are soft matter analogues of ASIs but based on interacting colloids constrained to move within a lattice of double wells [25, 26]. In contrast to ASIs that feature in-plane dipoles, the colloidal particles present out-of-plane, induced dipoles and pair interactions that can be tuned by an external field. The microscopic size of the particles allows the use of optical microscopy to visualize their dynamics and thus, to extract all relevant degrees of freedom. The particle ice was originally proposed with a set of double wells generated optically [25, 27], while experiments were realized by using lithographically patterned substrates [28–30]. Moreover, it was shown theoretically that, for a lattice of single coordination number z , the colloidal ice is analogous to an ASI since the low energy states fulfill similar ice-rules, i.e. minimization of the associated topological charge [31]. Such similarity however, breaks down for lattices of mixed

coordination such as decimated systems [32]. Indeed, in a colloidal ice, particles at a vertex tend to repel each other, and therefore the single vertex energy is different from ASI. If we consider the colloid as a token of a topological charge, then each vertex wants to push away as much charge as possible. In certain geometries this is impossible and the same trade-off, corresponding to the ice rule, is realized on each vertex. Thus, the colloidal ice for an extended, single coordinated lattice behaves as a spin ice [31, 33]. In other cases that is not true [32], as we show below for the Cairo geometry, and a transfer of topological charge takes place between vertices of different coordination, breaking the ice rule.

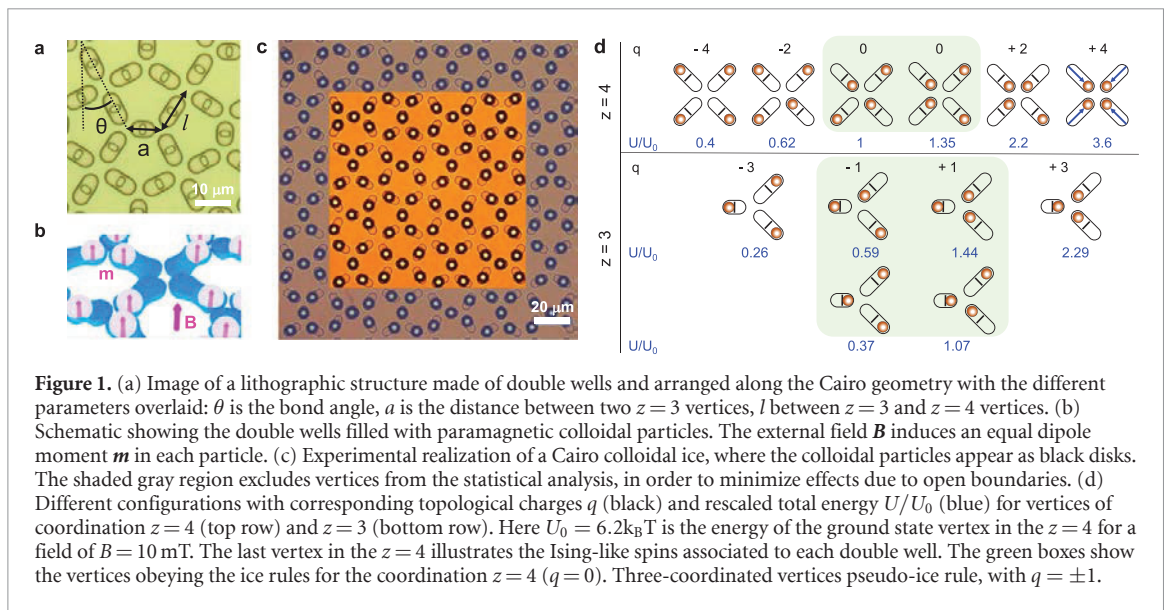
This fact underlines that particle based ice offers the possibility of investigating a rich set of physical phenomena, different than ASIs [30, 33–35]. And indeed many other recent realizations testify to the broader phenomenology of particle-based systems as models for geometric frustration. These include confined microgel particles [36–40], mechanical metamaterials [41–46], patterned superconductors [47, 48], skyrmions in liquid crystals [49, 50] and interacting macroscopic rods [51, 52].

In this article we experimentally realize a Cairo colloidal ice by confining repulsive paramagnetic colloidal particles within a lattice of lithographic double wells, as shown in figure 1(a). To place and move these particles within the topographic traps, we use a modified set of laser tweezers that generate an optical ring rather than a focalized spot. This strategy allows to easily trap and move paramagnetic particles, avoiding heating due to absorbed light. By investigating the low energy states, we find that topological charges can accumulate in different sublattices, breaking locally the ice rules. We complement our finding with Brownian dynamic simulations, which show good agreement with the experimental data in terms of fraction of vertices, topological charges and net chirality associated to each pentagonal plaquette of the Cairo lattice. Finally we perform simulations on an extended system to calculate chirality correlation functions and to elucidate the system frustration at high field strength.

2. The artificial colloidal ice

The schematic in figure 1(b) and the optical microscope image in figure 1(c) illustrate the basic features of a Cairo colloidal ice. The system presents a lattice of lithographic elliptical traps composed of two wells of lateral elevation $h \sim 3 \mu\text{m}$ that are connected by a small central hill. These wells are filled with paramagnetic colloidal particles of diameter $d = 10 \mu\text{m}$ and magnetic volume susceptibility $\kappa = 0.025$. A particle of volume $V = \pi d^3/6$ has to overcome a gravitational potential $U_g = \Delta\rho Vgh \sim 2000 k_B T$ to jump outside the double well due to thermal fluctuations. Here $\Delta\rho = \rho_p - \rho_w \sim 0.6 \text{g cm}^{-3}$ is the difference between the mass density of the particle (ρ_p) and the dispersing medium (ρ_w). Thus, the particles are essentially confined within the elliptical traps and cannot change their location from one well to another unless subjected to an external force, such as the repulsion from a neighboring colloid. We induce such repulsion by applying an external magnetic field \mathbf{B} perpendicular to the sample plane, figure 1(b). Once the field is applied, each particle acquires an induced dipole moment $\mathbf{m} = V\kappa\mathbf{B}/\mu_0$, being μ_0 the permeability of vacuum. Thus, a pair of particles (i, j) placed at a relative distance $r = |\mathbf{r}_i - \mathbf{r}_j|$ experience a repulsive dipolar interaction which is isotropic and inversely proportional to r^3 , $U_{dd} = \mu_0 m^2 / (4\pi r^3)$. This interaction potential can be tuned via the applied field, \mathbf{B} . For an amplitude of $B = 10 \text{mT}$, the potential strength is $U_{dd} = 122 k_B T$ for the closest distance between two particles in a $z = 3$ vertex being $r = 13 \mu\text{m}$, while is $U_{dd} = 4.7 k_B T$ for the farthest distance of $r = 38.4 \mu\text{m}$ in a $z = 4$ vertex in the Cairo geometry.

The mapping between the colloidal ice and an ASI [25] can be obtained by assigning an Ising-like spin to each double well, such that it points where the particle is located, figure 1(d). Using this mapping, one can distinguish between different type of vertices depending on the lattice coordination. For example, for the $z = 4$ (square lattice) there are 6 possible arrangements of the particles with different energetic weights, while for the $z = 3$ (honeycomb lattice) these reduce to 4. Moreover, in analogy to the ASI, one can assign a topological charge to each vertex defined here as $q = 2n - z$ being n the number of spins that point toward the vertex center. Note that we can talk of topological charges when considering the vertices within a lattice, not isolated ones. By this notion of charge, an extended lattice is overall charge-neutral, and thus charges appear in pairs and disappear only when annihilated by other defects in order to guarantee the charge conservation, $\sum q_i = 0$. For example, the vertex with four colloids pointing outwards ($q = -4$) is characterized by the lowest energetic weight of the $z = 4$, and thus, when considered alone it will be the natural state of repulsive colloids. However, within a lattice the $q = -4$ is topologically connected to the $q = +4$ due to particle conservation and thus they are unlikely to occur. One can prove that in a lattice, lower absolute values of the topological charges $|q| = 0, 1$, corresponding to the ice-rule, are favored [33]. The ice rules, highlighted by the green boxes in figure 1(d) are a prescription of the minimization of $|q|$, given by vertices with $q = 0$ for $z = 4$ and $q = \pm 1$ for $z = 3$. Indeed, even though the ice rules were originally defined



for a tetrahedral coordination system [53, 54], we find it useful to extend them to other coordination numbers as the $z = 3$, figure 1(d).

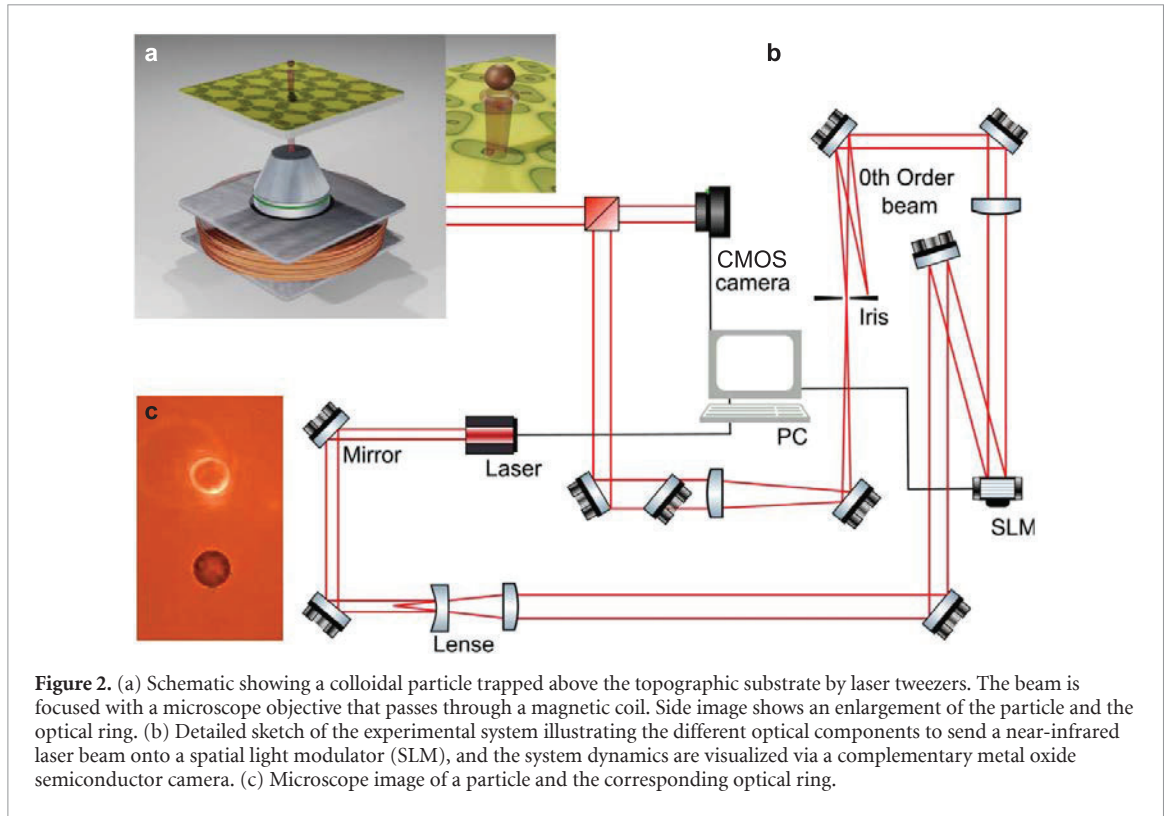
Regarding the Cairo geometry, we have a mixture of $z = 4$ and $z = 3$ vertices, the latter characterized by unequal lengths of the double wells, as shown in figure 1(d). Upon analysis of the total magnetic interaction energy of a vertex U , we find that the $z = 4$ vertices have same energy hierarchy as the square colloidal ice investigated in previous works [28, 29]. Here $U = \sum_{i=1}^{N_v-1} \sum_{j=i+1}^{N_v} U_{ij}^{dd}$, being N_v the number of particles in a vertex. However, the presence of the small double well in the $z = 3$ vertices, i.e. a length of $4.53 \mu\text{m}$ while in the $z = 4$ the length is $10 \mu\text{m}$, induces an energetic spitting of the vertices 1-in-2-out and 2-in-1-out depending on the location of the paramagnetic colloid. This energy difference between the $z = 3$ vertices, which does not affect the associated topological charge, is particular of the Cairo geometry, and it is not present in the $z = 3$ vertices of the classical honeycomb [55, 56] and triangular [57] colloidal ice, where all traps have the same length. Even if the energy difference is relatively small, as we will show later this will induce a disordered ground state.

3. Experimental methods

The Cairo lattice is realized via soft-lithography using polydimethylsiloxane (PDMS). This substrate was first designed using a commercial software (AutoCad, Adobe) and transferred above a 5 inch soda-lime glass substrate covered with a 500 nm Chromium (Cr) layer. The chosen geometric parameters, as shown in figure 1(a), are $a = 19.54 \mu\text{m}$, $l = 26.7 \mu\text{m}$ and $\theta = 30^\circ$. We use laser lithography (DWL 66, Heidelberg Instruments Mikrotechnik GmbH) to write the double wells on the substrate with a 405 nm laser diode working at a speed of $5.7 \text{ mm}^2 \text{ min}^{-1}$. After that, we replicate the double wells of the Cr mask in the PDMS following two steps. In the first one we duplicate the structure using an epoxy-based negative photoresist (SU-8) on top of a silicon wafer. Then we covered the structure with liquid PDMS by spinning the sample at 4000 rpm during 1 min with an angular speed of 2000 rpm (Spinner Ws-650Sz, Laurell). With this process we obtain a layer of $\approx 20 \mu\text{m}$ thickness. The PDMS is solidified by baking for 30 min at 95°C in a leveled hot plate. After solidification of the PDMS, we peel off the structure with the help of a cover glass (MENZEL-GLASER, Deckglaser). The resulting sample is $\sim 170 \mu\text{m}$ thick, and transparent enough to visible light.

Once fabricated, the sample is placed on the stage of an inverted optical microscope (TiU, Nikon) which is connected to a complementary metal oxide semiconductor camera (MQ013CG-E2, Ximea) able to record videos of the particle dynamics at 30 Hz. The microscope is equipped with a $40 \times$ oil immersion objective (Nikon, numerical aperture 1.3) which is used both for observation and optical trapping purpose.

One microscope port is modified in order to accommodate an incoming beam generated by a butterfly laser diode (wavelength $\lambda = 976$ nm, operated at a power of 70 mW, BL976-SAG300 Thorlabs). The optical path of the laser is composed of a series of lenses including a spatial light modulator (SLM, Hamamatsu X10468-03) which is commanded by a LCOS-SLM controller (Hamamatsu), figures 2(a) and (b). The holograms are generated with a custom made Labview program.



The SLM is used in the holographic optical tweezers (HOTs) which are composed of 4 lenses. The first two constitute a telescope and have focal lengths $f = -75$ mm (Thorlabs LC 1582-B) and $f = 175$ mm (Thorlabs LA 1229-B), respectively. After the SLM there is another telescope with a focal length of $f = 500$ mm (Thorlabs LA1908-B) which focuses the beam after being deflected in order to filter the 0 mode via a diaphragm, reaching a final lens of $f = 750$ mm (Thorlabs LA 1727-C), as shown in the detailed diagram of figure 2(b). In this work, we use polystyrene paramagnetic colloids having a nominal diameter of $d = 10$ μm , standard deviation < 0.5 μm that are highly doped with nanoscale iron oxide grains $\sim 20\%$ by (Sigma-Aldrich, Cat. number 496 64). Due to the optical absorption of the iron oxide grains, we have implemented a novel strategy to trap the colloids without damaging them due to the generated heat. Instead of using a single focalized spot, we program the SLM such that the deflected beam generates an optical ring as shown in figures 2(a) and (c).

The external magnetic field was generated via a custom made coil located below the sample. The magnetic coil is powered by an amplifier (BOP-20 10 M, KEPCO), that is computer controlled using a digital analogue card (NI 9269) with a custom made LabVIEW program. The field was applied via a ramp at a rate 0.05 mT s^{-1} until reaching a maximum value of 10 mT .

4. Numerical simulation

We complement the experiments performing Brownian dynamics simulations using as input parameters the experimental data. In particular, we use Euler's method to integrate the overdamped equations of motion for each colloidal particle i at position \mathbf{r}_i :

$$\gamma \frac{d\mathbf{r}_i}{dt} = \mathbf{F}_i^T + \mathbf{F}_i^{\text{dd}} + \boldsymbol{\eta} , \quad (1)$$

being $\gamma = 0.033$ pN s m^{-1} the friction coefficient. Further terms in equation (1) are the force from the topographic double well \mathbf{F}_i^T which is modeled as a piece-wise harmonic bistable potential,

$$\mathbf{F}_i^T = -\mathbf{e}_\perp k R_\perp + \mathbf{e}_\parallel \delta . \quad (2)$$

Here $(\mathbf{e}_\parallel, \mathbf{e}_\perp)$ are unit vectors oriented parallel and perpendicular with respect to the line of length L that joins the two minima in the double well, whose associated vector is $\mathbf{R} \equiv (R_\parallel, R_\perp)$. Moreover $\delta = \xi_1 R_\parallel$ if $|R_\parallel| \leq \frac{L}{2}$ and $\delta = k(\frac{L}{2} - |R_\parallel|)\text{sign}(R_\parallel)$ otherwise. As stiffness we use $k = 1 \cdot 10^{-4}$ pN nm^{-1} which keeps the

particle confined to the elongated region around the center of the trap, and $\xi_1 = 3 \text{ pN nm}^{-1}$ that creates a potential hill equivalent to the gravitational hill within the double wells.

The dipolar force on a particle i is given by,

$$\mathbf{F}_i^{\text{dd}} = \frac{3\mu_0}{4\pi} \sum_{j \neq i} \frac{m^2 \hat{r}_{ij}}{|r_{ij}|^4}, \quad (3)$$

being $\mu_0 = 4\pi \times 10^{-7} \text{ H m}^{-1}$ and $\hat{r}_{ij} = (\mathbf{r}_i - \mathbf{r}_j)/|\mathbf{r}_i - \mathbf{r}_j|$. Dipolar interactions are calculated in an iterative form such that the global field \mathbf{B} includes also that generated by all other dipoles. Moreover, we apply a large cut-off distance of $200 \mu\text{m}$ to consider the effect of long range dipolar interactions.

Finally the last term in equation (1) is a random force characterized by a zero mean, $\langle \boldsymbol{\eta} \rangle = 0$ and delta correlated, $\langle \boldsymbol{\eta}(t) \boldsymbol{\eta}(t') \rangle = 2k_B T \gamma \delta(t - t')$, being k_B the Boltzmann constant and $T = 300 \text{ K}$ the ambient temperature.

To reproduce the experimental results we start by solving equation (1) with $N_1 = 180$ particles which are arranged along 3×3 unit cells and open boundary conditions. We avoid the effects of the boundaries (charge accumulation) by excluding a shell of vertices from the statistical analysis, as shown in figure 1(c), and by increasing the number of realizations. We have checked that the effect of topological charge transfer occurs both in small (3×3 unit cells) and large (10×10 unit cells) system size. Note also that the effect of including the outer region will be to have new vertices of coordination number $z = 2$ where most of the positive topological charges accumulate. To consider a larger system when measuring the chirality correlation functions, we extend the simulations also to $N_2 = 2000$ particles, where 800 are arranged along the $z = 3$ vertices and 400 in the $z = 4$. This situation corresponds to a colloidal ice of 10×10 unit cells also with open boundary conditions. To avoid that most of the particles in the $z = 3$ vertices localize on top of the topographic hills, due to strong dipolar forces, we also reduce the particle magnetic susceptibility to $\kappa_2 = 0.005$ and raise the spring constant of the central hill to $\xi_2 = 25 \text{ pN nm}^{-1}$. In all cases, we numerically integrate the equation of motion using a time step of $\Delta t = 0.01 \text{ s}$.

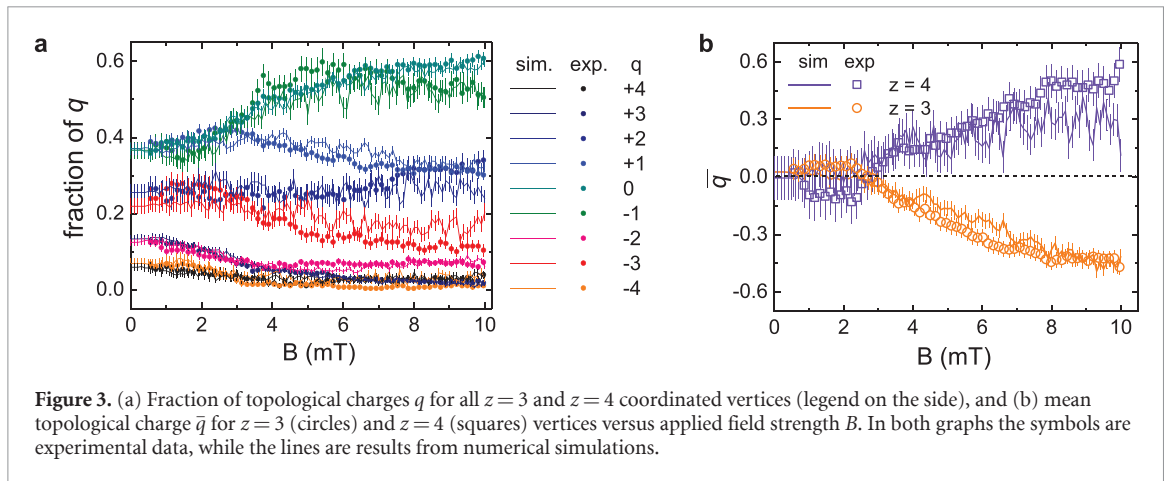
5. Measurements of the topological charges

We start our experiments by first randomly placing the particles with the optical ring within the double wells according to a random number generator. In the initial, random configuration the highly charged monopoles $q = \pm 4$ are the 10% of the total vertices, $q = \pm 3$ are the 15%, while the 25% of vertices corresponds to low charged $q = \pm 2$, the rest is left to the ice rule vertices. Then, we slowly raise the applied field with a ramp of 0.05 mT s^{-1} . Figure 3(a) shows the evolution of the fraction of topological charges as classified in figure 1(d), for the Cairo ice. By increasing \mathbf{B} , we find that already after $B \sim 3 \text{ mT}$, the fraction of high topological charges $q = \pm 4$ in the $z = 4$ and $q = \pm 3$ in the $z = 3$ vertices reduces almost to zero in favor of the low charged ones. In particular, vertices obeying the ice selection rules in the $z = 4$ rise up to the 50%, being only overcome by the $q = -1$ in the $z = 3$ ($\sim 60\%$), while the $q = +1$ reduces to $\sim 30\%$. This reduction is accompanied by a slight increase of the charged monopoles $q = +2$ and a decrease of the $q = -2$.

Crucially, figure 3(b) plots the average topological charge ($\bar{q} = \frac{1}{N_z} \sum q_z$, being N_z the number of vertices z) for vertices of coordination 3 and 4. It shows a net separation of topological charges between vertices of different coordination, and thus charge transfer between sublattices, breaking the ice rule. Thus, while the total topological charge is conserved, or $\sum q = 0$, at the sublattice level we observe a transfer of topological charges as the field reaches $B = 8 \text{ mT}$. A net fraction of positive monopoles accumulate in the $z = 4$ vertices, while the $z = 3$ vertices are, on average, negatively charged. Note also the relatively good agreement between experimental data (open symbols) and numerical simulations (continuous lines), which are plot together in both graphs, while small deviations fall within the experimental/simulation error bars.

Importantly, charge transfer effect between sublattices does not occur in an ASI, whose ice rule is instead robust in most geometries as it is inscribed into the energetics of the vertices. It only occurs in a colloidal ice with mixed coordination geometry such as the Cairo. This effect results from the different nature of geometric frustration in ASI and in the colloidal system [31]. While both systems display similar behavior in terms of vertex fraction for single coordination lattices, in a mixed coordination geometry the difference at the single vertex level emerges: repulsive colloids cannot emulate in-plane ferromagnetic spins as in ASI, and topological charges tend to redistribute in order to minimize the system energy.

While charge transfer and ice-rule fragility had been predicted [31] and experimentally verified [32] in a decimated square ice, the sign of this effect in the Cairo lattice is inverted. In [32], negative monopoles form on the $z = 4$, breaking the ice rule. In that case the $z = 3$ vertices, which unlike the $z = 4$ vertices are charged even when obeying the ice rule, do not violate such rule but screen the negative charge of the $z = 4$ vertices. This was done by changing their relative admixture of ± 1 charges, and thus assuming a net positive charge.



In the Cairo system instead, the mechanism is similar but the sign of the charges is inverted. This is because Cairo is structurally different from a decimated square, with shorter and longer traps and thus a more complex energetics, as shown in figure 1(d). This allows also for structural transitions in the sign of the transferred charge as Cairo is deformed, and which we study elsewhere, while here we focus only on the Cairo geometry.

5.1. Frustrated antiferrotoroidicity in the Cairo system

To better characterize the disorder of the charge-unbalanced, low-energy state of strongly-interacting Cairo colloidal ice, we study the chirality value, or associated toroidal moment, to each pentagonal plaquette. As shown in the inset in figure 4(a), this moment acquires a maximum value of $\chi = -1$ (+1) for a full counter clockwise (clockwise) cell. Two natural questions are, firstly whether the plaquettes are naturally chiral, and secondly what is the mutual arrangement of these chiralities. To answer the first question, note that for a single pentagonal plaquette, a configuration that is fully chiral obeys the ice rule, that we know breaks down at high fields. At the same time, the long range interactions among colloids in further neighboring traps favors chirality. In the Cairo geometry the plaquette chirality is also favored by the asymmetry in the vertices of coordination $z=3$. The particles within the shorter double wells require a smaller energetic cost to be displaced than that in the longer one. Thus, at high field strength the $z=4$ vertices prefer to follow the ice rules, and parallel plaquettes separated by the same $z=3$ vertex will acquire the same chirality that is opposite to that of plaquettes in nearest $z=3$ vertices, see small inset in figure 4(d), left. Now, independently of how the colloidal particle in the $z=3$ vertex is displaced, it will create always one fully chiral plaquette ($\chi = 1$) and another with a chirality of $3/5$ of the same sign (a nearest $z=3$ vertices will create a -1 and a $-3/5$). When normalized with respect to the number of plaquettes, we obtain a chirality value of 0.8.

Thus we expect that at large field strengths, the average absolute chirality of the systems, $\bar{\chi} = \frac{1}{N_{pl}} \sum_i |\chi_i|$ being N_{pl} the number of plaquette, would tend towards $\bar{\chi} \rightarrow 0.8$. However we found that this was not the case, as shown in figure 4(c), where both experiments and simulations show that at the largest applied field $\bar{\chi} \sim 0.5$. This lower value was due to the fact that, in the Cairo geometry, the magnetic colloids were found to locate above the central hill at the largest field amplitude, $B = 10$ mT. Indeed this effect is shown in the first graph in figure 4(b), where histograms of the particle positions from the simulations are reported for both the long and short double wells in the Cairo geometry. In this situation, since the trap bistability is lost, it is difficult to extract an accurate determination of $\bar{\chi}$. We note that the particle localization in the central hill at high field strength may be reminiscent of the symmetrisation of hydrogen bonds which is observed at high pressure ~ 70 GPa. In the latter case, the hydrogen atoms tend to localize in the middle between the two oxygen ones and the molecular character of water in ice is lost [58, 59].

To keep the bistability, we have performed further simulations using a larger system size and stronger confinement, i.e. increasing the hill spring constant from $\xi_1 \rightarrow \xi_2 = 25$ pN nm $^{-1}$ and decreasing the magnetic volume susceptibility to $\kappa_1 \rightarrow \kappa_2 = 0.005$. The resulting histograms of the particle positions, shown in the right panel of figure 4(b), confirm that for these new parameters the bistability is recovered even for a larger field of $B = 25$ mT. Thus, for the latter system, we obtain the value of $\bar{\chi} \sim 0.7$ at the largest field which is in the ballpark of our estimate $\bar{\chi} = 0.8$ based on a single plaquette. Note that figure 4(a) shows an alternation of sign among many nearest neighboring plaquettes. However, the lattice of the pentagonal plaquettes is not bipartite, and thus frustrates the anti alignment of the plaquettes. A configuration in which all the neighboring plaquettes have opposite chirality (e.g. the check board pattern observed for the square

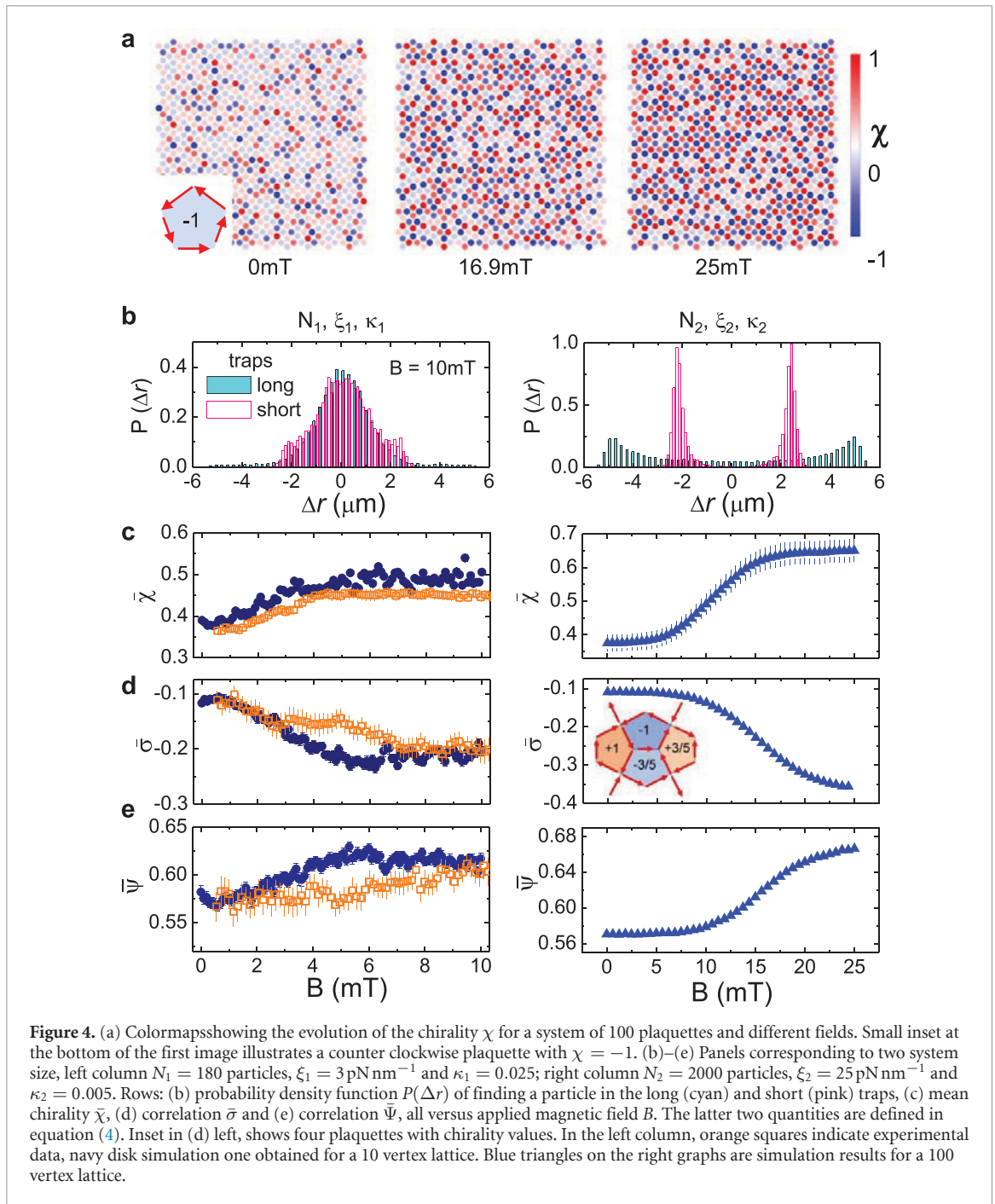


Figure 4. (a) Colormaps showing the evolution of the chirality χ for a system of 100 plaquettes and different fields. Small inset at the bottom of the first image illustrates a counter clockwise plaquette with $\chi = -1$. (b)–(e) Panels corresponding to two system size, left column $N_1 = 180$ particles, $\xi_1 = 3\text{pN nm}^{-1}$ and $\kappa_1 = 0.025$; right column $N_2 = 2000$ particles, $\xi_2 = 25\text{pN nm}^{-1}$ and $\kappa_2 = 0.005$. Rows: (b) probability density function $P(\Delta r)$ of finding a particle in the long (cyan) and short (pink) traps, (c) mean chirality $\bar{\chi}$, (d) correlation $\bar{\sigma}$ and (e) correlation $\bar{\Psi}$, all versus applied magnetic field B . The latter two quantities are defined in equation (4). Inset in (d) left, shows four plaquettes with chirality values. In the left column, orange squares indicate experimental data, navy disk simulation one obtained for a 10 vertex lattice. Blue triangles on the right graphs are simulation results for a 100 vertex lattice.

spin ice system [60]) is geometrically impossible which suggests that the system has, at least, a disordered landscape of low energy states. As figure 4(a) suggests, the configuration corresponds to an antiferrotoroid. Moreover, we have checked that also with the new numerical conditions (N_2, ξ_2, κ_2) we observe the topological charge transfer similar to figure 3(b).

To answer the second question, concerning the mutual distribution of chiralities, we note that figure 4(a) shows a largely antiferrotoroidal arrangement. However, the lattice of the plaquettes is frustrated and therefore no full antiferrotoroidicity can exist. We explore this effect by calculating the following nearest neighbor correlations:

$$\bar{\psi} = \frac{1}{N_{nn}} \sum_{\langle ij \rangle} \left(1 - \frac{\chi_i \chi_j}{|\chi_i \chi_j|} \right) \frac{1}{2}; \quad \bar{\sigma} = \frac{1}{N_{nn}} \sum_{\langle ij \rangle} \frac{\chi_i \chi_j}{\bar{\chi}}; \quad (4)$$

where the sum is performed over the N_{nn} nearest neighboring plaquettes. Both correlations counts how many links among nearest neighboring plaquettes are antiferrotoroidal, regardless of the intensity of the chiralities of the plaquettes. If all the nearest neighboring plaquettes were antiferrotoroidal (which is

impossible because of the frustration of the lattice of the plaquettes) then $\bar{\psi}$ would be equal to 1, and $\bar{\sigma} \rightarrow -1$. Moreover σ allows to distinguish between the ferrotoroidal and antiferrotoroidal behavior depending on whether positive or negative, respectively.

We plot $\bar{\psi}$ and $\bar{\sigma}$ in figures 4(d) and (e). In the left images, both correlations show similar trends between experiments and numerical simulations. For the large system size (right images) $\bar{\psi}$ increases steadily with the field reaching 0.68: almost the 68% of the links are anti-ferromagnetic, namely 3.5 over 5 nearest neighbors. This results also reflects the arrangement of the toroidal moments shown in figure 4(a) for $B = 25$ mT, where the system organizes in a lattice of full chiral cells placed in an alternating order. These results allow to characterize the disorder of the strongly coupled state of the Cairo ice in terms of plaquette chirality as a frustrated antiferrotoroid. The charge transfer prevents all plaquettes from reaching maximum chirality, while the lattice of the plaquettes frustrates antiferrotoroidicity, preventing order.

6. Conclusions

We have investigated the arrangement of repulsive magnetic colloids confined in a lattice of double wells in the Cairo geometry. To experimentally realize such structure we have modified the lithographic process and developed a novel technique to trap absorbing magnetic particles using an optical ring. This strategy could be extended to other works aiming at trapping light-adsorbing magnetic particles to avoid undesired heating effects. We have observed that the Cairo ice breaks the ice rule as predicted for mixed coordination geometries, however, it does so with an inversion of the net charge transfer with respect to a previous experimental realization [32]. Moreover we have characterized this novel ensemble but looking at the effective toroidal moment associated to each pentagonal plaquette. We have found that the strongly coupled ensemble of the Cairo colloidal ice is a massively degenerate antiferroid. Our results could be potentially observed in magnetic compounds characterized by parallel lattice planes with spin lying on a Cairo lattice and having strong horizontal and weak vertical interactions. These materials are currently matter of research interest [4, 5, 61–65], although monitoring the spin dynamics remain a challenging task.

Further extensions of our work include investigating the transition from Shakti to Cairo (ongoing) or using different size of particles to investigate hysteresis and memory effects [27, 35] that could emerge when the particles localize above the double wells [66]. Finally, it will be also interesting to investigate how the topological charges freeze or move after long time and the presence of aging of topological defects in our system. This will require longer observation time, beyond our current experimental capabilities, and thus could be a challenge for future work.

Data availability statement

All data that support the findings of this study are included within the article.

Acknowledgment

This project has received funding from the European Research Council (ERC) under the European Union's Horizon 2020 research and innovation programme (Grant Agreement No. 811234). P T acknowledge support the Generalitat de Catalunya under Program 'ICREA Acadèmia', the Spanish Ministry of Science and Innovation (no. PID2022-137713NB-C22) and the Agència de Gestió d'Ajuts Universitaris i de Recerca (no. 2021 SGR 00450). The work of Cristiano Nisoli was carried out under the auspices of the U S DoE through the Los Alamos National Laboratory, operated by Triad National Security, LLC (Contract No. 892333218NCA000001).

ORCID iDs

Carolina Rodríguez-Gallo  <https://orcid.org/0000-0002-2044-3189>

Antonio Ortiz-Ambriz  <https://orcid.org/0000-0002-8302-0861>

Cristiano Nisoli  <https://orcid.org/0000-0003-0053-1023>

Pietro Tierno  <https://orcid.org/0000-0002-0813-8683>

References

- [1] O'Keefe M and Hyde B G 1980 Philosophical Transactions of the Royal Society of London. Series A, Mathematical and Physical Sciences **295** 553–618
- [2] Shen Y and Wang Q 2022 *Phys. Rep.* **964** 1–42
- [3] Macmillan R H 1979 *Math. Gaz.* **63** 251–5

- [4] Ressouche E, Simonet V, Canals B, Gospodinov M and Skumryev V 2009 *Phys. Rev. Lett.* **103** 267204
- [5] Abakumov A M, Batuk D, Tsirlin A A, Prescher C, Dubrovinsky L, Sheptyakov D V, Schnelle W, Hadermann J and Van Tendeloo G 2013 *Phys. Rev. B* **87** 024423
- [6] Urumov V 2002 *J. Phys. A: Math. Gen.* **35** 7317
- [7] Ralko A 2011 *Phys. Rev. B* **84** 184434
- [8] Rojas M, Rojas O and de Souza S M 2012 *Phys. Rev. E* **86** 051116
- [9] Rousochatzakis I, Läuchli A M and Moessner R 2012 *Phys. Rev. B* **85** 104415
- [10] Wang R F et al 2006 *Nature* **439** 303–6
- [11] Nisoli C, Moessner R and Schiffer P 2013 *Rev. Mod. Phys.* **85** 1473–90
- [12] Skjærvø S H, Marrows C H, Stamps R L and Heyderman L J 2020 *Nat. Rev. Phys.* **2** 13–28
- [13] Mól L A S, Moura-Melo W A and Pereira A R 2010 *Phys. Rev. B* **82** 054434
- [14] Rougemaille N et al 2011 *Phys. Rev. Lett.* **106** 057209
- [15] Zhang S, Gilbert I, Nisoli C, Chern G W, Erickson M J, O'Brien L, Leighton C, Lammert P E, Crespi V H and Schiffer P 2013 *Nature* **500** 553–7
- [16] Gilbert I, Chern G W, Zhang S, O'Brien L, Fore B, Nisoli C and Schiffer P 2014 *Nat. Phys.* **10** 670–5
- [17] Perrin Y, Canals B and Rougemaille N 2016 *Nature* **540** 410–3
- [18] Canals B, Chioar I A, Nguyen V D, Hehn M, Lacour D, Montaigne F, Locatelli A, Menteş T O, Burgos B S and Rougemaille N 2016 *Nat. Commun.* **7** 11446
- [19] Vedmedenko E Y 2016 *Phys. Rev. Lett.* **116** 077202
- [20] Wang Y-L, Xiao Z-L, Snezhko A, Xu J, Ocola L E, Divan R, Pearson J E, Crabtree G W and Kwok W-K 2016 *Science* **352** 962–6
- [21] Saccone M, Hofhuis K, Huang Y L, Dhuey S, Chen Z, Scholl A, Chopdekar R V, van Dijken S and Farhan A 2019 *Phys. Rev. Mater.* **3** 104402
- [22] Makarova K et al 2021 *Phys. Rev. E* **103** 042129
- [23] Shevchenko Y, Strongin V, Kapitan V, Soldatov K, Makarov A, Padalko M, Volotovskii R and Nefedev K 2022 *Phys. Rev. E* **106** 064105
- [24] Merrigan C, Shohat D, Sirote C, Lahini Y, Nisoli C and Shokef Y 2022 arXiv:2204.04000
- [25] Libál A, Reichhardt C and Reichhardt C J O 2006 *Phys. Rev. Lett.* **97** 228302
- [26] Ortiz-Ambriz A, Nisoli C, Reichhardt C, Reichhardt C J O and Tierno P 2019 *Rev. Mod. Phys.* **91** 041003
- [27] Libál A, Reichhardt C and Olson Reichhardt C J 2012 *Phys. Rev. E* **86** 021406
- [28] Ortiz-Ambriz A and Tierno P 2016 *Nat. Commun.* **7** 10575
- [29] Loehr J, Ortiz-Ambriz A and Tierno P 2016 *Phys. Rev. Lett.* **117** 168001
- [30] Oğuz E C, Ortiz-Ambriz A, Shem-Tov H, Babià-Soler E, Tierno P and Shokef Y 2020 *Phys. Rev. Lett.* **124** 238003
- [31] Nisoli C 2014 *New J. Phys.* **16** 113049
- [32] Libál A, Lee D Y, Ortiz-Ambriz A, Reichhardt C, Reichhardt C J O, Tierno P and Nisoli C 2018 *Nat. Commun.* **9** 4146
- [33] Nisoli C 2018 *Phys. Rev. Lett.* **120** 167205
- [34] Libál A, Nisoli C, Reichhardt C and Reichhardt C J O 2017 *Sci. Rep.* **7** 651
- [35] Rodríguez-Gallo C, Ortiz-Ambriz A and Tierno P 2021 *Phys. Rev. Lett.* **126** 188001
- [36] Han Y, Shokef Y, Alsayed A M, Yunker P, Lubensky T C and Yodh A G 2008 *Nature* **456** 898–903
- [37] Shokef Y, Souslov A and Lubensky T C 2011 *Proc. Natl Acad. Sci.* **108** 11804–9
- [38] Shokef Y, Han Y, Souslov A, Yodh A G and Lubensky T C 2013 *Soft Matter* **9** 6565–70
- [39] Zhou D, Wang F, Li B, Lou X and Han Y 2017 *Phys. Rev. X* **7** 021030
- [40] Leoni F and Shokef Y 2017 *Phys. Rev. Lett.* **118** 218002
- [41] Kang S H, Shan S, Noorduyn W L, Khan M, Aizenberg J and Bertoldi K 2013 *Adv. Mater.* **25** 3380–5
- [42] Coulais C, Teomy E, de Reus K, Shokef Y and van Hecke M 2016 *Nature* **535** 529–32
- [43] Meeussen A S, Oguz E C, Shokef Y and van Hecke M 2020 *Nat. Phys.* **16** 307–11
- [44] Li S et al 2021 *Nature* **592** 386–91
- [45] Merrigan C, Nisoli C and Shokef Y 2021 *Phys. Rev. Res.* **3** 023174
- [46] Meng Z, Liu M, Yan H, Genin G M and Chen C Q 2022 *Sci. Adv.* **8** eabn5460
- [47] Libál A, Reichhardt C J O and Reichhardt C 2009 *Phys. Rev. Lett.* **102** 237004
- [48] Latimer M L, Berdiyrov G R, Xiao Z L, Peeters F M and Kwok W K 2013 *Phys. Rev. Lett.* **111** 067001
- [49] Ma F, Reichhardt C, Gan W, Reichhardt C J O and Lew W S 2016 *Phys. Rev. B* **94** 144405
- [50] Duzgun A and Nisoli C 2021 *Phys. Rev. Lett.* **126** 047801
- [51] Mellado P, Concha A and Mahadevan L 2012 *Phys. Rev. Lett.* **109** 257203
- [52] Mellado P, Concha A, Hofhuis K and Tapia I 2023 *Sci. Rep.* **13** 1245
- [53] Bernal J D and Fowler R H 1933 *J. Chem. Phys.* **1** 515–48
- [54] Pauling L 1935 *J. Am. Chem. Soc.* **57** 2680–84
- [55] Libál A, Nisoli C, Reichhardt C J O and Reichhardt C 2018 *Phys. Rev. Lett.* **120** 027204
- [56] Le Cunuder A, Frérot I, Ortiz-Ambriz A and Tierno P 2019 *Phys. Rev. B* **99** 140405
- [57] Lee D Y and Tierno P 2018 *Phys. Rev. Mater.* **2** 112601
- [58] Holzapfel W B 1972 *J. Chem. Phys.* **56** 712
- [59] Benoit M, Marx D and Parrinello M 1998 *Nature* **392** 258–61
- [60] Morgan J P, Stein A, Langridge S and Marrows C H 2011 *Nat. Phys.* **7** 75–79
- [61] Cumby J, Bayliss R D, Berry F J and Greaves C 2016 *Dalton Trans.* **45** 11801–6
- [62] Chattopadhyay S et al 2017 *Sci. Rep.* **7** 14506
- [63] Tsirlin A A, Rousochatzakis I, Filimonov D, Batuk D, Frontzek M and Abakumov A M 2017 *Phys. Rev. B* **96** 094420
- [64] Beauvois K, Simonet V, Petit S, Robert J, Bourdarot F, Gospodinov M, Mukhin A A, Ballou R, Skumryev V and Ressouche E 2020 *Phys. Rev. Lett.* **124** 127202
- [65] Le M D et al 2021 *Phys. Rev. B* **103** 104423
- [66] Rodríguez-Gallo C, Ortiz-Ambriz A and Tierno P 2021 *Phys. Rev. Res.* **3** 043023

Part VI

CONCLUSIONS

CONCLUSIONS

This thesis has focused on investigating different physical phenomena that emerge when a colloidal system displays geometric frustration. Such frustration emerges from the competition between the symmetry of the particle interactions and the geometry of an underlying lattice of double wells. The colloidal system has been modelled by using Brownian dynamic simulations, and it was also realized via experiments using soft lithography and optical tweezers. In part of this work, we also compare our results with theoretical predictions from our collaborator Dr. Cristiano Nisoli at Los Alamos National Lab (Los Alamos, USA). We show that our simulations are in quantitative and qualitative agreement with the experiments, and we have used them as a tool to explore a wide range of physical parameters. The thesis can be divided into four different parts. In each of them, we have addressed a different problem in a frustrated system using the colloidal artificial ice as a model.

In the first result of this thesis, reflected on publication of [Chapter 6](#) in [Section 6.1](#) and [76], we have explored the effects of pinning the colloids at the boundaries of an artificial colloidal ice to see its influence on the bulk behavior. We have also investigated the effect of varying the system size and how size influences the frustration of the system. In particular, we have used different types of boundary conditions: periodic boundaries, non-fixed boundaries, antiferromagnetic boundaries, domain wall boundaries, and a combination of the last two. Of all these types of lateral confinement, we found that antiferromagnetic boundaries are the most effective at reaching the ground state configuration rapidly. Since for finite size system the ground state configuration must be compatible with the boundaries, tuning these boundaries allows us to control the final state of the system. With domain wall boundaries and free boundaries, we observed an accumulation of topological charges close to the outer vertices. In domain wall boundary systems, both negative and positive charges accumulate on the lattice sides. For the free boundary system, we only observe an accumulation of negative topological charges. This behavior was expected due to the radial polarization effect, i.e., repulsive colloids are expelled from the lattice sides by the influence of repulsive and isotropic interactions between them. Finally, we realize and investigate the dynamics of topological charges in two different systems with a mixture of antiferromagnetic boundaries and domain wall corners. The first system presented an enclosed topological charge equal to ± 4 and the second equal to 0. In the first case, we observed spontaneous symmetry breaking where the domain wall corners were connected either vertically or horizontally by a string of vertices that were not in the ground state configuration. In the second case,

by increasing the applied field, the system is separated by a line of defects into two possible ground states. Previous works, mainly based on theoretical predictions, analyzed about fixed boundary conditions [45, 186–188]. The possibility of tuning the bulk behavior of a frustrated system by properly engineering the boundaries may inspire different technological applications based on interacting magnetic spin systems [189]. Moreover, this work has focused on a 2-fold degenerate ground state system, while natural systems can present a 6-fold degenerate ground state at a vertex level. Thus, further work can be done to further investigate the behavior of a highly degenerated system under fixed boundary conditions.

The second result, reflected in the publication reported in [Chapter 6 in Section 6.2](#) [145], was an attempt to recover the 6-fold degeneracy of a 3D magnetic spin system at a tetrahedron level using a square 2D Artificial Colloidal Ice. This project does not have any experimental realization due to the limitation of finding paramagnetic colloidal particles characterized by a particular value of the volumetric magnetic susceptibility. Thus, it was mainly a simulation work. To realize this degeneracy, we vary both the size of the traps and the particle's magnetic susceptibility. While, our calculations show that it was theoretically possible to achieve this degeneracy, we did not recover it numerically. Indeed, the presence of long-range interactions between the paramagnetic colloidal particles forced the system to reach the same ground state expected for a square Artificial Colloidal Ice filled with monodisperse particles. This behavior was obtained only for relatively small perpendicular magnetic fields (< 100 mT). For higher amplitudes (> 100 mT), the system displays a re-entrant behavior, where particles locate near the top of the central hill, due to high interparticle interaction. To further investigate this effect, we performed more simulations by varying the magnetic field rates. For ramp values below 0.035 mT/s we observed that the maximum amount of ground state vertices was reached for lower magnetic field values. On the other hand, at high field rates, the peak lowers its intensity until it disappears. We finally investigate the presence of memory by cycling our system under different magnetic field protocols. In the first applied cycle, we linearly increase the magnetic field from 0 mT to 200 mT and then decrease it at the same rate. We find that the system, after one cycle, exhibits a higher fraction of ground state vertices in comparison with the initial random configuration. The second cycle applied was performed for intermediate magnetic field values (around 100 mT). In this case, we computed the spin overlap order parameter, i.e., the normalized number of spins that conserve the spin orientation after each cycle. We observed that for slow system cycling rates, such order parameter increases by performing cycles around 0.25 to 0.45. Hence by performing 8 cycles the number of spins that conserve their orientation increases from the 25% to 45%. With this work, we propose an alternative way to achieve degeneracy in a square 2D ACI. These results indicate that, compared to ASI, the colloidal ice does not display a strong memory of its previous state. Such

effect could be attributed either to thermal fluctuations or disorder resulting from the different magnetic couplings between the two types of paramagnetic colloids. This work also complements other previous works that investigate the emergence of memory effects on ACI and ASI systems [190, 191].

In the third project, reflected in publication of [Chapter 6](#) in [Section 6.3](#) and [146] we studied the influence of varying the geometry in an ACI by keeping its topology invariant. We used a combination of numerical simulations and experiments to investigate how topological charges are affected by this transformation. The geometric transformation was performed between two types of mixed coordination lattices: the Cairo and the Shakti both with mixed coordination numbers $z = 3$ and $z = 4$. To be able to perform such a transformation by keeping the interparticle distance constant, we reduced the length of some double wells and used as a control parameter the bond angle θ , which was varied from 0° (Shakti lattice) to 30° (Cairo lattice). The main results obtained in this work were the observation of an accumulation of topological charges at a certain lattice location for almost all the observed angles except one. We observed a transfer of topological charge between different sublattices that can be tuned in sign and strength, and that this effect vanished at a crossing point, which behaves as an ice-rule point. The experimental realization of the Cairo geometry was performed with a new experimental protocol based on SU-8 photoresist on the top of a silicon wafer and the final substrate was made of PDMS on the top of a coverglass. The new fabrication protocol allowed me to obtain more reproducible samples and to extend the lifetime of the samples (up to one week), which substantially improved the experimental system compared to previous know-how in the group. Experiments were in quantitative agreement with numerical simulations. And by predicting an inversion of the charge transfer, we also predict via numerical simulations a crossing point deduced in simulations to be 27.3° . Additional work should be performed in this highly degenerate ACI with mixed coordination to better understand the nature of the transition induced by the geometric transformation. We expect that the results from these investigations could be further extended to other magnetic systems, such as in ASI and 3D natural frustrated materials.

In the last project, reflected on publication of [Chapter 6](#) in [Section 6.4](#) [147]. We investigate in detail the low-energy state of the Cairo lattice. In this lattice, the colloidal particles are arranged within double wells placed on the edges of irregular pentagons that tessellate the space. In this mixed coordination lattice, in the three coordination vertices, we impose that not all the bistable gravitational traps have the same dimension. We studied the evolution of the system by increasing linearly the magnetic field value, as in other projects. We computed diverse order parameters to characterize the low-energy states. Furthermore, we realized that at high interparticle magnetic interactions, the colloidal particles in the pentagon edges tend to have an antiferromagnetic configuration, generating antiferromagnetic chiral configurations. Thus, we computed the chirality of each pentagon at different magnetic field values.

We observed how the system evolves towards an antiferromagnetic configuration of plaquette, but it did not reach it due to geometric frustration. To further explore these phenomena, we also computed the fraction of frustrated neighboring pentagons, obtaining the values of 0.68, 3.5 of the 5 nearest neighbors pentagons were frustrated. Thus, we demonstrated that the Cairo lattice is a highly degenerate system and is a frustrated antiferrotoroid. However, reaching the zero-temperature state of the colloidal Cairo ice remains a challenge. Using Monte Carlo approaches could be an alternative to observe the low-energy state of this type of frustrated lattice.

To conclude, in this thesis, we have contributed to the multidisciplinary field of geometric frustration by using a 2D microscopic model system called Artificial Colloidal Ice. Apart from the four different articles that appear in this thesis, we have also learned and improved different soft-lithography techniques to miniaturize the system and thus to increase the role of thermal fluctuations at highly interacting states. We also designed more complex lattices beyond the ones explored in this thesis. For example: we tessellated the space with pentagons and heptagons, generating two types of odd loops, in comparison with the Cairo lattice that only has pentagons. Since all these results are still on a preliminary stage, we did not include them in this thesis.



Part VII

APPENDIX



PROTOCOL BASED ON AZ₁₅₁₂ HS RESIST

1. Clean a cover glass carefully with:
 - a) detergent + water
 - b) Deionized water
 - c) Acetone
 - d) Isopropanol
 - e) Dry with a Nitrogen gun
2. Dry the coverglass by placing it on a hot plate at 125°C during at least 10 minutes.
3. Spin coat TI primer at 4000 rpm for 20 s with an acceleration of 1000 rpm/s
4. Bake for 2 minutes in a hot plate at 120°C
5. Spin coat AZ₁₅₁₂ HS photoresist
 - a) during 5 s at 500 rpm with an acceleration of 250 rpm/s
 - b) during 30 s at 1000 rpm with an acceleration of 500 rpm/s
6. Bake for 3 minutes on a hot plate at 95°C
7. 5 seconds of hard contact
8. Expose during 3.4 s (with a UV light dose of 57,8 mJ/cm²) with i-line configuration, $\lambda = 365\text{nm}$
9. Develop for 7 s by deep dipping the sample in AZ 726 MIF

PROTOCOL USED TO REALIZE THE MICROSTRUCTURES BASED ON SU-8 AND PDMS REPLICA

1. Silica's master preparation:
 - a) Dehydration of the silicon wafer for 10 minutes at 200°C on a hot plate
 - b) Plasma cleaning of the silicon wafer for 1 minute at the pressure of 1 Torr
 - c) SU-8 3005 spin coating
 - i. During 10 s at 500 rpm with an acceleration of 100 rpm/s
 - ii. During 120 s at 4000 rpm with an acceleration of 300 rpm/s
 - d) Bake on a hot plate for 2 minutes at 95°C
 - e) Cool down to room temperature (wait ~ 2 minutes)
 - f) Expose during 5.6 s (with a UV light dose of 100 mJ/cm²) with i-line configuration, $\lambda = 365nm$
 - g) Perform post-exposure bake of the film on a hot plate
 - i. 1 minute at 65°C
 - ii. 1 minute at 95°C
 - h) Develop the film during 30 s with propylene-glycol monomethyl ether acetate
 - i) Bake on a hot plate for 30 minutes at 95°C and then 10 minutes at 65°C
2. Silica's master silanization:
 - a) Plasma cleaning of the silicon wafer with SU-8 microstructure during 1 minute at 1 Torr
 - b) Put the sample inside a vacuum chamber and place it near to a petri dish with a drop of Silane (SiH_4), and leave it for at least 1 hour.
3. PDMS preparation:
 - a) Put 100 g of silicone elastomer and 10 g of silicone elastomer curing agent in a plastic container
 - b) Mix both components vigorously with a glass bar until the mixture has a lot of small bubbles, the mixture will acquire a whiter color

- c) Put the plastic container and the PDMS mixture in a vacuum chamber until no bubbles are observed.
4. PDMS layer preparation:
 - a) Coat the silicon wafer in a spin coater at 4000 rpm during 1 minute with an acceleration of 2000 rpm/s
 - b) Bake the sample in a leveled oven for 4 h at 65°C or 30 min in a hot plate at 95°C
 5. PDMS lift-off process:
 - a) Clean a coverglass with soap+deionized water, deionized water, ethanol, acetone, and finally isopropanol
 - b) Dry the coverglass with a Nitrogen gun
 - c) Dehydrate the coverglass at 95°C for 10 minutes
 - d) Remove the master+PDMS layer from the oven and wait until room temperature is reached
 - e) Perform a plasma cleaning process as before on the coverglass and master+ PDMS layer
 - f) Put the clean face of coverglass on the top of the desired microstructure
 - g) Peel off carefully with a cutter

BISTABLE GRAVITATIONAL TRAP CHARACTERIZATION FOR A THERMAL ARTIFICIAL COLLOIDAL ICE

During this thesis, we also made an effort to obtain a thermal colloidal ice. An Artificial colloidal ice where the role of thermal fluctuations is high enough that colloidal particles can jump from one gravitational minima to the other. To reach this goal, we had to further miniaturize the system. And due to resolution limitation of the photolithography technique, we also had to change the design of the double wells and the shape of the traps. Thus, we designed the bistable traps as peanut shape with different values of the smaller width w , see [Figure 44](#) (a). We used the following values of w in the design: $1.8\mu\text{m}$, $1.6\mu\text{m}$, $1.4\mu\text{m}$, $1.2\mu\text{m}$ and $1\mu\text{m}$. We used the idea that in the smaller width of our gravitational trap, the electrostatic repulsion between the colloidal particle and the wall is bigger than in the gravitational minima. The higher repulsion in this width is due to the lower distance between the particle and the wall within the double well. This will make the repulsion between electric double layers higher. Hence, the particle will try to avoid being located in the middle. To verify this hypothesis, we prepared the sample by using the soft lithography protocol described in [Appendix B](#). Then, we prepared a colloidal suspension and deposited it on top of the lithographic substrate and finally sealed it with silicon paste or parafilm. We sonicated the sample for a few minutes to induce the wetting of the small grooves. Finally, we mounted the sample and ordered the colloids by optical tweezers. For those experiments, we used paramagnetic colloids of $2.8\mu\text{m}$ diameter (Dynabeads M-270, Invitrogen). We observed the behavior shown in [Figure 44](#) (b). Colloidal particles were able to jump from one minimum to the other due to Brownian motion. To further characterize the double well energy landscape, we assume thermodynamic equilibrium and use the Boltzmann distribution for the spatial probability density:

$$\rho(\mathbf{r}) = Z^{-1} \exp(-U(\mathbf{r})/k_B T) \quad (41)$$

Here, $U(\mathbf{r})$ is the potential energy as a function of particle position, and Z is a normalization constant. The probability density can be obtained directly from the particle positions $\mathbf{r}(t)$ extracted from the experiments [161]. And thus, the energy landscape that the particle feels on the top of the soft lithography groove can be calculated as shown in [Figure 44](#) (c). In agreement with our hypothesis reducing the double well central diameter increases the energy barrier seen by then particle to cross from one gravitational minima to the other.

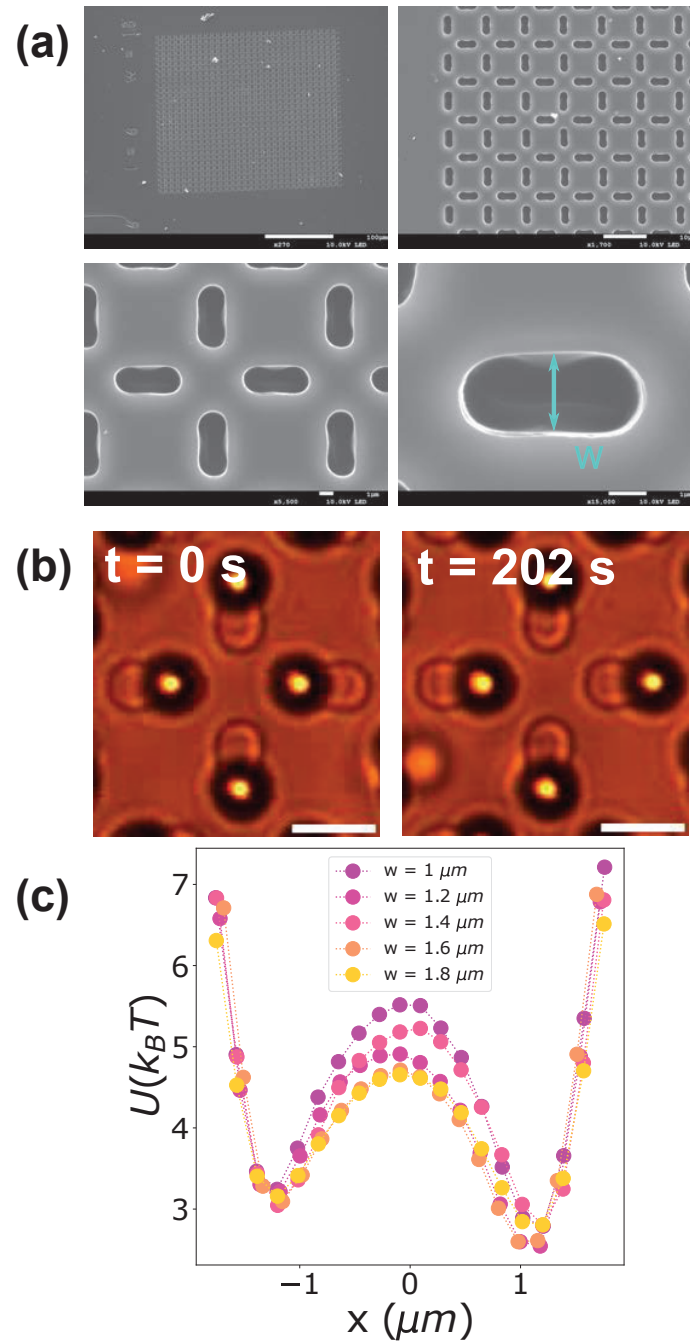


Figure 44: (a) SEM images of lithographic double well structures. Sequence of enlargements of the image of a square lattice. The smaller width (w) of the peanut-shaped trap is indicated with a cyan arrow. (b) Snapshots of particles position at a time $t = 0$ s and $t = 202$ s. In this time-lapse, Δt one particle has jumped from one gravitation minima to the other. (c) Potential energy as a function of particle position of a particle in the double well trap with different diameter (w) values.

BIBLIOGRAPHY

- [1] P.N. Pusey. *Liquids, Freezing and Glass Transition, course 10, Colloidal suspensions*. English. Elviesier Science Publisher, 1989.
- [2] Stefan Auer and Daan Frenkel. “Prediction of absolute crystal-nucleation rate in hard-sphere colloids.” In: *Nature* 409.6823 (2001), pp. 1020–1023. ISSN: 1476-4687.
- [3] Joseph D. Hutchinson, François A. Lavergne, and Roel P. A. Dullens. “Crystallization and grain growth in impurity-doped colloidal polycrystals.” In: *Phys. Rev. Mater.* 6 (7 2022), p. 075604.
- [4] Eric R. Weeks, J. C. Crocker, Andrew C. Levitt, Andrew Schofield, and D. A. Weitz. “Three-dimensional direct imaging of structural relaxation near the colloidal glass transition.” In: *Science* 287.5453 (2000), pp. 627–631. ISSN: 00368075.
- [5] K. N. Pham, A. M. Puertas, J. Bergenholtz, S. U. Egelhaaf, A. Moussaïd, P. N. Pusey, A. B. Schofield, M. E. Cates, H. Fuchs, and W. C.K. Poon. “Multiple glassy states in a simple model system.” In: *Science* 296.5565 (2002), pp. 104–106. ISSN: 00368075.
- [6] E J W Verwey. “Theory of the Stability of Lyophobic Colloids.” In: *The Journal of Physical and Colloid Chemistry* 51.3 (1947), pp. 631–636. ISSN: 0092-7023.
- [7] Yilong Han, Yair Shokef, Ahmed M Alsayed, Peter Yunker, Tom C Lubensky, and Arjun G Yodh. “Geometric frustration in buckled colloidal monolayers.” In: *Nature* 456.7224 (2008), pp. 898–903. ISSN: 1476-4687.
- [8] R F Wang et al. “Artificial ‘spin ice’ in a geometrically frustrated lattice of nanoscale ferromagnetic islands.” In: *Nature* 439.7074 (2006), pp. 303–306. ISSN: 1476-4687.
- [9] Sung Hoon Kang, Sicong Shan, Wim L Noorduyn, Mughees Khan, Joanna Aizenberg, and Katia Bertoldi. “Buckling-Induced Reversible Symmetry Breaking and Amplification of Chirality Using Supported Cellular Structures.” In: *Advanced Materials* 25.24 (2013), pp. 3380–3385.
- [10] A. Libal, C. J. Olson Reichhardt, and C. Reichhardt. “Creating Artificial Ice States Using Vortices in Nanostructured Superconductors.” In: *Phys. Rev. Lett.* 102 (23 2009), p. 237004.
- [11] Paula Mellado, Andres Concha, and L. Mahadevan. “Macroscopic Magnetic Frustration.” In: *Phys. Rev. Lett.* 109 (25 2012), p. 257203.

- [12] Yong-Lei Wang, Xiaoyu Ma, Jing Xu, Zhi-Li Xiao, Alexey Snezhko, Ralu Divan, Leonidas E Ocola, John E Pearson, Boldizar Janko, and Wai-Kwong Kwok. “Switchable geometric frustration in an artificial-spin-ice–superconductor heterosystem.” In: *Nature Nanotechnology* 13.7 (2018), pp. 560–565. ISSN: 1748-3395.
- [13] Analisa Hill, Michio Tanaka, Kevin B Aptowicz, Chandan K Mishra, A G Yodh, and Xiaoguang Ma. “Depletion-driven antiferromagnetic, paramagnetic, and ferromagnetic behavior in quasi-two-dimensional buckled colloidal solids.” In: *The Journal of Chemical Physics* 158.19 (2023), p. 194903. ISSN: 0021-9606.
- [14] Anne S Meeussen, Erdal C Oğuz, Yair Shokef, and Martin van Hecke. “Topological defects produce exotic mechanics in complex metamaterials.” In: *Nature Physics* 16.3 (2020), pp. 307–311. ISSN: 1745-2481.
- [15] E. Mengotti, L. J. Heyderman, A. Fraile Rodríguez, A. Bisig, L. Le Guyader, F. Nolting, and H. B. Braun. “Building blocks of an artificial kagome spin ice: Photoemission electron microscopy of arrays of ferromagnetic islands.” In: *Phys. Rev. B* 78 (14 2008), p. 144402.
- [16] M. Alfonso-Moro, V. Guisset, P. David, B. Canals, J. Coraux, and N. Rougemaille. “Geometrical Frustration, Correlated Disorder, and Emerging Order in a Corrugated C₆₀ Monolayer.” In: *Phys. Rev. Lett.* 131 (18 2023), p. 186201.
- [17] Ian Gilbert, Yuyang Lao, Isaac Carrasquillo, Liam O’Brien, Justin D Watts, Michael Manno, Chris Leighton, Andreas Scholl, Cristiano Nisoli, and Peter Schiffer. “Emergent reduced dimensionality by vertex frustration in artificial spin ice.” In: *Nature Physics* 12.2 (2016), pp. 162–165. ISSN: 1745-2481.
- [18] E. F. Shender and P. C. W. Holdsworth. “Order by Disorder and Topology in Frustrated Magnetic Systems.” In: *Fluctuations and Order: The New Synthesis*. Ed. by Mark Millonas. New York, NY: Springer US, 1996, pp. 259–279. ISBN: 978-1-4612-3992-5.
- [19] D. M. Dennison. “The Crystal Structure of Ice.” In: *Phys. Rev.* 17 (1 1921), pp. 20–22.
- [20] Sir W H Bragg. “The Crystal Structure of Ice.” In: *Proceedings of the Physical Society of London* 34.1 (1921), p. 98. ISSN: 1478-7814.
- [21] Linus Pauling. “The Structure and Entropy of Ice and of Other Crystals with Some Randomness of.” In: 1419.1920 (1929), pp. 2680–2684.
- [22] J W Stout and W.F. Giauque. “The Entropy of Water and the Third Law of Thermodynamics. The Heat Capacity of Ice from 15 to 273° K.” In: 58.1929 (1932).

- [23] W.F.Giauque and Muriel F. Ashley. "Molecular Rotation in Ice at 10° K. Free Energy of Formation and Entropy of Water." In: *Radiology* 19.1 (1932), pp. 66–66. ISSN: 0033-8419.
- [24] Thomas C Hansen. "The everlasting hunt for new ice phases." In: *Nature Communications* 12.1 (2021), p. 3161. ISSN: 2041-1723.
- [25] Peter Brügge and Erwin Mayer. "Complete vitrification in pure liquid water and dilute aqueous solutions." In: *Nature* 288.5791 (1980), pp. 569–571. ISSN: 1476-4687.
- [26] Giancarlo Franzese and Harry Eugene Stanley. *Water and Life: The Unique Properties of H₂O*. 2010. ISBN: 978-1-4398-0356-1.
- [27] Emma Marris. "Giant planets may host superionic water." In: *Nature* (2005). ISSN: 1476-4687.
- [28] Steven T Bramwell and Mark J Harris. "The history of spin ice." In: *Journal of Physics: Condensed Matter* 32.37 (2020), p. 374010.
- [29] D J P Morris et al. "Dirac Strings and Magnetic Monopoles in the Spin Ice Dy₂Ti₂O₇." In: *Science* 326.5951 (2009), pp. 411–414.
- [30] Jonas Greitemann. "Investigation of hidden multipolar spin order in frustrated magnets using interpretable machine learning techniques." 2019.
- [31] Roderich Moessner and Arthur P. Ramirez. "Geometrical Frustration." In: *Physics Today* (2006).
- [32] Steven T Bramwell and Michel J P Gingras. "Spin Ice State in Frustrated Magnetic Pyrochlore Materials." In: *Science* 294.5546 (2001), pp. 1495–1501.
- [33] Michel J P Gingras. *Spin Ice Lectures*, pp. 43–47. ISBN: 9783030708580.
- [34] R. Siddharthan, B. S. Shastry, A. P. Ramirez, A. Hayashi, R. J. Cava, and S. Rosenkranz. "Ising Pyrochlore Magnets: Low-Temperature Properties, "Ice Rules," and Beyond." In: *Phys. Rev. Lett.* 83 (9 1999), pp. 1854–1857.
- [35] Byron C. den Hertog and Michel J. P. Gingras. "Dipolar Interactions and Origin of Spin Ice in Ising Pyrochlore Magnets." In: *Phys. Rev. Lett.* 84 (15 2000), pp. 3430–3433.
- [36] A P Ramirez, A Hayashi, R J Cava, R Siddharthan, and B S Shastry. "Zero-point entropy in 'spin ice'." In: *Nature* 399.6734 (1999), pp. 333–335. ISSN: 1476-4687.
- [37] J D Bernal and R H Fowler. "A Theory of Water and Ionic Solution, with Particular Reference to Hydrogen and Hydroxyl Ions." In: *The Journal of Chemical Physics* 1.8 (2004), pp. 515–548. ISSN: 0021-9606.

- [38] C Castelnovo, R Moessner, and S L Sondhi. “Spin Ice, Fractionalization, and Topological Order.” In: *Annual Review of Condensed Matter Physics* 3.1 (2012), pp. 35–55.
- [39] S. V. Isakov, K. Gregor, R. Moessner, and S. L. Sondhi. “Dipolar Spin Correlations in Classical Pyrochlore Magnets.” In: *Phys. Rev. Lett.* 93 (16 2004), p. 167204.
- [40] Cristiano Nisoli. “Frustration(s) and the Ice Rule: From Natural Materials to the Deliberate Design of Exotic Behaviors BT - Frustrated Materials and Ferroic Glasses.” In: ed. by Turab Lookman and Xiaobing Ren. Cham: Springer International Publishing, 2018, pp. 57–99. ISBN: 978-3-319-96914-5.
- [41] C Castelnovo, R Moessner, and S L Sondhi. “Magnetic monopoles in spin ice.” In: *Nature* 451.7174 (2008), pp. 42–45. ISSN: 1476-4687.
- [42] Christopher L Henley. “The “Coulomb Phase” in Frustrated Systems.” In: *Annual Review of Condensed Matter Physics* 1.1 (2010), pp. 179–210.
- [43] Yilong Han. “Phase-space networks of geometrically frustrated systems.” In: *Phys. Rev. E* 80 (5 2009), p. 051102.
- [44] Leticia F Cugliandolo. “Artificial Spin-Ice and Vertex Models.” In: *Journal of Statistical Physics* 167.3 (2017), pp. 499–514. ISSN: 1572-9613.
- [45] F Colomo and A Sportiello. “Arctic Curves of the Six-Vertex Model on Generic Domains: The Tangent Method.” In: *Journal of Statistical Physics* 164.6 (2016), pp. 1488–1523. ISSN: 1572-9613.
- [46] F Colomo, A G Pronko, and P Zinn-Justin. “The arctic curve of the domain wall six-vertex model in its antiferroelectric regime.” In: *Journal of Statistical Mechanics: Theory and Experiment* 2010.03 (2010), p. L03002.
- [47] Elliott H. Lieb. “Exact Solution of the Problem of the Entropy of Two-Dimensional Ice.” In: *Phys. Rev. Lett.* 18 (17 1967), pp. 692–694.
- [48] A. W. Glaetzle, M. Dalmonte, R. Nath, I. Rousochatzakis, R. Moessner, and P. Zoller. “Quantum Spin-Ice and Dimer Models with Rydberg Atoms.” In: *Phys. Rev. X* 4 (4 2014), p. 041037.
- [49] Sandra H Skjærvø, Christopher H Marrows, Robert L Stamps, and Laura J Heyderman. “Advances in artificial spin ice.” In: *Nature Reviews Physics* 2.1 (2020), pp. 13–28. ISSN: 2522-5820.
- [50] Henry Stopfel, Erik Östman, Ioan Augustin Chioar, David Greving, Unnar B. Arnalds, Thomas P.A. Hase, Aaron Stein, Björgvin Hjörvarsson, and Vassilios Kapaklis. “Magnetic order and energy-scale hierarchy in artificial spin-ice structures.” In: *Physical Review B* 98.1 (2018). ISSN: 24699969.

- [51] Alan Farhan et al. “Emergent magnetic monopole dynamics in macroscopically degenerate artificial spin ice.” In: *Science Advances* 5.2 (2019), eaav6380.
- [52] H. Arava, N. Leo, D. Schildknecht, J. Cui, J. Vijayakumar, P. M. Derlet, A. Kleibert, and L. J. Heyderman. “Engineering Relaxation Pathways in Building Blocks of Artificial Spin Ice for Computation.” In: *Phys. Rev. Appl.* 11 (5 2019), p. 054086.
- [53] H. Arava, E. Y. Vedmedenko, J. Cui, J. Vijayakumar, A. Kleibert, and L. J. Heyderman. “Control of emergent magnetic monopole currents in artificial spin ice.” In: *Phys. Rev. B* 102 (14 2020), p. 144413.
- [54] Alan Farhan et al. “Nanoscale control of competing interactions and geometrical frustration in a dipolar trident lattice.” In: *Nature Communications* 8.1 (2017), p. 995. ISSN: 2041-1723.
- [55] Erik Ostman, Henry Stopfel, Ioan-Augustin Chioar, Unnar B Arnalds, Aaron Stein, Vassilios Kapaklis, and Bjorgvin Hjorvarsson. “Interaction modifiers in artificial spin ices.” In: *Nature Physics* 14.4 (2018), pp. 375–379. ISSN: 1745-2481.
- [56] M. Goryca, X. Zhang, J. Li, A. L. Balk, J. D. Watts, C. Leighton, C. Nisoli, P. Schiffer, and S. A. Crooker. “Field-Induced Magnetic Monopole Plasma in Artificial Spin Ice.” In: *Phys. Rev. X* 11 (1 2021), p. 011042.
- [57] Yann Perrin, Benjamin Canals, and Nicolas Rougemaille. “Quasidegenerate ice manifold in a purely two-dimensional square array of nanomagnets.” In: *Phys. Rev. B* 99 (22 2019), p. 224434.
- [58] R. P. Loreto, L. A. Morais, C. I.L.De Araujo, W. A. Moura-Melo, A. R. Pereira, R. C. Silva, F. S. Nascimento, and L. A.S. Mól. “Emergence and mobility of monopoles in a unidirectional arrangement of magnetic nanoislands.” In: *Nanotechnology* 26.29 (2015). ISSN: 13616528.
- [59] Sheng Zhang, Ian Gilbert, Cristiano Nisoli, Gia-Wei Chern, Michael J Erickson, Liam O’Brien, Chris Leighton, Paul E Lammert, Vincent H Crespi, and Peter Schiffer. “Crystallites of magnetic charges in artificial spin ice.” In: *Nature* 500.7464 (2013), pp. 553–557. ISSN: 1476-4687.
- [60] Paul E Lammert, Xianglin Ke, Jie Li, Cristiano Nisoli, David M Garand, Vincent H Crespi, and Peter Schiffer. “Direct entropy determination and application to artificial spin ice.” In: *Nature Physics* 6.10 (2010), pp. 786–789. ISSN: 1745-2481.
- [61] L Anghinolfi, H Luetkens, J Perron, M G Flokstra, O Sendetskyi, A Suter, T Prokscha, P M Derlet, S L Lee, and L J Heyderman. “Thermodynamic phase transitions in a frustrated magnetic metamaterial.” In: *Nature Communications* 6.1 (2015), p. 8278. ISSN: 2041-1723.

- [62] Elena Mengotti, Laura J Heyderman, Arantxa Fraile Rodríguez, Frithjof Nolting, Remo V Hügli, and Hans-Benjamin Braun. “Real-space observation of emergent magnetic monopoles and associated Dirac strings in artificial kagome spin ice.” In: *Nature Physics* 7.1 (2011), pp. 68–74. ISSN: 1745-2481.
- [63] L. A. S. Mol, A. R. Pereira, and W. A. Moura-Melo. “Extending spin ice concepts to another geometry: The artificial triangular spin ice.” In: *Phys. Rev. B* 85 (18 2012), p. 184410.
- [64] Hilal Saglam et al. “Entropy-driven order in an array of nanomagnets.” In: *Nature Physics* 18.6 (2022), pp. 706–712. ISSN: 1745-2481.
- [65] Ian Gilbert, Gia-Wei Chern, Sheng Zhang, Liam O’Brien, Bryce Fore, Cristiano Nisoli, and Peter Schiffer. “Emergent ice rule and magnetic charge screening from vertex frustration in artificial spin ice.” In: *Nature Physics* 10.9 (2014), pp. 670–675. ISSN: 1745-2481.
- [66] Yuyang Lao et al. “Classical topological order in the kinetics of artificial spin ice.” In: *Nature Physics* 14.7 (2018), pp. 723–727. ISSN: 1745-2481.
- [67] Kseniia Makarova et al. “Low-energy states, ground states, and variable frustrations of the finite-size dipolar Cairo lattices.” In: *Phys. Rev. E* 103 (4 2021), p. 042129.
- [68] Yong-Lei Wang, Zhi-Li Xiao, Alexey Snezhko, Jing Xu, Leonidas E Ocola, Ralu Divan, John E Pearson, George W Crabtree, and Wai-Kwong Kwok. “Rewritable artificial magnetic charge ice.” In: *Science* 352.6288 (2016), pp. 962–966.
- [69] Vineeth Mohanan Parakkat, Gavin M. Macauley, Robert L. Stamps, and Kannan M. Krishnan. “Configurable Artificial Spin Ice with Site-Specific Local Magnetic Fields.” In: *Phys. Rev. Lett.* 126 (1 2021), p. 017203.
- [70] Antonio Ortiz-Ambriz and Pietro Tierno. “Engineering of frustration in colloidal artificial ices realized on microfeatured grooved lattices.” In: *Nature Communications* 7 (2016), pp. 1–7. ISSN: 20411723.
- [71] A. Libál, C. Reichhardt, and C. J. Olson Reichhardt. “Realizing colloidal artificial ice on arrays of optical traps.” In: *Physical Review Letters* 97.22 (2006), pp. 1–4. ISSN: 00319007.
- [72] Dušan Babič and Clemens Bechinger. “Noise-enhanced performance of ratchet cellular automata.” In: *Physical Review Letters* 94.14 (2005), pp. 1–4. ISSN: 00319007.
- [73] D. Babič, C. Schmitt, and C. Bechinger. “Colloids as model systems for problems in statistical physics.” In: *Chaos* 15.2 (2005). ISSN: 10541500.
- [74] C. Schmitt, B. Dybiec, P. Hänggi, and C. Bechinger. “Stochastic resonance vs. resonant activation.” In: *Europhysics Letters* 74.6 (2006), pp. 937–943. ISSN: 02955075.

- [75] Johannes Loehr, Antonio Ortiz-Ambriz, and Pietro Tierno. “Defect dynamics in artificial colloidal ice: Real-time observation, manipulation, and logic gate.” In: *Physical Review Letters* 117.16 (2016), pp. 1–5. ISSN: 10797114.
- [76] Carolina Rodríguez-Gallo, Antonio Ortiz-Ambriz, and Pietro Tierno. “Topological Boundary Constraints in Artificial Colloidal Ice.” In: *Phys. Rev. Lett.* 126 (18 2021), p. 188001.
- [77] R J Hunter and L R White. *Foundations of Colloid Science*. Foundations of Colloid Science v. 1. Clarendon Press, 1987. ISBN: 9780198551874.
- [78] Robert J. Hunter. *Introduction to modern colloid science / Robert J. Hunter*. English. 1st ed. Oxford University Press Oxford, England ; New York ; Melbourne, 1993, viii, 338 p. : ISBN: 0198553870 0198553862.
- [79] W. B. Russel, D. A. Saville, and W. R. Schowalter. *Colloidal Dispersions*. Cambridge Monographs on Mechanics. Cambridge University Press, 1989.
- [80] Vinodhan N Manoharan. “Colloidal matter: Packing, geometry, and entropy.” In: *Science* 349.6251 (2015), p. 1253751.
- [81] Theodore Hueckel, Glen M Hocky, and Stefano Sacanna. “Total synthesis of colloidal matter.” In: *Nature Reviews Materials* 6.11 (2021), pp. 1053–1069. ISSN: 2058-8437.
- [82] P N Pusey and W van Megen. “Phase behaviour of concentrated suspensions of nearly hard colloidal spheres.” In: *Nature* 320.6060 (1986), pp. 340–342. ISSN: 1476-4687.
- [83] Alice L. Thorneywork, Joshua L. Abbott, Dirk G. A. L. Aarts, and Roel P. A. Dullens. “Two-Dimensional Melting of Colloidal Hard Spheres.” In: *Phys. Rev. Lett.* 118 (15 2017), p. 158001.
- [84] Marjolein N. van der Linden, Lachlan C. Alexander, Dirk G. A. L. Aarts, and Olivier Dauchot. “Interrupted Motility Induced Phase Separation in Aligning Active Colloids.” In: *Phys. Rev. Lett.* 123 (9 2019), p. 098001.
- [85] Arnout Imhof. “Three-Dimensional Photonic Crystals Made from Colloids.” In: *Nanoscale Materials*. Ed. by Luis M Liz-Marzán and Prashant V Kamat. Boston, MA: Springer US, 2003, pp. 423–454. ISBN: 978-0-306-48108-6.
- [86] Theodore L Einstein and Timothy J Stasevich. “Epitaxial Growth Writ Large.” In: *Science* 327.5964 (2010), pp. 423–424.
- [87] Clemens Bechinger, Roberto Di Leonardo, Hartmut Löwen, Charles Reichhardt, Giorgio Volpe, and Giovanni Volpe. “Active particles in complex and crowded environments.” In: *Reviews of Modern Physics* 88.4 (2016). ISSN: 15390756.

- [88] S. J. Ebbens. “Active colloids: Progress and challenges towards realising autonomous applications.” In: *Current Opinion in Colloid and Interface Science* 21 (2016), pp. 14–23. ISSN: 18790399.
- [89] Stephen J. Ebbens and Jonathan R. Howse. “In pursuit of propulsion at the nanoscale.” In: *Soft Matter* 6.4 (2010), pp. 726–738. ISSN: 1744683X.
- [90] L Alvarez, M A Fernandez-Rodriguez, A Alegria, S Arrese-Igor, K Zhao, M Kröger, and Lucio Isa. “Reconfigurable artificial microswimmers with internal feedback.” In: *Nature Communications* 12.1 (2021), p. 4762. ISSN: 2041-1723.
- [91] Giuseppe Gonnella, Davide Marenduzzo, Antonio Suma, and Adriano Tiribocchi. “Motility-induced phase separation and coarsening in active matter.” In: *Comptes Rendus Physique* 16.3 (2015), pp. 316–331. ISSN: 18781535.
- [92] Steven van Kesteren, Laura Alvarez, Silvia Arrese-Igor, Angel Alegria, and Lucio Isa. “Self-propelling colloids with finite state dynamics.” In: *Proceedings of the National Academy of Sciences* 120.11 (2023), e2213481120.
- [93] Stuart F Knowles, Marcus Fletcher, Jeffrey Mc Hugh, Max Earle, Ulrich F Keyser, and Alice L Thorneywork. “Observing capture with a colloidal model membrane channel.” In: *Journal of Physics: Condensed Matter* 34.34 (2022), p. 344001.
- [94] Alice L Thorneywork, Jannes Gladrow, Yujia Qing, Marc Rico-Pasto, Felix Ritort, Hagan Bayley, Anatoly B Kolomeisky, and Ulrich F Keyser. “Direct detection of molecular intermediates from first-passage times.” In: *Science Advances* 6.18 (2020), eaaz4642.
- [95] Yuanjin Zhao, Luoran Shang, Yao Cheng, and Zhongze Gu. “Spherical Colloidal Photonic Crystals.” In: *Accounts of Chemical Research* 47.12 (2014), pp. 3632–3642.
- [96] Gary L Hunter and Eric R Weeks. “The physics of the colloidal glass transition.” In: *Reports on Progress in Physics* 75.6 (2012), p. 66501.
- [97] Alexandre P. Solon, Joakim Stenhammar, Raphael Wittkowski, Mehran Kardar, Yariv Kafri, Michael E. Cates, and Julien Tailleur. “Pressure and Phase Equilibria in Interacting Active Brownian Spheres.” In: *Phys. Rev. Lett.* 114 (19 2015), p. 198301.
- [98] Carla Fernández-Rico, Massimiliano Chiappini, Taiki Yanagishima, Heidi de Sousa, Dirk G. A. L. Aarts, Marjolein Dijkstra, and Roel P. A. Dullens. “Shaping colloidal bananas to reveal biaxial, splay-bend nematic, and smectic phases.” In: *Science* 369.6506 (2020), pp. 950–955.
- [99] George Gabriel Stokes. “On the Effect of the Internal Friction of Fluids on the Motion of Pendulums.” In: *Mathematical and Physical Papers* (1850), pp. 1–10.

- [100] Don S Lemons and Anthony Gythiel. “Paul Langevin ’ s 1908 paper “ On the Theory of Brownian Motion ” [“ Sur la théorie du mouvement brownien ,” C . R . Acad . Sci . (Paris) 146 , 530 – 533 (1908)] Paul Langevin ’ s 1908 paper “ On the Theory of Brownian Motion ” ‘ orie du mouvement b.” In: *American Journal of Physics* 533.1908 (2010), pp. 530–533.
- [101] Arthur Genthon. “The concept of velocity in the history of Brownian motion.” In: *The European Physical Journal H* 45.49 (2020).
- [102] Gorka Muñoz-Gil et al. “Objective comparison of methods to decode anomalous diffusion.” In: *Nature Communications* 12.1 (2021). ISSN: 20411723.
- [103] Fernando A. Oliveira, Rogelma M.S. Ferreira, Luciano C. Lapas, and Mendeli H. Vainstein. “Anomalous diffusion: A basic mechanism for the evolution of inhomogeneous systems.” In: *Frontiers in Physics* 7.FEB (2019), pp. 1–17. ISSN: 2296424X.
- [104] Maciej Lisicki and Gerhard Nägele. “Colloidal Hydrodynamics and Interfacial Effects.” In: *Soft Matter at Aqueous Interfaces*. Ed. by Peter Lang and Yi Liu. Cham: Springer International Publishing, 2016, pp. 313–386. ISBN: 978-3-319-24502-7.
- [105] W B Russel, D A Saville, and W R Schowalter. *Colloidal Dispersions*. Cambridge: Cambridge University Press, 1989. ISBN: 9780521426008.
- [106] E M Purcell. “Life at low Reynolds number.” In: *American Journal of Physics* 45.1 (1977), pp. 3–11. ISSN: 0002-9505.
- [107] “Intermolecular and Surface Forces (Third Edition).” In: ed. by Jacob N. Israelachvili. Third Edition. San Diego: Academic Press, 2011, pp. xxiii–xxviii.
- [108] “Suspension Stability and Particle Capture.” In: *Physicochemical Hydrodynamics*. John Wiley and Sons, Ltd, 1994, pp. 237–275. ISBN: 9780471725138.
- [109] Longcheng Liu and Ivars Neretnieks. “Svensk Kärnbränslehantering AB Interaction between colloidal particles Literature Review.” In: February (2010).
- [110] F. London. “The general theory of molecular forces.” In: *Trans. Fara. Soc.* 8.8 (1936), pp. 8–26.
- [111] H.C. Hamaker. “ The london-van der Waals attraction between spherical particles.” In: *Physica IV, n 10 1* (1937).
- [112] Michael Kaszuba, Jason Corbett, Fraser Mc Neil Watson, and Andrew Jones. “High-concentration zeta potential measurements using light-scattering techniques.” In: *Philosophical Transactions of the Royal Society A: Mathematical, Physical and Engineering Sciences* 368.1927 (2010), pp. 4439–4451. ISSN: 1364503X.

- [113] Deborah Leckband and Jacob Israelachvili. “Intermolecular forces in biology.” In: *Quarterly Reviews of Biophysics* 34.2 (2001), 105–267.
- [114] Egor V Yakovlev et al. “Tunable two-dimensional assembly of colloidal particles in rotating electric fields.” In: *Scientific Reports* 7.1 (2017), p. 13727. ISSN: 2045-2322.
- [115] Florian Katzmeier, Bernhard Altaner, Jonathan List, Ulrich Gerland, and Friedrich C. Simmel. “Emergence of Colloidal Patterns in ac Electric Fields.” In: *Phys. Rev. Lett.* 128 (5 2022), p. 058002.
- [116] Ricard Alert, Jaume Casademunt, and Pietro Tierno. “Landscape-Inversion Phase Transition in Dipolar Colloids: Tuning the Structure and Dynamics of 2D Crystals.” In: *Phys. Rev. Lett.* 113 (19 2014), p. 198301.
- [117] Pietro Tierno. “Recent advances in anisotropic magnetic colloids: realization, assembly and applications.” In: *Phys. Chem. Chem. Phys.* 16.43 (2014), pp. 23515–23528.
- [118] Aldo Spatafora-Salazar, Dana M. Lobmeyer, Lucas H. P. Cunha, Kedar Joshi, and Sibani Lisa Biswal. “Hierarchical assemblies of superparamagnetic colloids in time-varying magnetic fields.” In: *Soft Matter* 17 (5 2021), pp. 1120–1155.
- [119] James E. Martin and Alexey Snezhko. “Driving self-assembly and emergent dynamics in colloidal suspensions by time-dependent magnetic fields.” In: 76.12 (Nov. 2013). ISSN: 0034-4885.
- [120] Weijia Wen, Lingyun Zhang, and Ping Sheng. “Planar Magnetic Colloidal Crystals.” In: *Phys. Rev. Lett.* 85 (25 2000), pp. 5464–5467.
- [121] Cristiano Nisoli. “The concept of spin ice graphs and a field theory for their charges.” In: *AIP Advances* 10.11 (2020). ISSN: 21583226.
- [122] Cristiano Nisoli, Jie Li, Xianglin Ke, D. Garand, Peter Schiffer, and Vincent H. Crespi. “Effective Temperature in an Interacting Vertex System: Theory and Experiment on Artificial Spin Ice.” In: *Phys. Rev. Lett.* 105 (4 2010), p. 047205.
- [123] D J P Morris et al. “Dirac Strings and Magnetic Monopoles in the Spin Ice Dy₂Ti₂O₇.” In: *Science* 326.5951 (2009), pp. 411–414.
- [124] Andrew D. King, Cristiano Nisoli, Edward D. Dahl, Gabriel Poulin-Lamarre, and Alejandro Lopez-Bezanilla. “Qubit spin ice.” In: *Science* 373.6554 (2021), pp. 576–580.
- [125] András Libál, Dong Yun Lee, Antonio Ortiz-Ambriz, Charles Reichhardt, Cynthia J O Reichhardt, Pietro Tierno, and Cristiano Nisoli. “Ice rule fragility via topological charge transfer in artificial colloidal ice.” In: *Nature Communications* 9.1 (2018), p. 4146. ISSN: 2041-1723.
- [126] Cristiano Nisoli. “Unexpected Phenomenology in Particle-Based Ice Absent in Magnetic Spin Ice.” In: *Phys. Rev. Lett.* 120 (16 2018), p. 167205.

- [127] Cristiano Nisoli. “Dumping topological charges on neighbors: ice manifolds for colloids and vortices.” In: *New Journal of Physics* 16.11 (2014), p. 113049.
- [128] Dong Yun Lee and Pietro Tierno. “Energetics and the ground state quest in an artificial triangular colloidal ice.” In: *Phys. Rev. Mater.* 2 (11 2018), p. 112601.
- [129] Gia-Wei Chern, Paula Mellado, and O. Tchernyshyov. “Two-Stage Ordering of Spins in Dipolar Spin Ice on the Kagome Lattice.” In: *Phys. Rev. Lett.* 106 (20 2011), p. 207202.
- [130] Gia Wei Chern and Oleg Tchernyshyov. “Magnetic charge and ordering in kagome spin ice.” In: *Philosophical Transactions of the Royal Society A: Mathematical, Physical and Engineering Sciences* 370.1981 (2012), pp. 5718–5737. ISSN: 1364503X.
- [131] A. Libal, C. Nisoli, C. J. O. Reichhardt, and C. Reichhardt. “Inner Phases of Colloidal Hexagonal Spin Ice.” In: *Phys. Rev. Lett.* 120 (2 2018), p. 027204.
- [132] Anne Le Cunuder, Irénée Frérot, Antonio Ortiz-Ambriz, and Pietro Tierno. “Competing orders in colloidal kagome ice: Importance of the in-trap motion of the particles.” In: *Phys. Rev. B* 99 (14 2019), p. 140405.
- [133] Henry Stopfel, Erik Ostman, Ioan-Augustin Chioar, David Greving, Unnar B. Arnalds, Thomas P. A. Hase, Aaron Stein, Björgvin Hjörvarsson, and Vassilios Kapaklis. “Magnetic order and energy-scale hierarchy in artificial spin-ice structures.” In: *Phys. Rev. B* 98 (1 2018), p. 014435.
- [134] Erdal C. O, Antonio Ortiz-Ambriz, Hadas Shem-Tov, Eric Babià-Soler, Pietro Tierno, and Yair Shokef. “Topology Restricts Quasidegeneracy in Sheared Square Colloidal Ice.” In: *Phys. Rev. Lett.* 124.23 (2020), p. 238003.
- [135] G. Moller and R. Moessner. “Artificial square ice and related dipolar nanoarrays.” In: *Physical Review Letters* 96.23 (2006), pp. 1–4. ISSN: 00319007.
- [136] Yann Perrin, Benjamin Canals, and Nicolas Rougemaille. “Extensive degeneracy, Coulomb phase and magnetic monopoles in artificial square ice.” In: *Nature* 540.7633 (2016), pp. 410–413. ISSN: 1476-4687.
- [137] F. Caravelli. “A model for the mediated artificial square ice phenomenology.” In: *Europhysics Letters* 130.4 (2020), p. 48001.
- [138] L. A. S. Mól, W. A. Moura-Melo, and A. R. Pereira. “Conditions for free magnetic monopoles in nanoscale square arrays of dipolar spin ice.” In: *Phys. Rev. B* 82 (5 2010), p. 054434.
- [139] R C Silva, F S Nascimento, L A S Mól, W A Moura-Melo, and A R Pereira. “Thermodynamics of elementary excitations in artificial magnetic square ice.” In: *New Journal of Physics* 14.1 (2012), p. 15008.

- [140] E. Y. Vedmedenko. “Dynamics of Bound Monopoles in Artificial Spin Ice: How to Store Energy in Dirac Strings.” In: *Phys. Rev. Lett.* 116 (7 2016), p. 077202.
- [141] S T Bramwell, S R Giblin, S Calder, R Aldus, D Prabhakaran, and T Fennell. “Measurement of the charge and current of magnetic monopoles in spin ice.” In: *Nature* 461.7266 (2009), pp. 956–959. ISSN: 1476-4687.
- [142] L A Mól, R L Silva, R C Silva, A R Pereira, W A Moura-Melo, and B V Costa. “Magnetic monopole and string excitations in two-dimensional spin ice.” In: *Journal of Applied Physics* 106.6 (2009), p. 63913. ISSN: 0021-8979.
- [143] Egon Matijević. “Introduction to Modern Colloid Science, Oxford University Press, 1993, viii + 338 pages.” In: *Langmuir* 12.2 (1996), p. 605. ISSN: 0743-7463.
- [144] Andrea Albano et al. “How to modify lammmps: From the prospective of a particle method researcher.” In: *ChemEngineering* 5.2 (2021), pp. 1–57. ISSN: 23057084.
- [145] Carolina Rodríguez-Gallo, Antonio Ortiz-Ambriz, and Pietro Tierno. “Degeneracy and hysteresis in a bidisperse colloidal ice.” In: *Phys. Rev. Res.* 3 (4 2021), p. 043023.
- [146] Carolina Rodríguez-Gallo, Antonio Ortiz-Ambriz, Cristiano, and Pietro Tierno. “Geometrical control of topological charge transfer in Shakti-colloidal ice.” In: *Communications Physics* 6.1 (2023), p. 113. ISSN: 2399-3650.
- [147] Carolina Rodríguez-Gallo, Antonio Ortiz-Ambriz, Cristiano Nisoli, and Pietro Tierno. “Ice rule breakdown and frustrated antiferrotoroidicity in an artificial colloidal Cairo ice.” In: *New Journal of Physics* 25.10 (2023), p. 103007.
- [148] Kotaro Oyama, Vadim Zeeb, Yuki Kawamura, Tomomi Arai, Mizuho Gotoh, Hideki Itoh, Takeshi Itabashi, Madoka Suzuki, and Shin’ichi Ishiwata. “Triggering of high-speed neurite outgrowth using an optical microheater.” In: *Scientific Reports* 5.1 (2015), p. 16611. ISSN: 2045-2322.
- [149] D. J. Carnegie, D. J. Stevenson, M. Mazilu, F. Gunn-Moore, and K. Dhoklakia. “Guided neuronal growth using optical line traps.” In: *Opt. Express* 16.14 (2008), pp. 10507–10517.
- [150] Steven M Block, David F Blair, and Howard C Berg. “Compliance of bacterial flagella measured with optical tweezers.” In: *Nature* 338.6215 (1989), pp. 514–518. ISSN: 1476-4687.
- [151] Jens-Christian Meiners and Stephen R. Quake. “Direct Measurement of Hydrodynamic Cross Correlations between Two Particles in an External Potential.” In: *Phys. Rev. Lett.* 82 (10 1999), pp. 2211–2214.

- [152] J. C. Crocker, J. A. Matteo, A. D. Dinsmore, and A. G. Yodh. “Entropic Attraction and Repulsion in Binary Colloids Probed with a Line Optical Tweezer.” In: *Phys. Rev. Lett.* 82 (21 1999), pp. 4352–4355.
- [153] R. Di Leonardo, S. Keen, F. Ianni, J. Leach, M. J. Padgett, and G. Ruocco. “Hydrodynamic interactions in two dimensions.” In: *Phys. Rev. E* 78 (3 2008), p. 031406.
- [154] Janderson R Rodrigues and Vilson R Almeida. “Tailoring Optical Forces Behavior in Nano-optomechanical Devices Immersed in Fluid Media.” In: *Scientific Reports* 7.1 (2017), p. 14325. ISSN: 2045-2322.
- [155] Jesper Glückstad. “Sorting particles with light.” In: *Nature Materials* 3.1 (2004), pp. 9–10. ISSN: 1476-4660.
- [156] Nicolas Descharmes, Ulagalandha Perumal Dharanipathy, Zhaolu Diao, Mario Tonin, and Romuald Houdré. “Single particle detection, manipulation and analysis with resonant optical trapping in photonic crystals.” In: *Lab Chip* 13 (16 2013), pp. 3268–3274.
- [157] Steven B. Smith, Yujia Cui, and Carlos Bustamante. “Overstretching B-DNA: The Elastic Response of Individual Double-Stranded and Single-Stranded DNA Molecules.” In: *Science* 271.5250 (1996), pp. 795–799.
- [158] A. Ashkin. “History of optical trapping and manipulation of small-neutral particle, atoms, and molecules.” In: *IEEE Journal of Selected Topics in Quantum Electronics* 6.6 (2000), pp. 841–856.
- [159] Philip H. Jones, Onofrio M. Maragò, and Giovanni Volpe. *Optical Tweezers: Principles and Applications*. Cambridge University Press, 2015.
- [160] A Ashkin and J M Dziedzic. “Observation of light scattering from non-spherical particles using optical levitation.” In: *Appl. Opt.* 19.5 (1980), pp. 660–668.
- [161] Lowell I McCann, Mark Dykman, and Brage Golding. “Thermally activated transitions in a bistable three-dimensional optical trap.” In: *Nature* 402.6763 (1999), pp. 785–787. ISSN: 1476-4687.
- [162] J Gladrow, M Ribezzi-Crivellari, F Ritort, and U F Keyser. “Experimental evidence of symmetry breaking of transition-path times.” In: *Nature Communications* 10.1 (2019), p. 55. ISSN: 2041-1723.
- [163] Jennifer E Curtis, Brian A Koss, and David G Grier. “Dynamic holographic optical tweezers.” In: *Optics Communications* 207.1 (2002), pp. 169–175. ISSN: 0030-4018.
- [164] David G Grier. “A revolution in optical manipulation.” In: *Nature* 424.6950 (2003), pp. 810–816. ISSN: 1476-4687.

- [165] Shampy Mansha, Parikshit Moitra, Xuewu Xu, Tobias W W Mass, Rasna Maruthiyodan Veetil, Xinan Liang, Shi-Qiang Li, Ramon Paniagua-Dominguez, and Arseniy I Kuznetsov. “High resolution multispectral spatial light modulators based on tunable Fabry-Perot nanocavities.” In: *Light: Science and Applications* 11.1 (2022), p. 141. ISSN: 2047-7538.
- [166] Y. Isomae, N. Sugawara, N. Iwasaki, T. Honda, and K. Amari. “Phase-only spatial light modulator having high reflectance, high-definition pixels and high photo-durability.” In: *Digital Optical Technologies 2021*. Ed. by Bernard C. Kress and Christophe Peroz. Vol. 11788. International Society for Optics and Photonics. SPIE, 2021, 117880T.
- [167] Miles Padgett and Roberto Di Leonardo. “Holographic optical tweezers and their relevance to lab on chip devices.” In: *Lab on a Chip* 11.7 (2011), pp. 1196–1205. ISSN: 14730189.
- [168] R. W. Gerchberg. “A practical algorithm for the determination of phase from image and diffraction plane pictures.” In: *Optik* 35 (1972), pp. 237–246.
- [169] Jan Gieseler et al. “Optical tweezers – from calibration to applications: a tutorial.” In: *Adv. Opt. Photon.* 13.1 (2021), pp. 74–241.
- [170] Ethan Schonbrun, Rafael Piestun, Pamela Jordan, Jon Cooper, Kurt D Wulff, Johannes Courtial, and Miles Padgett. “3D interferometric optical tweezers using a single spatial light modulator.” In: *Opt. Express* 13.10 (2005), pp. 3777–3786.
- [171] Daniel Espinosa, Diogo Soga, Sarah Alves, Leonardo De Boni, Sergio Carlos Zilio, and Antonio Martins Figueiredo Neto. “Investigation of the optical absorption of a magnetic colloid from the thermal to the electronic time-scale regime: measurement of the free-carrier absorption cross-section.” In: *J. Opt. Soc. Am. B* 29.3 (2012), pp. 280–285.
- [172] A. Del Campo and C. Greiner. “SU-8: A photoresist for high-aspect-ratio and 3D submicron lithography.” In: *Journal of Micromechanics and Microengineering* 17.6 (2007). ISSN: 09601317.
- [173] Rodrigo Martinez-Duarte and Marc J. Madou. “SU-8 photolithography and its impact on microfluidics.” In: *Microfluidics and Nanofluidics Handbook: Fabrication, Implementation, and Applications 2006* (2016), pp. 231–268.
- [174] Erik Enriquez, Daniel Shreiber, Éric Ngo, Mat Ivill, Samuel G Hirsch, Cory Hubbard, and Melanie W Cole. “Optimization of Thick Negative Photoresist for Fabrication of Interdigitated Capacitor Structures.” In: 2015.
- [175] Tiffany Baëtens and Steve Arscott. “Planarization and edge bead reduction of spin-coated polydimethylsiloxane.” In: *Journal of Micromechanics and Microengineering* 29.11 (2019), p. 115005.

- [176] Myeongwoo Kang, Jae Hwan Byun, Sangcheol Na, and Noo Li Jeon. "Fabrication of functional 3D multi-level microstructures on transparent substrates by one step back-side UV photolithography." In: *RSC Adv.* 7.22 (2017), pp. 13353–13361.
- [177] Stephan Urs Keller, D. Haefliger, and Anja Boisen. "Fabrication of thin SU-8 cantilevers: initial bending, release and time stability." English. In: *Journal of Micromechanics and Microengineering* 20.4 (2010), p. 45024. ISSN: 0960-1317.
- [178] Letizia Amato, Stephan S. Keller, Arto Heiskanen, Maria Dimaki, Jenny Emnéus, Anja Boisen, and Maria Tenje. "Fabrication of high-aspect ratio SU-8 micropillar arrays." English. In: *Microelectronic Engineering* 98 (2012). 37th International Conference on Micro and Nano Engineering, MNE 2011 ; Conference date: 19-09-2011 Through 23-09-2011, pp. 483–487. ISSN: 0167-9317.
- [179] Stephan Urs Keller, Gabriela Blagoi, Michael Lillemose, Daniel Häfliger, and Anja Boisen. "Processing of thin SU-8 films." English. In: *Journal of Micromechanics and Microengineering* 18.12 (2008), p. 125020. ISSN: 0960-1317.
- [180] H Lorenz, M Despont, N Fahrni, N LaBianca, P Renaud, and P Vettiger. "SU-8: a low-cost negative resist for MEMS." In: *Journal of Micromechanics and Microengineering* 7.3 (1997), p. 121.
- [181] Xin Cao, Emanuele Panizon, Andrea Vanossi, Nicola Manini, and Clemens Bechinger. "Orientational and directional locking of colloidal clusters driven across periodic surfaces." In: *Nature Physics* 15.8 (2019), pp. 776–780. ISSN: 1745-2481.
- [182] Sangeeta N Bhatia and Donald E Ingber. "Microfluidic organs-on-chips." In: *Nature Biotechnology* 32.8 (2014), pp. 760–772. ISSN: 1546-1696.
- [183] James Friend and Leslie Yeo. "Fabrication of microfluidic devices using polydimethylsiloxane." In: *Biomicrofluidics* 4.2 (2010). ISSN: 1932-1058.
- [184] Alessio Zaccone, Hua Wu, Marco Lattuada, and Massimo Morbidelli. "Correlation between Colloidal Stability and Surfactant Adsorption/Association Phenomena Studied by Light Scattering." In: *The Journal of Physical Chemistry B* 112.21 (2008), p. 6733. ISSN: 1520-6106.
- [185] John Crocker and David Grier. "Methods of Digital Video Microscopy for Colloidal Studies | Elsevier Enhanced Reader." In: *Journal of Colloid and Interface Science* 179.179 (1995), pp. 298–310.
- [186] Bryan Debin, Jean-François de Kemmeter, and Philippe Ruelle. *Fluctuations and arctic curve in the Aztec diamond.* 2023.

- [187] L. F. Cugliandolo, G. Gonnella, and A. Pelizzola. “Six-vertex model with domain wall boundary conditions in the Bethe-Peierls approximation.” In: *Journal of Statistical Mechanics: Theory and Experiment* 2015.6 (2015). ISSN: 17425468.
- [188] F Colomo and A G Pronko. “The Arctic Curve of the Domain-Wall Six-Vertex Model.” In: *Journal of Statistical Physics* 138.4 (2010), pp. 662–700. ISSN: 1572-9613.
- [189] *Computation in artificial spin ice*. Vol. ALIFE 2018: The 2018 Conference on Artificial Life. ALIFE 2023: Ghost in the Machine: Proceedings of the 2023 Artificial Life Conference. 2018, pp. 15–22.
- [190] A. Libál, C. Reichhardt, and C. J. Olson Reichhardt. “Hysteresis and return-point memory in colloidal artificial spin ice systems.” In: *Phys. Rev. E* 86 (2 2012), p. 021406.
- [191] Ian Gilbert, Gia-Wei Chern, Bryce Fore, Yuyang Lao, Sheng Zhang, Cristiano Nisoli, and Peter Schiffer. “Direct visualization of memory effects in artificial spin ice.” In: *Phys. Rev. B* 92 (10 2015), p. 104417.